Studies in particle astrophysics with the ANITA experiment

DISSERTATION

Presented in Partial Fulfillment of the Requirements for the Degree Doctor of Philosophy in the Graduate School of The Ohio State University

By

Oindree Banerjee, M.Sc.

Graduate Program in Physics

The Ohio State University

2018

Dissertation Committee:

Amy Connolly, Advisor

James Beatty

Christopher Hirata

Christopher Orban

Abstract

The Antarctic Impulsive Transient Antenna (ANITA) is a NASA long-duration balloon experiment with the primary goal of detecting ultra-high-energy ($> 10^{18}$ eV) neutrinos via the Askaryan Effect. In the fourth ANITA mission, the Tunable Universal Filter Frontend (TUFF) boards were deployed for mitigation of narrow-band, anthropogenic noise with tunable, switchable notch filters. They contributed to a factor of 2.8 higher total instrument livetime in ANITA-4 compared to ANITA-3. A search for a diffuse flux of ultra-high-energy neutrinos was conducted using the data collected during the ANITA-3 flight with a new approach where the Antarctic ice area is sectioned off into bins and a search is performed with different thresholds in different bins. The binned analysis methods were extended to the development of a search for neutrinos from Gamma Ray Bursts, implementing constraints in time, and for the first time, in direction. Lower analysis thresholds were achieved in a feasibility search even when extending the search to include longer afterglow periods.

Dedicated to Kris Dunlap and Dad

Acknowledgments

I thank the National Aeronautics and Space Administration and the National Science Foundation for supporting the research presented in this thesis. My work was also supported by collaborative visits funded by the Cosmology and Astroparticle Student and Postdoc Exchange Network (CASPEN). Sincerest thanks to the astronomy department at OSU for their generous support through teaching assistantships during my Ph.D. candidacy and defense. Thanks to my home department, physics, for all the support that allowed me to find the best fit for a research group for my Ph.D. Many thanks to the Ohio Supercomputer Center - what would I do without you, Oakley.

I am deeply grateful for the opportunity to work as a member of the Connolly group and the ANITA collaboration. I could not ask for a more well-rounded and adventure-filled Ph.D. for which I thank my advisor, Amy Connolly, and Peter Gorham, Jim Beatty, Patrick Allison, David Saltzberg, and Stephanie Wissel, among others. I am grateful for the support and friendship of postdocs Linda Cremonesi, Cosmin Deaconu, and Ben Strutt.

My sincerest thanks to Connolly group members and alumni, Carl Pfendner, Sam Stafford, Mike Sutherland, Kaeli Hughes, Brian Dailey, among others, for welcoming me into the group and supporting me through the years. Heartfelt thanks to my Ph.D. sibling and office-mate, Brian Clark. I cannot imagine realizing this dream without your friendship, daily support, lunches (including the Qdoba bowl you just brought me to my desk!), and elderberries, Brian. Love you to Antarctica and back!

I am deeply grateful to Mauricio Bustamante for all his help in learning about Gamma Ray Burst theories and for letting me include in this thesis a previously unpublished, beautiful figure he made. Thanks a ton to Mat Page for sharing many useful insights on observing

Gamma Ray Bursts. Thank you to everyone at Mullard Space Science Laboratory that helped to arrange my visit there and for showing me around! Special thanks to Brian Connolly for sharing his expertise in analysis which was very helpful in approaching a problem of removing noise from the ANITA data.

Special thanks to my teachers and mentors at South Point School and High School back in Kolkata. Many, many teachers there have made me who I am - I will specially mention my high school physics teacher Partha Pratim Roy (the famous PPR) - thank you, Sir.

I am extremely grateful for a wonderful undergraduate experience at NC State. Thank you to everyone there for not only welcoming me to school but to the United States! Special thanks to my amazing professors there: John Blondin, Stephen Reynolds, David Haase, Carla Frohlich, among others. Last but not least, I thank my first research advisor, Leslie Sombers, for giving me a chance to work in her lab as a freshman. That's where I got to be a scientist for the first time!

I thank my family - Ma, Baba, Dada, Mark, and Fuji, for everything. Now, we can move on with our lives. Thank you to my friends, especially, my best friend Twameka Kumar for being there for me since Nursery. Love you all lots.

Vita

Oct 17, 1990 ..... Born—Kolkata, India

May, 2013 ..... B.S., NC State University, Raleigh, NC

Dec, 2015 ..... M.S., Ohio State University, Columbus, OH

Publications

"Constraints on the Diffuse High-Energy Neutrino Flux from the Third Flight of ANITA", P. W. Gorham, P. Allison, **O. Banerjee** *et al.*, Physical Review D. I am a lead author and contributor of the new binned analysis presented, which is one of the three complementary analyses in the paper. Link to electronic version.

"Dynamic tunable notch filters for the Antarctic Impulsive Transient Antenna (ANITA)", P. Allison, **O. Banerjee** *et al.*, Nuclear Instruments and Methods A. I led this paper and served as **corresponding author**. This paper is on the filters that I played a lead role in commissioning for ANITA-4, that helped to triple the livetime of the experiment. Link to electronic version.

I am also a co-author on all ANITA publications (6 total) since Jan 2016.

Fields of Study

Major Field: Physics

Studies in Particle Astrophysics: Connolly group

Table of Contents

List of Figures

List of Abbreviations

AMPA Antenna Mounted Pre-amplifier. 15, 17, 30

ANITA ANtarctic Impulsive Transient Antenna. xv, 6, 8–12, 15, 17, 19, 21, 24, 25, 27, 29, 31, 33, 34, 36–39, 41–47, 49, 50, 52, 54, 55, 57, 58, 61, 63, 65, 68–70, 72, 81, 82, 85, 86, 100–103, 105, 107, 109, 110, 114, 118, 122, 123, 130, 134, 137–139, 143–146, 148, 151, 153–155, 159, 163, 166, 167

ARA Askaryan Radio Array. 6, 9–11

CMB Cosmic Microwave Background. 3

CR cosmic ray. 70, 72, 73, 137–139, 141, 142

CW continuous wave. 25, 27, 45, 52, 53, 145

Dec declination. 109, 110

EAS Extensive Air Shower. 63, 70, 75, 78, 82, 137–139, 148, 153

FFT Fast Fourier Transform. 52

FWHM full-width-at-half-maximum. 15, 25

GRB Gamma Ray Burst. xv, 1, 3, 93, 94, 96, 97, 99–107, 109, 110, 114, 116, 118, 121–123, 128, 129

GRBs Gamma Ray Bursts. xiv, xv, 1–4, 11, 93–102, 104–107, 109, 114–116, 121–123, 153

HPol horizontally polarized. 15, 17, 20, 44, 46, 50, 53, 63, 65, 67, 69, 70, 72, 73, 82, 83, 115, 125, 129, 137–139, 146, 164, 170

IRFCM Internal Radio Frequency Conditioning Module. 29

LABRADOR Large Analog Bandwidth Recorder And Digitizer with Ordered Readout. 23, 24, 33

LCP left circular polarization. 46, 53, 54, 60, 166

LDB Long Duration Balloon. 12

PCA Principal Component Analysis. 86, 87

RA right ascension. 109, 110

RCP right circular polarization. 46, 53, 60

RF radio frequency. 12, 15, 17, 20, 21, 23–25, 29–31, 33, 118, 131

SIP Science Instrument Package. 18

SM Standard Model. 145, 146

TUFF Tunable Universal Filter Frontend. 15, 18, 20, 24, 25, 27, 29–31, 33, 34, 153

UHE ultra-high-energy. 3, 4, 6–12, 15, 33, 36, 37, 41, 61, 63, 65, 69, 72, 99, 100, 102, 105, 115, 118, 121, 130, 137, 143, 151, 153

UHECR ultra-high-energy cosmic ray. 139

UHECRs ultra-high-energy cosmic rays. 70

VPol vertically polarized. 15, 17, 20, 44, 46, 49, 50, 63, 65, 67–70, 72, 75, 76, 82, 83, 123, 125, 137, 146, 163, 164, 170

Chapter 1
Introduction

1.1 Exciting astrophysics happen far, far away

We live in a boring part of the Universe. This allows life and the life sciences to thrive here. However, everything that is interesting in astrophysics takes place far, far away. For example, most GRBs take place about 1 Gpc away from us. That is over three billion light years away!

Why are GRBs interesting? Well, in short, they are Nature's most powerful accelerators and they outshine an entire galaxy when they occur, with luminosity $\sim 10^{52}$ erg/s. What is more, the physics behind these exotic events continue to remain mysterious for over 50 years. Figure 5 shows a depiction of a GRB.

1.2 Astrophysical messengers

Traditional astrophysical messengers are not able to completely probe physics that take place at the farthest distances and at the highest energies. Since the beginning of astronomy, we have relied on optical light to study objects in the sky. In the last few decades, we have started utilizing light of other wavelengths such as X-rays and gamma rays. However, light of energy 1 MeV and above can undergo pair production. Light of energy 13.6 eV gets absorbed by Hydrogen atoms, the most abundant element in the Universe, while light at other wavelengths gets absorbed by other atoms and molecules. Light is the astronomer's best friend, but there is an inevitable need for complementary messengers.

Figure 1.1: Depiction of a GRB. Picture Credit: NASA E/PO, Sonoma State University, Aurore Simonnet.

Fortunately, in the last century, we have opened up multiple new windows to peer into the Universe. About a 100 years ago, cosmic rays were discovered by Victor Hess in a balloon-based experiment. In the last several years, the IceCube neutrino observatory has discovered the first astrophysical neutrinos up to energies of a few PeV [10]. Moreover, gravitational waves were discovered by the LIGO collaboration in the last few years, confirming, for example, the association of short GRBs with neutron star - neutron star mergers [11]. Figure 1.2 summarizes the astrophysical messengers we have discovered so far.

1.3 Neutrinos as astrophysical messengers

Neutrinos are potentially perfect candidates for carrying information about distant particle accelerators all the way to us. Due to being neutral and weakly interacting, neutrinos would remain unattenuated and point straight back to their source. In this way, they would have a definite advantage over messengers such as cosmic rays. Neutrinos are the side product

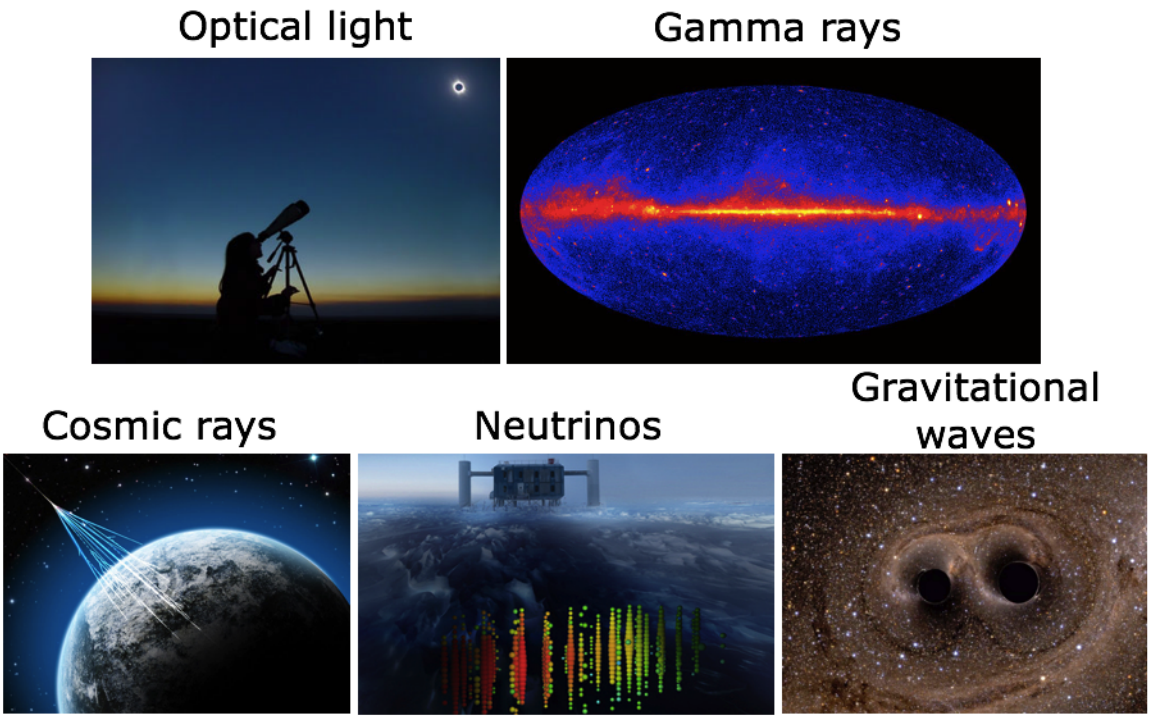

Figure 1.2: Astrophysical messengers. Pictures are all borrowed from Fermi, IceCube and LIGO collaborations, and the Internet.

of almost every nuclear reaction and can carry versatile information about particle physics taking place at cosmic distances. Their association with sources such as GRBs would confirm, for example, whether protons, in addition to electrons, get shock accelerated in the fireball model of the GRB [12].

Despite a lack of observation so far, ultra-high-energy (UHE) ($> 10^{18}$ eV) neutrinos are predicted to be produced in two ways, the more commonly referenced of which is known as the cosmogenic method. The cosmogenic method entails the interaction of cosmic rays with Cosmic Microwave Background (CMB) photons, as depicted in Figure 1.3a. UHE cosmic rays are predicted to travel only about 50 Mpc before they interact with CMB photons, a phenomenon known as the GZK Effect. This is thought to cause the sharp drop in flux at the highest energies as seen in Figure 1.3b. Such an interaction can also, potentially, lead to the production of UHE neutrinos, although no cosmogenic neutrinos have been observed so far.

The second way of producing UHE neutrinos is the astrophysical method, which is the one I find to be more motivating. The astrophysical method involves the production of UHE neutrinos in Nature's most powerful particle accelerators such as GRBs. This will be discussed in more detail in Chapter 5. In both the cosmogenic and astrophysical methods of producing UHE neutrinos, a commonly referenced process of production of the same is through the interaction of a proton and a photon creating intermediate pions, as shown in Figure 1.4.

1.4 Optical Cherenkov neutrino detectors

Optical Cherenkov neutrino experiments look for high energy neutrinos in the energy regime of $10^{11} - 10^{15}$ eV. In this section, we briefly introduce two optical Cherenkov experiments, IceCube and ANTARES. Being located in complementary hemispheres of the earth, these two experiments have complementary fields of view. Where they are on the energy scale as compared to other particle physics experiments is shown in Figure 1.5.

IceCube is the optical Cherenkov detector in the southern hemisphere. The observatory is located in the South Pole. The completed IceCube observatory is composed of 5160 digital optical modules (DOMs), each containing a 10−inch photomultiplier tube, with 60 DOMs placed at depths between 1450 and 2450 m on each of 86 vertical strings. The total instrumented volume of IceCube is $1\,\mathrm{km}^3$.

ANTARES is the optical Cherenkov detector in the northern hemisphere. It is located in the Mediterranean Sea. Located at a depth of 2.4 km, it consists of 12 vertical strings, separated from each other by a typical distance of 70 m. Each string is anchored to the seabed and held upright by a buoy at the top. Over a length of 350 m, it is equipped with 25 triplets of photo-multiplier tubes (PMTs), building a 3-dimensional array of 885 PMTs in total. The instrumented volume of ANTARES is $\sim 0.02\,\mathrm{km}^3$.

IceCube and ANTARES are both optimized for the detection of muons from charged current interactions of high energy astrophysical neutrinos. IceCube uses the Antarctic ice as a target medium for high energy neutrinos to interact in. ANTARES uses sea-

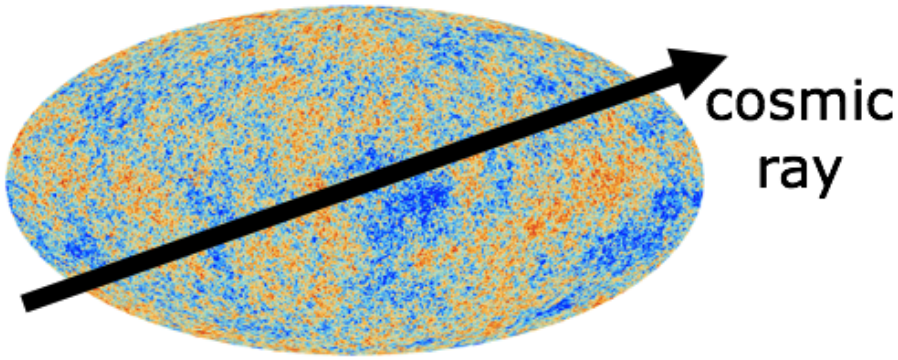

(a) t

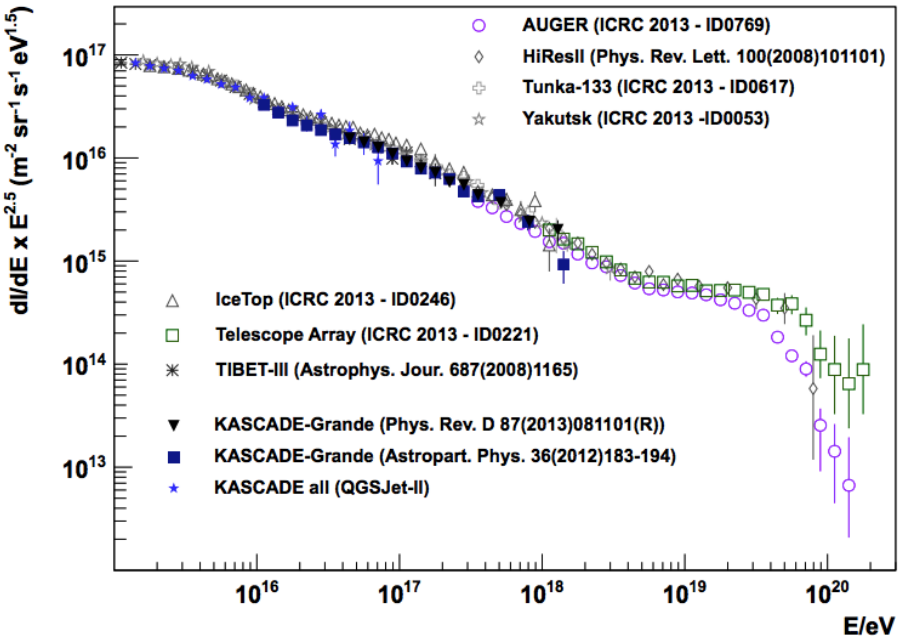

(b) b

Figure 1.3: Top: Depiction of a cosmic ray interacting with the CMB. Thanks to the Planck telescope for the CMB picture. Bottom: Energy spectra of cosmic rays measured by different experiments. Andreas Haungs showed this plot at the 13th International Conference on Topics in Astroparticle and Underground Physics. UHE cosmic rays can only travel for about 50 Mpc before they interact with CMB photons and lose energy, therefore, we see a sharply falling spectrum at about 10^{20} eV energy.

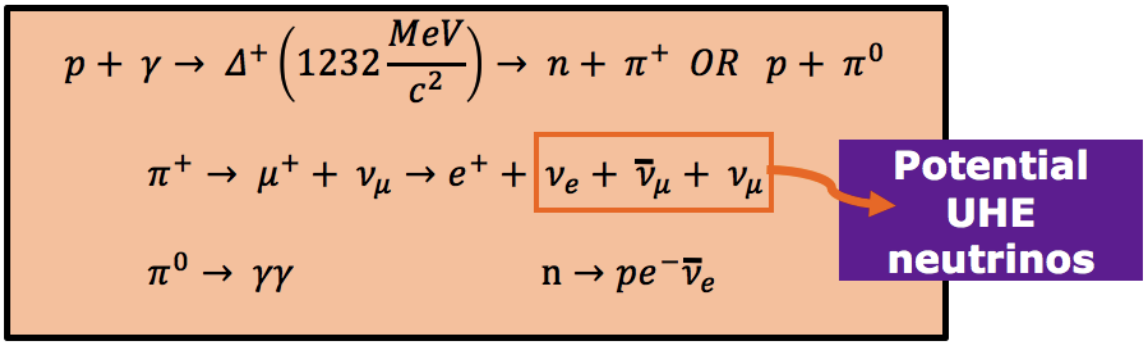

Figure 1.4: A process for production of UHE neutrinos.

water instead. They both look for optical Cherenkov signatures of high energy neutrino interactions. ANTARES is sensitive to neutrinos of energy 10 GeV - 100 TeV. IceCube was built to detect neutrinos of energy 100 GeV and higher. However, as shown in [13], IceCube can also detect neutrinos of energy of order MeV.

1.5 Radio Cherenkov neutrino detectors

Radio Cherenkov neutrino experiments look for UHE neutrinos in the energy regime of $> 10^{16}$ eV. The main challenge for detection by these experiments and a potential solution for detection are presented below. We also introduce two complementary radio Cherenkov experiments, ANITA and Askaryan Radio Array (ARA) in this section. Where they are on the energy scale as compared to other particle physics experiments is shown in Figure 1.5.

1.5.1 Challenge of detecting ultra-high-energy neutrinos

In this era of rapid growth in multi-messenger astronomy, UHE neutrinos remain undiscovered. One of the major challenges is that observation of these rare particles requires a huge detection volume. The interaction length of an EeV neutrino and a nucleus is about 300 km. Less than 0.01 UHE neutrinos are predicted to hit the earth per cubic kilometer per year, implying that to be sensitive to the UHE neutrino flux we need a detection volume much greater than a 100 cubic kilometers. Such a huge detection volume would be too expensive to instrument using optical Cherenkov detectors as optical light is attenuated over order

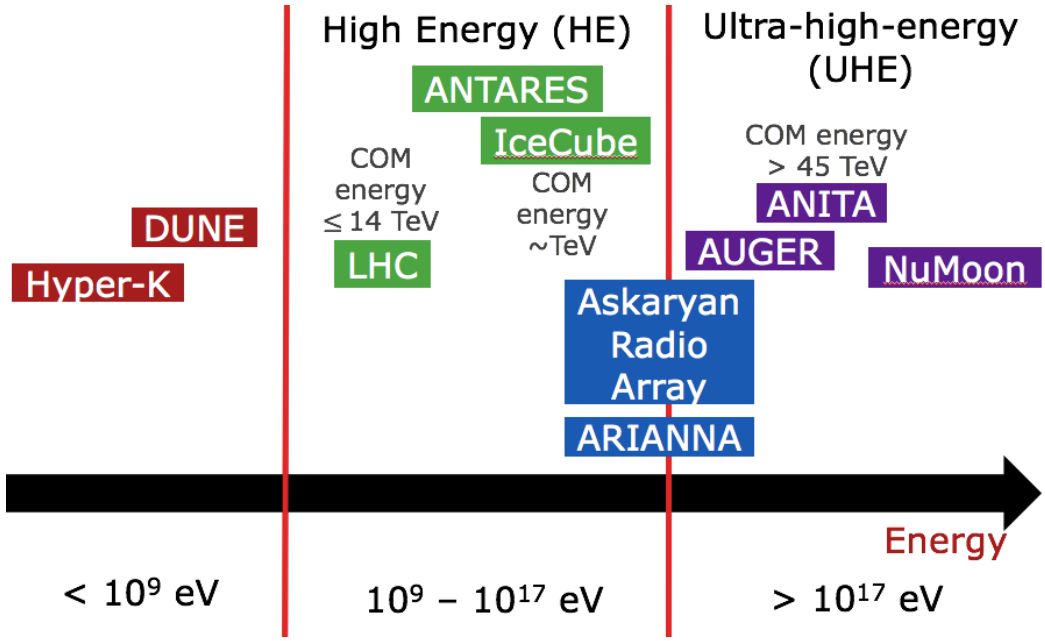

Figure 1.5: The ANITA experiment looks for particles, specifically, neutrinos of energies that are to close to the extreme right of the energy scale.

tens of meters.

1.5.2 Askaryan Effect

A proposal by [14], known as the Askaryan Effect, stating that UHE neutrinos could be observed through their interaction in a dielectric medium, comes to the rescue. The principle is that a relativistic, UHE neutrino would interact with a nucleus in a dielectric to produce a particle shower traveling in the medium at a speed greater than the speed of light in the medium. The particle shower would mainly consist of photons, electrons and positrons. As it travels through the dielectric, the particle shower develops about a 20% negative charge. This happens primarily due to Compton scattering of electrons in the medium (so electrons leaving the medium and joining the shower) and secondarily due to annihilation of positrons in the shower with electrons in the medium (so positrons leaving the shower). As this charged particle shower travels through the medium at a speed greater than the speed of light in the medium, Cherenkov radiation is produced. If this Cherenkov radiation is observed at wavelengths larger than the shower's transverse dimension of about 10 cm,

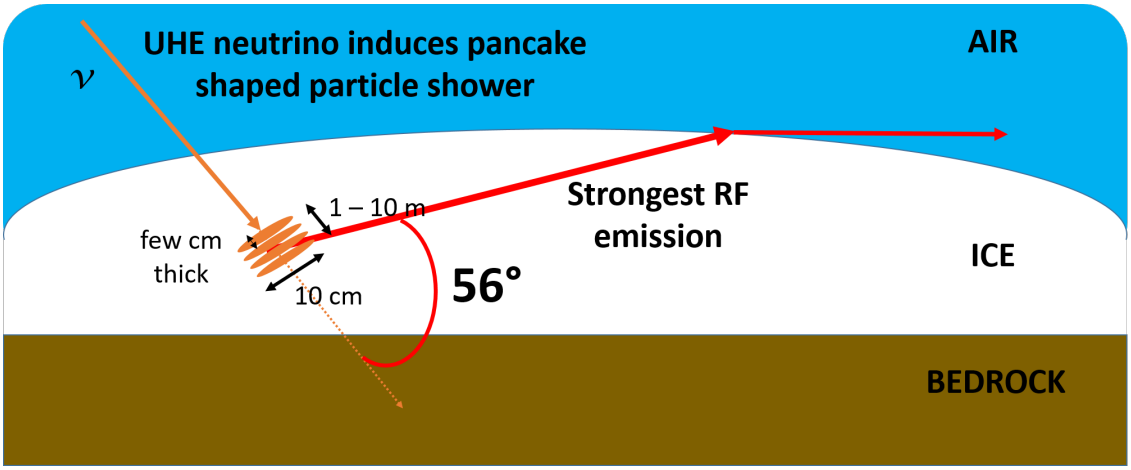

Figure 1.6: A UHE neutrino could start a pancake-shaped particle shower in the ice. Cherenkov radiation due to this particle shower would be coherent at wavelengths greater than the shower size of $\sim$ 10 cm, which correspond to radio waves.

then it would be seen as coherent waves in radio frequencies.

1.5.3 ANITA

ANITA is an experiment dedicated to discovering UHE neutrinos via the Askaryan Effect utilizing the Antarctic ice as the necessary dielectric target medium for neutrino interaction. Where ANITA's sensitivity lies in the energy scale as compared to other experiments in particle physics and particle astrophysics is presented in Figure 1.5. A cartoon of an UHE neutrino coming in to the ice and starting a particle shower that leads to Cherenkov radiation emitted coherently at an angle of about 56° is shown in Figure 1.6. ANITA looks for radio Cherenkov signals with an array of radio antennas. The ANITA detector is hung from a Helium-filled balloon and launched from near McMurdo Station, Antarctica, during the Austral Summer. After it is launched, ANITA floats up to an altitude of about 40 km and utilizes the polar vortex to fly in roughly circular orbits over the continent of Antarctica. At its float altitude, the balloon, upon gradual inflation, is bigger than the Ohio Stadium. There have been four flights of ANITA so far. These are summarized in Figure 1.7.

During its flight, at any given time, ANITA can scan about a **million** cubic kilometers of ice. This makes ANITA the neutrino detector with the largest instantaneous detection

Year	Flight	Length of flight	Status
2006 - 2007	ANITA-1	35 days	Data analysis published
2008 - 2009	ANITA-2	30 days	Data analysis published
2014 - 2015	ANITA-3	22 days	Results public now
2016	ANITA-4	27 days	Data analysis ongoing
2020?	ANITA-5	--	Improving digitizers and trigger

Figure 1.7: Summary of ANITA flights.

volume. The use of the radio Cherenkov technique goes hand in hand with covering a detection volume that is orders of magnitude larger than what is possible with optical Cherenkov techniques such as in IceCube (1 cubic km detection volume). Radio waves have attenuation lengths of order 1 km while optical light attenuates over order tens of meter. For ANITA, radio waves from neutrino cascades are produced in the ice, but then have to travel 40 km through air before they can reach the detector. Therefore, ANITA is sensitive only above about an EeV neutrino energy so it is looking for the rarest neutrinos. A cartoon of radio waves from a particle shower caused by an UHE neutrino in the ice reaching the ANITA detector is shown in Figure 1.8.

1.5.4 ARA

In contrast to a balloon-borne detector such as ANITA, ARA is ground-based and the ARA radio antennas are embedded in the ice of Antarctica. When ARA is deployed, it can, potentially observe all year round, as opposed to only about a month of observation time in ANITA.

The completed ARA detector will consist of 37 deep stations spaced 2 km apart at a

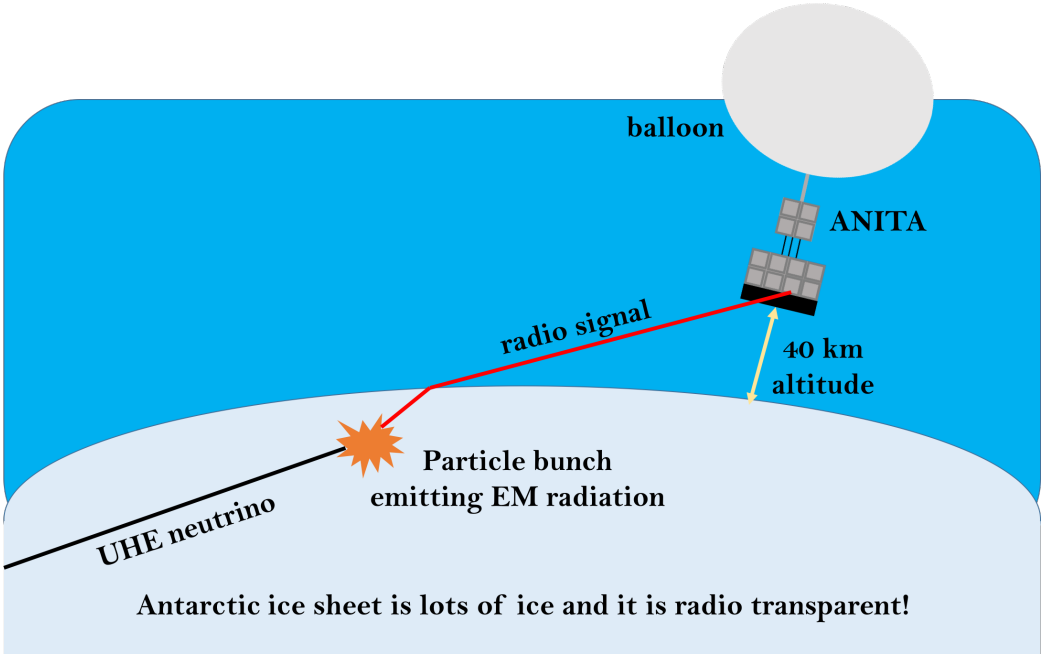

Figure 1.8: Concept of detection of UHE neutrinos with ANITA.

depth of 200 m. Currently, ARA has five deep stations in the ice. A station or a single array element consists of a cluster with around 16 embedded antennas, deployed up to 200 m deep in several vertical boreholes placed with about ten meters horizontal spacing to form a small sub-array [15]. ARA is highly modular in that each station comprises a standalone neutrino detector for its surrounding ice. All borehole antennas have a bandwidth of 150 MHz to 1 GHz.

Like ANITA, ARA too relies on the Askaryan Effect [14] for observation of UHE neutrinos. ARA, too, utilizes the Antarctic ice as a target medium for neutrino interactions to look for radio signatures from these interactions. The main distinction between ANITA and ARA is the area of target medium (ice) they each observe, and therefore, the neutrino energy range they are each sensitive to. ANITA observes an area of roughly a million km^2 and is sensitive to very rare neutrinos of energy $10^{18}\,\mathrm{eV}$ and above. ARA covers roughly a $200\,\mathrm{km}^2$ area and is sensitive to the neutrino energy range of $10^{16} - 10^{19}\,\mathrm{eV}$.

1.5.5 ARA vs. IceCube

The main distinction between ARA and IceCube is that ARA is able to observe a hundred times bigger target volume than IceCube with fewer detector units than IceCube. This is because the attenuation length of radio signals of the frequency range that ARA detects is $\sim$ 1 km allowing for a sparsely distributed array of detector units, whereas, the optical signals that IceCube detects are restricted to < 100 m lengths. The energy threshold determines the expected flux, and thus the size of the detector. With a smaller instrumented volume IceCube is typically sensitive to energies lower than the UHE regime, whereas, ARA is sensitive to ultra-high-energies up to 10^{19} eV.

1.6 Summary of remaining chapters

The work presented in this thesis is with regard to the ANITA experiment. Chapter 2 describes the ANITA instrument and highlights new electronics that tripled the instrument livetime of ANITA. Chapter 3 describes the development of a new technique for analysis known as the "binned analysis" with a focus on background reduction. The first physics results from this new analysis are presented in Chapter 4. Chapter 5 is a review of GRBs, my favorite transients, in the context that these exotic events could be sources of UHE neutrinos. Chapter 6 describes the developments in adapting the simulation and the binned analysis to a search for neutrinos from sources, specifically, GRBs. Mysteries, thoughts, ideas, and associated results are presented in Chapter 7.

Chapter 2
ANITA INSTRUMENT

2.1 ANITA payload

The **AN**tarctic **I**mpulsive **T**ransient **A**ntenna (ANITA) is a NASA-sponsored long-duration balloon experiment with the primary goal of detecting UHE neutrinos as broadband radio signals in the frequency range $200 - 1200\,\mathrm{MHz}$. The ANITA-4 payload at the NASA Long Duration Balloon (LDB) Facility is shown in Figure 2.1. The ANITA-4 payload just prior to launch and after launch at its float altitude through a telescope is shown in Figures 2.2 and 2.3. The most important parts of the ANITA payload are its radio frequency (RF) antennas and its signal processing units (most of which are inside the Instrument Box). A peer-reviewed description of these can be found in a recent publication that I led as the corresponding author [1]. Click here to find the electronic version of this paper.

2.1.1 Flight path and payload weight

The ANITA neutrino observatory is a NASA long-duration balloon-borne payload. After its launch from the NASA LDB Facility near McMurdo Station, the Summer polar vortex winds keep the ANITA payload flying in roughly circular loops above the continent of Antarctica. A lighter payload is able to reach higher altitudes where the polar vortex is spatially tighter. This leads to a more favorable flight path which, in turn, increases the chances of a longer flight and increased livetime. Most importantly, this keeps the payload from venturing out over the ocean and becoming unrecoverable.

There are strict weight restrictions on a balloon payload. This is why the ANITA

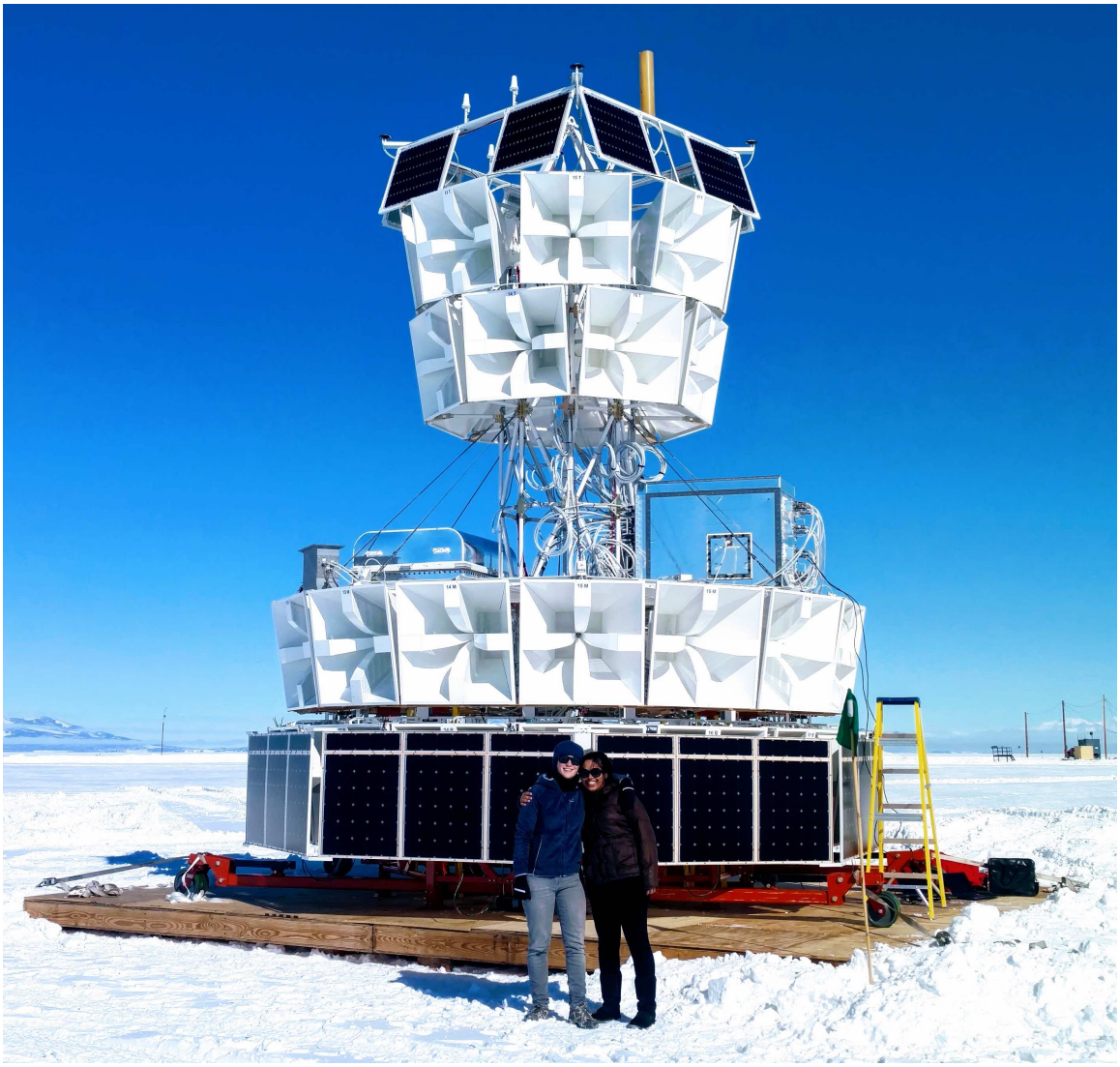

Figure 2.1: Linda Cremonesi and I during testing the GPS systems on ANITA-4 before its launch from near McMurdo Station, Antarctica. This shows the relative size of the instrument compared to humans. Picture credit: Steven Prohira.

Figure 2.2: Here NASA's balloon for the launch of ANITA-4 is being filled with Helium. When NASA takes the balloon out, one knows there will be a launch for real.

(a) ANITA-4 at launch

(b) ANITA-4 at float altitude

Figure 2.3: Left: The ANITA-4 payload attached to its balloon just before launch. Right: When ANITA gets close to its float altitude of about 40 km, one cannot see it from the ground with the naked eye. This is ANITA-4 through a telescope. Telescope picture credit: Steven Prohira.

gondola is made of hollow aluminum tubes connected by joints. The aluminum beams can be seen in Figure 2.5. A need for a light payload informed the design of the Tunable Universal Filter Frontend (TUFF) boards as detailed in Section 2.3. This helps to keep the payload weight under 5000 lb. The ANITA-4 payload weighed 4526 lb. For the first time, the ANITA-4 payload was able to reach above 40 km altitude for part of its flight. Furthermore, the ANITA-4 payload was able to maintain a more favorable flight path compared to the ANITA-3 payload, resulting in a longer flight of 27 days compared to 22 days in ANITA-3.

2.1.2 Radio antennas and Phi Sectors

ANITA looks for UHE neutrinos with RF antennas. Figure 2.4 shows myself standing next to one of these antennas during the integration and testing of ANITA-4 at the Columbia Scientific Balloon Facility in Palestine, TX in July of 2016. Custom-built by Seavey Engineering, they are 0.8 m long on a side, quad-ridged and horn-shaped. The antennas are broadband and highly-directional. They have an on-axis gain of ~ 10 dB with respect to isotropic gain. The 3 dB point of these antennas is $\sim 30°$.

There are 48 antennas on the ANITA-4 payload. They are mounted on the ANITA gondola covering 360° in azimuth. The antennas are arranged in three aligned rings of 16 antennas, termed the top, middle, and bottom rings. The top ring consists of two staggered sub-rings each having eight antennas. The full-width-at-half-maximum (FWHM) beamwidth of the antennas is approximately 45°. The antennas in the top ring are evenly spaced by 45° in azimuth. The two sub-rings in the top ring are offset by 22.5° for uniform coverage. The antennas in the middle ring are evenly spaced by 22.5°. The antennas in the bottom ring are evenly spaced by 22.5°. All the antennas are angled downward by 10° to preferentially observe signals coming from the ice as opposed to from the sky. Each group of three antennas in a vertical column, taking one antenna from each ring, forms a phi sector, viewing a 22.5° region in azimuth.

The antennas are dually-polarized with a feed each for horizontally polarized (HPol) and vertically polarized (VPol) signal. RF signal through each channel goes through the Antenna Mounted Pre-amplifier (AMPA) unit before entering the Instrument Box. There

Figure 2.4: Here I am standing next to one of the ANITA horn antennas before the hang test of the ANITA-4 mission at Columbia Scientific Balloon Facility in Palestine, TX. Picture credit: Jacob Gordon.

Figure 2.5: Andrew Ludwig and I working on integration and cabling of ANITA-4 at the NASA LDB facility near McMurdo Station, Antarctica. The aluminum beams that form the underlying structure of the payload can be seen here. Light aluminum beams help to abide by weight restrictions. Image credit: Nan Wang.

is an AMPA unit connected directly to the HPol and VPol outputs of each antenna. The AMPA contains a $200-1200\,\mathrm{MHz}$ bandpass filter, followed by an approximately $35\,\mathrm{dB}$ Low Noise Amplifier (LNA). The AMPA performs the first-stage amplification of the incoming RF signal. I led a camp (John Russell christened it "Campa") at the ANITA headquarters, University of Hawaii, in September of 2016, to finish assembling these AMPA units for the ANITA-4 flight. I show one of the 100 that I worked on assembling in Figure 2.6. These even involved a bit of careful soldering and using the heat gun!

2.1.3 Instrument Box and Science Instrument Package

The Instrument Box of ANITA sits on the payload's deck. Most of the signal processing in ANITA takes place inside the Instrument Box. Following the AMPA unit, the RF

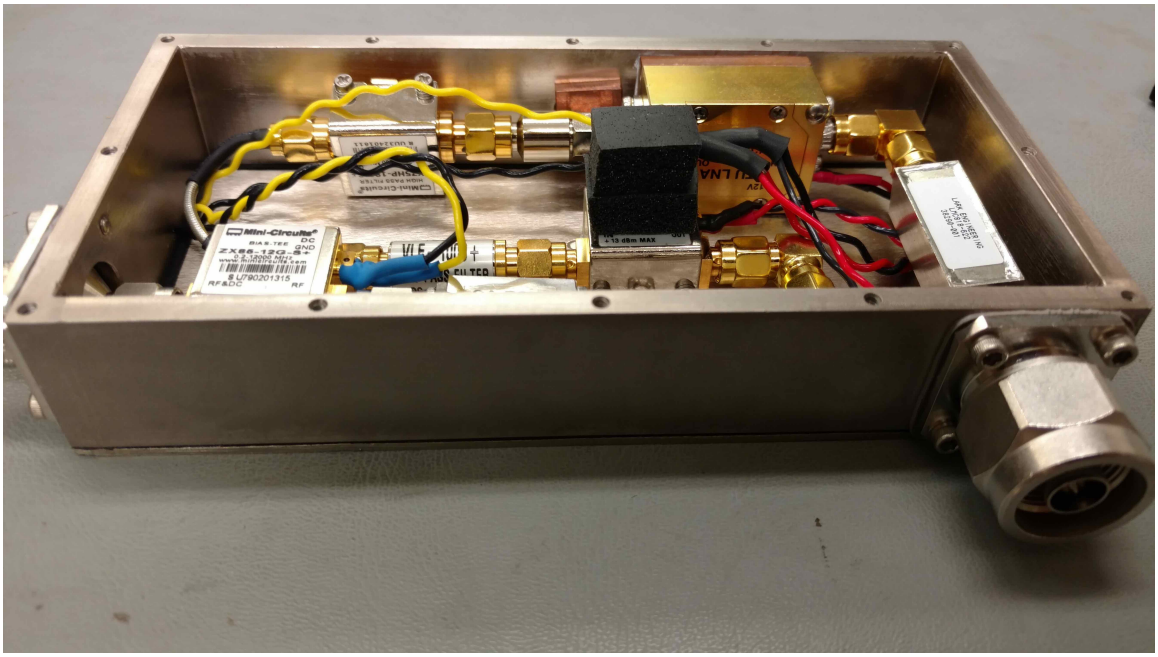

Figure 2.6: Rare picture of the inside of an AMPA from ANITA-4.

signal travels through 12 m of LMR240 coaxial cable to the Instrument Box. Inside the Instrument Box, the signal first goes through second-stage amplification and notch filtering both performed by the TUFF boards in ANITA-4. Then it passes through another set of bandpass filters before being split into digitization and triggering paths. The triggering and digitization processes are detailed in [1].

The Science Instrument Package (SIP) also sits on the payload's deck. The SIP is powered and controlled by NASA. It is used for flight control such as ballast release and flight termination. The SIP also provides a connection to the ANITA payload during flight through line-of-sight transmission, the Iridium satellite, and the Tracking and Data Satellite System (TDRSS). This allows us to monitor the payload continuously during the flight. A small fraction of data (less than 1%) is transferred from the payload through telemetry. Commands to perform different functions, such as tuning a TUFF notch filter, can be sent to the payload in real time using the SIP connection.

2.1.4 Power

There are unusual constraints on the total power budget of ANITA as it is a balloon payload. The ANITA-3 and ANITA-4 payloads operated on $\sim 500\,\mathrm{W}$ and $\sim 600\,\mathrm{W}$ respectively. The payload is solar-powered by photovoltaic (PV) cells. One set of PV cells are on top of the gondola. These are managed by NASA and used to power the SIP. The other set is termed the "drop-down PV array" and the PV cells in this set are arranged in eight 90-cell strings, laid out in an octagon around the bottom of the payload. The drop-down PV array powers the Instrument Box. Before launch, they partially cover up the antennas in the bottom ring, as seen in Figure 2. After launch, the eight strings are remotely instructed to drop down by the SIP, which fires a servo to deploy them below the bottom ring of antennas.

A charge controller distributes the output from the drop-down PV array to the payload as $24\,\mathrm{V}$, using DC-DC converters to provide $12\,\mathrm{V}$, $-12\,\mathrm{V}$, $3.3\,\mathrm{V}$ and $5\,\mathrm{V}$ to various systems. The charge controller is also connected to a battery farm of $12\,\mathrm{V}$ lead-acid batteries. Although there is daylight 24/7 in the Antarctic summer, the amount of power the PV array produces changes with the Sun's elevation during each 24 hour period. Thus, a battery farm is needed as backup. When the PV array is able to power the payload by itself, the charge controller charges the battery farm. This is in the Battery Box which is also placed on the deck.

2.1.5 GPS Systems and Heat dissipation

ANITA data analysis relies on location and orientation information of the payload. ANITA uses three GPS systems during flight: ADU5A, ADU5B and G12. These GPS antennas are located on top of the payload. The ADU5 systems provide heading, pitch and roll information. The G12 system updates absolute time on the flight computer through its Network Time Protocol (NTP) server. As backup to the GPS systems, there are four sun-sensor instruments, a magnetometer and accelerometer located on the deck.

At high altitudes of 35 km and above, the primary method of heat loss is radiation. Thus, many parts of the payload are painted white to reflect sunlight and regulate temperature.

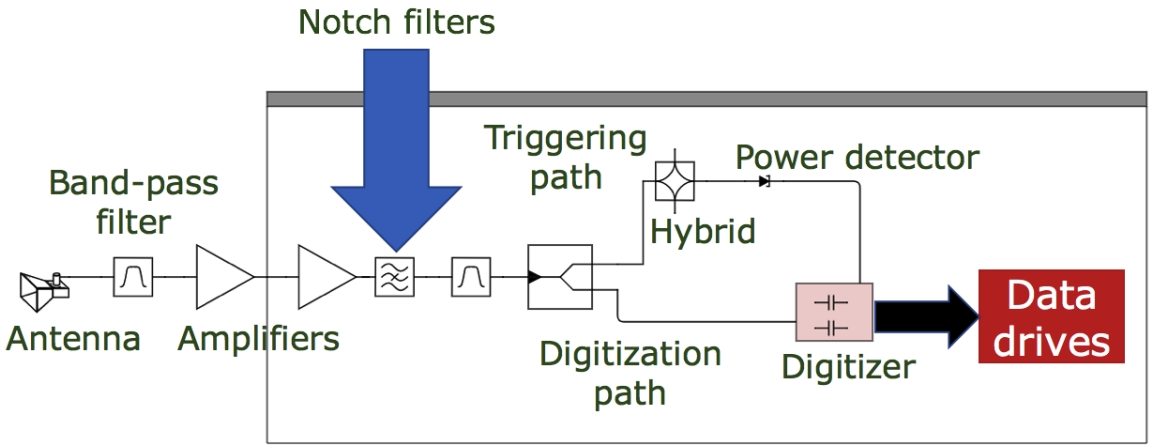

Figure 2.7: Simplified form of the signal processing chain in ANITA-4. A more detailed diagram can be found in [1]. The blue solid arrow shows where the TUFF notch filters are in the chain. More details on the TUFF boards and notch filters are presented later in this chapter.

Components producing large amounts of heat are connected to a teflon-coated, silver-tape-lined radiator plate on the Instrument Box.

2.2 ANITA Signal Processing

In this section we describe the signal processing chain for ANITA-4, and in particular the steps that are relevant to understanding the role of the TUFF boards. We will note when and where the ANITA-3 signal processing differed. Note that much of the contents of this section is also covered in [1]. The RF signal processing chain for ANITA-4 is illustrated in Figure 2.7.

2.2.1 Triggering

In the triggering path, the RF signals from both the VPol and HPol channels of a single antenna are passed through a 90° hybrid (hybrids were absent in ANITA-3). The outputs from the 90° hybrid are the left- and right- circular polarized (LCP and RCP) components of the combined VPol and HPol signals from an antenna. The hybrid outputs are input to the SURF (Sampling Unit for RF) high-occupancy RF Trigger (SHORT) unit before being

passed to the SURF board. Each SHORT takes four channels as its input. In a SHORT channel, the RF signal passes through a tunnel diode and an amplifier. The output of the SHORT is approximately proportional to the square of the voltages of the input RF signal integrated over approximately 5 ns. It is a measure of the power of the incoming signal and is typically a negative voltage. The SHORT output is routed to a SURF trigger input where it enters a discriminator that compares this negative voltage in Digital-to-Analog Converter (DAC) counts to the output of a software-controlled DAC threshold on the SURF, henceforth referred to as the SURF DAC threshold. The SURF DAC threshold is expressed in arbitrary units of DAC counts corresponding to voltages. Lower thresholds correspond to higher voltages and therefore, higher power of the incoming signal. The SURF DAC threshold can be changed during flight. Thresholds for the ANITA-3 and -4 flights are shown in Figure 2.8. During the ANITA-3 flight, CW interference overwhelmed the digitization system, forcing us to impose frequent and large changes in the SURF DAC thresholds. Note that the lower overall threshold for ANITA-4 is primarily due to the modified triggering scheme, which requires more overall coincidences between channels. The increased stability of the ANITA-4 thresholds, due to the CW mitigation schemes presented later, is clearly apparent.

Trigger logic: Due to power and bandwidth limitations, ANITA is not able to constantly record data. Digitization of data only occurs when the trigger conditions are satisfied. The ANITA-4 trigger consists of three triggering levels: Level 1, Level 2 and Level 3. The trigger requirements at each of these three levels is described below.

Level 1 trigger: The Sampling Unit for RF (SURF) board issues the Level 1 trigger. To form a Level 1 trigger, the SHORT outputs of the LCP and RCP channels from the same antenna are required to exceed the SURF DAC threshold within 4 ns. This LCP/RCP coincidence requirement was added to the ANITA-4 trigger to mitigate anthropogenic and thermal backgrounds. The signals of interest are known to be linearly polarized, whereas satellite emission is often circularly polarized and thermal noise is unpolarized. In the

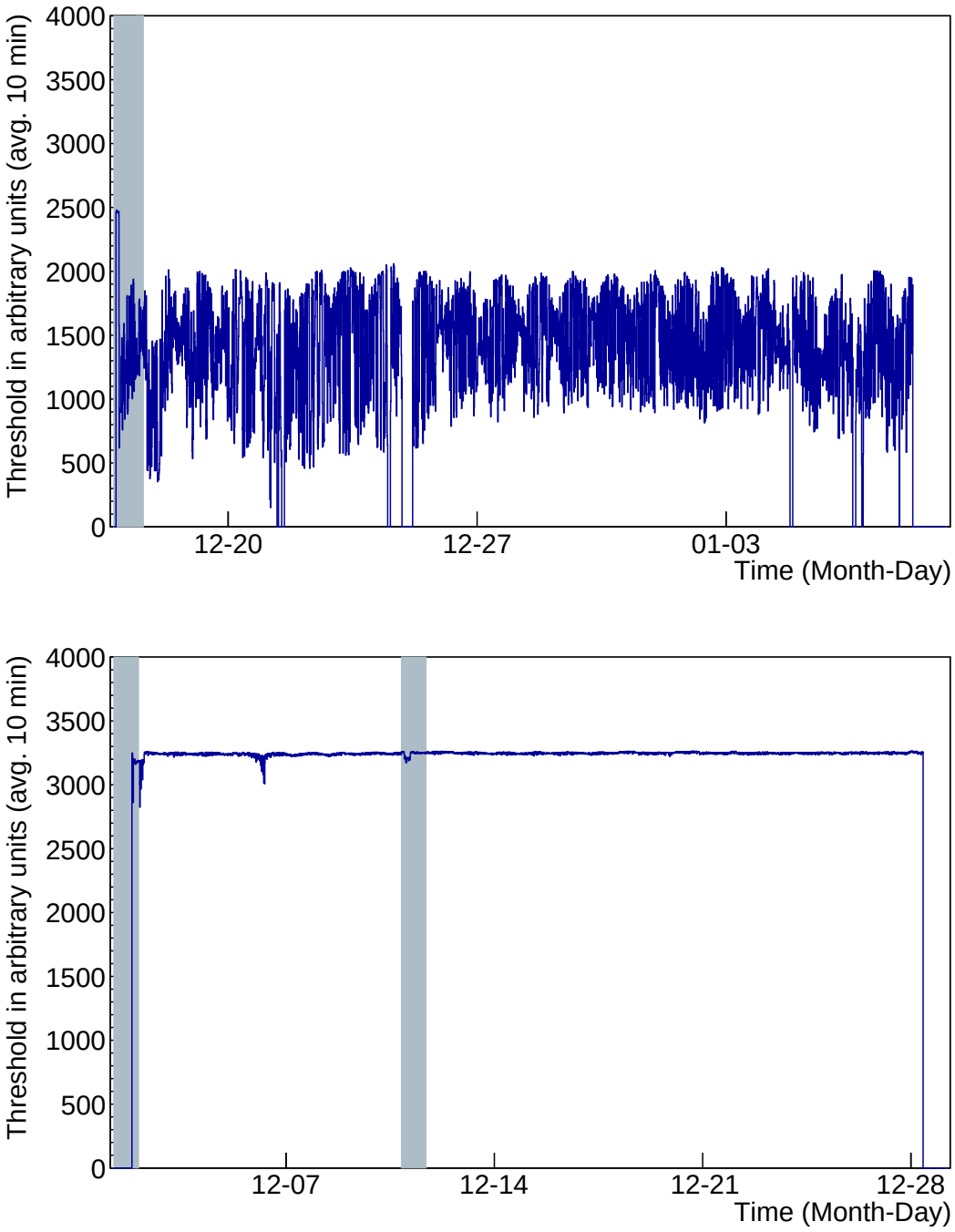

Figure 2.8: Thresholds during the ANITA-3 (top) and ANITA-4 (bottom) flights.

presence of a continuous source of CW signal such as satellites, the LCP/RCP coincidence may still allow a combination of circularly polarized satellite noise and the circularly polarized component of thermal noise to satisfy the Level 1 trigger requirement. Therefore, the LCP/RCP coincidence aids in reducing triggers induced by satellites but does not completely mitigate their effect.

Level 2 trigger: The SURF board issues the Level 2 trigger. A Level 1 trigger opens up a time window. If there are two Level 1 triggers in the same phi sector within the allowable time window, then a Level 2 trigger is issued. The allowable time window depends on which antenna had the first Level 1 trigger. Time windows of 16 ns, 12 ns and 4 ns in duration are opened up when a Level 1 trigger is issued in the bottom, middle and top ring respectively. These time windows were chosen to preferentially select signals coming up from the ice. The Level 2 trigger decisions are passed from the SURF boards to a dedicated triggering board called the Triggering Unit for RF (TURF). The Level 2 trigger timing in ANITA-4 differed from that used in ANITA-3 as changes were made to further restrict the allowed timing of the antenna coincidences to better match timing expected from an incoming plane wave.

Level 3 trigger: The TURF board issues the Level 3 trigger. A field programmable gate array (FPGA) on the TURF board monitors Level 2 triggers. A Level 3 trigger is issued by the TURF board when there are Level 2 triggers in two adjacent phi sectors within 10 ns. When there is a Level 3 trigger, the TURF board instructs the SURF board to begin digitization.

2.2.2 Digitization

The digitization of the signal is performed by the SURF board. There are twelve SURF boards, each containing four custom-built Application Specific Integrated Circuits called Large Analog Bandwidth Recorder And Digitizer with Ordered Readout (LABRADOR).

LABRADOR chip and digitization deadtime: ANITA-4 uses the third generation of LABRADOR chips that are described by Varner *et al.* [16]. Each LABRADOR chip

has a 260-element switched capacitor array (SCA) for each of its 9 input channels, with one channel used for timing synchronization. The RF signal entering a SURF gets split and fed into four parallel LABRADOR chips (forming four "buffers" for digitization). The SCAs sample waveform data at the rate of 2.6 GSa/s. At any moment, the charge stored in an SCA is a 100 ns record of the signal voltage. This 100 ns snapshot of the incoming plane wave is known as an "event." When a Level 3 trigger occurs, a single LABRADOR chip stops sampling and is "held." It then digitizes the stored data, which is then read out by the flight computer, taking approximately $5 - 10$ ms. If all four LABRADOR chips are held, the trigger is "dead" and the accumulated time when the trigger is dead is recorded as digitization deadtime by the TURF board.

Masking: During ANITA-3, digitization deadtime due to high levels of anthropogenic noise was reduced by excluding certain phi sectors from participating in the Level 3 trigger. This is called phi-masking. Alternatively, specific channels (each antenna has two channels) were excluded from participating in the Level 1 trigger. This is called channel-masking. Together these are referred to as masking. Because of CW interference by military communications satellites, over half of the payload had to be masked during most of the ANITA-3 flight. This strongly motivated the creation of the TUFF boards with tunable, switchable notch filters.

Data storage: All ANITA data is stored on-board with less than 1% of it transmitted to the ground during flight by telemetry. This is why payload recovery is critical. The primary storage devices are two HGST UltraStar He6 disks, each with 6 TB capacity. These two Helium drives contain identical copies of the data for redundancy in case of a drive failure. Additionally, there are six 1 TB Solid State Drives for secondary data storage.

2.3 Tunable Universal Filter Frontend

For ANITA-4, we built and deployed 16 TUFF boards (not counting spares) with six channels each for the 96 total full-band RF channels of ANITA. Figure 2.7 shows, for a single RF

channel in ANITA-4, where the TUFF boards are in the signal processing chain. Details on these boards, their function and performance, as well as a portion of the contents of this section, are presented in [1].

2.3.1 The problem: modulated continuous wave interference

The principal challenge of the ANITA experiment is to distinguish neutrino signals from RF noise. The two main sources of noise are thermal radiation by the Antarctic ice and anthropogenic noise, much of which is modulated continuous wave (CW) interference.

While Antarctica itself is relatively free of CW transmissions, except for bases of human activity, transmissions from geosynchronous satellites are continuously in view. The average FWHM beamwidth of the ANITA antennas is approximately 45°. Although the ANITA antennas are canted downward by 10°, the beam of the antennas extends to horizontal from the perspective of the payload and above. The Antarctic science bases, the most prominent being McMurdo and South Pole Station, are more radio-loud than the rest of the continent, producing CW interference, for example, in the $430 - 460$ MHz band.

CW interference due to military satellites has affected all ANITA flights. ANITA-1 (Dec. 2006 - Jan. 2007) and ANITA-2 (Dec. 2008 - Jan. 2009) observed CW interference primarily in the $240 - 270$ MHz band, peaking at 260 MHz. This frequency range is predominantly used by the aging Fleet Satellite (FLTSAT) Communications System and the Ultra High Frequency Follow-On (UFO) System, both serving the United States Department of Defense since year 1978 and 1993 respectively. In addition to CW interference at 260 MHz, ANITA-III (Dec. 2014 - Jan. 2015) observed CW interference at 375 MHz which is thought to be due to the newer Mobile User Objective System (MUOS) satellites that were launched during the period from Feb. 2012 - June 2016 [17]. The CW signals generate events with excess power in left circular polarization (shown for the first time in Stafford's thesis [18]) above the horizon, in approximately stationary positions.

The ANITA-3 experiment was most affected by CW interference due to military satellites. The first and second peaks in the power spectrum shown in Figure 2.9 were present during all and about half, respectively, of the ANITA-3 flight. Due to the design of the

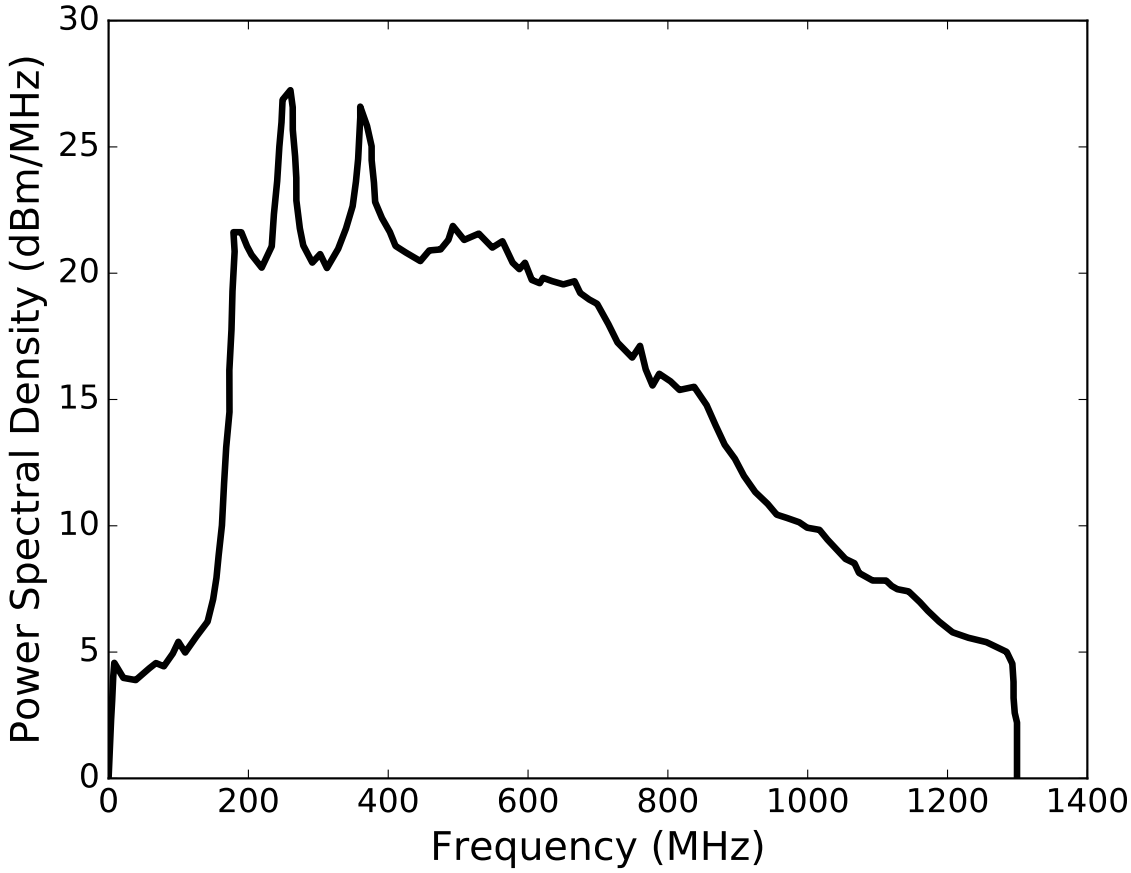

Figure 2.9: This averaged (over 2 mins) power spectrum shows the two CW peaks caused by military satellites that greatly reduced the instrument livetime (instrument livetime was only 31.6%) of the ANITA-3 flight.

ANITA-1 and ANITA-2 trigger, which required coincidences among different frequency bands, the CW interference did not overwhelm the acquisition system. However, ANITA-3 was redesigned for improved sensitivity and based its trigger decisions on full-bandwidth ($200-1200\,\mathrm{MHz}$) signals. The modulation present in the CW interference produced trigger rates far in excess of the digitization system's readout capabilities ($\sim 50\,\mathrm{Hz}$) for thresholds comparable to those used in previous flights. Thus, the ANITA-3 experiment was susceptible to digitization deadtime throughout the flight.

The lesson learned from the ANITA-3 flight was that a new method of mitigation of CW signal was critical for the ANITA-4 flight. Before ANITA-4, the available methods to reduce digitization deadtime were masking and decreasing thresholds when in the presence of higher levels of noise. A decrease in thresholds corresponds to higher power of the incoming signal. Masking and decreasing thresholds come at the cost of instrument livetime [1] and sensitivity to neutrinos, respectively. For about 90% of the time during the ANITA-3 flight, masking was used to veto triggers from over half of the payload field-of-view to keep the trigger rate at or below $50\,\mathrm{Hz}$. This significantly lowered the total instrument livetime. For ANITA-4, the TUFF boards were built with tunable notch filters to restore triggering efficiencies in the presence of CW interference. Additionally, the 90° hybrids, previously deployed in ANITA-1 as described in our design paper [19], were added to the ANITA-4 trigger system by requiring a coincidence between left- and right- circularly polarized signals.

2.3.2 Design and construction

In April of 2016, NASA gave the ANITA collaboration the go ahead to attempt a launch of the ANITA-4 mission at the end of that same year. From May - July of 2016, I worked on constructing and testing the TUFF boards. Constructing them involved soldering several thousand parts on to the boards. This was done by a small team at OSU, including myself, Jacob Gordon and Michael Kovacevich. Patrick Allison designed the boards and supervised our work. Testing of the boards was done in different stages and involved frequent measurement of the TUFF response using the network analyzer, making measurements of the

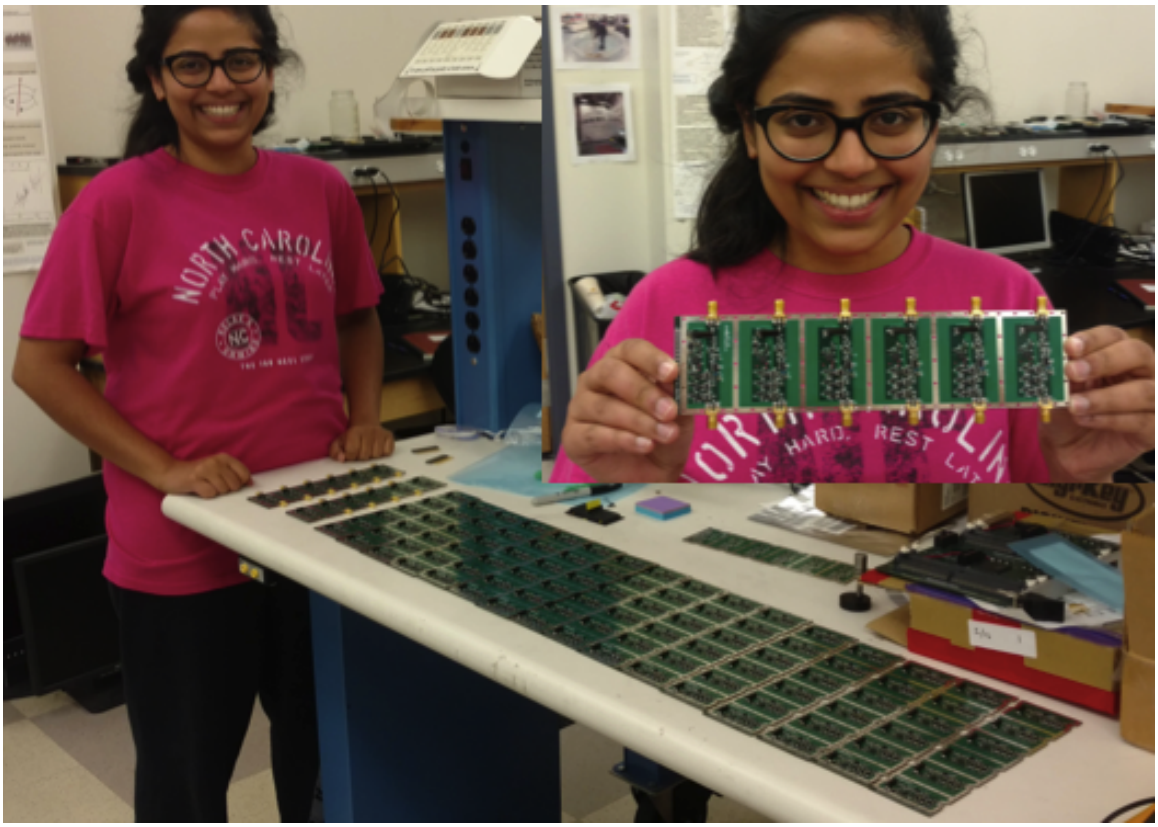

Figure 2.10: During the construction of the TUFF boards at OSU (May - July of 2016). The picture of myself holding one of the boards gives an idea for their size and shape. Clearly, building these boards made me very happy.

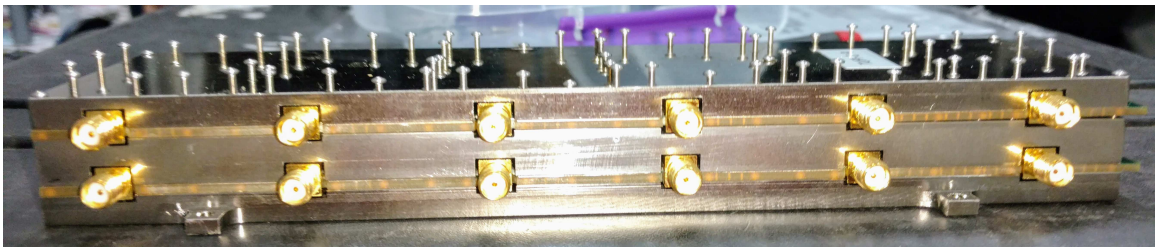

Figure 2.11: Pairs of TUFF boards were enclosed within aluminum cases with RF padding on the inside. The enclosures were held shut with the help of the screws shown here. Even a slight problem with the case design could make it very difficult to put the screws in or take them out. In fact, these screws became the bane of our existence during integration and testing of ANITA-4, and demonstrated how important it was to get the design of the cases right. Thanks to Christian Miki for designing the case.

board's current, capacitance, etc. with the multimeter, and performing experiments using the thermal and vacuum chambers. Figure 2.10 shows myself holding a TUFF board and standing next to a freshly soldered batch of TUFF boards.

The design of the TUFF board was affected by the low power budget of ANITA as well as the weight and size restrictions of a balloon mission, as described in Section 2.1. The TUFF boards needed to be low-power, compact and light. A single channel is about twice the size of a quarter dollar coin. Each printed circuit board has four layers of copper with an FR-4 dielectric material. The TUFF boards operate on 3.3 V and 4.7 V power sources provided by a MIC5504 from Microchip Technologies Inc. and a ADM7171 from Analog Devices Inc. Both voltage regulators draw from a 5 V source supplied by the DC/DC unit in the ANITA Instrument Box. A single TUFF channel consumes only 330 mW of power. The total power consumed by the ANITA payload is approximately 800 W.

Two TUFF boards were assembled into a final 12-channel aluminum housing as shown in Figure 2.11. This provides heat-sinking, structural support, and RF isolation. Two of these 12-channel modules were placed inside an Internal Radio Frequency Conditioning Module (IRFCM) inside the Instrument Box of ANITA. Figure 2.12 shows the inside of an IRFCM. Each TUFF channel has four main components which are described in the following subsections.

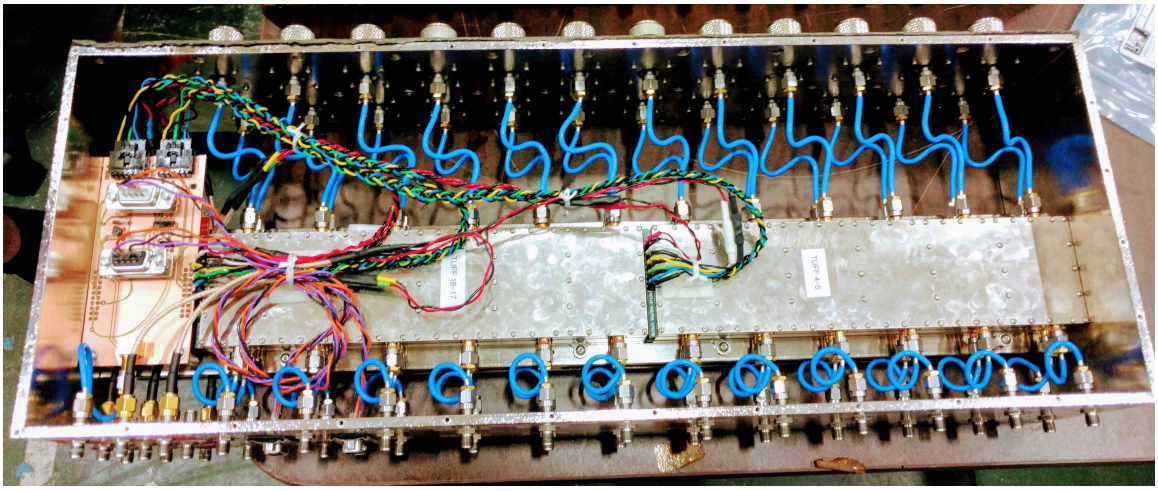

Figure 2.12: Rare picture of the inside of an Internal Radio Frequency Conditioning Module (IRFCM) holding two TUFF modules and a TUFF master. There are four total IRFCMs.

2.3.3 Amplifiers and bias tee

There are two amplifiers connected in series that together produce second-stage RF power amplification of approximately 45 dB. AMP 1 is a BGA2851 by NXP Semiconductors and AMP 2 is an ADL5545 by Analog Devices. There is an attenuator producing 1 dB of attenuation to the RF signal as it leaves AMP 1 and before it enters AMP 2. The BGA2851 provides a gain of 24.8 dB at 950 MHz. It has a noise figure of 3.2 dB at 950 MHz. It consumes 7 mA of current at a supply voltage of 5 V, or 35 mW of power. The ADL5545 provides a gain of 24.1 dB with broadband operation from $30 - 6000$ MHz. Out-of-band power at frequencies above 2 GHz is suppressed by a filter on each TUFF channel. Additionally, there are band-pass filters immediately after the TUFF boards in the signal processing chain allowing power only in the frequency range $200 - 1200$ MHz. The ADL5545 has a noise figure of 2.9 dB at 900 MHz and a 1 dB compression point (P1dB) of 18.1 dBm at 900 MHz. It consumes 56 mA of current at a supply voltage of 5 V, or 300 mW of power. Thus, this amplifier consumes the majority of the power required by a single TUFF channel.

There is a bias tee on each TUFF channel that remotely powers the AMPA unit at the other end of the coaxial cable connecting an AMPA and that channel. It consists of a 4310LC inductor by Coilcraft in series with a 0.1 μF capacitor. The inductor delivers DC to

the AMPA unit while the capacitor prevents DC from passing through to the signal path of the TUFF channel. The bias tee allows RF signal traveling from the AMPA unit through the coaxial cable to pass through to the rest of the signal path of the TUFF channel.

Notch filters

There are three tunable, switchable notch filters for mitigation of CW noise at the default frequencies of 260 MHz (Notch 1), 375 MHz (Notch 2) and 460 MHz (Notch 3). The measured as well as simulated gain, phase and group delay of a TUFF channel, with the first two notch filters activated (most common configuration used during the ANITA-4 flight) and all filters de-activated, is shown in Figure 2.13. The TUFF notches were able to achieve a maximum attenuation of approximately 13 dB, and were implemented as a simple RLC trap, with the resistance R originating from the parasitic on-resistance of a dual-pole, single-throw RF switch and the DC resistance of the remaining components. This is approximately $6 - 7\,\Omega$. The inductance L is fixed at 56 nH. The capacitance C is a combination of a fixed capacitor and a PE64906 variable capacitor from Peregrine Semiconductor. Simulations using the device model of the variable capacitor also suggested that the mounting pads of the components contribute $\sim$ 0.6 pF of parasitic capacitance.

With the tuning capability of the variable capacitor, the resonant frequency of the RLC circuit was modified during flight to dynamically mitigate CW interference. The variable capacitor in a notch can be tuned in 32 discrete steps of 119 fF in the range $0.9 - 4.6$ pF and for each notch, is connected in series or parallel with a constant capacitance. For Notch 1, the variable capacitor is in parallel with a 1.8 pF capacitor. For Notches 2 and 3, the variable capacitor is in series with a 12.0 pF (Notch 2) and a 1.5 pF (Notch 3) capacitor for increased tuning capability.

2.3.4 Microcontroller

We use an ultra-low-power microcontroller, specifically a MSP430G2102 by Texas Instruments. This features a powerful 16-bit Reduced Instruction Set Computing (RISC) central processing unit (CPU). There are five low-power modes optimized for extended battery

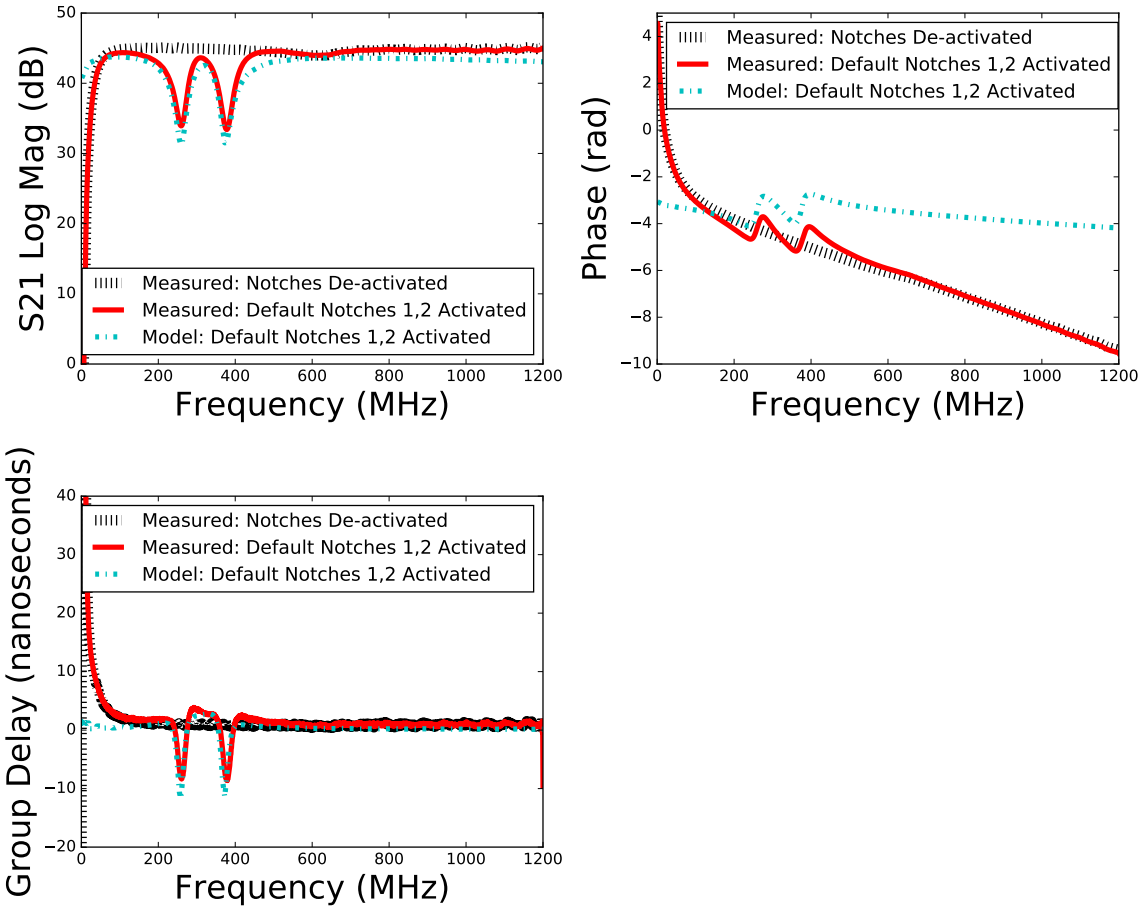

Figure 2.13: The gain, phase and group delay as measured and simulated for a TUFF channel with the first two notch filters activated (most common configuration used during the ANITA-4 flight) and all notch filters de-activated.

life. The active mode consumes 220 μA at 1 MHz and 2.2 V. The standby mode consumes only 0.5 μA and the RAM retention-off mode consumes 0.1 μA. The digitally-controlled oscillator allows wake-up from low-power modes to active mode in less than 1 μs.

During the ANITA-4 flight, commands could be sent using the SIP connection to set the state of the variable capacitor of each TUFF notch filter via the microcontroller of that channel. This was done in real time if a re-tune of a notch filter was necessary to mitigate CW interference. Commands could be sent to de-activate or activate a notch filter using the switch associated with each notch. Each microcontroller has the capability to communicate over universal serial communication interface.

2.4 Impact of the TUFF boards

The TUFF boards had a large impact on the livetime of ANITA. There are two types of livetime in ANITA, which are described below.

Digitization livetime In ANITA, deadtime due to digitization by all four LABRADOR chips of the SURF board is recorded by the TURF board, as illustrated in Figure 2.7. This deadtime is recorded as a fraction of a second. Digitization livetime per second can be obtained by subtracting this from one. Increasing the digitization livetime increases the probability of receiving RF signal due to an UHE neutrino.

Instrument livetime At any given time, the digitization livetime multiplied by the fraction of unmasked phi sectors (after accounting for channel-masking) gives us the instrument livetime per second. In other words, instrument livetime accounts for the fraction of observable ice in azimuth after accounting for masking.

2.4.1 3x instrument livetime

The most significant impact of the TUFF boards was the great reduction in the need for masking to mitigate noise during the ANITA-4 flight as compared to ANITA-3. This can be seen in Figure 2.14. The striking reduction in masking and increase in digitization livetime,

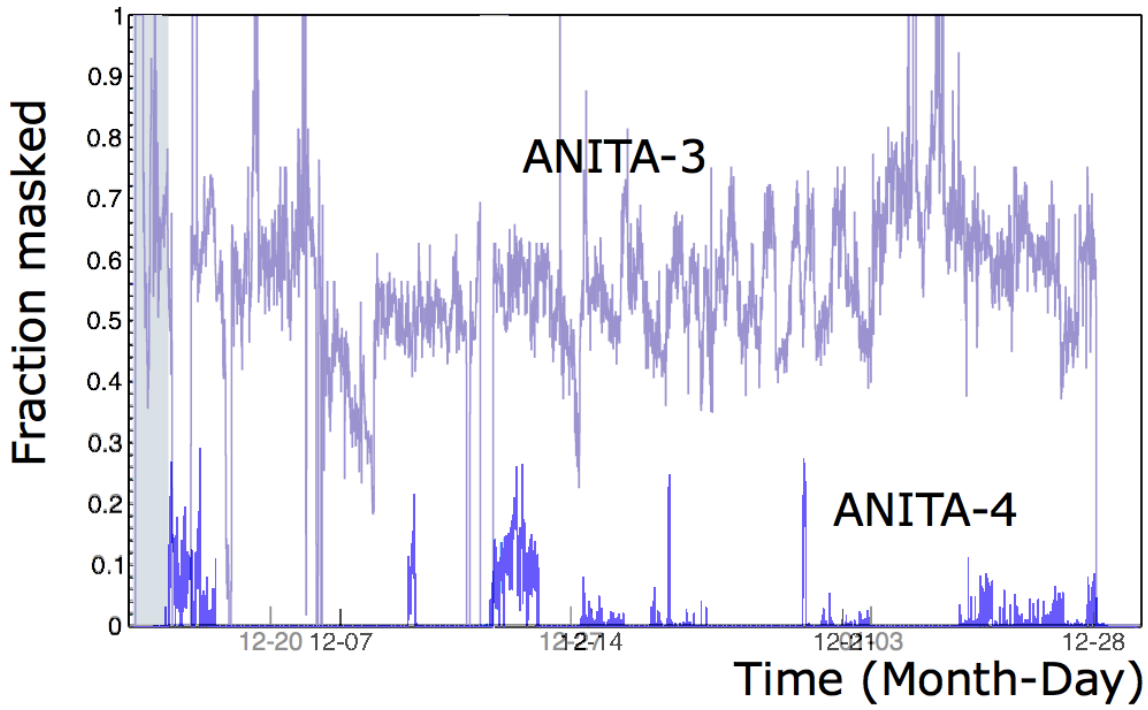

Figure 2.14: Fractional masking implemented in the ANITA-4 and ANITA-3 (faded) flights as a function of time. The TUFF notch filters helped to reduce the need for masking and thereby, tripled the instrument livetime of the experiment.

as a result of implementing the TUFF notch filters, contributed to over 91.3% instrument livetime in ANITA-4 compared to the 31.6% in ANITA-3. The performance and impact of the TUFF boards are described in detail in [1], along with visuals comparing the digitization and instrument livetime, thresholds and masking in ANITA-3 and ANITA-4.

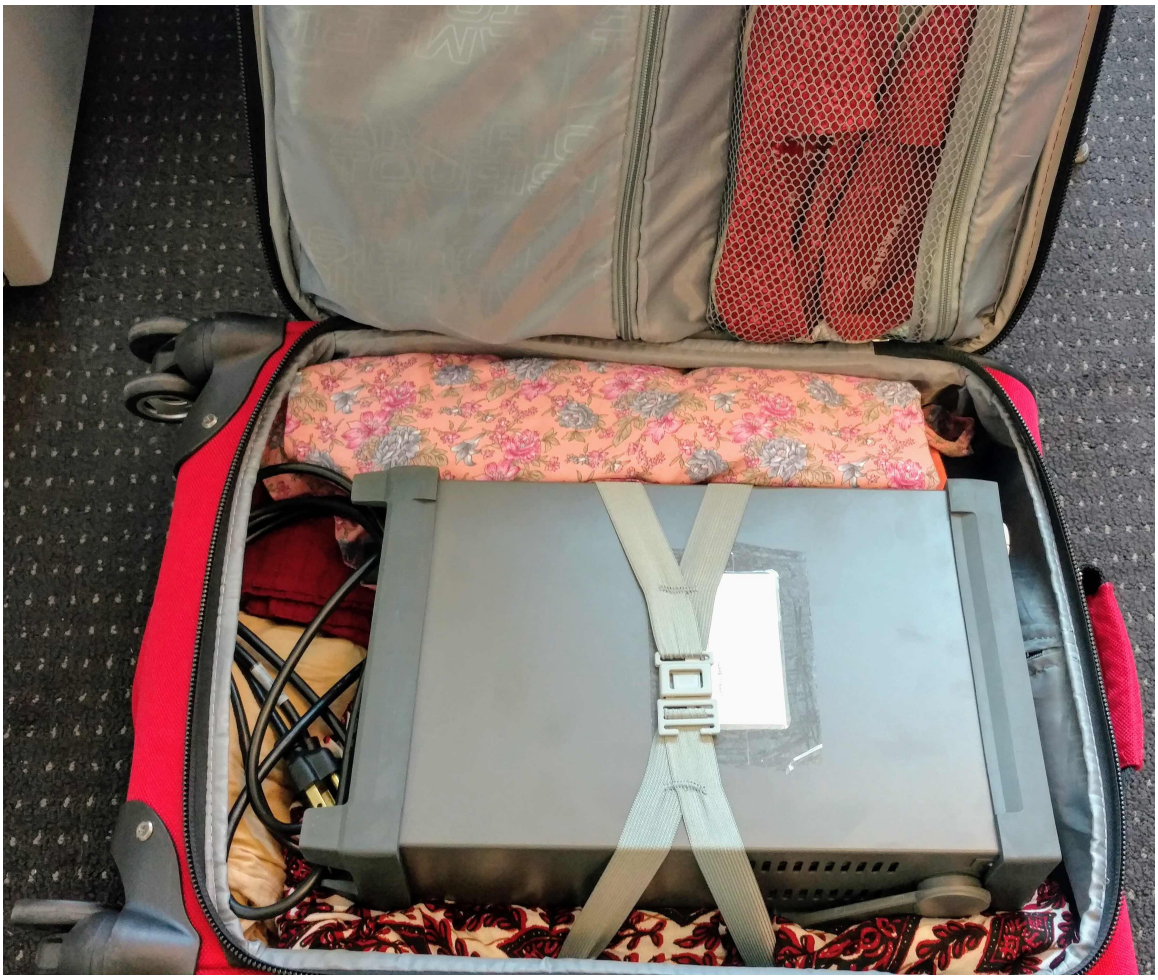

Figure 2.15: Bonus: This is the bag I packed for my trip to Palestine, TX, for the hang test of ANITA-4. I packed my own power supply. TUFF boards needed to be tested in Palestine for the integration and hang test, and they needed power. I thought it pertinent to carry my own as other folks' power supplies simply cannot be trusted, especially in challenging situations. This is from Jim Beatty's stash of lab equipment that he may let you borrow for such occasions. The highlight is I got this through airport security by telling the officers all about ANITA!

Chapter 3

Binned analysis: Developing a new technique focused on background reduction

ANITA is a NASA long-duration balloon experiment for the detection of UHE ($> 10^{18}$ eV) neutrinos. In this chapter, we present details of the development of a new technique for analysis using data collected during the second and third flights of ANITA. The approach used in this new technique is to section off the Antarctic ice into bins and perform a search with different thresholds in each bin. This new strategy was tested on data from the second flight of ANITA which took place in 2008−2009 [20] before being used to search for neutrinos in data from the ANITA-3 flight which took place in 2014 − 2015 [18, 21]. This "binned analysis" is complementary to other ANITA analyses that are centered around clustering of events on the continent.

3.1 Searching for Neutrinos with ANITA

With 48 dual-polarized, horn antennas on-board, ANITA looks for the Askaryan radio signature of UHE neutrinos in the 200 − 1200 MHz band. ANITA has a three-level trigger that requires excursions in power over thermal noise expectations with relative delays that are consistent with what is expected from a plane wave incident on the payload. ANITA records "events" as 100 ns-long voltage waveforms from each polarization of each antenna, sampled at 2.6 GHz.

3.1.1 Motivation

Searches for UHE neutrinos in the ANITA data are conducted following a couple of different techniques. Traditionally, searches have used methods centered around event clustering, henceforth referred to as clustering analyses. After selecting for events with high signal-to-noise ratios that reconstruct to the continent, these analyses search for events that do not cluster with other events and whose reconstructed place of origin on the ice are not consistent with any known bases or locations of known human activity. In the searches for a diffuse flux of UHE neutrinos in data collected during the ANITA-1 flight in $2006 - 2007$ and the ANITA-2 flight in $2008 - 2009$, as presented in [22] and [3] respectively, in the absence of signal, we placed the strongest limits on the flux of cosmic neutrinos in the $10^{18} - 10^{21}$ eV energy regime. The analysis presented in this chapter uses a different "binned" approach and complements the clustering analyses in terms of its sensitivity to neutrinos in different regions of ice.

The motivation behind the binned analysis is to maintain sensitivity for neutrinos even in regions of ice where sources of anthropogenic noise are present. In the clustering analysis, a neutrino candidate would be in the form of a "non-base singlet" or an event that would pass what is known as the "clustering cut." A clustering cut attempts to remove anthropogenic backgrounds by eliminating all events that are less than a certain minimum distance away from any bases and/or "hot spots" of human activity as well as from any other events that passed all other cuts. In a clustering analysis, regions of ice near other high SNR, reconstructing events or near regions of human activity are removed from the search. The binned analysis instead attempts to use all of the ice, and searches for events that stand out among other events that reconstruct to the same region.

Figure 3.1 shows the area of ice used for neutrino searching in one of the two independent clustering analyses of the ANITA-3 data [2]. The red points in the figure denote simulated neutrinos that fail the clustering cut while the blue points denote those that pass. Here, neutrinos are simulated using the Kotera model flux [23]. As seen in Figure 3.1, the clustering cut removes regions of ice and results in losses in sensitivity to a cosmogenic

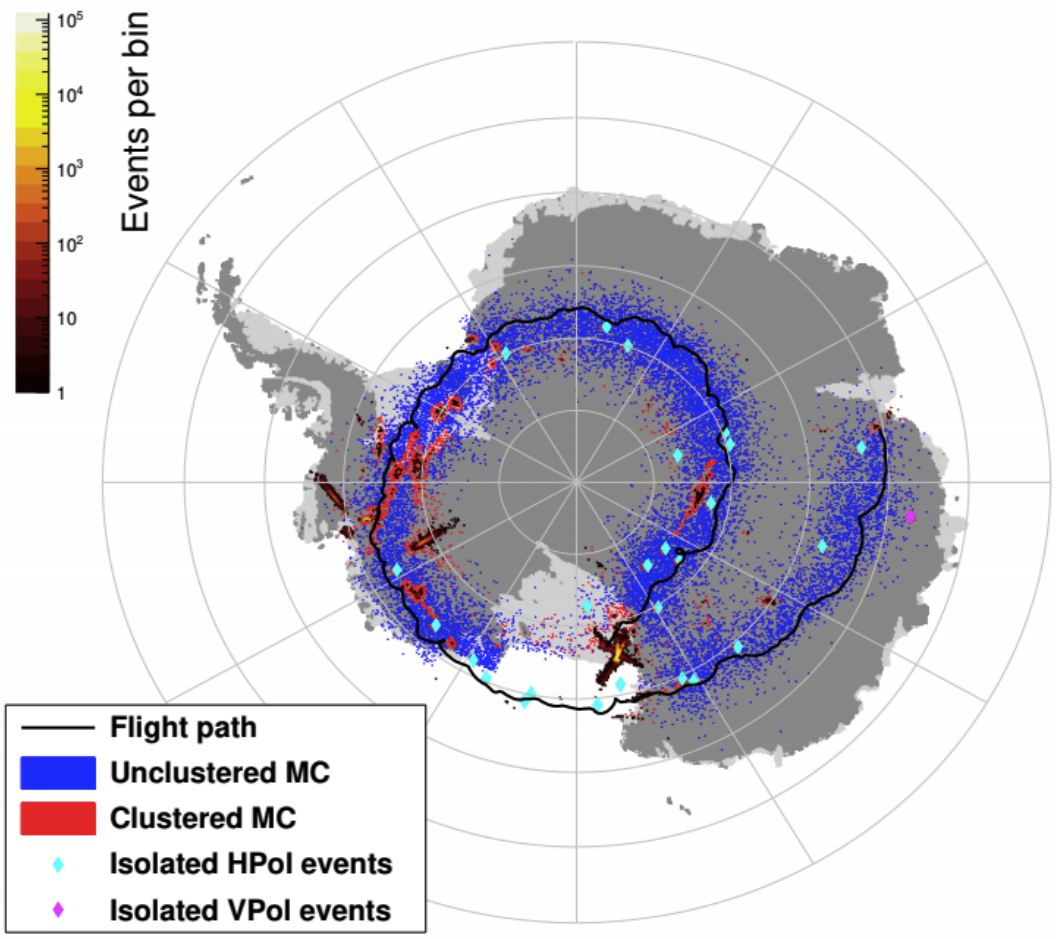

Figure 3.1: This is a figure from the clustering analysis performed by Ben Strutt during his postdoc at UCLA [2]. Blue points represent simulated neutrinos that pass the clustering cut, while red points indicate ones that fail. The teal points show candidates of extensive air showers. The single pink point shows the neutrino candidate from this analysis.

neutrino flux. We attempt to recover part of this sensitivity in the binned analysis. In this chapter, we present the binned analysis strategy and methods with a focus on background reduction. The work shown here is built upon modules completed by other binned analysts as are detailed in their theses [18, 20, 21].

3.2 Binned analysis approach

In the binned analysis, the Antarctic ice observed by the ANITA payload is sectioned off into bins of nearly equal area. For this we use the Healpix package [24], normally used to

bin the sky for use in cosmology, but here it is used to bin the earth. Figure 3.2 shows Healpix binning for the ANITA-2 and -3 binned analyses where the coordinate system is centered at the South Pole. We overlay an outline of the continent of Antarctica and the flight path for the particular flight. The binned approach attempts to maintain the ability to search for neutrinos in as many bins as possible where we are sensitive.

Figure 3.2a shows simulated neutrinos as reconstructing to different bins in the ANITA-2 binned analysis. The color in these bins is representative of ANITA's sensitivity to neutrinos in that bin where sensitivity is in arbitrary units. It can be seen that the sensitivity to neutrinos varies bin to bin. Some parts of the continent have larger ice depth than others, and typically, ANITA is more sensitive to neutrinos in these parts.

Figure 3.2b shows events from the 10% data before final cuts as reconstructing to different bins in the ANITA-3 binned analysis. These events are dominated by noise. In ANITA, noise events are mainly either due to thermal radiation from the ice or from human activities. It can be seen that some bins have more events than others as indicated by the color in that bin. This is mainly because some parts of the continent have more human activity than others. In other words, in some bins the anthropogenic backgrounds are larger than others, and in those bins we will need a higher threshold for our analysis cuts than those bins where the events that reconstruct there are predominantly triggered due to thermal noise fluctuations. Figure 3.3 shows the efficiency as a function of SNR in the ANITA-2 binned analysis.

3.2.1 Bins and event weights

One of the features of the binned analysis is that we sort events into different bins. The bin in which an event falls is determined by tracing its reconstruction direction back to the surface of Antarctica. Using functions written in the ANITA analysis tools by Ryan Nichol, and BEDMAP2, a dataset of the surface elevation of Antarctica, the location at which the event came out of the ice is found. This location in longitude and latitude can be used to locate which Healpix bin an event falls in. Events that are very close to the boundary between bins are assigned a weight based on how much of a one-standard-deviation error

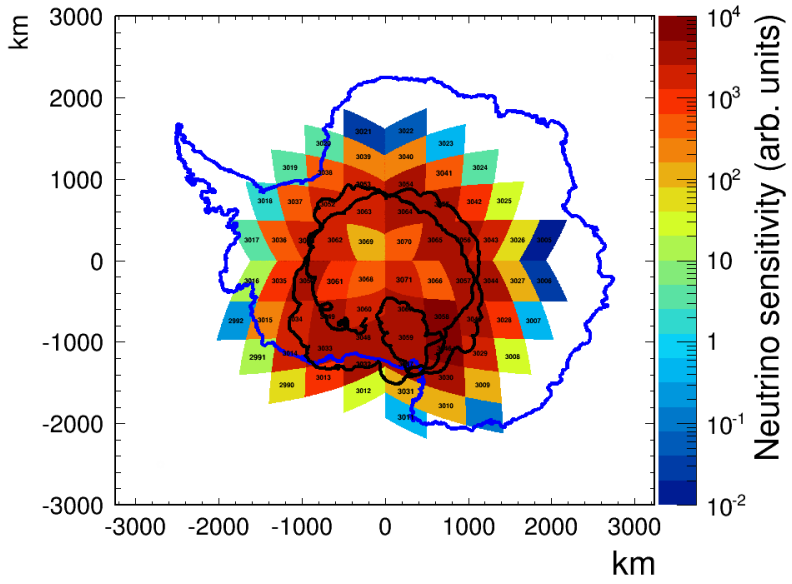

(a) ANITA-2 simulated neutrinos showing sensitivity in different bins

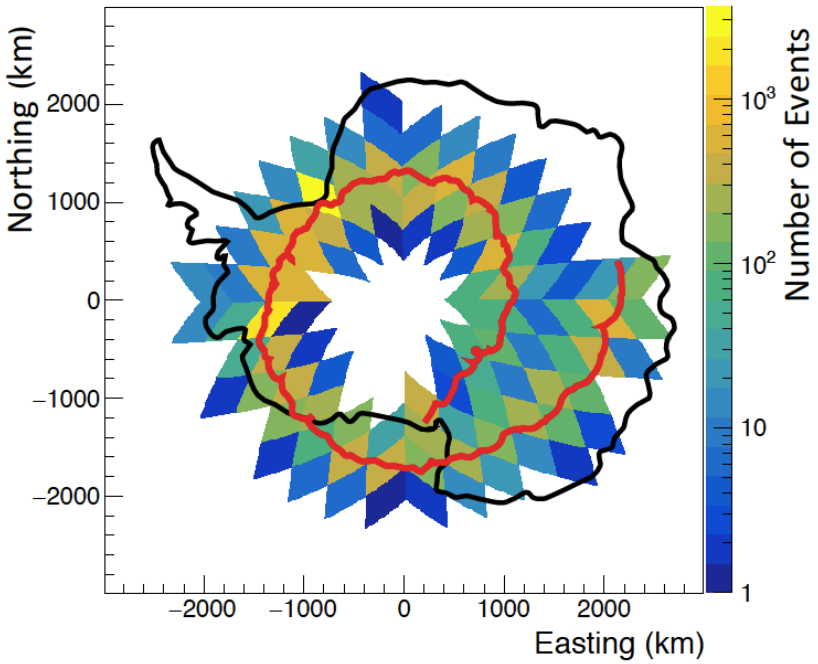

(b) ANITA-3 10% data showing noise levels in different bins

Figure 3.2: Top: Simulated neutrinos in the ANITA-2 flight. Bottom: 10% data before final cuts in the ANITA-3 flight. In both plots, color represents the number of events in that bin. An outline of Antarctica and the flight path are overlaid. It can be seen from the top plot that the sensitivity to neutrinos is different in different bins. Typically, sensitivity is larger in parts of the continent with greater ice depth.

ellipse around the event, based on uncertainty in the event's reconstructed angels, is inside of the bin. Events that fall entirely inside of one bin have a weight of one.

3.2.2 Blinding

ANITA uses blinding strategies to ensure that analyzers do not know which events will be considered candidates while they are designing cuts. Blinding approaches have varied among different ANITA analyses, and are briefly summarized here.

Beginning with ANITA-2, each ANITA data set has been "salted" with an unknown number (on order a few) fake candidates. These are calibration pulser events whose origin on the continent have been scrambled. Once final cuts have been imposed, these so-called inserted events are removed.

The published ANITA-2 clustering analysis, presented in [3], also used an "ABCD" approach where we categorized events according to how they clustered with other events, and stayed blind to events that were isolated from other events and from other bases until the final step before removing inserted events. The ABCD refers to four different categories of clusters: multiplets associated with bases (base clusters), singlets associated with bases (base singlets), multiplets that are not associated with bases (non-base clusters), and the blinded non-base singlets.

In the binned analysis presented here, in addition to salting, we use 10% of the dataset (the burn sample) for understanding backgrounds and setting cuts, while being blind to the remaining 90% of the data until the final step where we impose cuts on the 90% set to identify candidates.

3.3 Background reduction

The ANITA experiment records millions of events, most of which are noise. Eight, 26, 80, and 97 million events were recorded in the ANITA-1, -2, -3, and -4 flights, respectively. As UHE neutrino hunters, we are looking for extremely rare events in the ANITA data. The name of the game, therefore, is to remove noise from the data or apply "cuts". Cuts

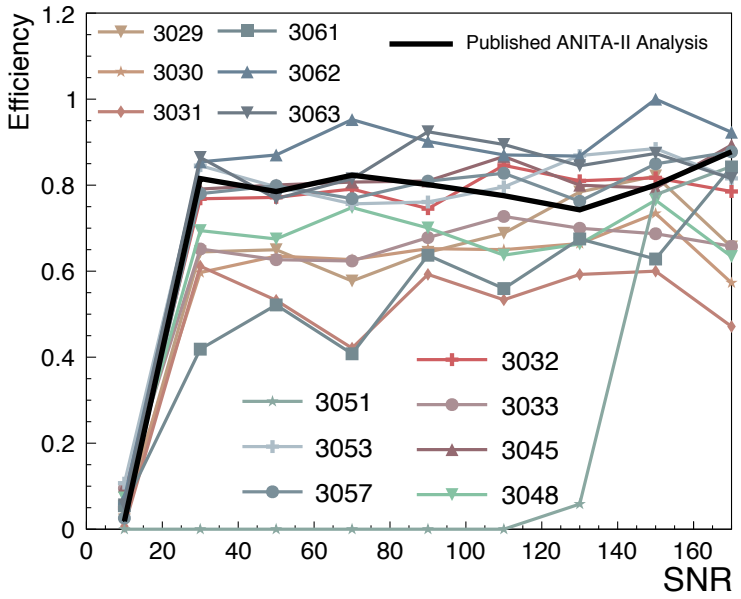

Figure 3.3: Efficiency as a function of SNR in the ANITA-2 binned analysis. The solid, black line shows the efficiency for the ANITA-2 clustering analysis [3]. While the clustering analysis would have a single curve for efficiency, the binned analysis has such a curve in each bin kept in the analysis.

are roughly categorized as quality, analysis and final analysis cuts. To give an idea, this is briefly described for the ANITA-3 binned analysis in the following subsections. Details on cuts can also be found in [18, 20, 21].

3.3.1 Quality cuts

The first stage of cuts made are known as quality cuts. These cuts mainly remove events that do not meet basic standards involving the trigger and digitizer. We also try to remove noise events caused by the payload itself in this phase of the analysis.

No Trigger Cut

The No Trigger Cut requires the recorded event to have a triggering phi sector. If the event did not cause a phi sector to trigger, then it is cut.

Trigger Type Cut

This cut requires the trigger type to be a radio frequency (RF) trigger. Events that are not RF triggers are cut.

SURF Saturation Cut

The SURF's operating range only extends up to 1.5 V. If an event's waveform goes beyond that operating range, it can become distorted. Due to this, events with more than three waveforms that exceed 1.5 V are cut.

DC Offset Cut

Some events have waveforms with noticeable DC offsets. This is thought to be due to digitization problems. If an event has a mean value in their waveform of greater than 100 mV in any channel, it is cut.

Short-trace Cut

A complete waveform in ANITA-3 has 240 data entries or samples. If an event has less than 240 samples for any reason, it is considered incomplete and cut.

Payload Blast Cut

Payload blast events are events that appear to be coming from the payload itself. They are both impulsive and often have a high SNR. Because of these features, payload blast events can be quite problematic to our analysis. Both this cut and the nadir noise events cut are designed to remove payload blast events. This cut removes events that have an L3 trigger across 6 or more phi sectors. Payload blasts are able to trigger many channels.

Nadir Noise Cut

The peak voltages in the bottom ring antennas of payload blast events are dramatically larger than the peak voltages in the top ring. This cut is designed based on this feature. If

the maximum peak voltage in the top ring is less than one half the maximum peak voltage in the bottom ring, the event is cut. Note that we have also seen blast events where the reverse is true, that is the top antennas have higher peak voltage than the bottom, although this is relatively rare. Surviving "reverse blast" events are removed by hand at the end with no cut dedicated to their removal in the earlier stages of the analysis.

3.3.2 Stage 1 Analysis Cuts

Analysis cuts are performed in two stages in the ANITA-3 binned analysis. In this section, we describe the cuts implemented in the first stage. Most cuts at this stage are involved with event reconstruction. Calibration pulser events are also removed in this phase of the analysis.

Solar Reflection Cut

The reflection of the sun off of the ice is a hot spot for noise events [18]. Events that point to within 5 degrees of the sun's reflection are cut. For events that triggered in VPol, their reconstruction in VPol is used, and for events that triggered in HPol, their reconstruction in HPol is used.

Reconstruct to Continent Cut

For a neutrino search, we only expect to see neutrino signals from the ice. Thus events that do not reconstruct back to the continent are cut.

Elevation Angle Cut

ANITA antennas have a 6dB fall off at 22.5 degrees from boresight, and point to 10 degrees below the horizontal. This means any signals arriving from below -35° (slightly more than $22.5 + 10$) should be greatly reduced in power. Many of the events we do see from those angles are misreconstructions. Events that reconstruct to angles above the continent are similarly thought to be misreconstructions. Events that reconstruct to above 6.0° below

the horizontal (corresponds to the horizon of ANITA), or below 35.0° below the horizontal are cut in this analysis.

Triggering Phi-sector Direction Cut

An event that reconstructs to a phi sector in which it did not cause an L3 trigger is regarded with suspicion as they are thought to be misreconstructed. Events that do not trigger in the phi sector they reconstruct into, are cut.

Calibration Pulser Cut

Events originating from WAIS and LDB are cut if their nanosecond time-stamp is consistent with the calibration pulses coming from these locations. A quantity called "nsDiff" is calculated for events to determine if they come from a calibration pulser.

$$nsDiff = sourceDelay - triggerTimeNs + pulserNsTime; \tag{3.1}$$

3.3.3 Stage 2 Analysis Cuts

Analysis cuts are performed in two stages in the ANITA-3 binned analysis. In this section, we describe cuts performed in the second stage. Cuts in this phase of the analysis are in place mainly to ensure that only impulsive events survive after this point. Cuts based on the circular polarization of events are also implemented at this stage as developed in [18].

Ratio of Highest Peak Cut

Neutrino signals are expected to be highly impulsive, which is expected to render as a single distinct peak in the correlation map. CW and thermal noise, however, are expected to produce multiple peaks. If the ratio of the second largest to largest peak in the correlation map is more than 0.9, then the event is cut.

Correlation Peak Cut

A highly impulsive event should have a large peak value on its correlation map. Events with a correlation peak value below 0.04 are cut. Correlation peak values are determined for an event by performing interferometry to obtain correlation maps of the sky for the event in all polarizations and then finding the maximum value in the maps. The VPol or HPol map is used for the cut depending on whether the event triggered in VPol or HPol.

Hilbert Peak Cut

Impulsive events should have the majority of their power concentrated over a small window in time. They should also have a high peak power value within that time window. The Hilbert peak is a measure of both of these. Events with a Hilbert peak value below 25 mV are cut.

Circular polarization Peak Separation Cut

The threshold for the circularly-polarized peak separation cut was optimized in [18] for the ANITA-3 binned analysis. This cut removes an event if the correlation peak in LCP is more than 46° from its correlation peak in RCP.

Circular polarization Peak Strength Cut

The threshold for the circular polarization peak strength cut was also optimized in [18]. The circular polarization peak strength is the peak value of the correlation map in circular polarization (left circular polarization (LCP) or right circular polarization (RCP)). It is expected that a neutrino signal should have its power split up evenly between LCP and RCP. The cut removes an event if either the LCP or RCP peak is below 0.015. In practice, the two circular polarization cuts primarily remove thermal noise as thermal noise is not linearly polarized.

3.3.4 Final Analysis Cuts

Linear Discriminant Cut (LD Cut)

The linear discriminant cut or LD cut is meant to be the final cut in the binned analysis. This cut was developed starting with the ANITA-2 binned analysis and improved in the ANITA-3 binned analysis. Figure 3.4 shows a 2-dimensional distribution of SNR of the coherent waveform in the vertical axis plotted against, in the horizontal axis, the peak value of the cross correlation of events from the 10% dataset that reconstructed to Bin 2970 of the ANITA-3 binned analysis.

The linear discriminant is visualized as a red line in the top plot of Figure 3.4. The equation for this line is shown in Equation 3.2. All events to the right of the line are allowed to pass the LD cut. The slope of this line was optimized in [18] and calculated to be -6.0. The y-intercept of the line is optimized separately for each bin in the binned analysis as described in [2, 18, 20, 21].

The y-intercept of the red line in the top plot of Figure 3.4 is known as the LD cut. The value of this y-intercept is individually calculated for each bin in the analysis following an optimization process. To calculate the y-intercept for a bin, the y-intercepts associated with the events in that bin are plotted as shown in the bottom plot of Figure 3.4 and fit to an exponential. This plot shows the distribution of y-intercepts associated with events from the 10% sample that reconstructed to Bin 2970 of the ANITA-3 binned analysis, with the differential number of events that would be cut by the corresponding choice of y-intercept, shown in the vertical axis of the bottom plot in Figure 3.4. The exponential fit appears linear in this plot as it is a log-linear plot and is pictured with a red line. The final y-intercept or LD cut for this bin is denoted by the vertical blue line.

$$\text{LD} = \text{SNR} - \text{slope} \cdot \text{Correlation Peak} \tag{3.2}$$

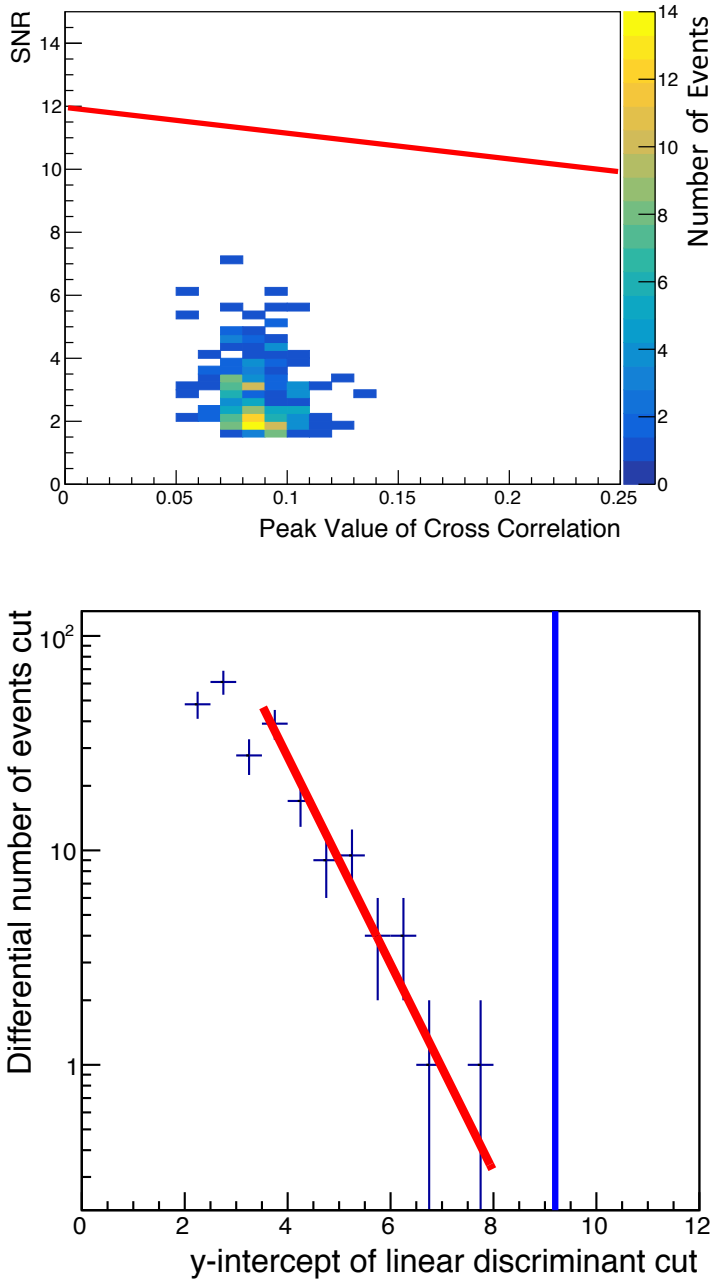

Figure 3.4: Top: The voltage SNR of the coherently summed waveform as a function of peak cross-correlation value for events in the 10% dataset of the ANITA-3 binned analysis, reconstructing to Bin 2970, in the vertical polarization analysis. The red line shows the linear discriminant for this bin with an optimized slope. The y-intercept of this linear discriminant is not yet optimized. Bottom: The y-intercept associated with the events from Bin 2970 fit to an exponential. The vertical blue line shows the optimized LD cut for this bin.

Bin cut

A bin is cut from the analysis if it does not meet certain requirements. In previous attempts of the binned analysis [18, 21], a bin was cut if it did not have five consecutive histogram bins with bin content values in descending order in the distribution of y-intercepts for a bin. As described in Chapter 4, this rule was later updated. A distribution of y-intercepts is shown in the bottom plot of Figure 3.4. A bin was also cut if the exponential fit to the distribution of y-intercepts returned a bad p-value. A p-value less than 0.05 and greater than 0.999 was considered bad. In [18, 21], a bin was rejected if the background estimate for that bin was greater than 1.0. This rule was also later updated as discussed in Chapter 4. Finally, bins with the lowest neutrino sensitivity, as derived from simulation, were also cut. Neutrino sensitivity for a bin is estimated based on the number of simulated neutrinos that pass all cuts before the LD cut and reconstruct to that bin. More simulated neutrinos mean that area of the ice is more sensitive to neutrinos. The least sensitive bins with cumulative sensitivity of less than 1% (after all previous bin cuts) are removed for low sensitivity. These bins are used as a sideband in the analysis.

Cut on events with a weight less than 0.5

Events with an event weight of less than 0.5 are cut. An event weight of less than 0.5 corresponds to the event being less than 50% likely to have come from the Healpix bin it is seen passing in. We want passing events to pass in the Healpix bin they are mostly within.

3.4 The problem: Too many background events passing in the binned analysis

Reducing background events was one of the biggest priorities in the development of the binned analysis. The binned analysis was first tested using data from the ANITA-2 flight. In this first pass at the binned analysis, it was found that too many events passed final cuts. In the VPol channel of the analysis, 2.6 background events were expected to pass. Three isolated events were found to pass which was consistent with the background expectation.

Event Number	Day	Time	Strong pol
18523070	Jan 8 2009	10:11:39 PM	HPol
18523574	Jan 8 2009	10:12:10 PM	HPol
18524721	Jan 8 2009	10:13:14 PM	HPol
18538216	Jan 8 2009	10:26:23 PM	HPol and VPol
18561517	Jan 8 2009	10:53:38 PM	HPol

Figure 3.5: Summary of excess events passing in Bin 3045 of the ANITA-2 binned analysis.

However, **21 excess** events were found to require a clustering cut at the end. Requiring a clustering cut at the end should ideally be avoided in the binned analysis which is principled on recovering ice that is deemed unusable by the clustering analyses. In total, **40 events** passed all cuts prior to the clustering cut, of which **24** were strong in VPol, **26** in HPol and **10** in both. Two of the 40 events were inserted, so the total number of background events to account for was **38**.

My goal was to remove such background events to consequently reduce analysis thresholds for the end goal of increasing sensitivity to neutrinos. This involved studying the data to obtain a deeper understanding of different classes of background. I started by focusing on the excess events passing in Bin 3045 of the ANITA-2 binned analysis. This was the bin with the highest sensitivity in the ANITA-2 binned analysis. Events passing all but the clustering cut **and reconstructing** to this bin are summarized in Figure 3.5. The five events all took place on January 8, 2009 within minutes of each other.

3.4.1 Fun with FFTs

I investigated the ANITA-2 data for background that might appear at regular intervals of time and found bumps in the data throughout the flight as shown in Figure 3.6a. These

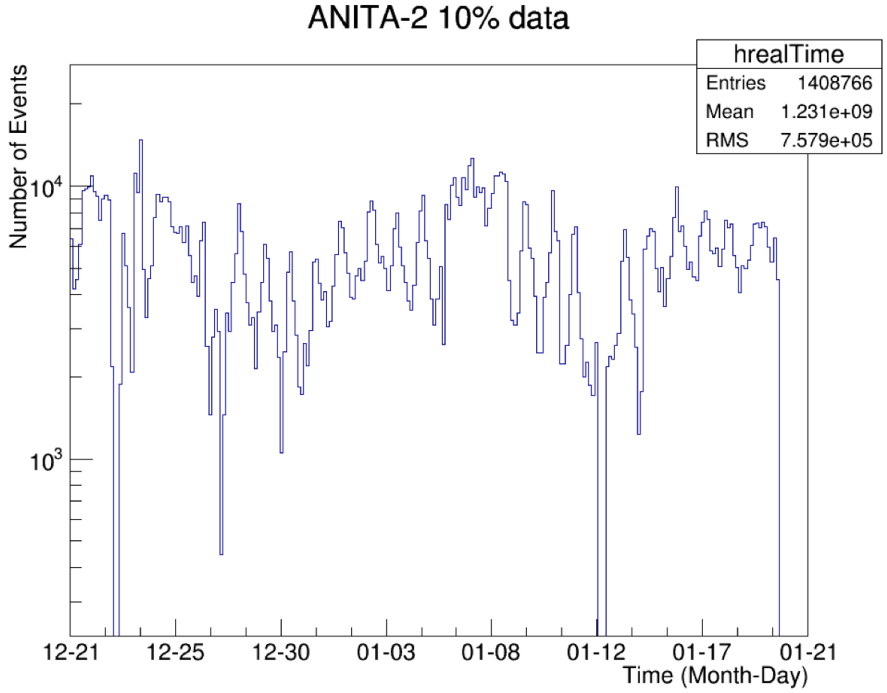

(a) Bumps

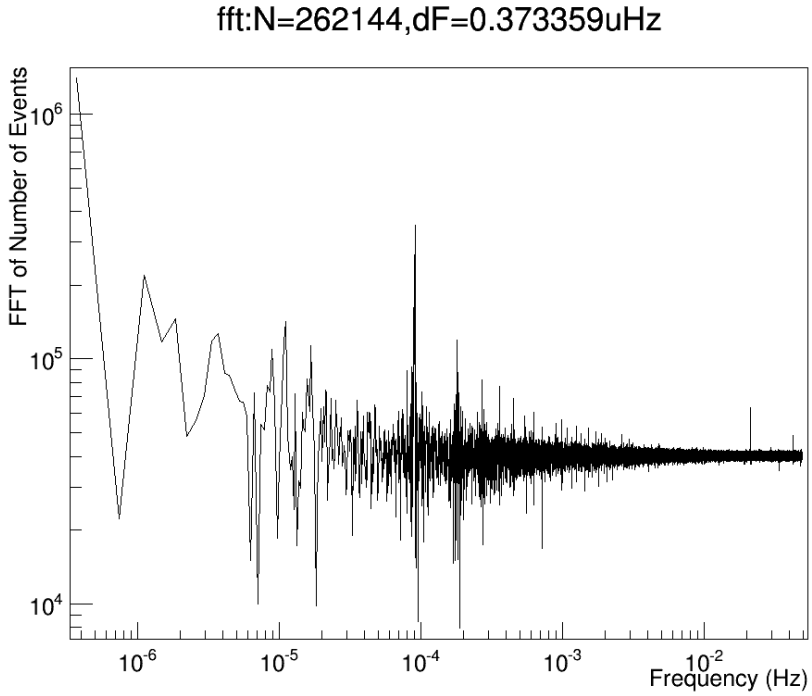

(b) FFT

Figure 3.6: Distribution of number of events as a function of time during the ANITA-2 flight (top) and the FFT of the same (bottom).

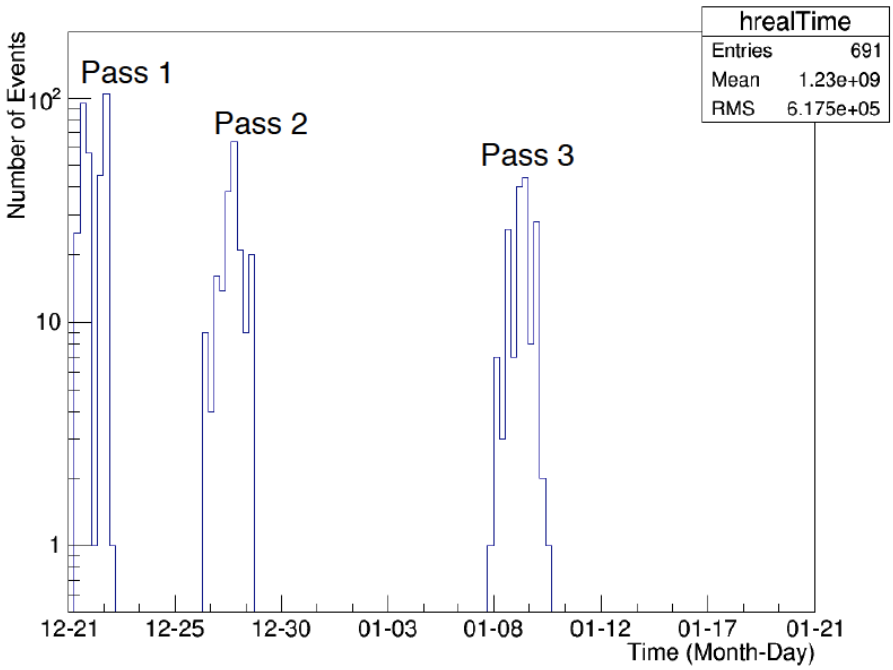

Figure 3.7: The three passes of the ANITA payload over Bin 3045 in the ANITA-2 binned analysis.

bumps seemed to appear at a period of a day, by eye, which would correspond to about $> 10^{-5}$ Hz. I calculated the Fast Fourier Transform (FFT) of the full flight which is shown in Figure 3.6b. The highest peak in the FFT is at $> 10^{-4}$ Hz.

The ANITA payload flew over Bin 3045 thrice during the ANITA-2 flight. I calculated the FFT of the region in time for each pass of the payload over Bin 3045, including January 8 (which is when the excess events from Bin 3045 were recorded) region in time for events that reconstructed to Bin 3045 as shown in Figure 3.8. Interesting features were present in the FFT, one of which was accounted for by the removal of software triggered events from the data. Both a regularly triggered event and the removal of such events can cause peaks at the corresponding frequency in the FFT.

3.5 Satellite contamination

We hypothesized that modulated CW noise from satellites might have contributed to the events passing all but a clustering cut in Bin 3045 of the ANITA-2 binned analysis. Re-

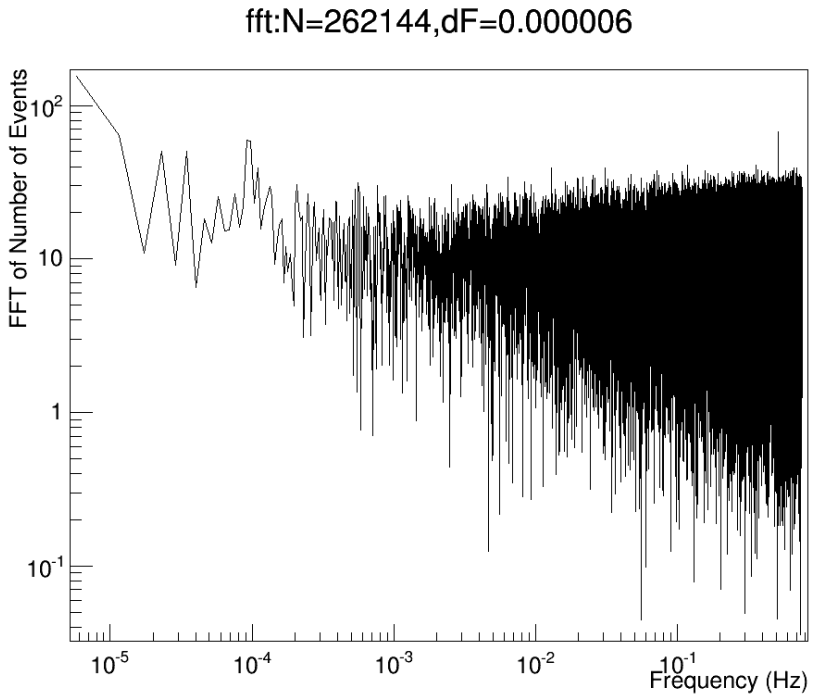

Figure 3.8: FFT of the January 8 region in time of the ANITA-2 flight for only events that reconstruct to bin 3045.

construction maps of these events are shown in Figure 3.9. We noted that the events were strong in HPol as well as LCP and RCP.

3.5.1 Communication satellites

There are numerous human-made satellites in orbit around the earth. Geosynchronous satellites have orbital period that matches earth's rotation on its axis, which takes one sidereal day of 23 hours 56 minutes and 4 seconds. Geostationary satellites have circular, geosynchronous equatorial orbits at 35,786 km (22,236 mi) above the earth's equator and follow the direction of the earth's rotation. There are about a thousand geostationary satellites in orbit around the earth at the moment. Most communication satellites are geostationary. To a stationary observer on earth, the position of a geostationary satellite is fixed in the sky.

Radio, CW interference due to communication satellites, particularly military commu-

nication satellites, have been suspected to contribute to noise events for all ANITA flights and particularly the ANITA-3 flight. This is discussed further in Chapter 2 Section 2.3. We began to suspect that this effect might be seen as an over-density of events at certain longitudes as a function of the azimuthal angle of reconstruction of events. ANITA has 360° coverage in azimuth. Although geostationary satellites would be seen as fixed in the sky, the ANITA payload itself moves. In fact, as ANITA orbits over Antarctica, it traverses across all longitudes. Different geostationary satellites are present at different longitudes, and depending on the latitude of the payload, can be viewable by ANITA.

3.5.2 Satellite stripe plot

I made the now-(in)famous "satellite stripe plot" which is shown in Figure 3.10. In this plot, the longitude of the ANITA payload is in the vertical axis and the azimuthal reconstruction angle of events using their waveforms in LCP is in the horizontal axis. Note that the quantity in the horizontal axis, phi, is **corrected for heading** of the payload and calculated in ROOT as follows:

$$phi = fmod((phi_{LCP} - heading + 360), 360) \tag{3.3}$$

The color axis represents the number of events with red indicating more events and blue indicating less events. Over-densities of events can be seen as stripes at certain longitudes, consistent with the hypothesis that satellites could be causing these. I made this plot first using data from the ANITA-2 flight, and then also for ANITA-3. Figure 3.11 shows the satellite stripe plot made using the 90% data passing quality cuts from the ANITA-2 flight on the left and the 10% data passing quality cuts from the ANITA-3 flight on the right. It can be seen that the **same** stripes are present in the data from **both** flights.

When events that had passed all but a clustering cut in the ANITA-2 and ANITA-3 binned analyses were overlaid on the corresponding satellite stripe plots, the plot thickened. All five events passing in Bin 3045 in the ANITA-2 binned analysis were on one of the stripes. In fact, **16 out of the 38** total non-inserted excess events that had passed all but

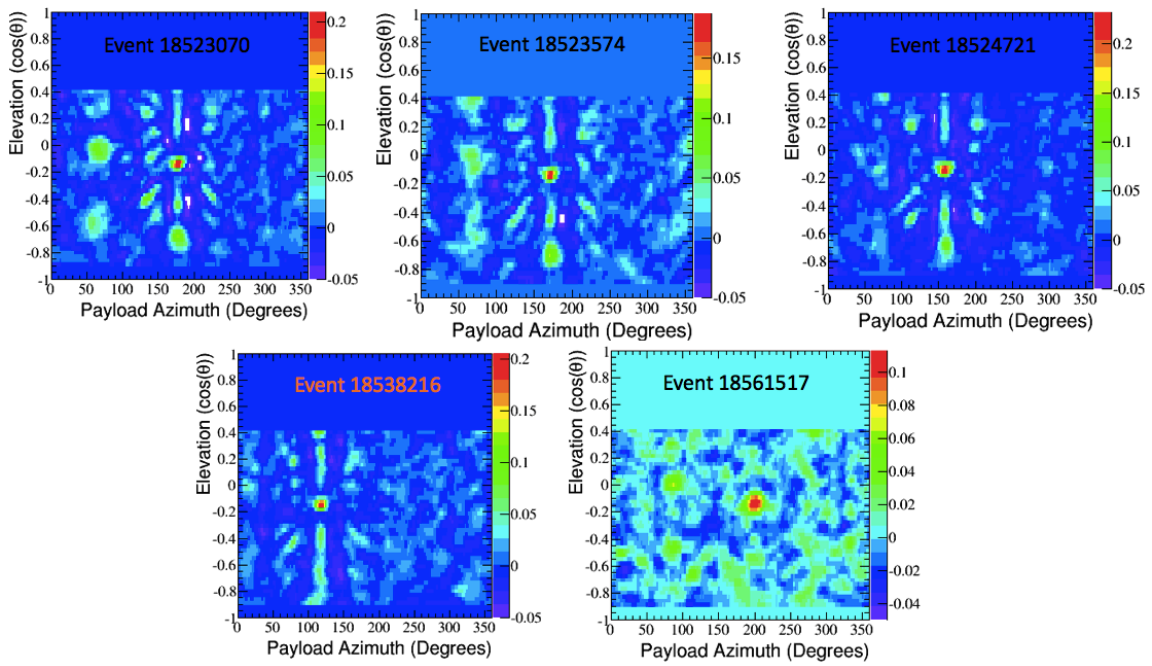

Figure 3.9: Reconstruction maps of the events that passed all but a clustering cut in Bin 3045 of the ANITA-2 binned analysis. These maps are found using the left-circularly polarized waveforms of these events. That is the polarization associated with satellites.

the clustering cut in the ANITA-2 binned analysis landed on top of these stripes. These are labeled in Figure 3.10. Five of the eight events that had passed in the binned analysis of the ANITA-3 10% data as reported in [18] were also on stripes.

3.6 Satellite stripe cut

Our goal was to reduce the number of events passing final cuts in the binned analysis that reconstructed to a satellite stripe. For this, it was necessary to determine equations for the upper and lower bound of each stripe.

3.6.1 Equations of Midlines

Equations for lines denoting approximately the middle of each stripe, referred to as "mid-lines", were determined as shown in Equation 3.4. These are NOT the final equations used to implement the satellite stripe cut that we discuss in Section 3.6.3, however, these midlines

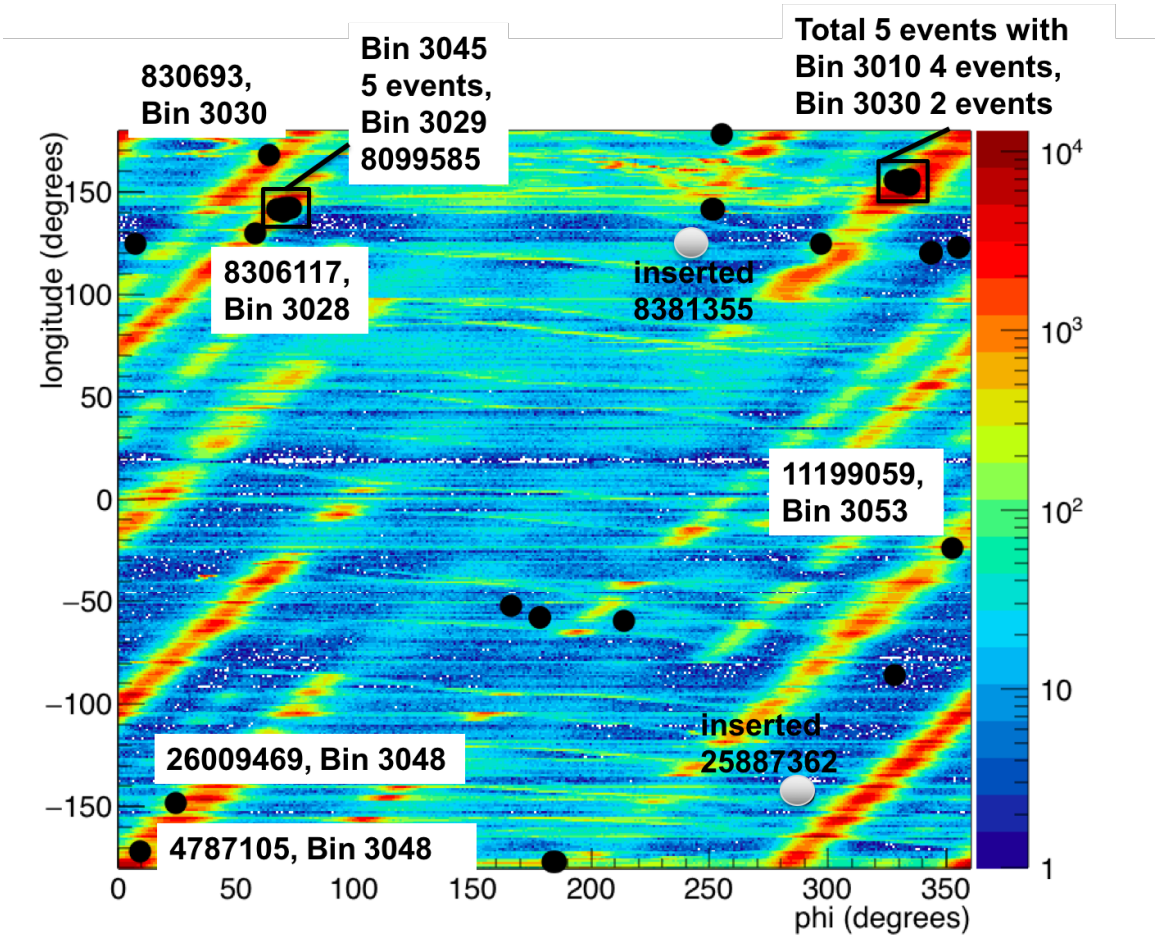

Figure 3.10: ANITA-2 satellite stripe plot with events labeled.

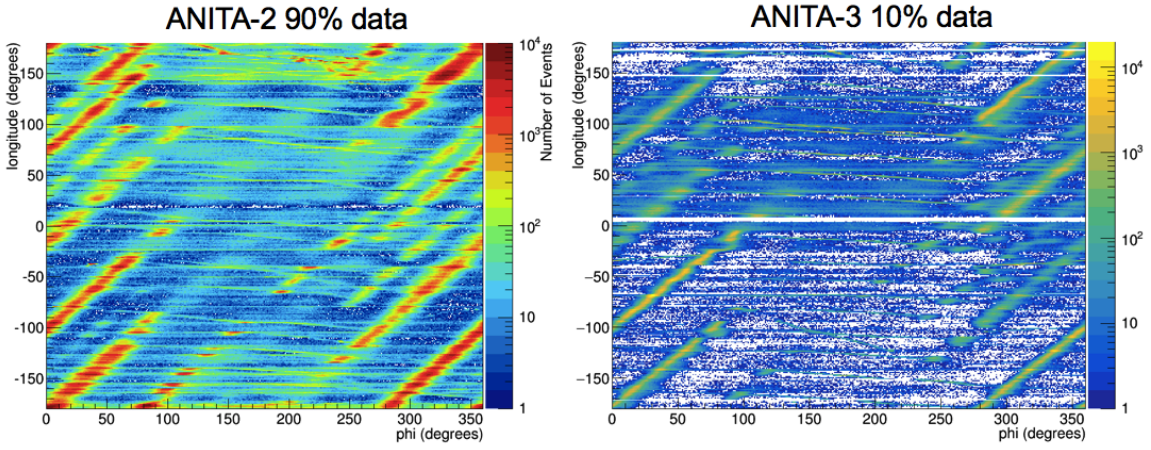

Figure 3.11: Same stripes in both ANITA-2 and ANITA-3 flights.

are the starting point in determining the final equations following the methods described in Section 3.6.2.

$$\begin{cases} stripe\ 1 : longitude = phi - 182.615 \\ stripe\ 2 : longitude = phi - 100.435 \\ stripe\ 3 : longitude = phi - 20.035 \\ stripe\ 4 : longitude = phi + 32.81 \\ stripe\ 5 : longitude = phi + 75.485 \\ stripe\ 6 : longitude = phi + 101.3225 \end{cases} \tag{3.4}$$

In the above equations, longitude is the quantity in the vertical axis and phi is the quantity in the horizontal axis of Figures 3.10 and 3.11. Again, note that the phi here is corrected for heading and given by Equation C.1.

3.6.2 Phi difference distribution

Using the relations in Equation 3.4, cuts for the lower and upper bound of each stripe could be determined. The phi in these equations is called the "expected phi". A broader stripe was used that more than covered each stripe. In this broader stripe the difference between the phi of each event and the expected phi, that is, $phi - expected\ phi$, was calculated. A distribution of this difference in phi and the expected phi, henceforth referred to as the "phi difference distribution" was plotted for each stripe. This distribution for stripe 5 and using data from the ANITA-2 flight is shown in Figure 3.12.

The left and right tail of each phi difference distribution was fit to a line which was subtracted off. This was meant to help reduce the continuum present in the distribution. Then each phi difference distribution was fit to a combination of gaussian functions. The equation for the fit as calculated using ROOT is shown in Equation 3.5.

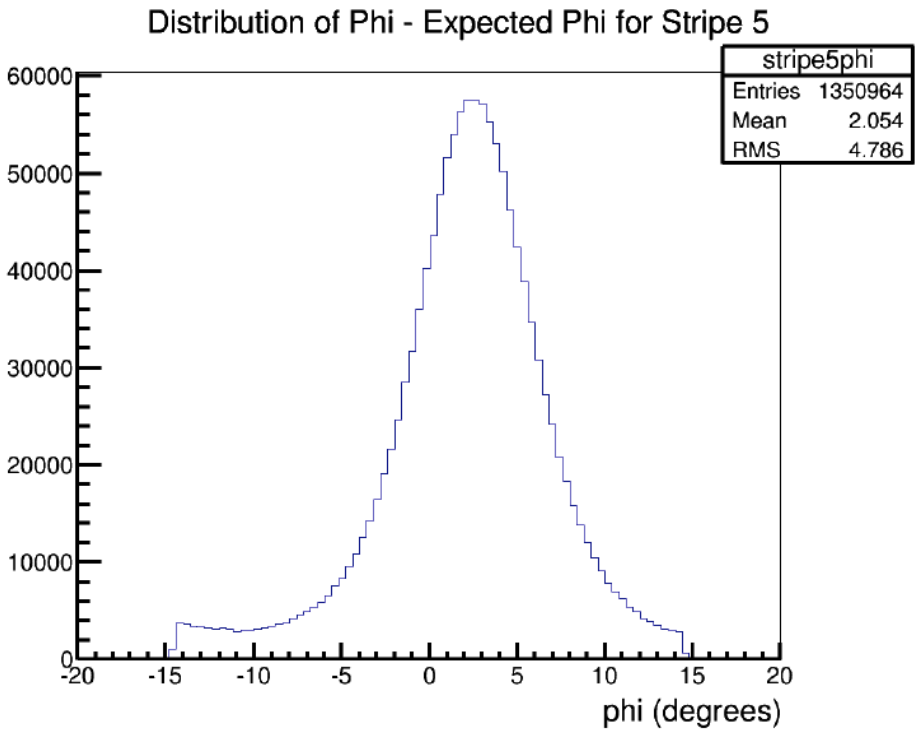

Figure 3.12: Distribution of phi

$$fit_{gauss} = [0] * exp(-(pow((x - [1]), 2))/(2 * pow([2], 2)))+ \\ [3] * exp(-(pow((x - [4]), 2))/(2 * pow([5], 2)))+ \\ [6] * exp(-(pow((x - [7]), 2))/(2 * pow([8], 2))) \quad (3.5)$$

For the ANITA-3 analysis in [2, 21], cuts were chosen on the left and right tails of the fit to the phi difference distribution of each stripe using events just before the final LD cut. These events included a preliminary low LD cut given by:

$$LD\ cut > 4.0 \quad (3.6)$$

where the LD cut is calculated as follows:

$$LD\ cut = cohSnr2 * (-6.0) + cPeak \tag{3.7}$$

where cohSnr2 is the quantity in the vertical axis and cPeak is the quantity in the horizontal axis of Figure 3.4.

The cuts were chosen with the motivation to reduce the number of events passing that sit on a satellite stripe by a factor of 100. The cuts and the corresponding estimate on how many events should pass that sit on a stripe are presented in Table 3.6.2. It was found that stripes 5 and 6 actually needed to have sub-stripes that had to be cut rather than the entire stripe. The cut on the left side of the phi difference distribution fit is denoted as the "left cut" while the cut on the right side of the phi difference distribution fit is denoted as the "right cut". The number of events passing these cuts was also calculated to make sure it was consistent with only 1% of events in the stripe. Before the satellite stripe cut was implemented, roughly 100 events were expected to pass that would sit on stripes. This cut would allow a factor of 100 fewer or 1 event to pass that would sit on a stripe.

Stripe name	Left cut	Right cut	Number of events passing
Stripe 1	-10.8	10.8	10.77 out of 988.67
Stripe 2	-6.2	11.0	18.78 out of 1701
Stripe 3	-26.3	-13.4	141.5 out of 13902
Stripe 4	26.5	39.3	135.6 out of 13754
Stripe 5a	-22.99	-16.5	0.406 out of 34.263
Stripe 5b	-6.0	12.2	1.34 out of 139.57
Stripe 6a	3.0	8.5	0.27 out of 31.197
Stripe 6b	23.2	32.8	0.93 out of 93.086

3.6.3 Equations for stripes

Combining the cuts in Table 3.6.2 with the equations of midlines in Equation 3.4, we obtained equations for lines for the lower and upper bound of each stripe. These are shown

in Equations 3.8 and 3.9.

$$\begin{cases} Stripe\ 1\ upper : longitude = phi - 171.815 \\ Stripe\ 1\ lower : longitude = phi - 193.415 \\ Stripe\ 2\ upper : longitude = phi - 89.435 \\ Stripe\ 2\ lower : longitude = phi - 106.635 \\ Stripe\ 3\ upper : longitude = phi - 33.435 \\ Stripe\ 3\ lower : longitude = phi - 46.335 \\ Stripe\ 4\ upper : longitude = phi + 72.11 \\ Stripe\ 4\ lower : longitude = phi + 59.31 \end{cases} \tag{3.8}$$

$$\begin{cases} Stripe\ 5a\ upper : longitude = phi + 58.985 \\ Stripe\ 5a\ lower : longitude = phi + 52.495 \\ Stripe\ 5b\ upper : longitude = phi + 87.685 \\ Stripe\ 5b\ lower : longitude = phi + 69.485 \\ Stripe\ 6a\ upper : longitude = phi + 109.823 \\ Stripe\ 6a\ lower : longitude = phi + 104.323 \\ Stripe\ 6b\ upper : longitude = phi + 134.123 \\ Stripe\ 6b\ lower : longitude = phi + 124.523 \end{cases} \tag{3.9}$$

We wanted to recover some events within stripes utilizing the property that satellite-contaminated events were thought to have larger peak value of cross-correlation in LCP than in RCP. Therefore, within a stripe we required the condition that the peak value of cross-correlation in RCP divided by that in LCP had to be greater than some number. These numbers were chosen by trying different cuts on the ratio of RCP/LCP that made the phi difference distributions of the stripes flatter. The final numbers are shown in Equation 3.10.

Flight	Analysis	Dataset	Analyst	Excess events	Num. on stripes	%
ANITA-2	Diffuse	90%	B. Dailey	38	16	42%
ANITA-3	Diffuse	10%	S. Stafford	9	6	67%

Table 3.1: Summary of results motivating the satellite stripe cut.

$$\begin{cases} Stripe\ 1 : \frac{Peak_{RCP}}{Peak_{LCP}} = 1.7 \\ Stripe\ 2 : \frac{Peak_{RCP}}{Peak_{LCP}} = 2.2 \\ Stripe\ 3 : \frac{Peak_{RCP}}{Peak_{LCP}} = 2.2 \\ Stripe\ 4 : \frac{Peak_{RCP}}{Peak_{LCP}} = 1.7 \\ Stripe\ 5 : \frac{Peak_{RCP}}{Peak_{LCP}} = 2.0 \\ Stripe\ 6 : \frac{Peak_{RCP}}{Peak_{LCP}} = 2.0 \end{cases} \tag{3.10}$$

3.6.4 Summary and impact

The satellite stripe cut was developed to mitigate the problem of excess events passing final cuts in previous attempts of the binned analysis to search for a diffuse flux of UHE neutrinos in data from the ANITA-2 and -3 flights. A large fraction of the excess events were on the satellite stripes as summarized in Table 3.1. This led to the hypothesis that satellites in orbit around the earth could be causing anthropogenic noise lined up with the satellites in azimuth to pass the trigger and get recorded as data by ANITA. These satellites could be causing events to pass our analysis cuts too without a satellite stripe cut in place. The excess events showing up as stripes in Figures 3.10 and 3.11 support this hypothesis and imply that most of the ANITA triggered events are actually along stripes and satellite-contaminated.

The goal of the satellite stripe cut was to remove satellite-contaminated events from the dataset. Upon implementation, the stripe cut removed 69% of events (after a few quality cuts) in the ANITA-3 data, dramatically reducing the dataset. The price paid was that

17.8% of simulated neutrinos were also lost due to this cut. Events in viewing gaps expected for satellites at 0 degrees with respected to the equator were retained. The name of the function used to do this is `canANITASeeStripe`.

The problem with satellite contamination was deemed severe enough to implement this overall harsh cut. However, in the future, the satellite stripe cut could be implemented with certain modifications such as taking into account the reconstructed azimuthal direction of events and retaining events that produced triggers on a side of the payload that is not facing the satellites.

Chapter 4

First physics results from the binned analysis

ANITA is a NASA long-duration balloon experiment for the detection of UHE ($> 10^{18}$ eV) neutrinos. The third flight of the ANITA experiment took place during Dec 19, 2014 to Jan 10, 2015. In this chapter, we present results of a search for a diffuse flux of UHE neutrinos in data collected during this flight. These results have been made public now [2], however, in this chapter, we provide details that were not covered in the publication draft.

4.1 Short summary of published results

Three independent blind searches for a diffuse flux of UHE neutrinos and one dedicated search for Extensive Air Shower (EAS) candidates were conducted. About 20 EAS candidates and one neutrino candidate were found. Their reconstructed locations overlaid on a map of the continent along with the ANITA-3 flight path are shown in Figure 4.1. The candidates are all impulsive, isolated events. The neutrino candidate is VPol and the EAS candidates are HPol. One of the EAS candidates is an unusual, upgoing event, referred to as the mystery event 2. This is further discussed in Chapter 7.

In the absence of a discovery, we present the new limit in Figure 4.2. In this plot, there is flux in the vertical axis and energy in the horizontal axis. The neutrino background estimate quoted in the paper was: $0.7^{+0.5}_{-0.3}$, therefore, the neutrino candidate was consistent with background. However, an *a posteriori* analysis found features of the neutrino candidate that will be used to improve future analyses. In Figure 4.2, constraints from other experiments

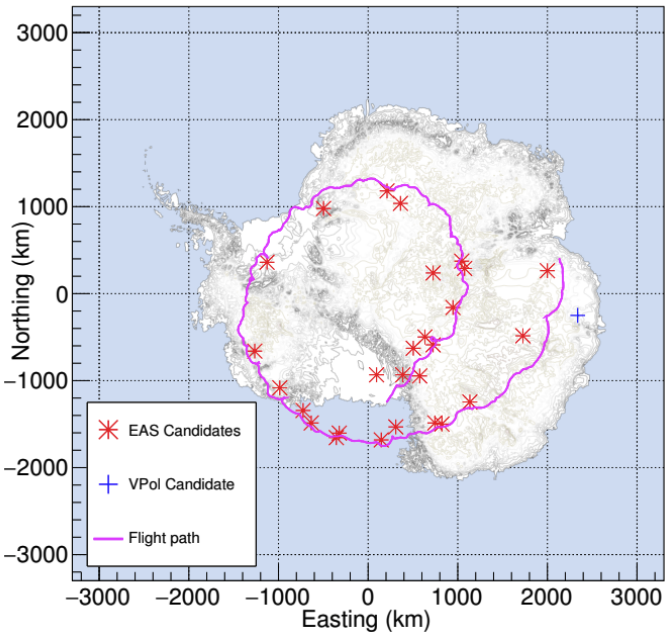

Figure 4.1: Results from the ANITA-3 flight. Red stars denote EAS candidates. The blue plus denotes the neutrino candidate. These results are summarized in [2].

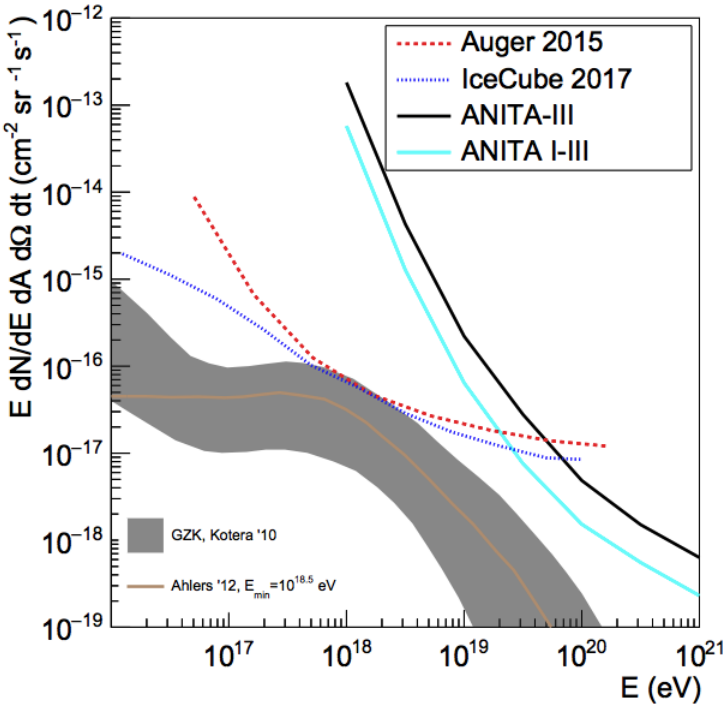

Figure 4.2: New limit from a search for UHE neutrinos in data from the third flight of ANITA.

such as Auger and IceCube are also presented. Both the ANITA-3 limit and the combined ANITA-1 through -3 limit are shown. Note that there is a part of the range of energies in the horizontal axis where ANITA is the only experiment with sensitivity.

4.2 What led to the first physics results in the binned analysis

The binned analysis to search for a diffuse flux of UHE neutrinos in the ANITA-3 data was a team effort as evident from other theses [18, 21]. Developments to find results from the 10% data were presented in [18]. Systematic uncertainties were added to the analysis in [21]. The problem of excess background that was seen in previous attempts of the binned analysis as in [20] for ANITA-2 and [18] for ANITA-3 was also largely corrected by incorporating conservative cuts such as the satellite stripe cut which is described in Chapter 3. A critical problem remained, which was the loss of sensitivity.

4.2.1 Improving sensitivity in the binned analysis

Increasing the sensitivity of the binned analysis played a critical role in publishing the first physics results from this analysis. Here, sensitivity means keeping ice where we are sensitive to neutrinos. Before I started working on improving the sensitivity of the analysis, the sensitivity in the HPol channel of the analysis was 27% and the sensitivity in the VPol channel of the analysis was 44%. This was partly due to removing many bins from the analysis. Twelve bins were being kept in the HPol channel and 22 bins were being kept in the VPol channel of the analysis. It was important to improve these numbers.

Updating the exponential fit requirements

Improving the logic for deciding which bins fulfill the requirements needed before of having their data be fit to an exponential helped to increase the sensitivity of the binned analysis. As has been explained before, at a later stage of the binned analysis, the y-intercept of the LD cut of data in each bin is fit to an exponential as part of the optimization process of the LD cut and only bins that satisfy certain rules can be fit to an exponential.

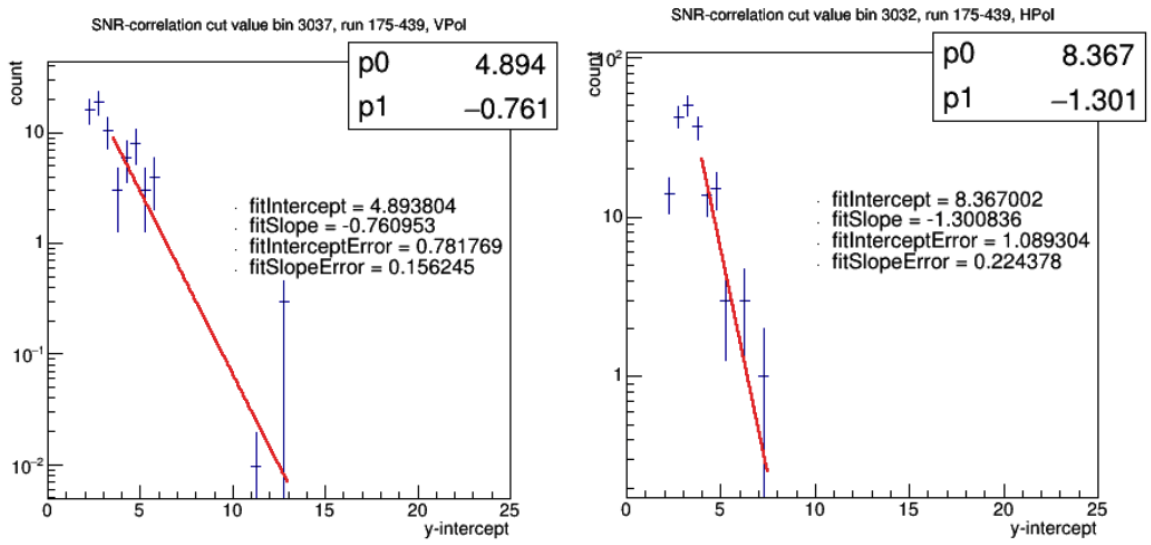

Figure 4.3: Exponential fit for LD cut was updated. Now, the fit has to have at least 5 histogram bins with data and with at least 5 total events.

I updated the rules to allow a Healpix bin to be kept if the exponential fit to its data has at least five histogram bins and if the distribution has at least five total events. Previously, bins where consecutive histogram bins in the fit did not have data were rejected. Also, bins where the values of the histogram bin content were not in descending order were rejected. Figure 4.3 shows two such bins that would have failed the previous rules, but that are now acceptable and thus, would be kept in the analysis.

Keeping high background bins

Keeping bins that were being rejected previously for having higher background also helped to improve the sensitivity of the binned analysis. Bins with background greater than 1 were not being kept in the analysis before. I forced the background of these bins down to 0.1 by increasing the LD cut in these bins by hand instead of using their optimized LD cut. Figure 4.4 shows one such bin that would have been rejected before due to higher background, but was kept in the analysis now.

This allowed for a very strong signal, if present in such a bin, to be found by the binned analysis as it would have to pass the stricter LD cut. In many cases, however, the LD cut

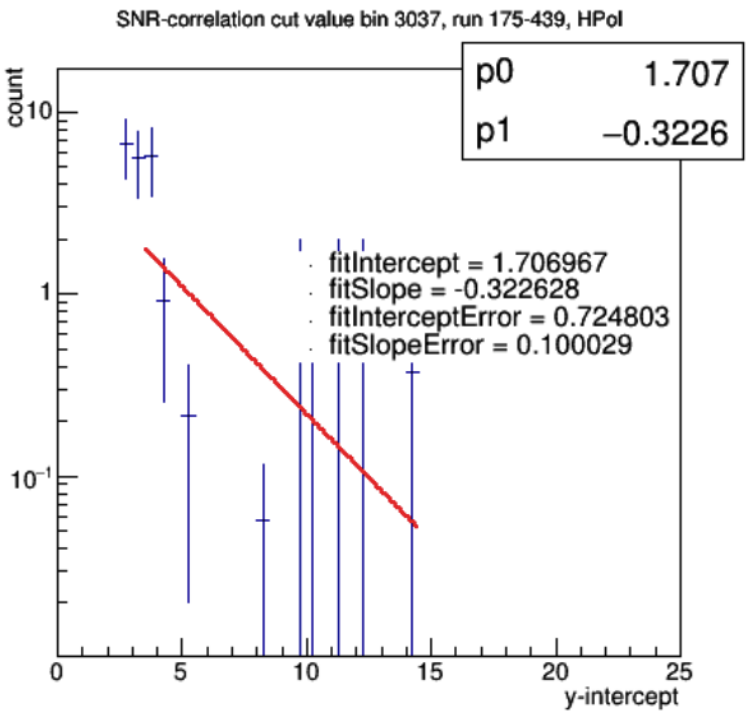

Figure 4.4: Bins with high background (> 1) now get optimized cut tuned to allow expected background of 0.1.

had to be made only a little bit stricter, for example, from 10 to 11, as the background in that bin was just over 1. Keeping such bins only made sense and helped the analysis overall.

Summary

To summarize, I updated the requirements for which bins satisfied the rules for getting fitted to an exponential, and started to keep bins with higher background by forcing their LD cuts to be stricter. These helped to increase the number of bins in the analysis. Now I could keep 29 bins in the HPol channel and 37 bins in the VPol channel. Consequently, this improved the sensitivity of the analysis and now the numbers were 75% in the HPol channel and 63% in the VPol channel. These are summarized in Table 4.1.

	Bins kept in H	Bins kept in V	Sensitivity in H	Sensitivity in V
Before	12	22	27%	44%
After	29	37	75%	63%

Table 4.1: Before and after summary showing improvement of the binned analysis.

4.3 Background estimate

The background was estimated for each bin in the VPol box using a simple extrapolation of the exponential fit for that bin. As described in Chapter 3, the distribution of y-intercepts associated with events in each bin was fit to an exponential distribution. An estimate of the background was calculated for each bin following the relation in Equation 4.3.

$$Background = \frac{-0.9}{sampleFrac * fitSlope * w} \exp(fitSlope * optCutVal + fitIntercept)$$

The number of background events expected to pass final cuts in each bin used in the VPol analysis is shown in Figure 4.5. This plot shows the estimated background in each bin with a solid black bar. The number of simulated neutrinos passing final cuts in the same bins is shown with shaded orange bars. The number of simulated neutrinos passing in a bin is a measure of the sensitivity of that bin to neutrinos. Here, the number of simulated neutrinos is in arbitrary units.

It can be seen from Figure 4.5 that a variety of bins were kept in the ANITA-3 binned analysis. Some bins had a larger number of expected background events than others. Some bins had greater sensitivity to neutrinos than others. This is the key difference between the binned analysis and other complementary analyses: parts of the continent with more noise can be retained in the binned analysis using a stricter LD cut than parts of the continent with less noise, with the goal of keeping as much of the continent as possible where we are sensitive to neutrinos.

The LD cut used in each bin kept in the VPol analysis is shown in Figure 4.6 as a function of the number of events in that bin before final cuts. Final cuts include the LD

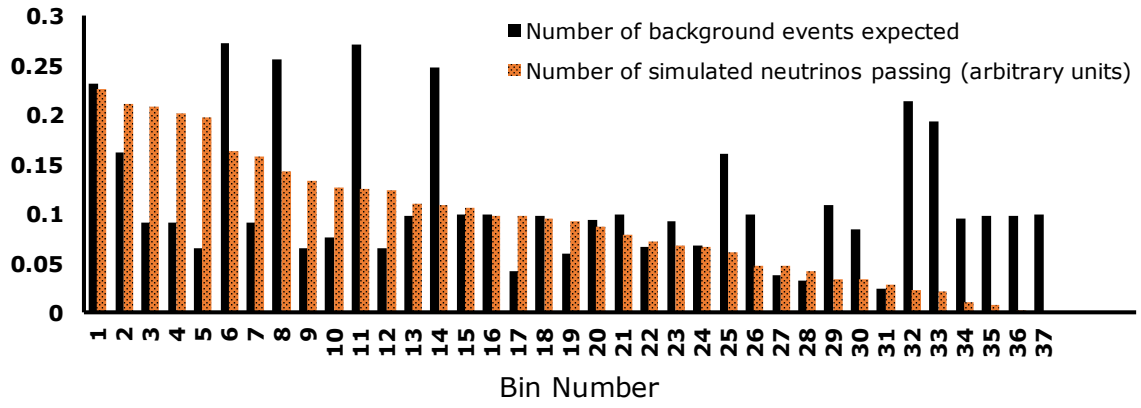

Figure 4.5: Distribution of background estimates (solid black bars) and number of simulated neutrinos passing (shaded orange bars) final cuts in each bin used in the VPol box.

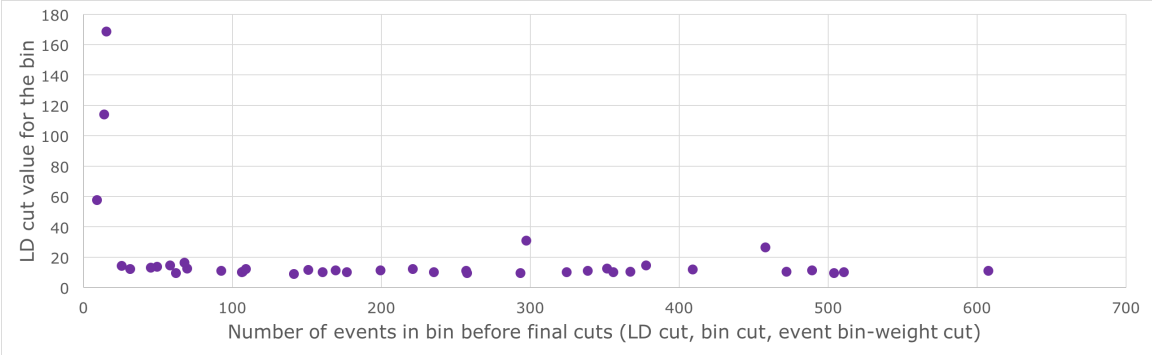

Figure 4.6: Distribution of LD cuts as a function of number of events in the bin before final cuts.

cut, bin cut, and event bin-weight cut. It can be seen that the distribution of LD cuts is mostly flat with a few being larger than others.

4.4 Box opening results in the binned analysis

The binned analysis was one of the three independent blind analyses performed on the ANITA-3 data to search for a diffuse flux of UHE neutrinos [2]. Analysis cuts were determined using only 10% of the data. To find candidates, the data was unblinded in this analysis in three stages: HPol box opening, VPol sideband box opening, and VPol box opening.

The HPol box consists of events in the 90% data that are horizontally polarized. In general, neutrinos are not expected in the HPol box. EAS candidates, however, are. The binned analysis did not optimize its search to find EAS candidates. We used 29 bins in the HPol box.

The sideband channel consists of events in the 90% data that reconstruct to bins that account for less than 1% of the cumulative sensitivity and are usually ones lacking ice depth. There was no HPol sideband channel is this search, that is, no events in the 90% HPol channel that reconstructed to zero sensitivity bins. There were four bins in the sideband VPol channel.

The VPol box consists of events in the 90% data that are vertically polarized. This is the most important box in this search. The VPol box is where neutrinos would be expected. We used 37 bins in the VPol box.

Before opening the HPol and VPol boxes, we decided to remove certain types of events if they were found: payload blasts or events that obviously require a quality cut, and clustering events. It is challenging to design cuts that remove all payload blasts. These types of events were known to pass quality and analysis cuts before. So, we decided that if we found such events in the boxes, we would remove them by hand. This simply means that we would look at the waveforms of the events and if they had the distinct features of payload blasts or other low-quality events, they would be removed. We also reserved the right to remove any groups of events in the boxes that appeared to be part of a cluster. A cluster is a group of events that are near each other (within 40 km). Such events are typically associated with anthropogenic noise and deemed worthy of removal.

4.4.1 Cosmic ray candidates and cRay scores

Although primarily commissioned as a neutrino detector, ANITA is sensitive to radio signatures of ultra-high-energy cosmic rays (UHECRs) and have made observations of cosmic ray (CR) events in the HPol channel of all analyses. Indeed the HPol channel of the signal box is mainly expected to yield CR candidates, not neutrinos. The exception to this general expectation comes in the form of the mystery events that are discussed in Chapter 7.

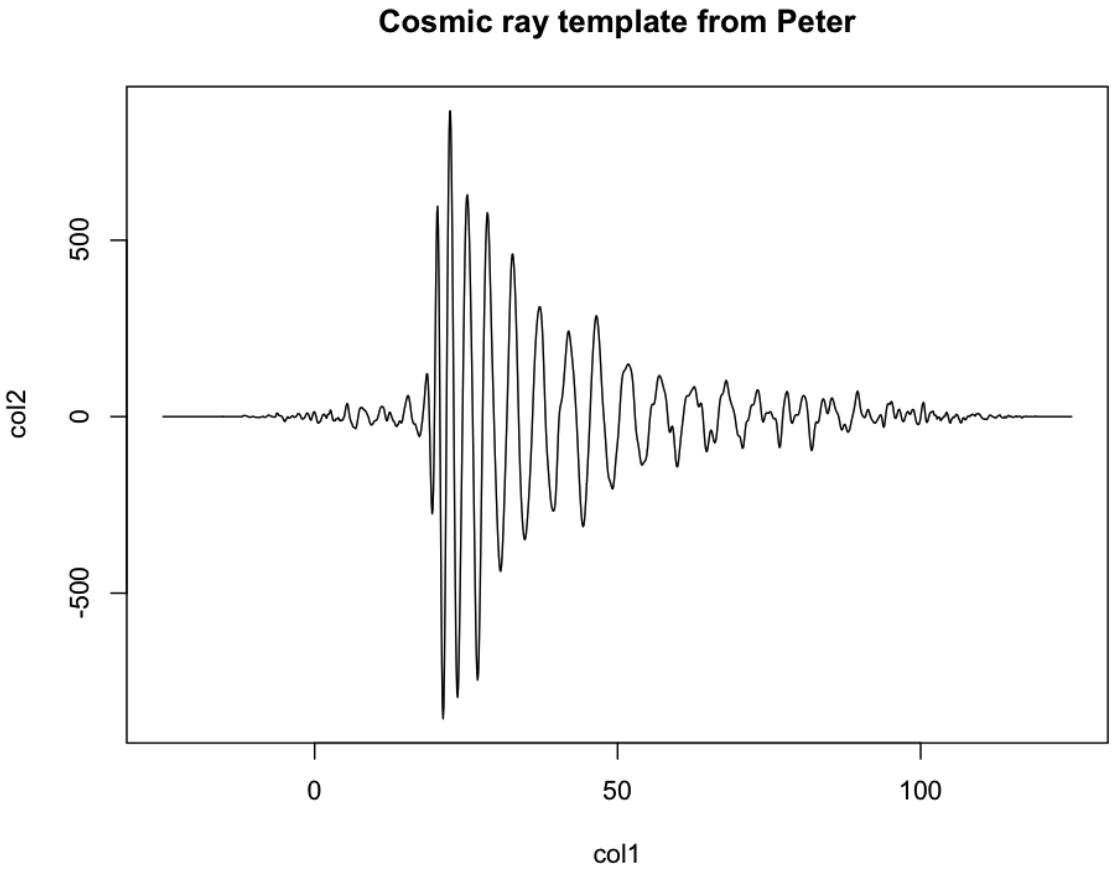

Figure 4.7: Cosmic ray template used in [4]. P. Gorham provided the numbers to make this figure.

The binned analysis to search for a diffuse flux of UHE neutrinos in the ANITA-3 data was focused on finding the best limit on a diffuse neutrino flux, and not on finding CR candidates. The HPol channel of the binned analysis was treated the same as the VPol channel in spite of the difference in the type of candidate expected in each.

A complementary analysis described in [4] was dedicated to a search for CR candidates. In this analysis, a template matching technique was implemented to search for CR candidates. The CR template utilized in the analysis is shown in Figure 4.7. According to this analysis, this is what a CR candidate should look like. By comparing processed waveforms of events recorded in the flight to this template, an evaluation was made on how CR-like they were. This evaluation was presented as a number, known as the cRay score, for each event. Events with cRay scores above 0.55 were chosen as CR candidates. Note that to be a CR candidate the event also had to pass all other cuts in the analysis, most importantly, the clustering cut.

In the binned analysis, events passing final cuts in the HPol channel were put through the procedure of comparison with the CR template and a cRay score was determined for each one. These results are summarized in Table 4.2 and discussed in Section 4.4.2.

4.4.2 HPol box opening results

On opening the HPol box consisting of 29 bins, three types of events were found: isolated events, events that required a clustering cut, and payload blast events. There were seven isolated events, seven payload blast events, and 27 clustering events. These events came from both bins where the LD cut was optimized, referred to as "normal bins" and bins where the LD cut, after optimization, was increased due to high background (> 1) in the bin to reduce the latter to 0.1, referred to as "high background bins".

Of the seven isolated HPol candidates, three were accepted by the collaboration as CR candidates. Two of these were also found in complementary analyses, with one coming from a normal bin and the other from a high background bin in this analysis.

Two new CR candidates were found in the binned analysis. Both events 48837708 and 56038445 were rejected by other searches due to their clustering cut, with 48837708 being

Event	Pol	Run	Bin	Weight	Lat	Lon	cRay[4]	Notes
48837708	H	311	3057	1.0	-79.1	-72.3	0.8	New CR candidate
56038445	H	334	3042	0.6	-79.9	-123.1	0.7	New CR candidate
58592863	H	343	3025	1.0	-76.9	-118.5	0.8	CR candidate
33484995	H	250	3048	1.0	-80.3	19.4	0.7	CR candidate
59130831	H	346	3042	1.0	-77.2	-128.5	0.4	cRay score < 0.6
15478875	H	175	3052	1.0	-82.7	124.1	0.5	cRay score < 0.6
30306654	H	241	3033	1.0	-77.7	26.2	0.3	cRay score < 0.6

Table 4.2: Isolated events found from opening the HPol box. The top event is not found in other analyses and is found in the binned analysis in a bin that was kept after increasing the LD cut. This event was published as a CR candidate. The events in blue font are CR candidates in other analyses as well. The fourth CR candidate was not deemed CR enough by other analysts and did not make the CR list in the publication. Three of the isolated events had CRay scores below 0.6, the chosen cutoff.

closer to the chosen clustering threshold than 56038445. This led to 48837708 being deemed acceptable as a CR candidate by the collaboration while 56038445 was not. Event 48837708 was listed as a CR in the publication [2], while 56038445 was not. Note, however, that both have cRay scores above 0.55.

Both events 48837708 and 56038445 were found in high background bins in the binned analysis. This confirms that it was a good idea to keep the high background bins in the binned analysis. We summarize results from the HPol box opening, starting with the isolated events in Table 4.2.

Events that needed a clustering or quality (blast) cut were found in both the normal and the high background bins. Events that needed a clustering or quality (blast) cut after opening the HPol box of normal bins are presented in Table 4.3. It can be seen that five blasts and 11 clustering events were found in the normal bins. All of the clustering events in this group were part of a tight cluster and reconstructed to a single bin, Bin 3046. Events that needed a clustering or quality (blast) cut after opening the HPol box of high background bins are presented in Table 4.4. Two blasts and 16 clustering events were found in the high background bins. Six of the clustering events reconstructed to Bin 3057 and three to Bin 3024. Doublets were found in Bins 3018 and 2997. The clustering event from Bin 3019 clustered with the event 77973578 that passed in the 10% dataset.

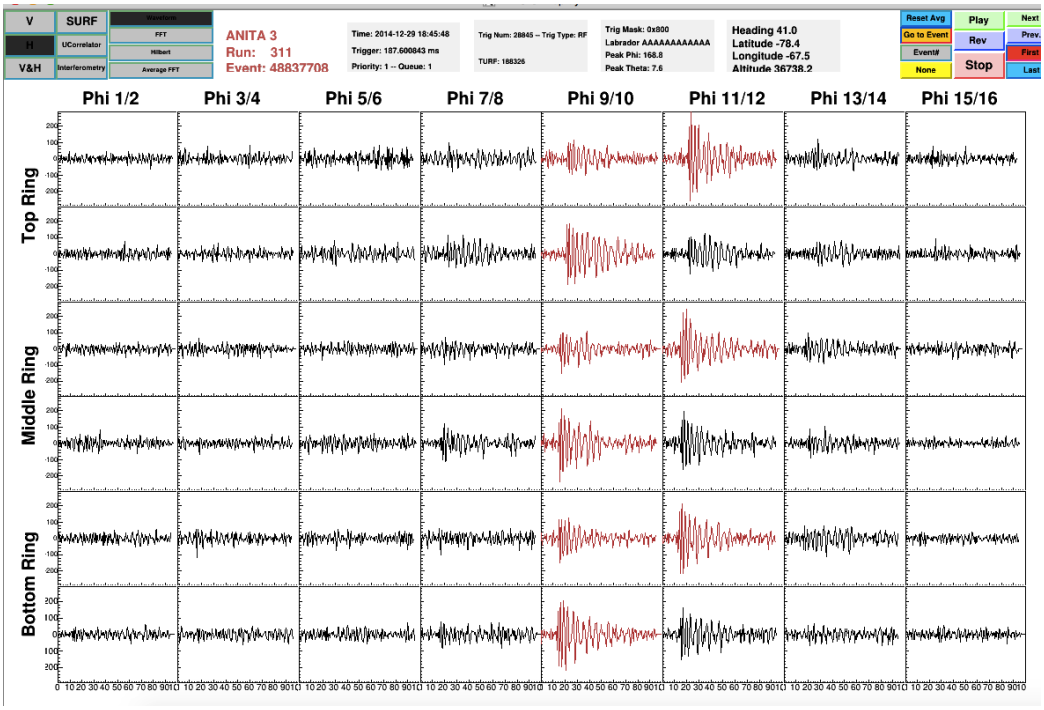

Figure 4.8: The new cosmic ray candidate that I found that was published as such [2].

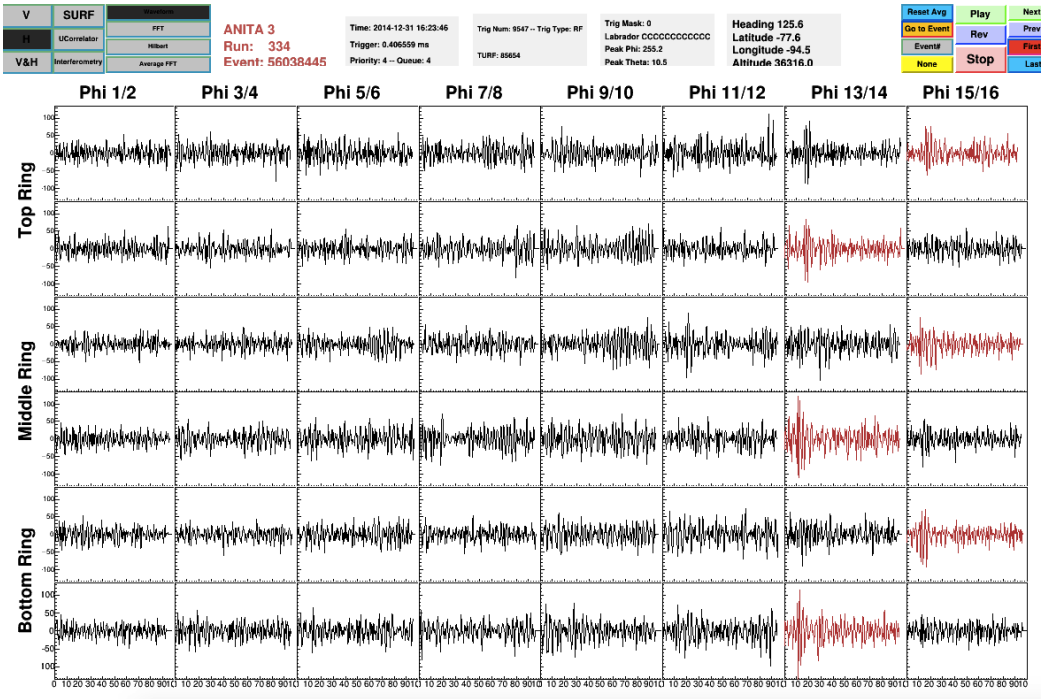

Figure 4.9: Cosmic ray candidate that I found that did not make the list of CR candidates in publication [2].

Event	Pol	Run	Bin	Weight	Lat	Lon	Notes
15406158	H	175	3052	1.0	-83.0	126.4	Blast
20646656	H	202	3035	1.0	-80.4	83.4	Blast
23937896	H	216	3050	1.0	-80.5	59.7	Blast
28876488	H	236	3049	1.0	-79.2	37.6	Blast
82011215	H	429	2994	1.0	-71.5	97.8	Blast
40579667	H	280	3046	1.0	-77.8	-34.3	Clusters
40993619	H	281	3046	1.0	-77.8	-34.3	Clusters
41049372	H	281	3046	1.0	-77.9	-34.3	Clusters
41064920	H	281	3046	1.0	-77.9	-34.2	Clusters
41073934	H	281	3046	1.0	-77.8	-34.4	Clusters
41103084	H	281	3046	1.0	-77.8	-34.3	Clusters
44543143	H	296	3046	1.0	-77.8	-34.3	Clusters
44600768	H	296	3046	1.0	-77.8	-34.4	Clusters
44677846	H	296	3046	1.0	-77.9	-34.6	Clusters
44678128	H	296	3046	1.0	-77.9	-34.6	Clusters
44678408	H	296	3046	1.0	-77.8	-34.5	Clusters

Table 4.3: Events that needed a clustering or quality (blast) cut in the bins kept in the HPol box that used a normal LD cut.

We present a table of EAS candidates found by complementary analyses and note the reason why we cut an event if it was removed in the binned analysis in Table 4.5. Of the 23 total EAS candidates found in other analyses, two events were also found by the binned analysis. Five events were cut by the satellite stripe cut and three by the elevation angle cut. Five were removed due to the LD cut and six due to the bin cut. One was removed due to the reconstruction to continent cut and lastly, one by the triggering phi-sector direction cut. The LD cut and bin cut are unique to the methods of the binned analysis, therefore, it is not too surprising that EAS candidates were found by other analyses that were removed in the binned analysis due to these cuts. A brief discussion on the cuts that removed the other EAS candidates is presented in Section 4.4.5.

4.4.3 VPol sideband results

The VPol sideband consisted of four bins: Bins 2975, 2978, 2900, and 3001. Nothing was found to pass in Bin 2900. One event, a payload blast event (64175392), was found in Bin 3001. Bins 2975 and 2978 had events that needed a clustering cut and are summarized in

Event	Pol	Run	Bin	Weight	Lat	Lon	Notes
74047179	H	399	2998	1.0	-74.2	153.8	Blast
80333037	H	422	2995	1.0	-71.8	107.9	Blast
19567583	H	196	3018	1.0	-77.5	110.0	Clusters
19567584	H	196	3018	1.0	-77.7	109.4	Clusters
78361533	H	415	3019	1.0	-75.8	125.2	Clusters w/ 10%
76096974	H	407	2997	1.0	-73.5	136.2	Clusters
77072568	H	410	2997	1.0	-73.8	136.3	Clusters
63842646	H	362	3024	1.0	-76.3	-144.4	Clusters
64166505	H	364	3024	1.0	-76.3	-144.4	Clusters
64216077	H	364	3024	1.0	-76.3	-144.4	Clusters
77136488	H	410	3037	1.0	-75.7	122.0	Clusters
77320292	H	411	3037	0.6	-75.6	122.7	Clusters
55584513	H	332	3057	0.7	-79.9	-82.2	Clusters
55616654	H	332	3057	0.5	-79.9	-81.9	Clusters
55827553	H	333	3057	0.8	-79.9	-81.6	Clusters
56128670	H	334	3057	0.9	-79.9	-81.4	Clusters
56141471	H	334	3057	0.5	-79.9	-81.7	Clusters
56142587	H	334	3057	0.6	-79.8	-81.8	Clusters

Table 4.4: Events that needed a clustering or quality (blast) cut in the bins kept in the HPol box where the LD cut had to be increased manually to reduce the background to 0.1.

Table 4.6.

4.4.4 VPol box opening results

On opening the VPol box consisting of 37 bins, three types of events were found: isolated events, events that required a clustering cut, and events that required a quality cut. Twenty-eight total events were found to require a quality cut, of which there were 26 blasts, one reverse blast, and one digitizer glitch. These are presented in Table 4.7. Two isolated events were found along with six clusters of events. There were 65 total events in the clusters, with two clusters of doublets (Cluster A and B), one cluster of a quadruplet (Cluster E), one cluster of six events (Cluster F), one cluster of 10 events (Cluster C), and one cluster of 41 events. Out of 37 bins kept in the analysis, seven had clusters in them, with the largest cluster having events in neighboring bins. Information on the two singlets and events from Clusters A, B, C, E, and F are summarized in Table 4.8. Events from Cluster D, the largest cluster, are presented in Table 4.9. Cluster D spanned two neighboring bins, Bin 3016 and

Run number	Event number	Notes
343	58592863	Passed in our analysis
250	33484995	Passed in our analysis
215	23695286	Satellite stripe cut
248	32907848	Satellite stripe cut
282	41475569	Satellite stripe cut
389	71766273	Satellite stripe cut
401	74592579	Satellite stripe cut
176	15717147	Elevation angle cut
371	66313844	Elevation angle cut
377	68298837	Elevation angle cut
210	22345215	Triggering phi-sector direction cut
230	27142546	Reconstruct to continent cut
185	16952229	LD cut
195	19459851	LD cut
424	80840274	LD cut
357	62273732	LD cut
404	75277769	LD cut
367	65187079	Bin cut
388	71171108	Bin cut
284	41529195	Bin cut
435	83877990	Bin cut
383	70013898	Bin cut
397	73726742	Bin cut

Table 4.5: EAS candidates that passed in complementary, independent analyses and notes mentioning whether they were found in the ANITA-3 binned analysis and the cut that removed them if they were not.

Event	Pol	Run	Bin	Weight	Lat	Lon	Notes
59664991	V	348	2978	1.0	-77.0	-120.3	Clusters
59827186	V	348	2978	0.9	-76.1	-124.4	Clusters
63140350	V	360	2978	0.6	-76.8	-122.1	Clusters
66702609	V	372	2975	1.0	-74.2	-163.6	Clusters
66703250	V	372	2975	1.0	-74.2	-163.5	Clusters
66993765	V	372	2975	0.5	-73.9	-165.7	Clusters
66998800	V	372	2975	1.0	-73.9	-165.7	Clusters

Table 4.6: Events that needed a clustering cut in the bins kept in the VPol sideband.

Event	Pol	Run	Bin	Weight	Notes
23403916	V	214	3014	0.8	Blast
26057131	V	226	3013	0.9	Blast
28375047	V	234	3013	0.5	Blast
15530637	V	175	3037	1.0	Blast
15674317	V	176	3037	1.0	Blast
17560872	V	186	3037	0.9	Blast
28630479	V	235	3015	0.9	Blast
19827626	V	199	3016	1.0	Blast
20816129	V	202	3016	1.0	Blast
21316845	V	205	3016	1.0	Blast
23424326	V	214	3016	1.0	Blast
27111458	V	230	3016	1.0	Blast
81047217	V	425	2936	1.0	Blast
80064184	V	421	2937	1.0	Blast
29186465	V	237	2990	1.0	Blast
43985101	V	294	3029	1.0	Blast
47073555	V	304	3029	1.0	Blast
34747246	V	253	3011	1.0	Blast
41311124	V	282	3010	1.0	Blast
77170232	V	410	2939	1.0	Blast
35083936	V	254	3012	1.0	Blast
16349293	V	178	3019	1.0	Blast
73435197	V	396	2998	1.0	Blast
23644493	V	215	3015	1.0	Blast (unusual)
36330022	V	264	2988	1.0	Blast (unusual)
32335164	V	246	2988	1.0	Blast (Weaker)
30088525	V	239	3013	1.0	Reverse blast
44980727	V	297	3029	1.0	Digitizer glitch

Table 4.7: Events that needed a quality cut in the VPol box opening. These events should ideally not survive at this late stage in the analysis.

3017.

4.4.5 Cuts and how they affected results

In the binned analysis, for certain classes of data, we decided to be conservative and strict about removing events as compared to the complementary analyses in [2]. As evident from Table 4.5, this had direct consequences such as the removal of five EAS candidates found in complementary analyses due to the satellite stripe cut.

Cluster	Event	Pol	Run	Bin	Weight	Latitude	Longitude
Singlet 1	73750661	V	397	2998	0.9	-77.3	163.4
Singlet 2	21702154	V	207	3037	1.0	-82.7	118.4
Cluster A	21781993	V	207	3018	0.5	-82.7	115.2
Cluster A	21947412	V	208	3018	0.6	-82.5	116.1
Cluster B	56459663	V	336	3004	0.8	-79.3	-111.9
Cluster B	56969580	V	338	3004	0.7	-79.4	-112.1
Cluster C	58062347	V	342	2979	1.0	-74.8	-103.8
Cluster C	58062403	V	342	2979	1.0	-74.9	-103.8
Cluster C	58071804	V	342	2979	1.0	-74.9	-104.0
Cluster C	58131099	V	342	2979	1.0	-74.9	-103.8
Cluster C	58144350	V	342	2979	1.0	-74.9	-103.9
Cluster C	58153597	V	342	2979	1.0	-75.0	-104.1
Cluster C	58159803	V	342	2979	0.5	-74.9	-103.7
Cluster C	58177755	V	342	2979	0.7	-75.0	-103.8
Cluster C	58179281	V	342	2979	0.5	-75.1	-103.8
Cluster C	58181857	V	342	2979	1.0	-75.0	-103.9
Cluster E	47632317	V	307	3029	1.0	-80.2	-53.3
Cluster E	47951770	V	308	3029	0.5	-80.4	-54.4
Cluster E	48140904	V	309	3029	0.9	-80.4	-54.1
Cluster E	48494265	V	310	3029	0.9	-80.4	-53.7
Cluster F	59004777	V	345	3003	1.0	-77.2	-128.9
Cluster F	59130831	V	346	3003	1.0	-77.2	-127.6
Cluster F	59134776	V	346	3003	1.0	-77.2	-127.8
Cluster F	59137346	V	346	3003	1.0	-77.2	-128.8
Cluster F	59368912	V	347	3003	1.0	-77.2	-127.2
Cluster F	59983596	V	348	3003	1.0	-77.2	-126.5

Table 4.8: Two singlets and clustering events from Clusters A, B, C, E, and F from the VPol box opening. The events from Cluster A cluster with each other, the ones from Cluster B with each other, and so on.

Cluster	Event	Pol	Run	Bin	Weight	Latitude	Longitude
Cluster D	18179581	V	188	3016	0.9	-82.3	87.9
Cluster D	18240623	V	189	3016	0.8	-82.6	88.5
Cluster D	18331098	V	189	3016	0.9	-82.5	88.3
Cluster D	18396031	V	189	3016	0.9	-82.6	87.7
Cluster D	15594676	V	175	3017	0.5	-82.1	98.2
Cluster D	18087496	V	188	3017	0.9	-82.5	91.1
Cluster D	18133151	V	188	3017	1.0	-82.1	92.2
Cluster D	18209356	V	189	3017	1.0	-82.2	92.9
Cluster D	18296165	V	189	3017	0.5	-82.5	89.7
Cluster D	18341673	V	189	3017	0.9	-82.4	90.7
Cluster D	18353641	V	189	3017	1.0	-82.3	92.8
Cluster D	18365043	V	189	3017	1.0	-82.3	92.1
Cluster D	18372783	V	189	3017	1.0	-82.2	93.8
Cluster D	18382466	V	189	3017	1.0	-82.4	92.4
Cluster D	18419733	V	190	3017	1.0	-82.3	91.5
Cluster D	18433631	V	190	3017	1.0	-82.3	93.8
Cluster D	18443929	V	190	3017	1.0	-82.2	94.4
Cluster D	18450544	V	190	3017	1.0	-82.4	92.7
Cluster D	18508748	V	191	3017	1.0	-82.6	91.4
Cluster D	18532272	V	191	3017	1.0	-82.3	93.3
Cluster D	18541894	V	191	3017	1.0	-82.4	92.8
Cluster D	18552841	V	191	3017	1.0	-82.5	92.8
Cluster D	18568335	V	191	3017	1.0	-82.4	92.4
Cluster D	18576702	V	191	3017	1.0	-82.4	93.1
Cluster D	18586686	V	191	3017	1.0	-82.3	93.3
Cluster D	18595690	V	191	3017	1.0	-82.4	92.8
Cluster D	18608870	V	191	3017	1.0	-82.6	91.4
Cluster D	18621534	V	191	3017	1.0	-82.6	91.2
Cluster D	18635697	V	191	3017	1.0	-82.1	95.3
Cluster D	18651969	V	191	3017	1.0	-82.5	92.8
Cluster D	18666728	V	191	3017	1.0	-82.1	96.3
Cluster D	18691047	V	192	3017	1.0	-82.6	91.6
Cluster D	18698189	V	192	3017	1.0	-82.6	91.9
Cluster D	18705214	V	192	3017	1.0	-82.4	93.4
Cluster D	18713826	V	192	3017	1.0	-82.5	93.5
Cluster D	18735313	V	192	3017	1.0	-82.7	91.4
Cluster D	18744776	V	192	3017	1.0	-82.1	95.7
Cluster D	18759001	V	192	3017	1.0	-82.4	93.7
Cluster D	18780262	V	192	3017	1.0	-82.4	93.8
Cluster D	18798470	V	192	3017	1.0	-82.1	96.3
Cluster D	18835347	V	192	3017	1.0	-82.3	95.0

Table 4.9: Clustering events in Cluster D from the VPol box opening. This cluster spanned two bins, Bin 3016 and 3017.

However, the development of the satellite stripe cut in the binned analysis was well-motivated. The satellite stripe cut was developed to avoid problems discovered in previous attempts of the binned analysis where excess events were found to be lying on stripes. Although the satellite stripe cut was not implemented in the complementary analyses, in the binned analysis, we chose to regard events that sat on stripes conservatively, and aggressively cut them.

The elevation angle cut, triggering phi-sector direction cut, and reconstruct to continent cut are all reasonable cuts to implement and have been used in analyses of previous flights. However, the complementary ANITA-3 analyses chose not to implement these, while in the binned analysis, again, we chose to be more strict about removing these kinds of noise events, and implemented these cuts.

One might, of course, wonder why, in the binned analysis, events were found requiring last minute quality cuts in spite of being more conservative about removing noise events. Although the binned analysis was meant to have more conservative cuts, we realized at a late stage of the analysis, that the cuts designed to remove payload blasts were not strict enough. Requiring at least six phi sectors to trigger in order to deem an event as a blast is too strong a requirement. There are many blasts that trigger fewer phi sectors. Requiring the ratio of top over bottom ring peak voltages to be greater than 0.5 is not particularly sophisticated either. Moreover, this does not remove reverse blast events where the top ring peak voltage is greater than the bottom ring.

The complementary ANITA-3 analyses were relatively successful in removing payload blast events, however, their recipe for cutting these noise events were not made public in time to adapt them into the binned analysis. In the future, cuts to remove payload blast events should be updated, potentially following what was done in the other analyses. There are ongoing, alternative efforts to remove payload blast events as well which we discuss in Section 4.7.

Besides excess blast events, events that needed a last minute clustering cut were also found in the ANITA-3 binned analysis, despite efforts to aggressively remove noise events. Although ideally no events would need a clustering cut in the binned analysis, the situation

with clustering did improve compared to the ANITA-2 binned analysis. Excess events in ANITA-2 were not as tightly clustered and were sometimes a few degrees apart in longitude and latitude. The excess events in the ANITA-3 binned analysis were all tightly clustered to within a fraction of a degree. The clustering algorithm used and loss in efficiency due to clustering are discussed in Section 4.5. We also note that the clustering events could be utilized as an opportunity to study and classify background data to improve analysis cuts in the future.

4.4.6 Summary of box opening results

The 90% data in the HPol and VPol channels of the ANITA-3 binned analysis was unblinded after applying quality, analysis and final cuts. Before unblinding, we decided to remove certain types of events if they were found. These would be events that obviously required a quality cut such as payload blast events and events that clustered. Such excess events were found upon opening both the HPol and VPol boxes. In the HPol box, seven payload blast and 27 clustering events were removed. In the VPol box, 26 payload blast, one reverse blast, one digitizer glitch, and 65 clustering events were removed.

Isolated events were found in both the HPol and VPol boxes. Seven isolated events were found in HPol. Of these, three were made public as EAS candidates. One of these three was a new EAS candidate found only in this analysis. The remaining four isolated events in HPol were thought to be background events based on an investigation of their features after the unblinding. Two isolated events were found in VPol. These two events reconstructed to bins 2998 and 3037 and were consistent with the estimated background in those bins. No excess over background was found and a limit was placed on the Kotera maximum model [23] as shown in Figure 4.2.

4.5 Clustering as a last step

Events requiring a clustering cut as a last step were found in the HPol and VPol boxes of the ANITA-3 binned analysis. In contrast to the complementary analyses, a clustering

cut is not central to the methods of the binned analysis. However, it was decided prior to unblinding that a clustering cut would be implemented if groups of events were found in the HPol and VPol boxes that appeared to be close to each other.

This kind of last minute clustering, although ideally would not be necessary, is quite different from using clustering as a primary method to cut data in the search for neutrinos. In complementary analyses, clustering removes thousands of events. In this analysis, clustering was utilized to remove 27 events in HPol and 65 events in VPol.

To determine which events clustered and which were isolated, all 101 events were used, combining excess events in both the HPol and VPol channels, and counting isolated events. In other words, the clustering cut both removed events that clustered and identified events that were isolated. This was done following the clustering algorithm used in [3].

Figure 4.10 shows the cluster multiplicity as a function of cluster size for the clusters found in the HPol and VPol boxes. The cluster multiplicity is the total number of clusters found of a given type of cluster. The cluster size is the number of events in a given cluster. A linear fit to the distribution in Figure 4.10 was used to estimate the singlet background from the clustering cut used on excess events. This background was estimated to be 2.2 events.

4.5.1 Important validation

Figure 4.11 shows the cluster size as a function of event population before final cuts in the bins kept in the VPol analysis. Each cluster size is denoted by a unique color, for example, the singlets are shown in red, doublets in blue, and so on. This shows that the need for a last step clustering cut is not affected by the number of events in a bin before final cuts. In other words, it is not necessarily the case that clustering was needed in bins with more noise. This validates our decision to keep these bins and shows that we can successfully keep bins with more noise as well as bins with less noise. Although we strive towards not needing clustering at all, this is an important validation of the binned analysis.

Finally, although it may be tempting to regard the need for clustering as a last step in the binned analysis as a significant failure of the analysis, the cost of clustering is negligible

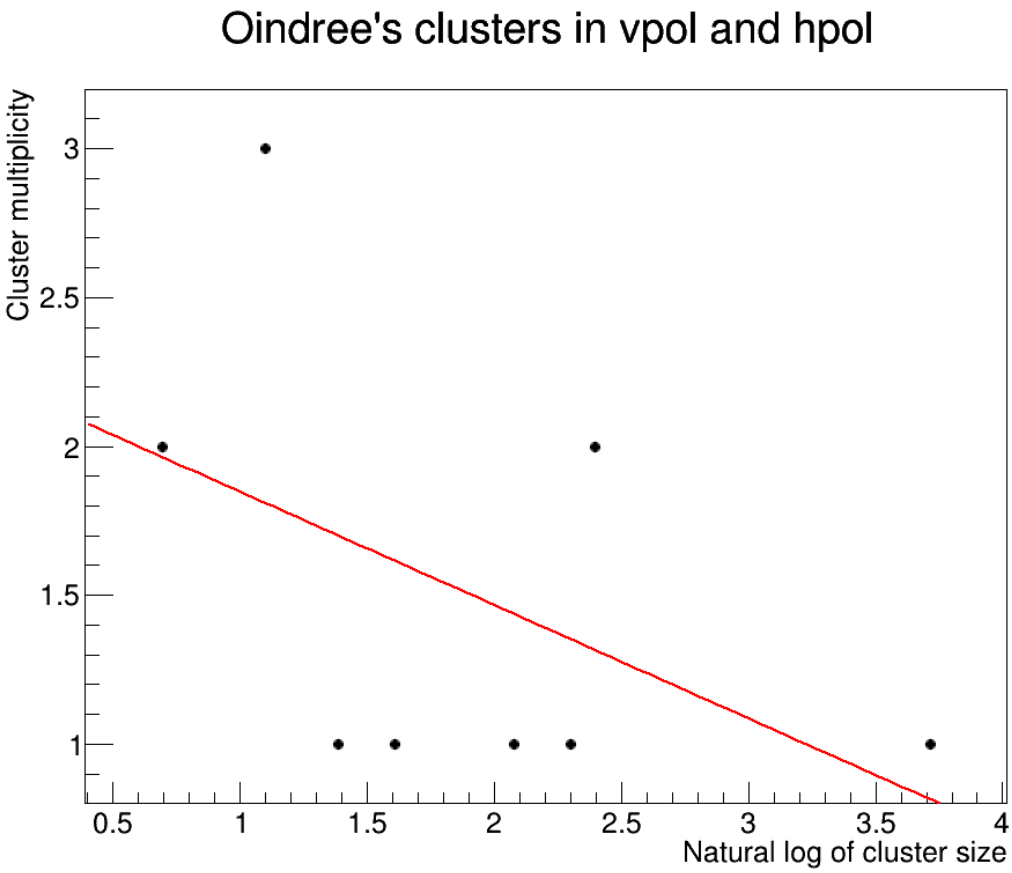

Figure 4.10: Cluster multiplicity as a function of cluster size. The fit to this distribution was used to calculate a background estimate from the clustering cut.

in the analysis. Indeed the efficiency loss due to clustering was calculated to be 0.1%.

4.6 Complementary efficiency

The efficiency of the analysis is calculated using the number of simulated neutrinos that pass all cuts. The efficiency of the binned analysis was 6.91%, after accounting for efficiency loss due to clustering. Although this efficiency is low and needs to be improved in the future, a large fraction of this efficiency is complementary to that of one of the clustering analyses (Analysis A) described in [2]. This was found by calculating the number of neutrinos that was kept in the binned analysis which was not kept in the complementary analysis.

The number of neutrinos kept in the binned analysis that the complementary analysis

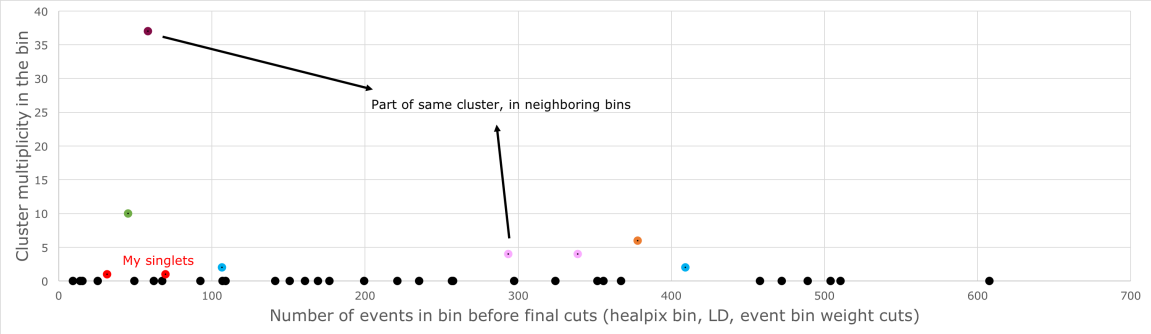

Figure 4.11: Cluster size as a function of event population before final cuts in the VPol analysis. There does not appear to be a trend suggesting a greater likelihood of finding clusters in bins with more events before final cuts. This is an important validation of the binned analysis.

did not keep was 35.9 (for a given number of neutrinos thrown in the Monte Carlo) and the total number of neutrinos kept in the binned analysis was 142.3. Therefore, 25.2% of the neutrinos kept in the binned analysis was not kept in the complementary analysis. This 25.2% of the efficiency of the binned analysis is, therefore, complementary and can be added to the other analysis. The efficiency that would be added is calculated to be 1.7%, which is small but not insignificant. If the overall efficiency of the binned analysis were to improve, its complementary efficiency which could be directly added to the efficiency of other analyses would be greater as well.

4.7 Blastfamy: Team effort to remove payload blasts

I developed a project called Blastfamy to guide undergraduate students through the process of learning how to use ANITA analysis tools and to apply that towards finding payload blast specimens in the data. These blasts would then be used as a training sample to perform an analysis potentially involving machine learning to remove all such blasts from the dataset. An example of a blast event can be seen in Figure 4.12.

4.7.1 Principal Component Analysis

I performed some tests with the ANITA-3 data to determine the potential of blast removal with unsupervised methods such as Principal Component Analysis (PCA), following valuable communication on the topic with Brian Connolly. I used a spreadsheet having the values of 10 features of events from the ANITA-3 data and performed a PCA on it with R. Results from this can be seen in Figures 4.13 and 4.14.

PCA is an analysis technique mainly used to reduce the dimensionality of a multi-dimension dataset. In my test, the initial dimension of the dataset is 10. The PCA successfully reduces this by calculating linear combinations from the features and determining which linear combinations can describe the data the best. The coefficients of the features in the linear combinations can be seen in Figure 4.13. Ten principal components are calculated here using linear combinations of the 10 features. It can be seen from the bottom plot that the first two or three principal components are the most important ones as the variances associated with each one fall off exponentially. This is how PCA is able to reduce the dimensionality of the problem.

The first two principal components are plotted in the top plot of Figure 4.14. The resulting image resembles a knee. In this "knee plot", we can see that there are a group of events in the bottom left, separated from the main knee. These bottom left events on the knee plot were checked. They were not blasts, and instead looked thermal-like to me. There is also a tail present in the knee plot and the events in this tail were also checked. The tail events were all low-quality events such as digitizer glitches. An example each of the bottom left events and tail events can be seen in Figure 4.15. The knee plot was re-made with a few known blast events overlaid. These events were in the thick of the knee and not easily separable as seen in Figure 4.16. From this, I concluded that more work needed to be done to reject blasts following these methods.

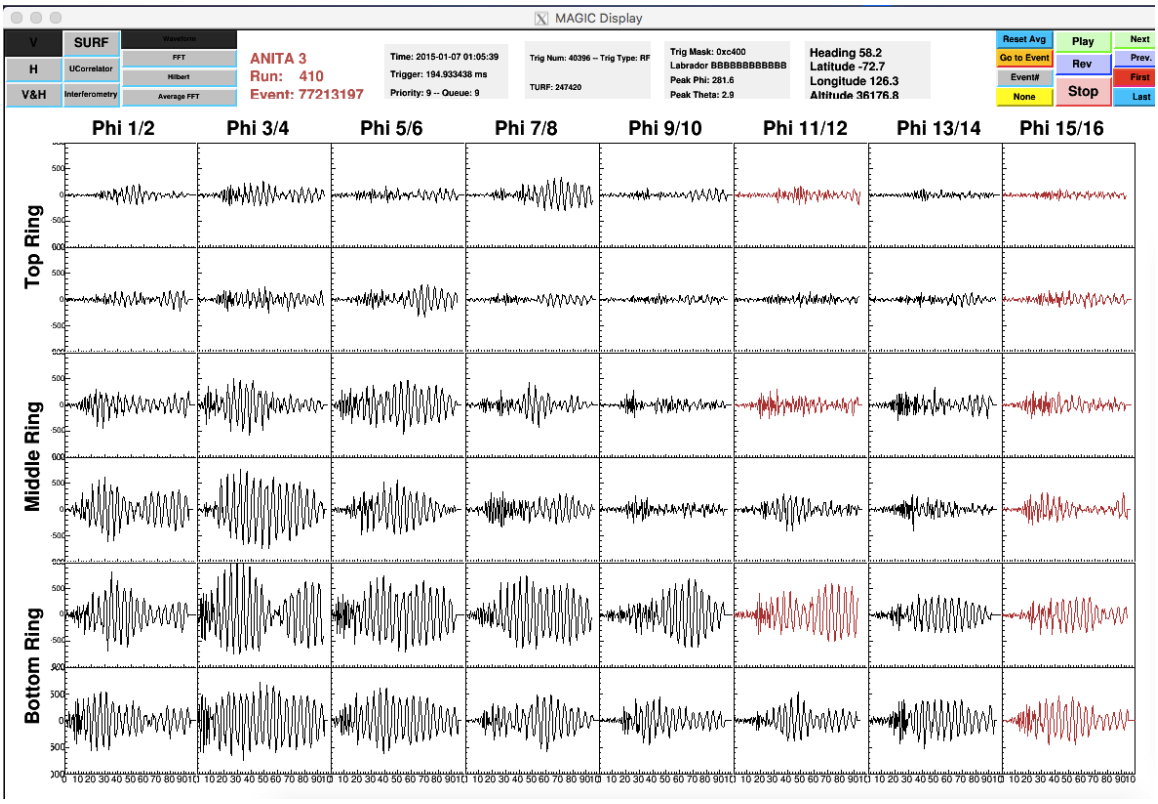

Figure 4.12: Example of a payload blast event. Waveforms received by all antennas in VPol are shown here.

Future

This method of PCA can certainly be improved, for example, by using more and better features. A quick test with 27 features yielded the variances shown in Figure 4.17. A more advanced method of analysis such as a Linear Discriminant Analysis, which is a semi-supervised method, could also be implemented in the future by using the principal components generated from features of a sample of all blast events as the training dataset.

```
> source("/Users/oindreebanerjee/Rstuff/12-19-17/oindree_pca.R")
Standard deviations:
 [1] 1.5780418 1.2733106 1.1077280 1.0406774 0.9864838 0.9160845 0.7989496 0.7390824
 [9] 0.6627740 0.3770938

Rotation:
                         PC1         PC2          PC3         PC4         PC5         PC6
maxRatio          0.592555556 -0.12424840  0.075585987  0.01098914 -0.01455119  0.01775083
maxReverseRatio -0.546541087  0.14606415 -0.089157083 -0.01543097  0.03502794 -0.03355773
maxRms            0.527884162 -0.10353572  0.079064923  0.01698664 -0.01741445  0.02508101
c0               -0.062819717  0.30898308  0.618135499  0.06648890 -0.07563361  0.39882437
c1                0.161103512  0.46839269 -0.139803315 -0.05038104  0.55986762 -0.23655296
c2               -0.019983316 -0.14702564 -0.002901442 -0.74700142  0.31037300  0.54370914
c3                0.085584107  0.53347887  0.254111983  0.10887854 -0.23625986  0.20883612
c4               -0.009519735  0.08105122  0.447877918 -0.56418105 -0.16417180 -0.65975053
c5                0.079577283  0.19328627 -0.446635043 -0.30640737 -0.69437306  0.09165239
c6                0.165714406  0.53619080 -0.337329572 -0.10169641  0.13352678  0.00291228
                          PC7           PC8          PC9         PC10
maxRatio          0.0115590217  0.0007798782  0.112382678 -0.783782707
maxReverseRatio -0.0421414005 -0.0429601737 -0.615646757 -0.535514261
maxRms           -0.0008538246 -0.0249195053 -0.777645240  0.312718255
c0                0.5900756850  0.0235793338 -0.013871570 -0.018757240
c1                0.1803041727 -0.5730739241  0.039904374  0.025416409
c2               -0.1642479298 -0.0320806835  0.001923028  0.001819138
c3               -0.7129643909 -0.1498022892  0.036876709  0.009906334
c4               -0.0284673138  0.1067206088 -0.004046537  0.002448591
c5                0.2714324997 -0.3141364710  0.005074018  0.001538118
c6                0.0872310642  0.7314521305 -0.020654177  0.002967019
>
```

Figure 4.13: PCs printed out.

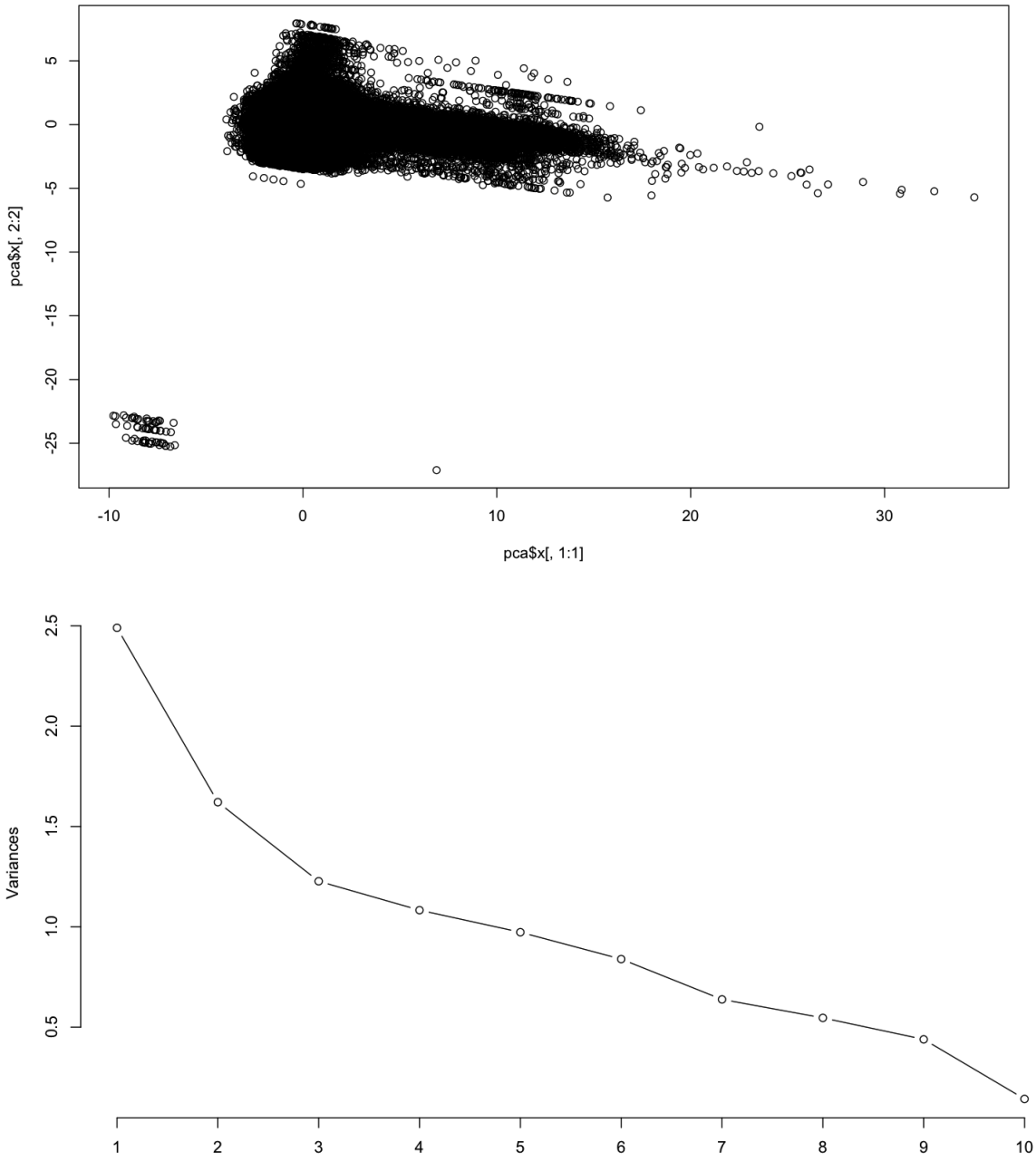

Figure 4.14: Principal components and variances using 10 features. The knee plot is presented at the top here.

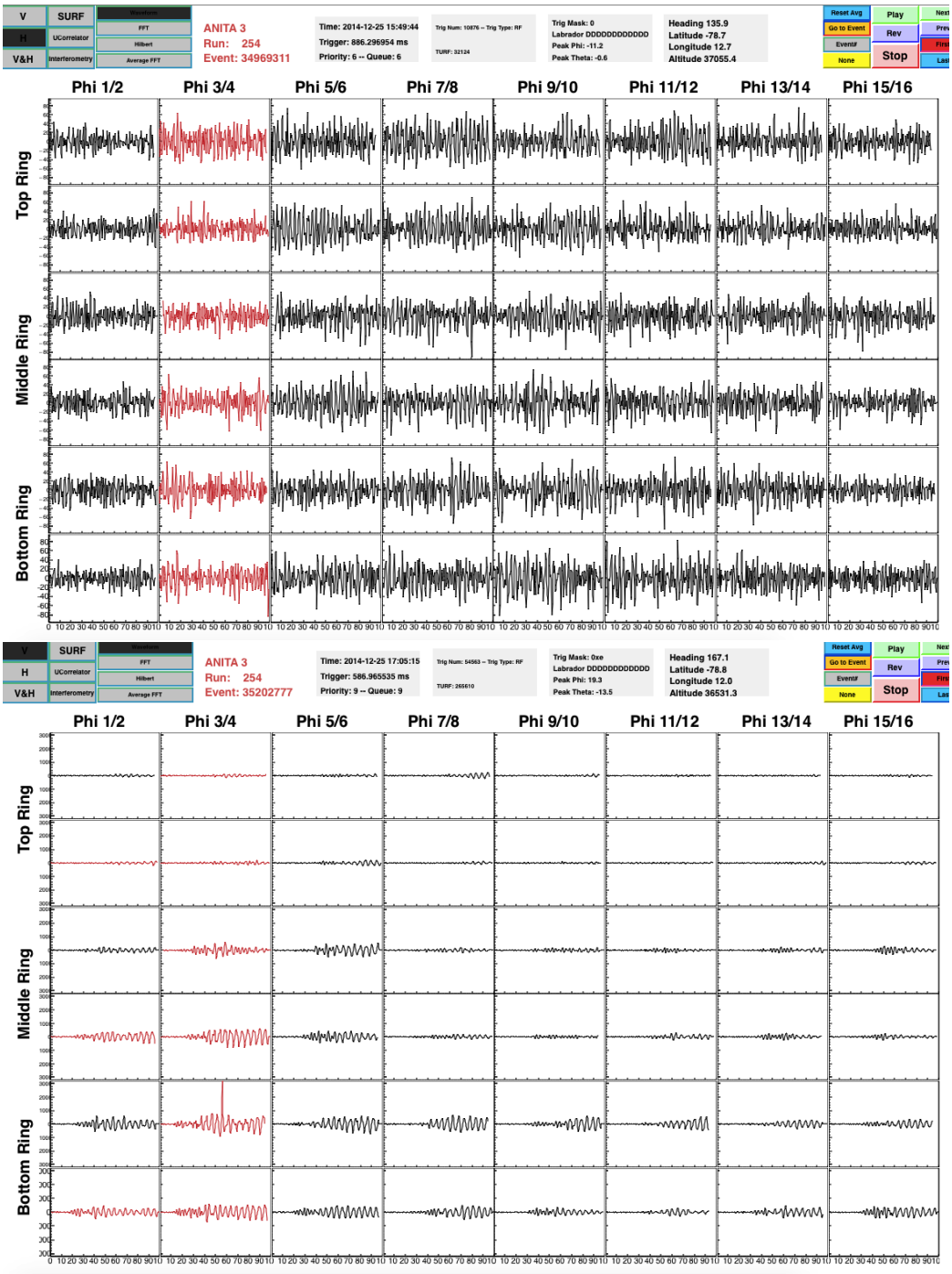

Figure 4.15: Example of a bottom left event from the knee plot (top) and tail event from the knee plot (bottom).

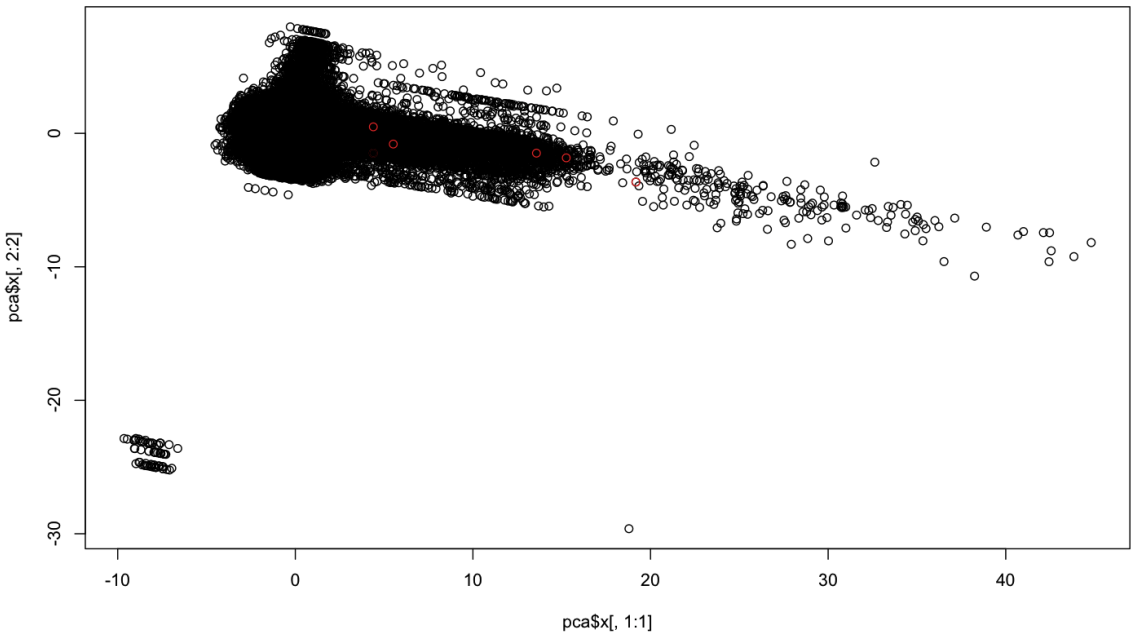

Figure 4.16: Blasts overlaid on knee plot.

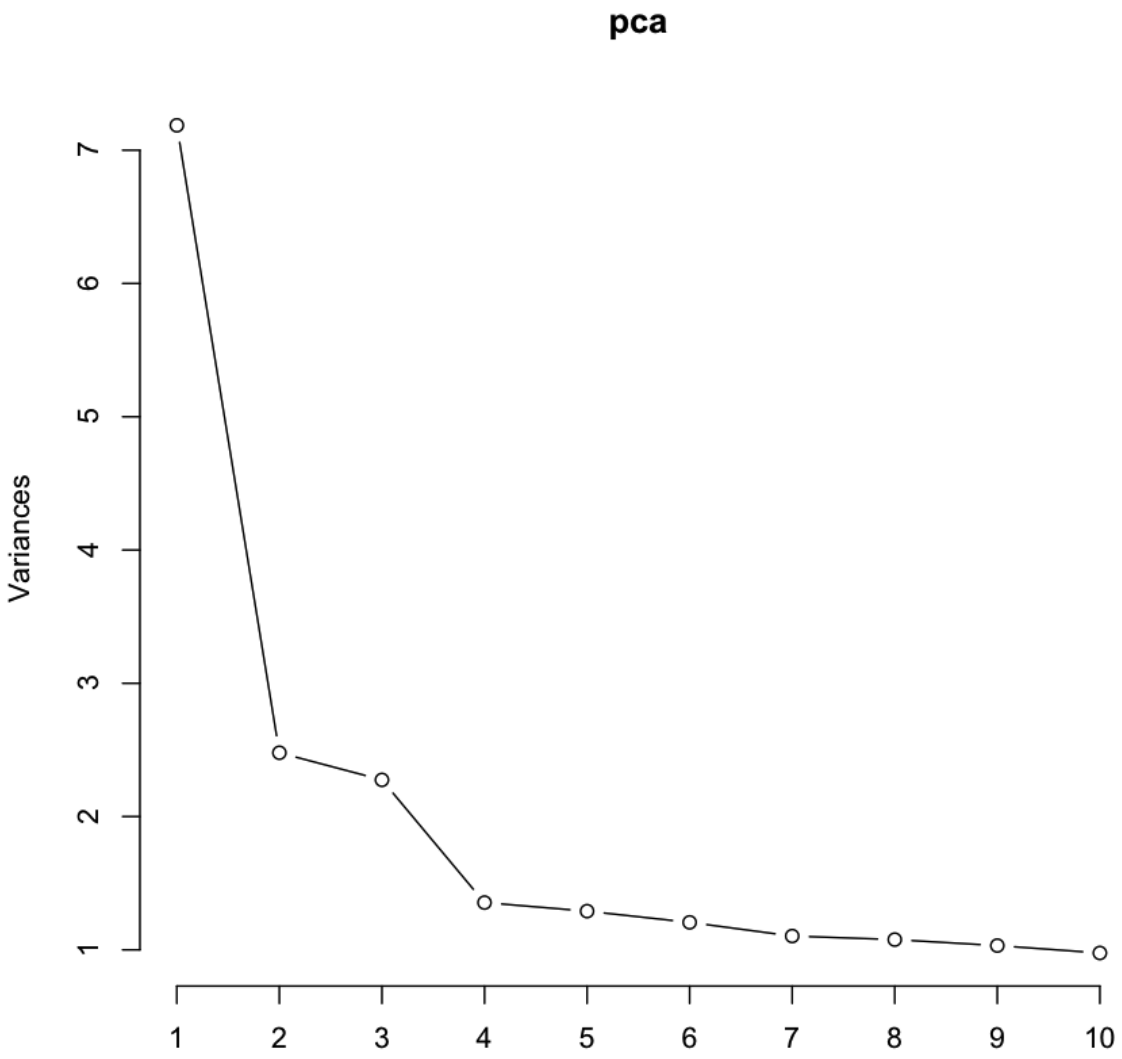

Figure 4.17: Variances from using 27 features.

Chapter 5

Review of my favorite transients: Gamma Ray Bursts

5.1 Introduction

GRBs are the most luminous transient events in the observed Universe. When they occur, they outshine an entire galaxy [25, 26]. Gamma-ray luminosities of GRBs are of the order $10^{52}\,\mathrm{erg\,s^{-1}}$ which can be compared to the $10^{33}\,\mathrm{erg\,s^{-1}}$ emitted by our Sun, $10^{41}\,\mathrm{erg\,s^{-1}}$ by a supernova and $10^{45}\,\mathrm{erg\,s^{-1}}$ by a whole galaxy.

First discovered in 1967 by the Vela satellites flown by the U.S. Department of Defense, GRBs continue to intrigue and puzzle scientists to this day. However, research in the past decades have revealed much about them including that they are extragalactic in origin, isotropically distributed and that they come in at least two populations.

GRBs are classified as **long** if they last for $t_{GRB} > 2\,\mathrm{s}$ and **short** if they last for $t_{GRB} < 2\,\mathrm{s}$. Long bursts are associated with the collapse of massive stars or hypernovae and short bursts are associated with mergers of binaries composed of neutron star-neutron star or neutron star-black hole [25].

In August of 2017, for the first time in history, multimessenger observation of a short GRB was performed by the LIGO, Virgo and Fermi collaborations, confirming the association of short GRBs with a binary neutron star merger [11]. This marked the first observation of a messenger other than photons from a GRB. Indeed, no other messengers or particles have been known to come from GRBs, although theories predict that GRBs are

environments where particles could get accelerated to the highest energies.

The detection of GRB **neutrinos** would provide unambiguous proof for hadronic acceleration in these cosmic explosions and could also explain the origin of the cosmic ray flux at ultra-high energies. From gamma-ray observations alone, theorists have hypothesized that regardless of the nature of the underlying source or progenitor, GRBs are produced by the dissipation of the kinetic energy of a relativistically expanding fireball. Protons may be Fermi accelerated in this dissipation region to energies $> 10^{20}$ eV. Interactions between fireball gamma-ray photons of energy ~ 1 MeV and accelerated protons of energy $\sim 10^{15}$ eV could lead to photo-meson production of pions which upon decaying would result in an accompanying burst of $\sim 10^{14}$ eV neutrinos (Waxman *et al.* [12, 27]).

5.1.1 GRB emission

GRBs are characterized by a two-part emission: **prompt** and **afterglow**. Gamma-rays are emitted during the prompt emission period followed by softer and softer photons such as X-rays, UV rays, and so on during the afterglow emission period. As discussed in Section 5.2, neutrinos are predicted from GRBs following an opposite spectrum to that of photons, in other words, harder and harder energy neutrinos with time. The type of emissions from a GRB is summarized in Figure 5.1.

As can be seen in Figure 5.1, GRBs are extremely diverse. The prompt emission is typically between 0.2 and 20 seconds long. Note that the prompt emission can, occasionally, last for several hundreds of seconds as was seen in the case of a 5400 second long GRB that was reported in [28]. The afterglow emission time period for GRBs is even more diverse. The afterglows can last from anywhere between few minutes to several months. Swift scientist at the Mullard Space Science Laboratory, Mat Page, showed me the flux vs. time plot of a GRB with afterglow observations in X-ray that continued for over a year! Mat shared that eventually the observers decided to move on and assign observation time to other objects.

Afterglow records might not be available for a few other reasons. Sometimes, afterglows are not observed at all as no telescope is pointing at the object for follow-up in afterglow. So, the absence of a record for an afterglow does not necessarily mean that there was no

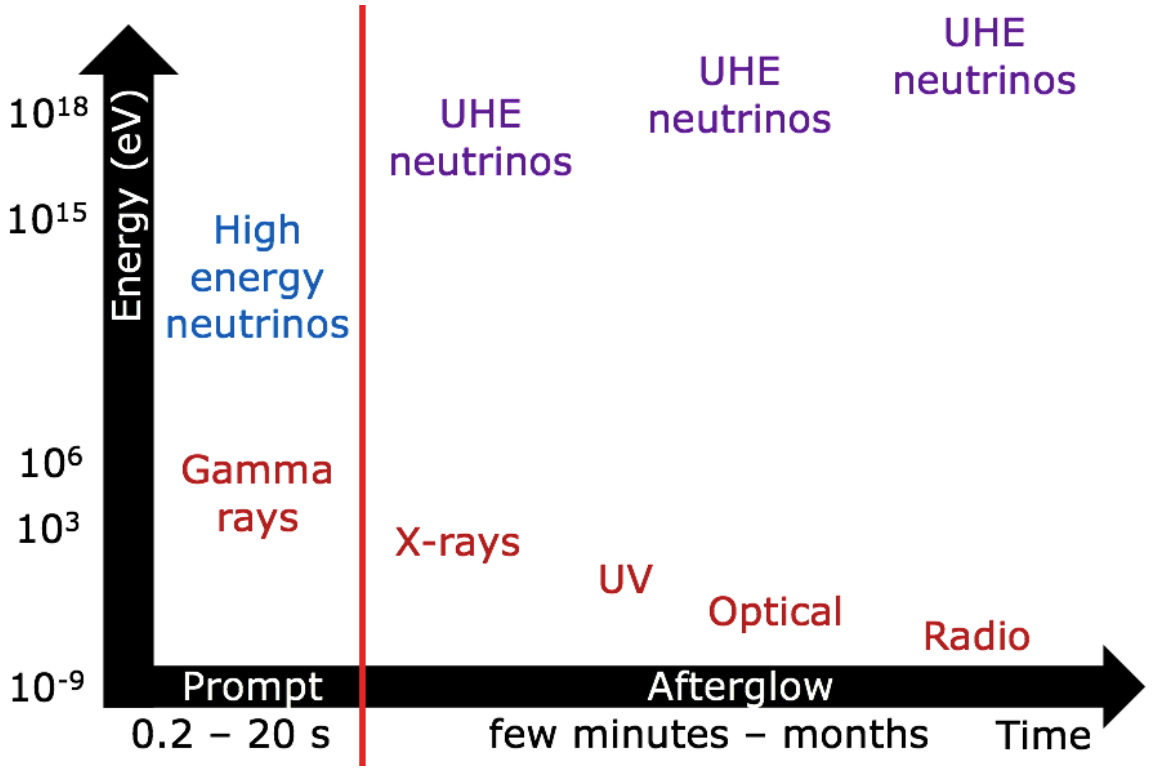

Figure 5.1: Illustration of the predicted emission from GRBs. Note that GRBs are extremely diverse. Most importantly, note that UHE neutrinos are more likely to be produced during the afterglow of a GRB, as opposed to during its prompt emission.

afterglow. Moreover, afterglow photons can get absorbed by dust and not be able to reach us. Thanks to my discussions with Swift observers at Mullard Space Science Laboratory for these insights.

5.2 GRB theory in the early days

The most widely accepted theory for GRBs endorses a relativistic fireball. The observation of gamma-rays (photons) guided this theory. In fact, the observed photon spectrum was the starting point for GRB theorists. Up until 1994, GRBs had been observed to emit photons in the energy range between a few keV and a few tens of MeV. In 1994, however, a very energetic burst was reported by [28] that emitted photons of energy up to 18 GeV. Other observations such as by the Fermi observatory [29] have confirmed this hardness of the photon spectrum from GRBs. It was argued that since observed photons from the gamma-ray emitting region of the GRB do make it out to us, the optical depth in this region, $\tau_{\gamma\gamma}$ must be < 1. Now, the optical depth $\tau_{\gamma\gamma}$ is a function of the Lorentz factor Γ (see review by Waxman [12]) and thus from $\tau_{\gamma\gamma}$ it was obtained that the gamma-ray emitting region in a GRB must be moving with a Lorentz factor $\Gamma \geq 100$. Thus, the fireball model says that the gamma-ray emitting region of a GRB is relativistically expanding.

It was theorized that GRBs are produced by the dissipation of the kinetic energy of a relativistically expanding fireball. The expanding fireball has regions of over-density moving at different speeds. When these regions collide, shocks are produced. Particles are accelerated to relativistic speeds. The relativistic ejecta of a GRB may undergo internal collisions resulting in prompt emission as well as collisions with the interstellar medium resulting in afterglow emission. In these collisions, shock accelerated electrons emit synchrotron and inverse-Compton radiation in the form of gamma-rays. Thus, it was theorized that part of the kinetic energy of the GRB is the source of the observed gamma-radiation. It may be that the kinetic energy is converted to energy of electrons, energy in magnetic fields and energy of protons. A helpful review on these theories can be found in [25].

No neutrinos are produced in the leptonic theory of GRBs. In the leptonic theory of

GRBs, most of the kinetic energy of the GRB is assumed to go into energy of the electrons (leptons) and the electrons then emit gamma-radiation in the form of synchrotron and inverse-Compton radiation. There are no interacting baryons and no neutrinos produced in this picture.

5.2.1 Neutrinos from GRBs

Neutrinos are predicted in the hadronic theory of GRBs. This is summarized in Figure 5.2. The hadronic theory says that protons are also shock accelerated in the dissipation region and may interact with photons of the gamma-radiation to produce pions. The hadronic picture allows for the production of neutrinos and is supported by Waxman-Bahcall. The photo-meson interaction resulting in the intermediate Δ^+ of mass 1232 MeV is thought to dominate neutrino production in the work of Waxman-Bahcall [12, 27, 30–32].

$$p + \gamma \longrightarrow \Delta^+(1232\,\mathrm{MeV}) \longrightarrow n + \pi^+ \;\; \mathrm{OR} \;\; p + \pi^0$$

$$\pi^+ \longrightarrow \mu^+ + \nu_\mu \longrightarrow e^+ + \nu_e + \bar{\nu_\mu} + \nu_\mu$$

$$\pi^0 \longrightarrow \gamma\gamma$$

According to Waxman-Bahcall [27], approximately half the time, the photo-meson interaction of an accelerated proton with a gamma-ray photon creates a neutron and half the time, a proton. When a neutron is created, it can escape the magnetic fields of the GRB into space, $\beta-$decay into a proton and reach Earth as cosmic rays. Since GRBs are some of Nature's most powerful accelerators, it is only natural to hypothesize that the highest energy cosmic rays observed with energy $\sim 10^{20}$ eV might come from GRBs. It was theorized by Waxman-Bahcall [27, 30–32] that the neutron created in the above reaction was a source of cosmic rays. To ensure that GRBs could be the source of both cosmic rays and neutrinos, the following was assumed in [30, 32].

$$\tau_{pp} \sim \tau_{np} \sim \tau_{p\gamma} \sim \tau_{n\gamma} \sim 1$$

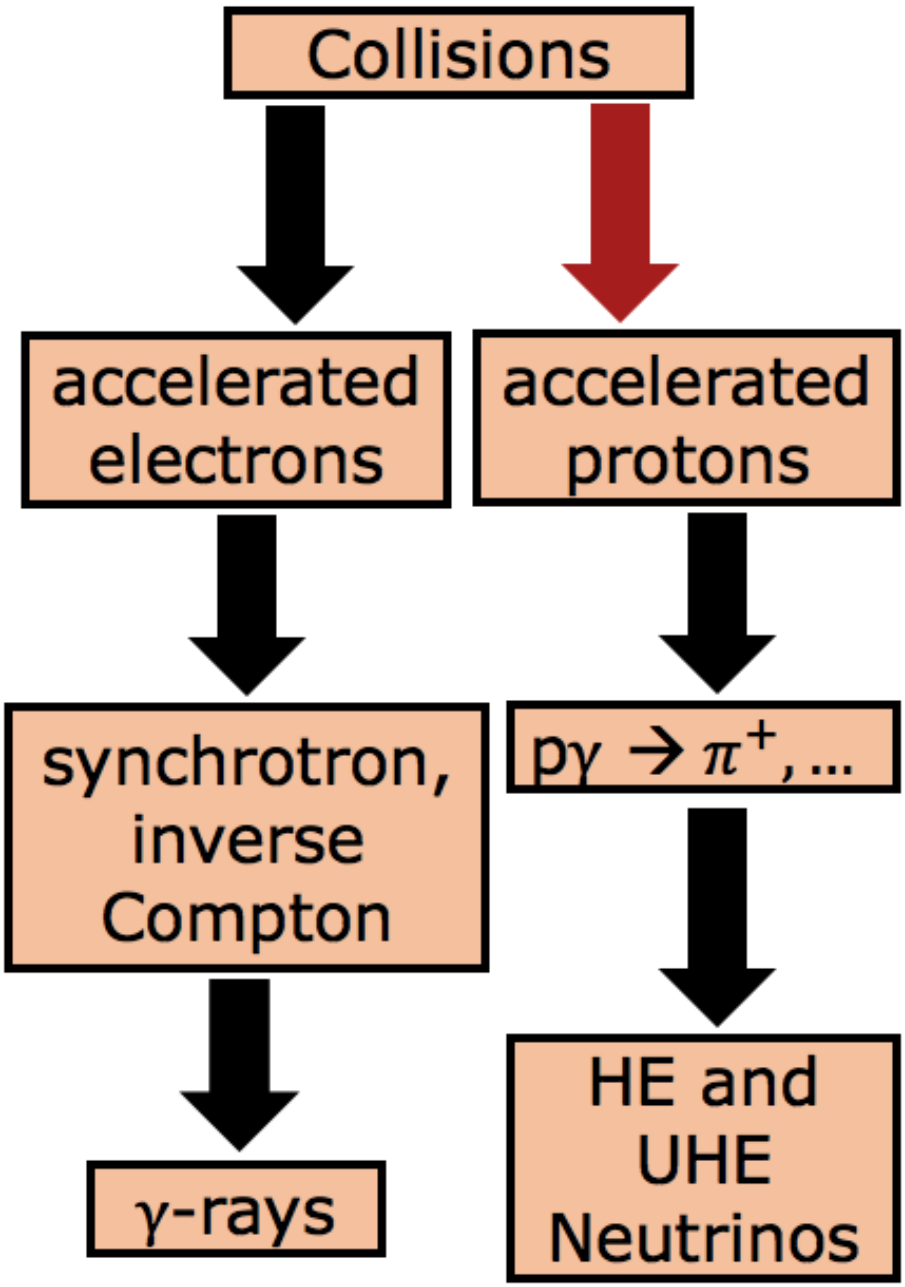

Figure 5.2: Summary of the hadronic theory of GRBs. This theory predicts the production of high energy and ultra-high-energy neutrinos from GRBs.

This way protons needed to interact at least once in the source with photons before they could leave the source. The charged pion would decay to produce neutrinos and the neutral pion would decay to produce more gamma-rays. The mean pion energy was 20% of the energy of the proton producing the pion (Waxman *et al.* [27]). This energy was roughly evenly distributed between the π^+ decay products. So each neutrino coming out of this process would have roughly 5% of the energy of the original proton. From particle kinematics the following key relation between observed photon energy ε_γ and the accelerated proton's energy ε_p at the photo-meson threshold of the $\Delta-$resonance was obtained.

$$\varepsilon_\gamma \varepsilon_p = 0.15 - 0.2\,\mathrm{GeV}^2\,\Gamma^2$$

Inserting in the above equation a typical observed gamma-ray energy of 1 MeV and a Lorentz factor Γ of 100, Waxman-Bahcall found a characteristic proton energy of $\sim 2 \times 10^6$ GeV or 2×10^{15} eV, which would produce neutrinos of energy $\sim 10^{14}$ eV. In the hadronic picture proposed by Waxman-Bahcall [27, 30–32], these high energy neutrinos result from **internal shocks** within the fireball and accompany the **prompt emission** of gamma-rays.

UHE neutrinos are thought to result from collisions of the expanding fireball with its **surrounding medium**. Inserting in Equation 5.2.1 a typical afterglow photon energy of 100 eV and Lorentz factor Γ of 100, neutrino energies of order 10^{18} eV were found. It was theorized that protons accelerated in the dissipation region of a GRB may interact with photons of the prompt emission as well as photons of the afterglow emission producing charged pions that may decay into high energy and UHE neutrinos.

Waxman and Bahcall [27] predicted that a km^2 neutrino detector should detect $\sim 10 - 100$ neutrinos of energy $\sim 10^{14}$ eV per year correlated with GRBs. In [30] Waxman-Bahcall showed that cosmic ray observations set a model-independent upper bound to the intensity of high energy neutrinos produced by photo-meson or $p-p$ interactions in GRB sources of size not much larger than the proton photo-meson or $p-p$ mean free path. The upper bound is as follows:

$$E_\nu^2 \, \Phi_\nu < 2 \times 10^{-8} \, \mathrm{GeV \, cm^{-2} \, s^{-1} \, sr^{-1}}$$

Post the study of GRB afterglows, it was predicted by Waxman-Bahcall in [31] that the expected detection rate of UHE ($10^{17} - 10^{19}$ eV) muon neutrinos is $\sim 0.06/\mathrm{km^2 yr}$ over 2π steradian. In [32] they further showed that the upper bound mentioned above is robust and cannot be evaded by invoking magnetic fields, hidden fluxes of extragalactic protons, etc.

The detection of GRB neutrinos would provide unambiguous proof for hadronic acceleration in these cosmic explosions and could also explain the origin of the cosmic ray flux at ultra-high energies. The above theoretical predictions for neutrino fluences from GRBs were put to the test by experimental searches for high energy neutrinos. We discuss the relevant experimental work and results in the following section.

5.3 Previous searches for UHE neutrinos from Gamma Ray Bursts

In this section, we discuss the GRB neutrino searches conducted by the ANITA collaboration in 2011 and the ARA collaboration in 2015. Since these experiments typically conduct diffuse searches, we include a brief overview of how a GRB neutrino search is different from a diffuse search.

5.3.1 GRB neutrino search vs. Diffuse search

Experiments such as IceCube, ANTARES, ANITA and ARA typically conduct diffuse searches for neutrinos. In diffuse searches, experimenters do not know where neutrinos might be coming from and when. Because experimenters do not know when the signal will arrive in time or direction, to effectively account for backgrounds, thresholds for power and voltage measured must typically be set very high, meaning that experimenters diminish their chance of actually finding a neutrino signal. In setting thresholds high, experiments lose neutrinos. This is an efficiency hit scientists are willing to take to make confident statements about signals they do see. For the GRB neutrino search conducted by each

of these experiments, the experimenters knew when and from where neutrinos could be expected. During analysis, for each GRB, scientists had the option to study the data that is temporally close to the expected neutrino events in order to figure out the background for that GRB. From the individual background for each GRB, analysis cuts for each GRB could be determined. In a GRB neutrino search, because searches are carried out over shorter time windows and over smaller portions of the sky, analysts can loosen their cuts, and lower thresholds necessary for voltage and power. This typically means GRB neutrino searches have better signal-to-noise ratio than diffuse neutrino searches because for the same backgrounds, analysis cuts can be made looser.

5.3.2 First GRB search by ANITA (2011)

In 2011, ANITA set the first limits on the UHE neutrino fluence at energies greater than 10^{18} eV from GRBs in an analysis by Vieregg and Palladino *et al* [5]. The second flight of the ANITA experiment launched on December 21 2008, flew for 31 days, 28.5 of which were live days, and recorded over 26 million triggers. Over 98.5% of the recorded events were fluctuations of thermal noise.

The authors stated that ANITA is most sensitive to neutrinos which come from between the horizon ($-6.5°$) and a payload elevation angle (angle above the horizontal) of $-25°$ [5]. Figure 6.3 in Chapter 6 shows the range of angles that were found to be allowed for simulated neutrinos generated using an isotropic flux following the Kotera model.

The authors reminded us that there are two ways (geometries) that ANITA can view the radio emission from a neutrino interacting in the ice: direct and reflected. The direct observation occurs when ANITA observes the radio impulse directly from the interaction of an upgoing neutrino. The reflected observation occurs when ANITA receives the radio impulse reflected off of the bottom of an ice shelf (sea water interface) from the interactions of a downgoing neutrino. Since UHE neutrinos are absorbed as they travel through the Earth, most of ANITA's direct events would be associated with neutrinos that skim across the ice.

During the 31 day flight of ANITA-2, 26 GRBs were recorded by Swift or Fermi. Of

these, only 12 occurred during what the authors considered to be quiet detection periods, or having thermal-like background, while the remaining 14 had significant anthropogenic noise associated with them.

A blind analysis was performed for the GRB-coincident neutrino search. During the analysis period of setting the cuts, the analysts were blinded to the 10 minutes of signal region having possible neutrino events. Analysis cuts were set on regions of time which should contain no neutrino events, and then applied in the prompt (10 minutes) and precursor emission (100 seconds before start of burst) windows for each burst. To set the analysis cuts, the background period was chosen to be the 55 minutes starting 1 hour before each burst and the 55 minutes starting 5 minutes after each burst (for a total of 1 hour and 50 minutes). This allowed the use of events close to the signal region in time as a background sample without ruling out the possibility of extended prompt or precursor neutrino emission.

No events were found in the prompt emission or the precursor windows of the observed bursts. A limit was set for each burst individually on the prompt UHE neutrino fluence using a Feldman-Cousins 90% confidence interval, the duration of the burst, and the acceptance calculated using a Monte Carlo simulation. For each GRB, the Monte Carlo was configured to simulate a point source at the location of the burst, fixed ANITA at the location of the payload during the burst, and assumed an input E^{-4} (for UHE) spectrum.

None of the 26 GRBs during the flight had a payload elevation angle between -25° and the horizon which is where the authors claimed ANITA has the best chance of seeing direct neutrino events. Of the 12 GRBs observed during quiet time, the most promising direct observation geometry was thought to be from GRB 090113 at an elevation angle of -25.7° although this still suffered from poor geometry. ANITA placed a 90% confidence level limit on the E^{-4} prompt neutrino fluence for energies $10^{17}\,\mathrm{eV} < E < 10^{21}\,\mathrm{eV}$ of $E^4\,\Phi = 1.5 \times 10^{20}\,\mathrm{GeV}^3\,\mathrm{cm}^{-2}$ from GRB 090113.

Figure 5.3 shows the three best limits placed by ANITA in this GRB-coincident search. The red and green dashed lines are the "direct" limits and the blue dashed line is the "reflected" limit. Note that the reflected limit is the best limit. The "reflected" limit comes

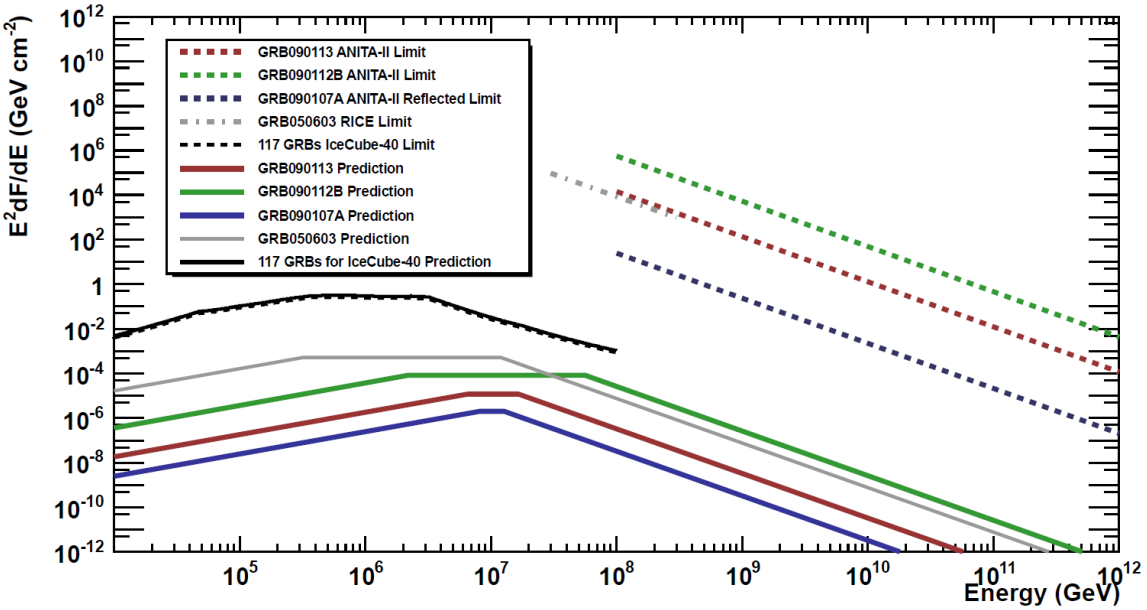

Figure 5.3: Figure from ANITA publication on a GRB search [5]. The two best "direct" limits by ANITA on the UHE neutrino fluence from the blind analysis are from GRB 090113 and GRB 090112B. These are shown with red and green dashed lines respectively. The "reflected" limit is from GRB 090107A, shown with a blue dashed line. RICE (Besson *et al.* 2007) and IceCube (2012) [6] limits are also shown. The IceCube limit is an aggregate limit based on 117 individual GRBs, and is based on a fluence prediction from Guetta *et al.* (2004) [5, 7].

from a GRB with an elevation angle of 0.5°, that is, a neutrino from this GRB would be down-going. It seems the authors stipulated that a down-going neutrino can only be seen by reflection off of an ice-shelf. Since this GRB was at a time when the payload was flying over the Ross Ice Shelf, the authors considered this GRB even though its background was not thermal-like. However, the authors did not consider GRB 090111 which had an elevation angle of 1.7° because the payload was not over the Ross Ice Shelf when this GRB took place. Finally, note that the green dashed-line limit is almost two orders of magnitude worse than the red dashed-line limit. Both GRBs corresponding to these two limits had poor geometry or elevation angle of −25.7° (red dashed-line) and −26.8° (green dashed-line), respectively. Therefore, it is not surprising that these limits are not very tight. It is interesting, however, that a difference in elevation angle of just a degree can potentially make the limit much worse.

5.3.3 First GRB search by ARA (2015)

In 2015, the ARA collaboration presented an UHE GRB neutrino fluence limit from 57 selected GRBs and the first limit on the UHE GRB quasi-diffuse neutrino flux for energies 10^{16} eV to 10^{19} eV [8] using data collected by ARA in prototype form (ARA Testbed) [15]. See Figure 5.4 and Figure 5.5.

The quasi-diffuse flux is an estimation of the average GRB flux calculated from a statistically representative set of GRBs and is useful in comparing limits between experiments that observe different sets of bursts.

Predictions for GRB neutrino fluences were calculated using NeuCosmA [33, 34]. For all GRBs, the bulk Lorentz factor of the fireball Γ was assumed to be 316 and the baryonic loading (ratio of fractional proton energy to fractional electron energy) was assumed to be 10. As ARA is sensitive to all neutrino flavors, neutrino fluence predictions for all three flavors were obtained from NeuCosmA with 1:1:1 flavor ratio assumption. AraSim, a Monte-Carlo simulation software package used within the ARA collaboration, was used to simulate neutrino signals as they would be observed by the detector. It simulates the full chain of neutrino events such as the neutrino's path through the Earth, radio Cherenkov emission,

the path and response of the emitted signal in the ice, and the trigger and data acquisition mechanisms of the detector [8].

Among 589 GRBs monitored by the Gamma Ray Coordinate Network (GCN) catalog from January 2011 to December 2012 over the entire sky, 57 GRBs were selected for analysis because they occurred during a period of low anthropogenic background and high stability of the station and fell within the geometric acceptance.

Drawing on the blinding technique of analysis carried out by the ANITA GRB neutrino search, the ARA collaboration performed a blind analysis with two un-blinding steps. ARA, too, used the 55 minutes before 1 hour and the 55 minutes after 5 minutes of a burst to study the background for each burst. For an extra step of caution, initially, only 10% of the total 110 minutes of data temporally close to the 10 minutes of signal region was used to get cuts. Then, the remaining 90% was used to get cuts and it was checked that these cuts were consistent with the ones from the initial 10%. Only after this two-step method of getting analysis cuts was the analyzer unblinded to the signal region. In the search for UHE neutrinos from 57 GRBs in [8], 0 events were observed, which was consistent with 0.11 expected background events.

5.4 Current theories

The flux of neutrinos emitted during the afterglow period of GRBs is most interesting to ANITA. This is because it is during the afterglow period of GRBs that UHE neutrinos with energy $> 10^{18}$ eV are predicted. Some of the earliest calculations for afterglow neutrino fluxes came from Waxman and Bahcall, for example, in [31]. Since then, several other models have been developed, such as, by Kohta in [35].

The afterglow neutrino spectrum depends on the matter profile of the interstellar medium. This makes sense as the afterglow emission is due to collisions of the GRB plasma shells with the external material surrounding it, that is, the interstellar medium. Figure 5.6 shows a plot made by GRB theorist Mauricio Bustamante. This shows the diffuse afterglow neutrino spectrum for two choices of matter profile and for the case where

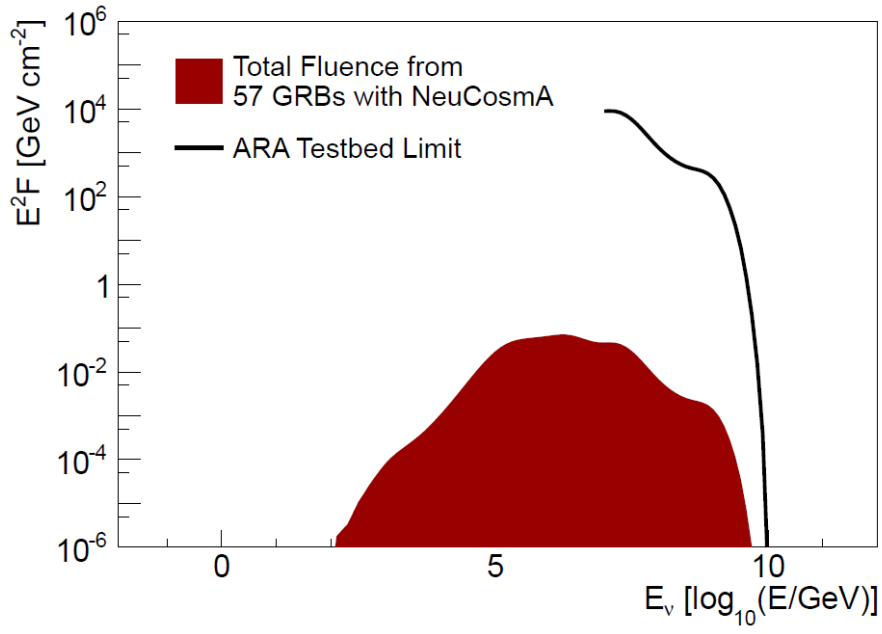

Figure 5.4: Figure from ARA publication on a GRB search [8]. The limit on the UHE GRB neutrino fluence from 57 GRBs used for ARA analysis. Total fluence from NeuCosmA for the 57 GRBs is shown with a red shaded area and the limit from the ARA Testbed above 10^{16} eV is shown with a black solid curve.

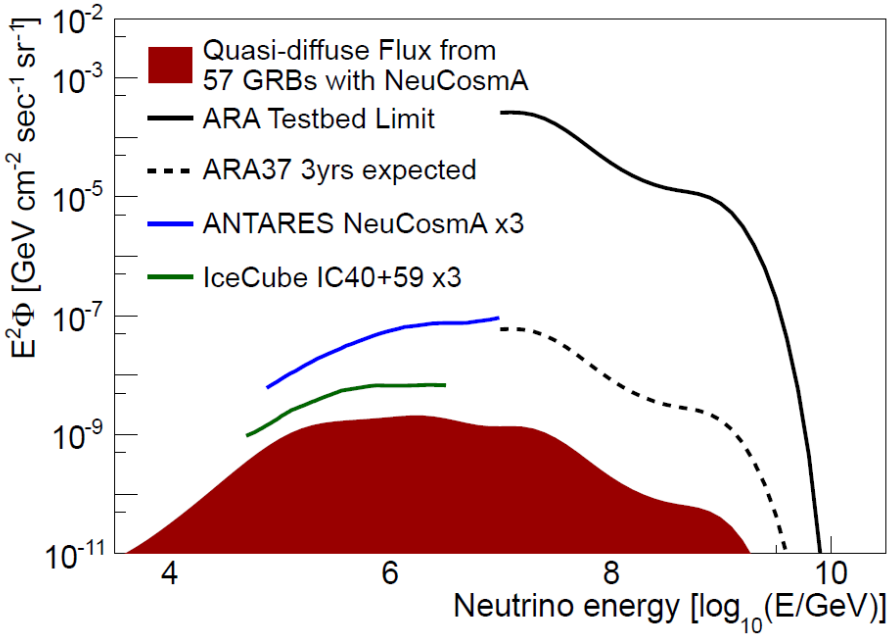

Figure 5.5: Figure from ARA publication on a GRB search [8]. The inferred quasi-diffuse all flavor flux limit from the selected 57 GRBs. IceCube and ANTARES limits are from [6] and [9], respectively.

the afterglow is due to late internal collisions.

Figure 5.6 helps to summarize why ANITA should include GRB afterglows in a GRB neutrino search. Late internal collisions are a variation of the prompt phase collisions, shown in solid pink in Figure 5.6. As can be seen from the horizontal axis representing energy in units of GeV, this late prompt phase model produces a neutrino flux only upto about $> 10^9$ GeV or 10^{18} eV. If a late prompt model cannot produce neutrinos above 10^{18} eV, a regular prompt model is even less expected to do so. In contrast, the afterglow models shown in solid green and blue in Figure 5.6 go above 10^{18} eV. This is where ANITA starts to become sensitive. Therefore, in order to detect neutrinos from GRBs with ANITA it would be best to include afterglow periods.

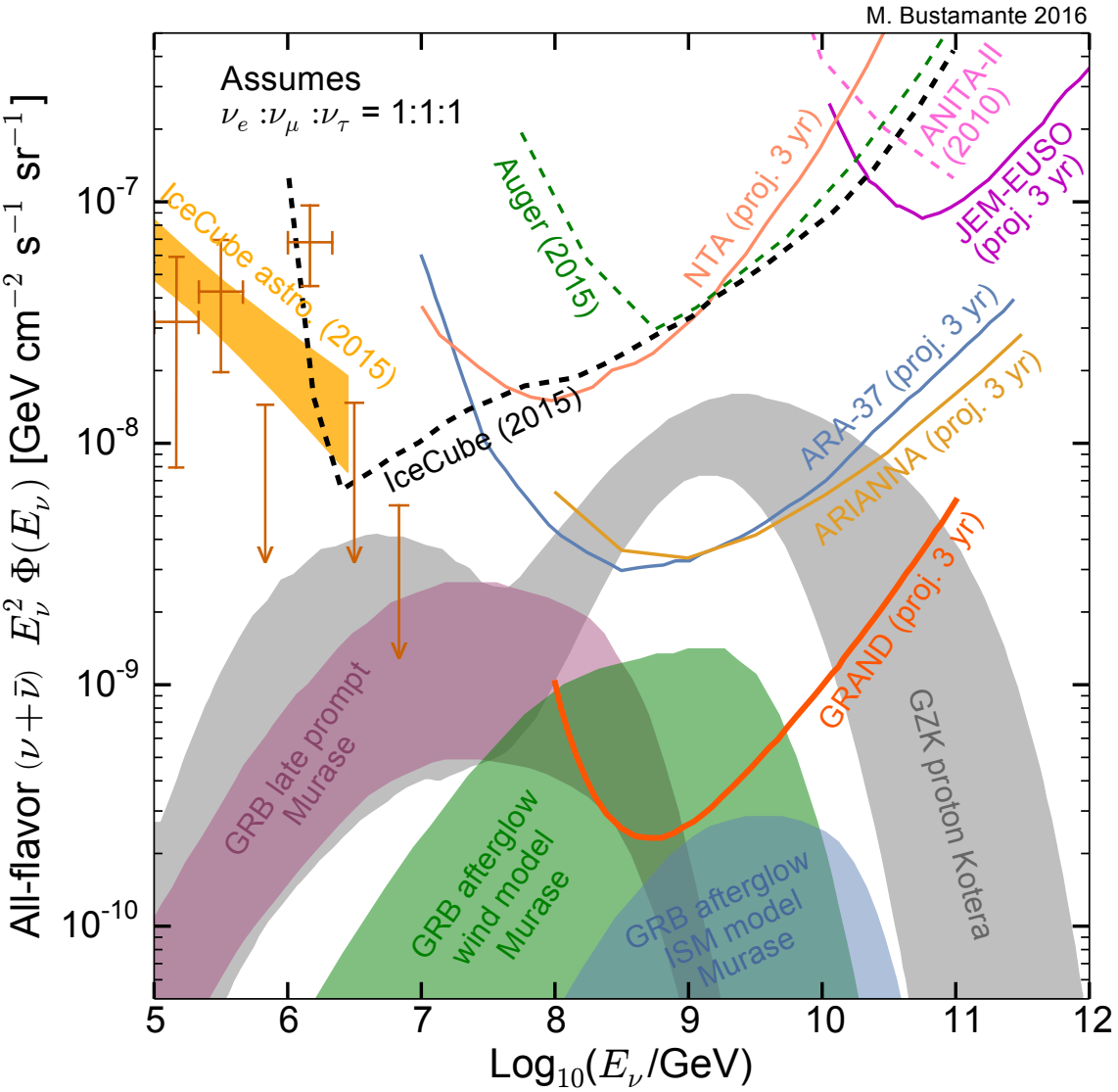

Figure 5.6: Figure by Mauricio Bustamante, unpublished. This shows different models for neutrino spectra.

Chapter 6

Development of the first GRB search in ANITA constrained in direction and time

6.1 Gamma Ray Bursts during the ANITA-3 flight

The IceCube catalog was used to determine which GRBs took place during the third flight of ANITA. The catalog provides information such as the GRB name, which day the GRB occurred, the time of trigger in UTC, the time over which a burst emits from 5% of its total measured counts to 95%, the right ascension (RA), and the declination (Dec), among other properties. There were 18 GRBs during ANITA-3. Relevant information on these GRBs as obtained from the catalog are shown in Table 6.1.

Table 6.2 shows information on the GRBs that was either calculated or found in data. The "Catalog UT" column shows the unixtime calculated for each GRB using the date and time provided by the catalog (code in Figure 6.1). "Closest recorded UT" is the closest unixtime recorded by ANITA corresponding to the unixtime calculated from the catalog. It can be seen that this closest recorded unixtime is the same as the catalog unixtime for all except one GRB. GRB141225A took place on December 25, 2014 which is when the ANITA-3 flight was temporarily out of commission due to technical problems, therefore, the closest recorded unixtime for this GRB is not identical to the catalog unixtime. Also shown in Table 6.2, are the run number that corresponds to each GRB unixtime, and the longitude, latitude, and altitude of the ANITA payload at that time. Longitude and latitude

GRB name	Date	UTT (Trigger)	T90	RA	Dec
141220A	12-20-14	6:02:51	8.448	195.058	32.146
141221A	12-21-14	8:07:10	36.9	198.287	8.205
141221B	12-21-14	21:31:48	32.51	126.02	-74.21
141222A	12-22-14	7:08:55	8.448	178.04	-57.35
141222B	12-22-14	16:34:30	34.05	97.43	40.13
141223A	12-23-14	5:45:37	94.2	147.38	-20.71
141225A	12-25-14	23:01:13	56.32	138.778	33.792
141226A	12-26-14	21:07:24	38.65	163.85	28.39
141229A	12-29-14	11:48:59	13.82	71.479	-18.956
141229B	12-29-14	21:52:10	22.02	170.1	23.06
141230A	12-30-14	3:24:22	9.86	56.98	1.59
141230B	12-30-14	20:00:25	28.93	181.47	11.65
141230C	12-30-14	20:54:05	0.22	246.93	-40.18
150101A	01-01-15	6:28:53	0.24	312.603	36.733
150101B	01-01-15	15:23:34	0.08	188.0	-10.956
150103A	01-03-15	20:02:18	49.1	131.666	-48.886
150105A	01-05-15	6:10:00	73.73	124.32	-14.78
150106A	01-06-15	22:05:56	79.88	40.83	0.31

Table 6.1: Information from the IceCube catalog on the Gamma Ray Bursts that took place during the ANITA-3 flight. T90 is in seconds. RA and Dec are in degrees.

are shown in degrees. Altitude is in meters.

6.1.1 GRB direction: elevation angle and azimuth

To determine the relevant direction associated with each GRB, it is necessary to calculate the altitude or elevation angle, and azimuth of each GRB with respect to the ANITA payload. This can be done by utilizing the date, time, RA, and Dec of each GRB, as provided by the catalog, and the longitude, latitude, and altitude of the ANITA payload (the observer) at the time of each GRB. In other words, the elevation angle and azimuth can be calculated for each GRB using a combination of the information presented in Tables 6.1 and 6.2. The elevation angle and azimuth are calculated for each GRB using the Python code shown in Figure 6.2. The calculated elevation angles and azimuths are presented in Table 6.3.

GRB	Catalog UT	Closest recorded UT	Run	Pl. Lon	Pl. Lat	Pl. Alt
141220A	1419055371	1419055371	175	126.3	-82.0	36215.0
141221A	1419149230	1419149230	192	104.5	-80.7	36602.1
141221B	1419197508	1419197508	200	90.6	-80.0	35001.6
141222A	1419232135	1419232135	207	80.4	-80.2	36680.9
141222B	1419266070	1419266070	212	71.1	-80.3	35927.8
141223A	1419313537	1419313537	219	59.5	-79.4	36609.9
141225A	1419548473	1419542007	256	8.1	-78.5	35701.9
141226A	1419628044	1419628044	272	-11.8	-78.4	36456.3
141229A	1419853739	1419853739	308	-62.1	-78.5	36240.1
141229B	1419889930	1419889930	313	-69.3	-78.9	36860.6
141230A	1419909862	1419909862	316	-68.7	-78.5	35935.1
141230B	1419969625	1419969625	324	-82.1	-78.1	36999.1
141230C	1419972845	1419972845	324	-82.3	-78.1	36903.9
150101A	1420093733	1420093733	341	-106.5	-76.1	34812.8
150101B	1420125814	1420125814	345	-114.1	-76.5	36160.5
150103A	1420315338	1420315338	371	-159.3	-74.6	36762.1
150105A	1420438200	1420438200	389	169.9	-74.5	37034.5
150106A	1420581956	1420581956	409	129.7	-72.9	35453.3

Table 6.2: Information that I calculated or found in the data for each GRB during the ANITA-3 flight. Note that the longitude, latitude, and altitude are for the ANITA payload. Longitude and latitude are in degrees. Altitude of ANITA is in meters.

```
def main():
  datetimelist = numpy.zeros((rows, columns))
  datetimelist = [["2014,12,20","6:02:51"],..]
  for i in range(rows):
    stringdate = datetimelist[i][0]
    stringtime = datetimelist[i][1]
    objectdate = date(*map(int, (stringdate.split(","))))
    assert objectdate ==
    datetime.datetime.strptime(stringdate, "%Y,%m,%d").date()
    unixtime = calendar.timegm(objectdate.timetuple())
    timeseconds = sum(int(x) * 60 ** i
    for i,x in enumerate(reversed(stringtime.split(":"))))
    unixtime = unixtime + timeseconds
main()
```

Figure 6.1: Code to calculate unixtime of each GRB from date and time from the catalog. This produced the "Catalog UT" shown in Table 6.2.

GRB	Azimuth (degrees)	Elevation angle (degrees)
141220A	254.48	-34.54
141221A	243.88	-12.34
141221B	316.33	83.06
141222A	245.82	54.49
141222B	41.79	-33.14
141223A	266.01	20.41
141225A	46.19	-26.10
141226A	117.67	-34.25
141229A	216.78	9.78
141229B	172.51	-34.02
141230A	336.03	8.84
141230B	226.89	-19.92
141230C	266.61	40.56
150101A	230.28	-46.49
150101B	328.30	22.67
150103A	233.77	41.27
150105A	120.18	7.33
150106A	194.23	-16.95

Table 6.3: Elevation angle and azimuth of each GRB during the ANITA-3 flight. Note that these angles need to be adjusted to be consistent with the coordinate system of icemc for elevation angle and azimuth. Technique for finding these angles has been verified using the case of mystery event 2.

```
from astropy.coordinates import EarthLocation, SkyCoord, AltAz
from astropy.time import Time
from astropy import units as u
from astropy.coordinates import AltAz
def main():
  grb_list = pd.read_csv
  ('/Users/oindreebanerjee/python/A3_GRB_List_For_Astropy.csv')
  for i in range(0,grb_list.shape[0]):
    Anita_location = EarthLocation(lon = grb_list.loc[: ,
    "ANITA_Longitude_Begin"][i], lat = 90 + grb_list.loc[: ,
    "ANITA_Latitude_Begin"][i], height = grb_list.loc[: ,
    "ANITA_Altitude_Begin"][i] * u.m)
    time_string = grb_list.loc[: , "Date"][i] + " "
    + grb_list.loc[: , "Time"][i]
    grb_time = Time(time_string)
    Anita_frame = AltAz(location = Anita_location,
    obstime = grb_time)
    coord = SkyCoord(grb_list.loc[: , "GRB_RA"][i] * u.degree,
    grb_list.loc[: , "GRB_Dec"][i] * u.degree)
    coordAnita = coord.transform_to(Anita_frame)
main()
```

Figure 6.2: Code to calculate elevation angle and azimuth of each GRB. This produced the angles shown in Table 6.3.

RA	Dec	Pl. Lon	Pl. Lat	Pl. Alt	Date	Time
50.78203	38.65498	126.5	-81.6	35861.0	2014-12-20	8:33:22

Table 6.4: Info on mystery event 2. The longitude, latitude, and altitude reported here are that of the ANITA payload during the event.

Verification of angles

To verify that I am calculating the correct elevation angles and azimuths for the GRBs, I used known information on a special event from ANITA-3, known as the mystery event 2 [4]. The event number for this event is 15717147. The relevant information on mystery event 2 is shown in Table 6.4. Using these as inputs, I calculated the elevation angle and azimuth of the mystery event 2. I got -35.0 degrees for elevation angle and 61.6 degrees for azimuth which match what was found in [4]. The GRB angles shown in Table 6.3 were calculated using the same method so these should be correct as well.

6.1.2 Selecting GRBs for the search

Initially, only the GRBs shown in red font in Table 6.3 were selected for the purpose of performing a binned search for GRB neutrinos. The reason behind this selection is based on the distribution of elevation angles shown in Figure 6.3. A distribution of elevation angles of weighted simulated neutrinos using an isotropic Kotera flux is shown in Figure 6.3. This shows that most simulated neutrinos viewable by ANITA have elevation angles that are within a range of about -15 to about 12 degrees. Therefore, the GRBs with elevation angles of -12.34, 9.78, 8.84, and 7.33 degrees were initially selected for the search.

Mystery-event-like elevation angles

There are several GRBs in the sample shown in Table 6.3 that have elevation angles similar to that of the mystery event observations reported by ANITA in [4, 36]. In general, such a signal that involves a steep elevation angle like that of the mystery events is not expected to be detected via the Askaryan Effect. Both mystery events were observed utilizing their geomagnetic radiation due to associated air showers. Such signals are expected to have a

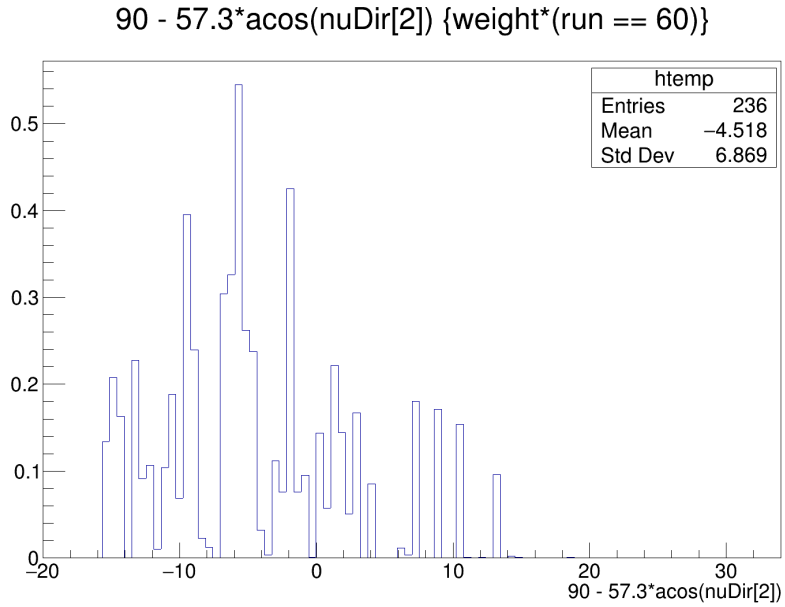

Figure 6.3: Distribution of elevation angles of weighted simulated neutrinos using an isotropic Kotera flux. This distribution shows the allowed range of elevation angles of signals that ANITA can view as simulated by icemc.

strong HPol content and typically regarded as cosmic ray signatures, although in the case of the mystery events, the origin of the events is still under study. To accommodate mystery-event-like elevation angles, the GRBs with steeper elevation angles were also included.

At that point, few GRBs remained with elevation angles above the horizon. These were also included in the search, although the geometry associated with them would be challenging for detection. To summarize, all 18 GRBs were included in the search for UHE neutrinos.

6.2 Sub-threshold search

An important feature of a search involving transient sources such as GRBs is that analysis cuts or thresholds can be reduced as compared to the search for a diffuse flux of neutrinos. When searching for a diffuse flux of neutrinos, one has to search for neutrinos throughout the flight. In a diffuse search, we use 10% of the data to set analysis cuts and search using the remaining 90% data. Most of the data, whether it is the 10% set or the 90%, is noise

or background events. The analysis cuts are set based on this huge amount of background.

In contrast, GRBs take place at specific times, so the search for neutrinos from them can be constrained in time. A spatial direction is also associated with each GRB, therefore, the search can also be constrained in direction. When the search is constrained in time and/or direction, the dataset is dramatically reduced. Thus, the background levels in the search are automatically lowered. This allows us to set lower analysis cuts. In other words, a GRB search is a sub-threshold search. In the case of the binned analysis, the expectation is that a sub-threshold search will translate to lower LD cut values.

6.2.1 Idea behind reduced LD cuts

The idea behind lowering LD cuts for the GRB search as compared to the diffuse search is illustrated in Figure 6.4. Reducing the dataset by constraining the search in direction and/or time pushes the exponentially-falling distribution down as pictured with the down-pointing black arrow. Requiring the same number of background events to pass the LD cut pushes the cut to the left as pictured by the left-pointing black arrow. If the dataset is reduced by a factor F and the slope of the fit (solid red line) in Figure 6.4 is given by $-b$ then the reduced LD cut is given by the relation in Equation 6.1. This relation is obtained by setting the background calculated using the diffuse LD cut, cut_{old}, equal to the background calculated using the GRB LD cut, cut_{new}.

$$cut_{old} - cut_{new} = \frac{1}{b} \ln F \tag{6.1}$$

6.3 Constraining in direction and time

Since GRBs are transient point sources, a search for neutrinos coming from GRBs can be constrained in time and direction. Both the time and direction associated with a GRB are available in the catalog as shown in Table 6.1. Therefore, the data used to conduct the search for a neutrino from a GRB can be narrowed down based on this information.

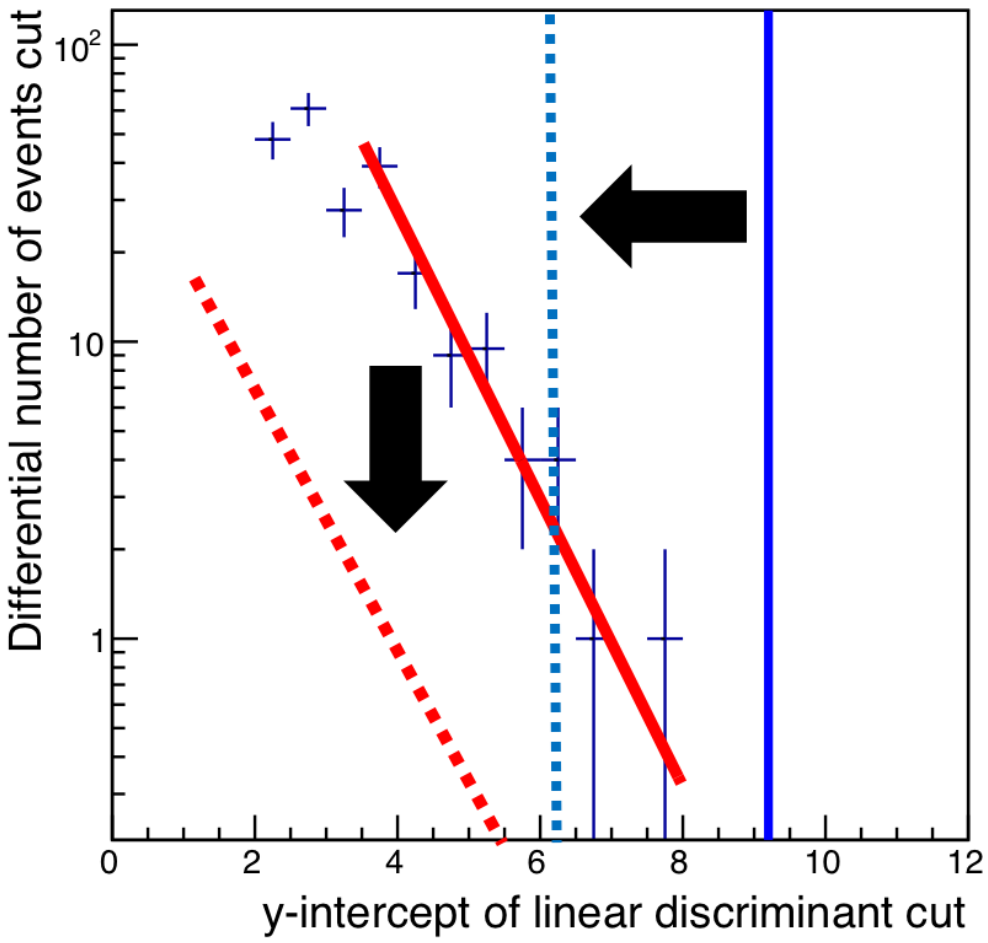

Figure 6.4: Reducing the dataset by constraining in time and direction while allowing the same number of background events to pass the LD cut allows us to lower the cut. The shifts shown with solid black arrows here are not the actual shifts, but illustrations.

6.3.1 Neutrino vs. RF direction

The direction associated with a UHE neutrino and the direction associated with the resulting RF from that neutrino are not the same. Care must be taken to properly account for this difference in the elevation angle and azimuth associated with the GRB itself and the RF signature of neutrinos from that GRB.

The ANITA simulation icemc can be used to calculate the difference between the neutrino direction and the RF direction. In icemc, the neutrino direction, RF direction, and payload position are given by the vectors shown using red arrows in the top part of Figure 6.5. The elevation angle of the RF as seen by the payload can be obtained via evaluation of the dot product of the `n_exit2bn[2]` vector (referred in short as `rf` in Figure 6.5) and the `r_bn` vector. Similarly, the elevation angle of the neutrino as seen by the payload can be obtained by taking the dot product of the `nnu` vector with the `r_bn` vector. The difference in azimuthal angle associated with the RF and the neutrino as seen by the payload can be obtained by first finding the components of `rf` and `nnu` that are perpendicular to `r_bn`, as shown in the bottom part of Figure 6.5, and then taking their dot product.

Figure 6.6 shows a two-dimensional distribution of the difference in elevation angle (theta) and azimuthal angle (phi) as seen by the payload of the neutrino and RF direction. This distribution is made with weighted simulated neutrinos that passed all triggers and were recorded as events in the `passing_events` tree in icemc. Note that icemc was run using the standard diffuse setting here so neutrinos thrown in the Monte Carlo would come from random directions, rather than a set source direction, however, the effect of seeing the RF at a different direction than the corresponding neutrino direction is clearly seen here.

6.3.2 Direction constraint

Figure 6.6 helps to quantify the difference between the neutrino direction and the RF direction. It is a two-dimensional distribution where color represents the number of weighted simulated neutrinos. The difference between the neutrino direction and the RF direction in their azimuthal angle is shown along the horizontal axis. The difference in the elevation

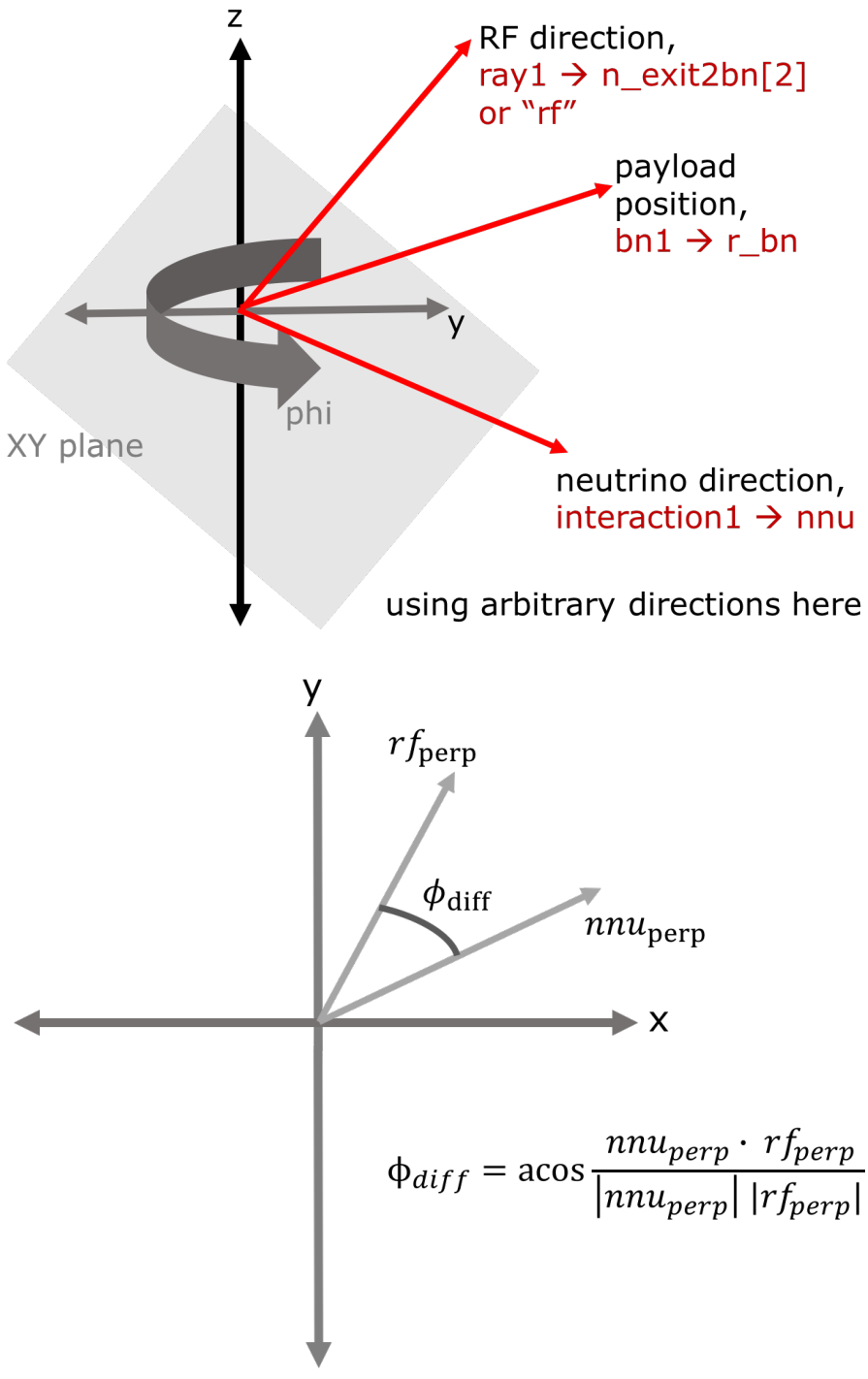

Figure 6.5: Visualization of angles involved in the calculation of the difference in elevation angle and azimuthal angle between neutrino and its associated RF direction.

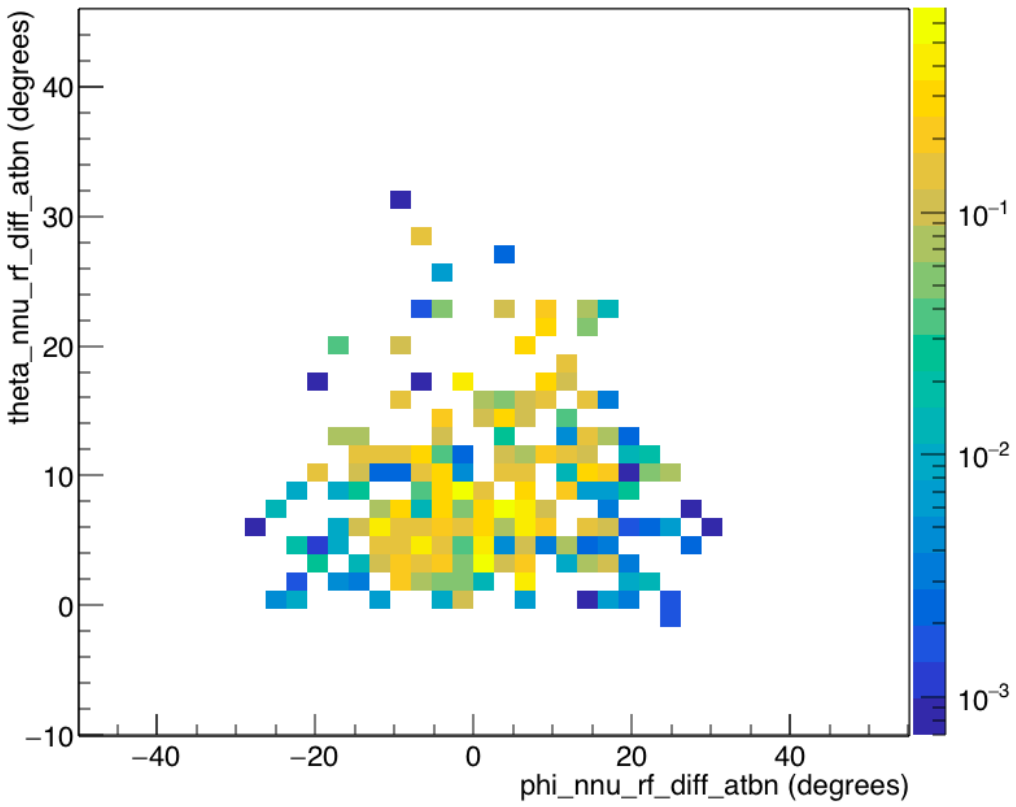

Figure 6.6: Two-dimensional distribution of the difference in elevation angle (theta) in the vertical axis and the difference in azimuthal angle (phi) in the horizontal axis of the neutrino and RF direction. All angles are as seen by the payload.

angle is shown in the vertical axis. The azimuthal angle difference has a spread between about -20 and 20 degrees, while the elevation angle goes from little under 0 degrees to about 30 degrees. Given this distribution, a conservative approach would be to do the search for neutrinos from a GRB in a patch of the sky covering about 1200 square degrees, that is, in a 30 degrees by 40 degrees area. Ideally, however, we would reduce the size of the search area in direction.

As a first pass, for the direction constraint, data events with reconstructed azimuth within five degrees of the azimuth of each GRB were allowed to participate in the search. Meaning, if the azimuth associated with a GRB were to be 50 degrees, then events with reconstructed azimuth in the range of 45 - 55 degrees would be allowed in the search. In a second test, for the direction constraint in azimuth, data events with azimuth within 60 degrees of the azimuth of the GRB were allowed in the search. In both passes, no GRB-specific constraint on elevation angle was imposed on the data. The usual cut of allowing events with elevation angle in the range -6 to -35 degrees was in place.

6.3.3 Afterglows and time constraint

The data allowed to participate in the GRB search should be constrained in time keeping the afterglow emission period of GRBs in mind. UHE neutrinos are expected with higher probability during the afterglow emission of a GRB, as opposed to the prompt emission. GRBs are highly versatile, and both the prompt and afterglow periods can vary greatly from one GRB to another. The afterglow period, in particular, can be anywhere from a few minutes to days or even months.

All GRB neutrino searches in the past have been constrained in time to no more than 10 minutes. In this search, during the first test with five degree azimuth windows, the time was constrained to seven hours. When the azimuth window was widened to 60 degrees, the time was constrained to 45 minutes. This was to ensure that the number of events participating in the search in both cases is about the same so as to get similar reduced analysis thresholds. So if the direction window is widened the time window has to be shortened. Since there is a physics motivation (afterglows) to pursue searches in longer time windows, improving the

constraint in direction is a suitable goal.

6.4 Blinding

The search developed in this chapter is meant to be a blind analysis. Blinding means that all analysis cuts are determined using a subset of the data or a "burn" sample that is not included in the actual search. In other words, there is a "background region" and a "signal region" of data. The background region is used for characterization of the background and determination of analysis cuts. The signal region is used to perform the actual search for a signal. In the diffuse search, a 10% dataset is chosen as the background region and the remaining 90% dataset is the signal region. Possible signal present in the signal region is not allowed to bias the analysis cuts and therefore, the search is blind.

Blinding in the GRB search is similarly motivated as in the diffuse search, however, it is implemented differently. The GRB search, too, has a background region and a signal region. These are defined below.

6.4.1 Background region

Events from the 100% ANITA-3 dataset that were recorded in the chosen time window **before** the start of each GRB and having a reconstructed azimuth in the chosen azimuth window around the GRB are considered to be in the background region of each GRB. All of these events for all 18 GRBs taken together is the total background region of the search. Note that for a GRB search, we can use the 100% dataset instead of only 10% as in the diffuse search. Moreover, the background region is constrained in time and direction, also in contrast to the diffuse search.

6.4.2 Signal region

Events from the 100% ANITA-3 dataset that were recorded in the chosen time window **after** the start of each GRB and having reconstructed azimuth in the chosen azimuth window around the azimuth of the GRB are considered to be in the signal region of each GRB.

All of these events for all 18 GRBs taken together is the total signal region of the search. Again, note that the signal region of a GRB search is constrained in time and direction, automatically reducing the number of background events that would need to get cut by the analysis.

6.5 Binned analysis

A search for GRB neutrinos was developed using the ANITA-3 data following a variation of the binned analysis methods discussed in Chapters 3 and 4. In the binned analysis, the intended final cut is the LD cut. This cut is determined based on the distribution of y-intercepts of events in each geographical bin. Each distribution is fitted to an exponential function. The LD cut is optimized to produce the best limit on the chosen model of neutrino production. Details on the optimization process can be found in [18, 20, 21].

The search for GRB neutrinos in the ANITA-3 data was performed after the completion of the search for a diffuse flux of neutrinos in the ANITA-3 data. Therefore, the fundamental methods of the binned analysis were already developed to conduct a search. Adapting these methods to a GRB neutrino search involved certain modifications which we discuss in this section along with other details of the analysis.

6.5.1 Combining bins

Due to the time and direction constraints on the data participating in the GRB search, the overall dataset is greatly reduced. There are only 6860 events in the background region of the GRB search compared to 82762 events in the background region of the diffuse search, just before final cuts. Having fewer events in the background or signal region makes it challenging to have enough events in each bin to perform the binned analysis. Therefore, in the GRB search, certain bins were combined as necessary.

Bins were combined only in the VPol channel of the analysis. Bins with similar LD cuts in the diffuse search were combined as shown in Table 6.5.

Bin number	Diffuse LD cut	Combined bin number
2991	8.7	
2997	9.3	
2936	9.3	3010
3016	9.4	
3010	9.4	
2989	9.9	
3030	9.9	
3011	9.9	3013
3013	10	
2990	10	
3018	10.1	
2988	10.1	
2937	10.2	3018
2938	10.3	
3008	10.4	
2901	10.8	
3015	10.9	
3029	10.9	
3014	11.0	3015
2971	11.1	
3007	11.2	
2977	11.2	
2973	11.5	
3004	11.7	
2970	12.0	
2939	12.1	
2998	12.2	3012
3037	12.3	
3012	12.5	
2979	13.1	
3019	13.5	
2935	14.3	
3003	14.4	3017
3017	14.6	

Table 6.5: Bins that were combined in the VPol channel. The number in the third column is the name given to the combined bin for that group. In practice, the events from each group of bins were treated as all belonging to the bin in the third column in order to combine the bins for the analysis.

6.5.2 Distributions from the background region

Events from the background region are processed through the different stages of the binned analysis. Before final cuts, distributions of y-intercepts of events are made for each bin. In the case of the VPol analysis, bins are combined as shown in Table 6.5 and distributions are made for the resulting combined bins. In the case of the HPol analysis, bins are not combined and standard bins are used. These distributions are fitted to an exponential function. An optimized LD cut is chosen on the tail of each distribution and the background for that bin is estimated by integrating from the LD cut value to infinity.

At the stage of fitting the data in each bin to an exponential, some bins are lost. Bins that have less than five histogram bins with data or less than five events in the fit are not allowed to participate further in the analysis. Bins where the data cannot be fitted to an exponential or have a p-value less than 0.05 are lost as well. Distributions of data from the background region in the bins kept in the HPol and VPol channels and associated exponential fits are shown in Figures 6.7 and 6.8.

6.5.3 Background estimates

The number of background events estimated to pass the optimized LD cut in each bin is calculated by integrating the tail of the exponential fit in that bin from the LD cut value to infinity. The bin number, total events in the bin prior to the LD cut, p-value of the exponential fit, estimated background along with errors are shown for the HPol and VPol channel analyses in Table 6.6.

In the first pass, in the HPol channel, three singlet bins were used. In the VPol channel, three combined bins as well as one singlet bin was used. The singlet bin used in VPol was not kept in the diffuse search due to having a p-value less than 0.05 in the diffuse search. In the second pass, in the HPol channel, three singlet bins were used. In the VPol channel, three combined bins and three singlet bins were used. Two of the singlet bins from this test were not kept in the diffuse search, again, due to p-value being less than 0.05 in that search.

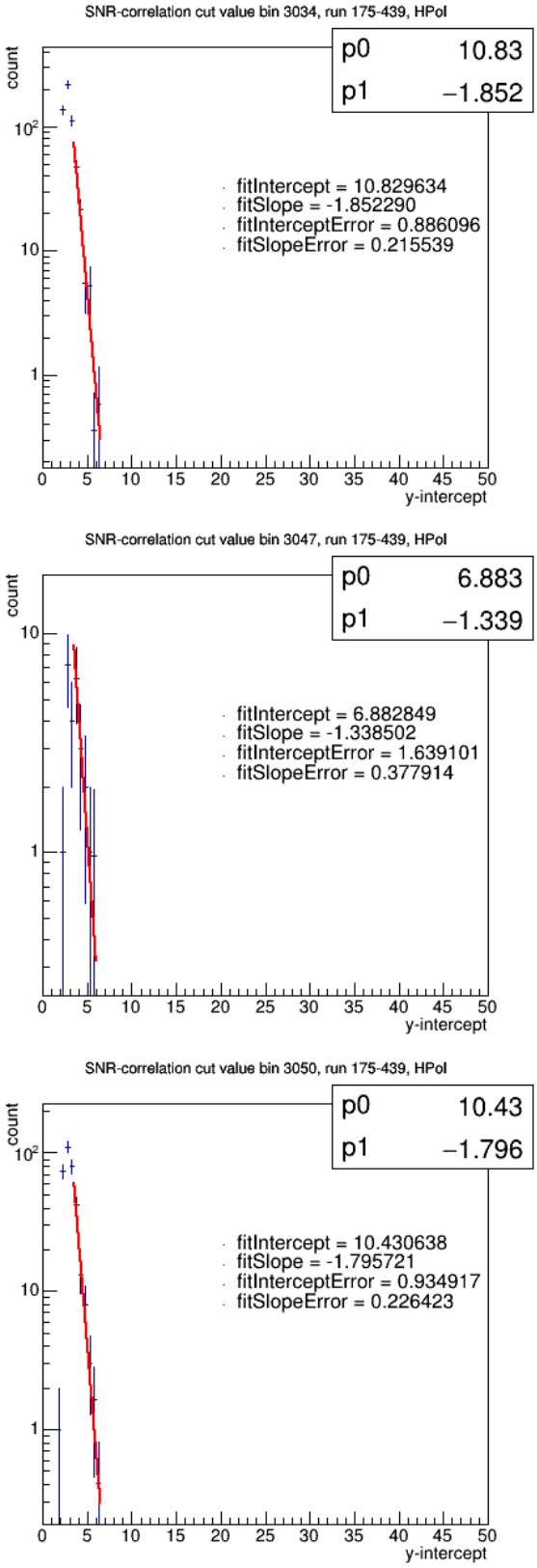

Figure 6.7: Distributions from the background region in bins kept in the HPol analysis.

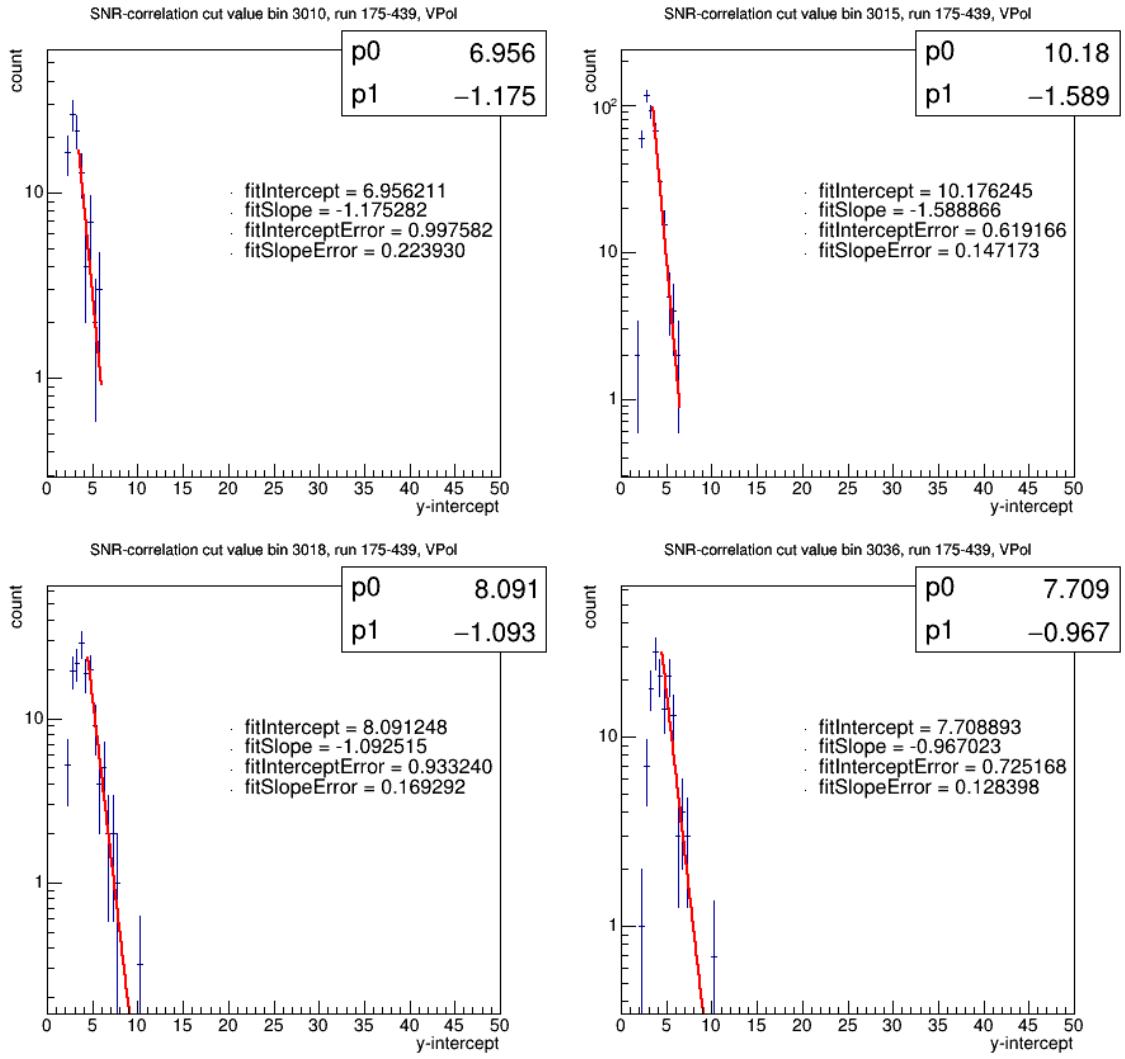

Figure 6.8: Distributions from the background region in bins kept in the VPol analysis.

Bin	Pol	Total events	LD cut	p-value	Bg est	Bg Hi	Bg Lo	Diffuse LD cut
3034	H	548.1	6.9	0.7	0.30	0.46	0.22	9.1
3047	H	25.4	6.7	0.9	0.33	0.71	0.22	9.6
3050	H	333.0	6.8	0.9	0.36	0.57	0.27	13.7
3010	V	93.4	8.5	0.4	0.15	0.31	0.09	8.7 - 9.4
3015	V	393.5	8.1	0.9	0.17	0.25	0.13	10.8 - 11.2
3018	V	137.2	9.6	0.9	0.32	0.54	0.23	10.1 - 10.4
3036	V	133.8	11.7	0.1	0.11	0.19	0.07	Bad p-value
3034	H	149.6	8.8	0.9	0.48	0.86	0.35	9.1
3035	H	49.1	6.8	0.5	0.82	1.53	0.57	10.0
3050	H	122.9	8.5	0.8	0.20	0.33	0.14	13.7
3010	V	119.1	7.2	0.7	0.23	0.43	0.15	8.7 - 9.4
3015	V	625.9	9.3	0.7	0.41	0.58	0.33	10.8 - 11.2
3018	V	53.7	9.1	0.6	0.37	0.77	0.25	10.1 - 10.4
3021	V	144.8	13.1	0.65	0.69	1.00	0.52	26.24
3028	V	114.8	7.5	0.9	0.22	0.47	0.14	Bad p-value
3036	V	111.9	7.8	0.9	0.44	0.77	0.30	Bad p-value

Table 6.6: Information on the GRB analysis in the HPol and VPol channels from two passes: top using smaller azimuth window and larger time window, bottom using larger azimuth window and smaller time window in the search. Bin numbers along with number of events in the bin, optimized LD cut, p-value of the exponential fit, background estimate along with errors, are shown. The right most column shows the LD cut for the bin in the diffuse search for comparison with the LD cut in the GRB search. Note that bins 3010, 3015, and 3018 were obtained by combining multiple bins.

Note that the second pass was optimized using 100 pseudo-experiments to calculate the background estimates whereas the first pass was optimized using 5000. The background estimates are expected to be less accurate when fewer pseudo-experiments are performed. For the final optimization, it is recommended to use 5000 pseudo-experiments to calculate background estimates as was done for the diffuse search.

6.5.4 LD cuts

Table 6.6 shows the LD cuts for the different bins kept in the GRB search. The right most column of the table shows the LD cut value that was calculated for the bin or bins (in case of combining) in the diffuse search. This can be compared to the third column and seen that the LD cut calculated in the GRB search is always lower than the LD cut for the bin

in the diffuse search. In case of the combined bins, the LD cut is always lower than the lowest LD cut associated with the bins used in combining.

It would be pertinent to check whether the LD cuts have been lowered in the GRB search by the amount predicted by Equation 6.1, however, a few things must be kept in mind. It would only make sense to compare the LD cuts for the GRB vs. diffuse search for bins with similar distributions and exponential fits in both the GRB and diffuse search. In cases where bins had to be combined to conduct the GRB search this cannot be the case. Specifically, bins 3010, 3015, and 3018 are combined bins in the GRB search, taking data from multiple bins, so these combined bins cannot be compared to the singlet bins 3010, 3015, and 3018 in the diffuse search. Moreover, LD cuts should only be compared when the corresponding background estimate for the bin in both the GRB and diffuse search is the same.

I checked for the case of bin 3034 in the HPol channel and found that the difference in LD cuts according to Equation 6.1 should be 4.7. This is using F of 2700 and b of 1.7. The b for the distribution for this bin in the GRB search is 1.8 and that in the diffuse search is 1.6, so I used 1.7. The 2700 comes from taking the ratio of the time for the whole flight over the time when signal is present ((22 days x 24 hours) / 7 hours) multiplied by the ratio of total azimuth over the chosen azimuth window (360 degrees / 10 degrees). The actual difference in the LD cuts, however, is 2.2. It must be noted that the background estimates were not the same for this bin in the GRB vs. diffuse search, which is a requirement for Equation 6.1 to be true. In the diffuse search, the background estimate was 0.36 with a high error of 0.60 and a low error of 0.24. In the GRB search, the background estimate was 0.30 with a high error of 0.46 and a low error of 0.22. For the final calculation, I would recommend checking that the backgrounds presented in Table 6.6 are not overestimated due to accounting for unnecessary systematic uncertainties.

6.6 Simulating neutrinos from a source direction

In addition to applying analysis cuts to the data, all cuts are also applied to simulated neutrinos. This is done in order to determine the efficiency of the analysis and to set a limit on the chosen model of neutrino production, in the absence of a discovery. In order to perform an analysis to search for neutrinos from specific sources, rather than from all directions, it is necessary to have the capability to simulate neutrinos from those sources. Although ANITA has had the capability to simulate a diffuse flux of UHE neutrinos, there was not yet a method in place to simulate neutrinos from specified sources.

6.6.1 Overview of icemc

The ANITA simulation package is known as icemc. This is maintained on GitHub at this link: https://github.com/anitaNeutrino/icemc. It mainly consists of several classes, such as, the `Primaries`, `balloon`, `ray`, and `icemodel` classes and a main executable code called `icemc`. The executable code `icemc` contains a Monte Carlo algorithm. Inside `icemc`, all the classes are instantiated and associated functions are called. Settings such as the number of neutrinos to throw in the Monte Carlo, the energy of neutrinos, which ANITA flight, can be initialized using an inputs file, for example, the `inputs.anita3.conf` file associated with the ANITA-3 simulation.

Inside `icemc`, there is a for loop over `NNU`, the number of neutrinos specified in the inputs file. Cuts are applied at different stages to the neutrinos that don't meet the criteria to be observable by ANITA. Cuts are implemented with the command `continue`, that is, the code skips to the next neutrino in the loop when there is a cut. The first set of `continues` are shown in Figure 6.9.

The main functions that are called in the loop and their purpose are briefly described below.

PickBalloonPosition

This is a function in the `balloon` class. It picks the balloon position and at the same time sets the masks and thresholds.

PickDownwardInteractionPoint

This is a function in the `balloon` class. It sets the interaction point in the ice.

GetSurfaceNormal

This is a function in the `ray` class. It finds the normal to the surface taking into account the tilt from the differential heights between neighboring bins.

GetRFExit

This is a function in the `ray` class. At this stage, Snell's law is used to get the first guess at the direction of the RF as it leaves ice surface. The starting guess was to use the direction that is simply radially outward from interaction position. This now takes into account the balloon position and the surface normal.

GetDirection

This is a function written in `icemc.cc`. It picks a neutrino direction such that its Cerenkov cone is close enough to the balloon line of sight that we have a "chance in hell" of seeing the signal.

GetViewAngle

This is a function written in `icemc.cc`. It finds the angle between the ray and the neutrino direction.

WhereDoesItEnter

This is a function in the `earthmodel` class. It finds the neutrino entry point.

Getchord

This is a function in the `earthmodel` class. It finds the length of the chord through the earth that the neutrino would have had to travel.

IsAbsorbed

This is a function in `icemc.cc`. It takes the best case scenario chord length and finds the corresponding weight of the neutrino.

GetVmMHz

This is a function in the `signal` class. It finds the magnitude of the signal.

TaperVmMHz

This is a function in the `signal` class. It applies the angular dependence of the signal. The difference between the "viewangle" and the Cerenkov angle is multiplied by the signal to account for the fast fall-off from being on-cone.

6.6.2 Source mode

A source mode was developed in icemc for the purpose of running it for neutrinos coming from a specified source. A setting was added to the `Settings` class to make a source mode which when turned on in the `inputs` file, switches icemc to the source mode. In the source mode, the neutrino direction, `nnu`, is set using an addition to the function `GetDirection`. Additionally, a new function called `PickGrbDirection` has been added to the `Primaries` class.

Tests of the source mode are shown in Figure 6.10. The top two plots are made with the source setting on, that is, by setting the neutrino direction to a specific vector: (-1,0,0) on the left and (1,0,0) on the right. There is no time constraint in the top plots. The bottom plot is made by imposing a time constraint of 6 hours in addition to setting `nnu` to (1,0,0).

```
if (interaction1->noway)
  continue;
count1->noway[whichray]++;

if (interaction1->wheredoesitleave_err)
  continue;
count1->wheredoesitleave_err[whichray]++;

if (interaction1->neverseesice)
  continue;
count1->neverseesice[whichray]++;

if (interaction1->wheredoesitenterice_err)
  continue;
count1->wheredoesitenterice_err[whichray]++

if (interaction1->toohigh)
  continue;
count1->toohigh[whichray]++;

if (interaction1->toolow)
  continue;
count1->toolow[whichray]++;

if (bn1->WHICHPATH==3)
  interaction1=int_banana;

if (!interaction1->iceinteraction)
  continue;
count1->iceinteraction[whichray]++;

if (beyondhorizon) {
  continue;
}
```

Figure 6.9: The first set of cuts on neutrinos thrown in the Monte Carlo.

An outline of Antarctica is shown in these plots in blue and the ANITA-3 flight path in red. The black dots are simulated neutrinos that passed the trigger.

The positions of the black dots shown in Figure 6.10 are consistent with the neutrinos coming from a source on the left (top left plot) and from the right (top right plot), however, it is apparent that no neutrino passed on the right side of the continent in the top left plot. Upon investigating the cause of nothing passing on the right side, it was found that `count1->nchanceinhell2` was an order of magnitude smaller on the right side than on the left side of the continent. Therefore, the cut just before `count1->nchanceinhell2` is counted was investigated and it was verified that the quantity, "chance", in short, being checked against the threshold in this cut was also smaller on the right side. The distributions for "chance" on the right and left side are shown by the top plots of Figure 6.11. The quantity `Tools::dMax(vmmhz,Anita::NFREQ)` within "chance" is the one responsible for "chance" being smaller, as verified from its distributions. The term "chance" here is used to denote in short the following expression in `icemc`.

"chance" = `settings1->CHANCEINHELL_FACTOR*Tools::dMax(vmmhz,Anita::NFREQ)*heff_max*0.5*(anita1->bwmin/1.E6)`

The earliest place in the code where the distribution for `Tools::dMax(vmmhz,Anita::NFREQ)` is different for right versus left was investigated. It was found that it was different before and after the function `TaperVmMHz`, which has several inputs, including `viewangle`. It was found that the variable `viewangle` was different for the left versus right side as shown by the bottom distributions of Figure 6.11. This variable is set in a function in `icemc.cc` called `GetViewAngle`. This function takes `nnu` as an input, and was examined for any possible errors. No error was found, however, it was noted that the quantity `viewangle` was being calculated by taking the dot product of two vectors, `nnu` and `nrf2_iceside` and then finding the acosine, resulting in the angle returned being indistinguishable from its negative.

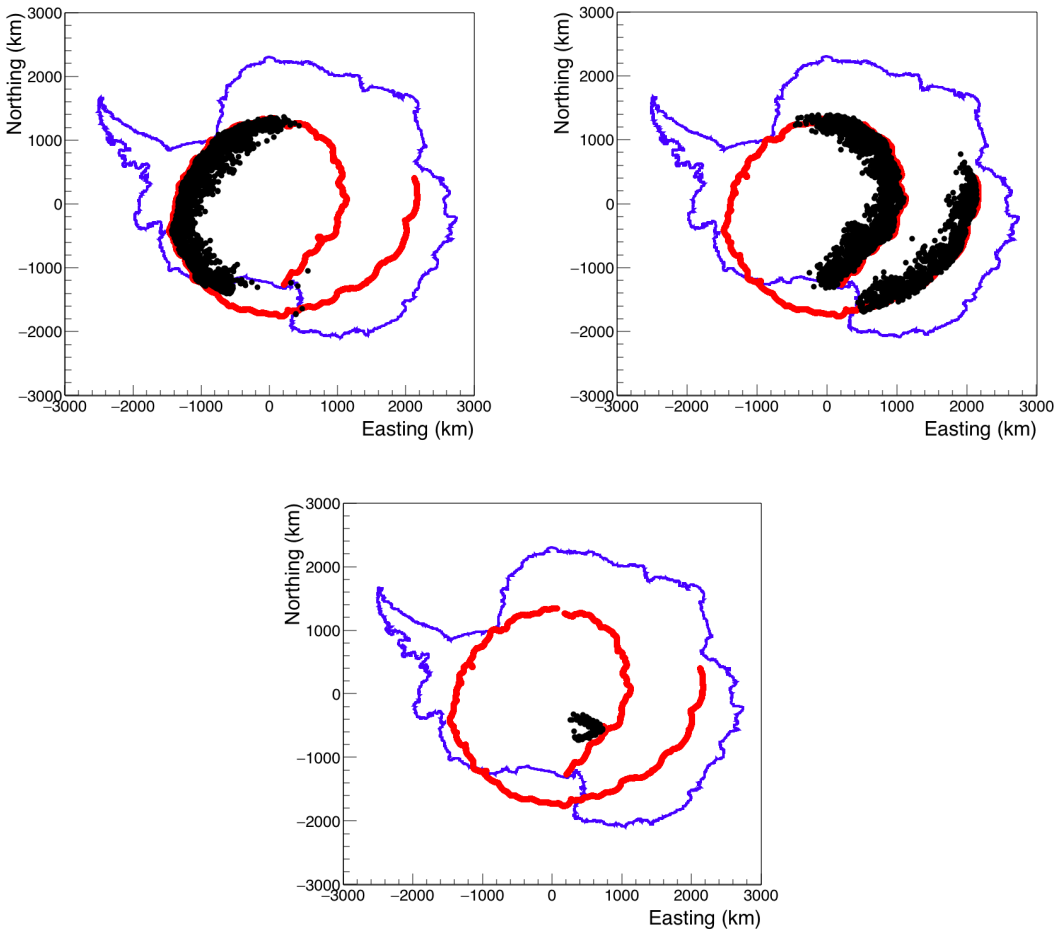

Figure 6.10: Tests of the source setting in icemc. The figure on the top left shows simulated neutrinos using neutrino direction vector (-1,0,0) and top right using neutrino direction vector (1,0,0). The figure on the bottom shows simulated neutrinos with an additional constraint on time. The bottom figure is for a source emitting neutrinos for 6 hours.

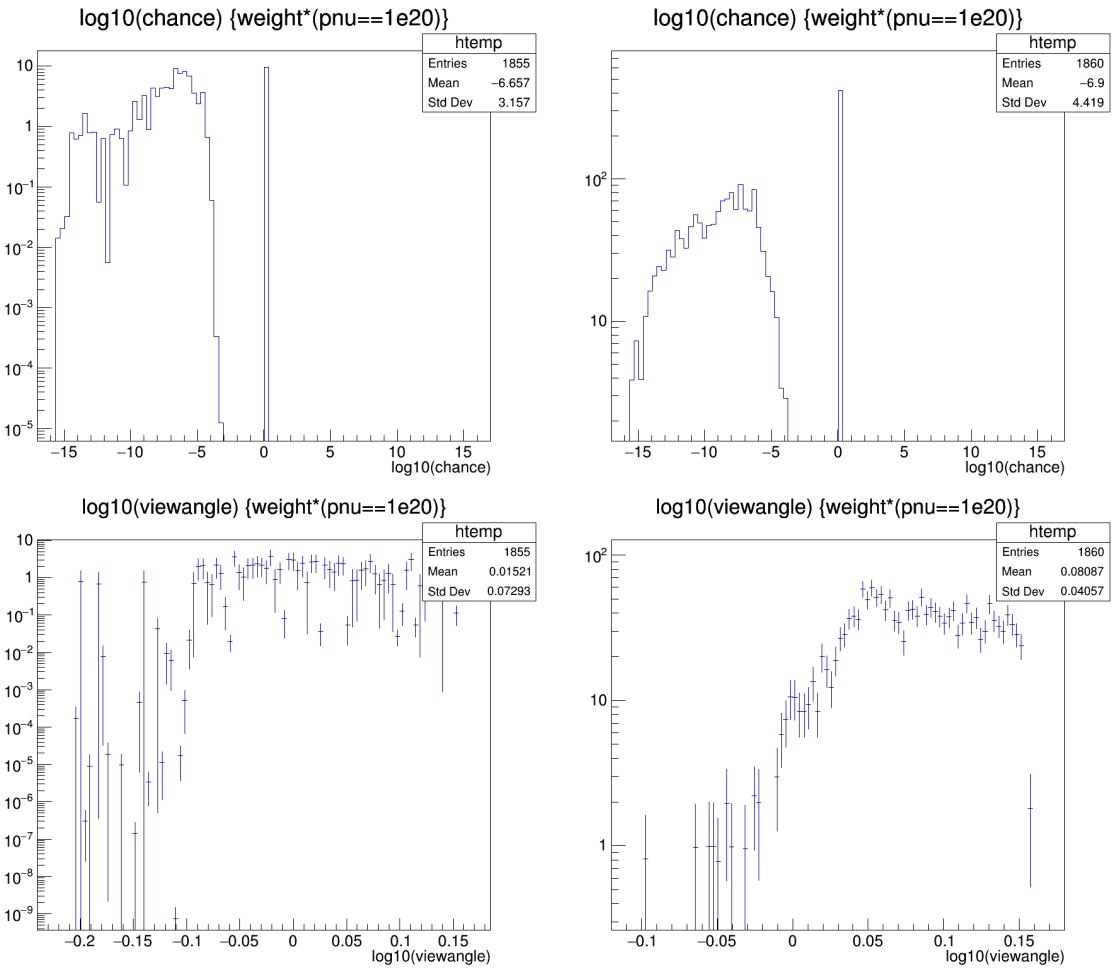

Figure 6.11: Distributions showing differences in the values of quantities calculated for simulated neutrinos on the left (left) and right (right) side of the continent.

Chapter 7

Mysteries and concluding remarks

7.1 Extensive Air Showers

Although built primarily for the detection of UHE neutrinos, ANITA is able to observe radio waves from EAS or CR interactions in the air in a sideband channel. Neutrino candidates in ANITA are expected to be primarily VPol, while CR candidates are primarily HPol. Interaction of the charged particles in the air with the local vertically upward-pointing geomagnetic field renders the radio signal from CR candidates its HPol signature. This is a fortunate difference between radio signal from neutrinos and that from cosmic rays.

Although ANITA has not yet discovered UHE neutrinos, it has measured signal from several CR candidates. There were 16 CR candidates in the ANITA-1 flight, a few in the ANITA-2 flight and about 20 in the ANITA-3 flight. Fewer CR candidates were measured in the ANITA-2 flight as the hardware was designed to not trigger on HPol events in this flight.

There are two ways in which ANITA can measure the radio signature of EAS. These are 1) direct and 2) reflected as shown in a cartoon in Figure 7.1. Radio waves due to CR initiated particle showers in the air interacting with the local geomagnetic field can either reach the ANITA payload directly as shown with a red line in the cartoon on the left side. Or, radio waves from the particle shower interaction with the geomagnetic field can reach the payload by reflection off of the ice as shown with two red lines in the cartoon on the

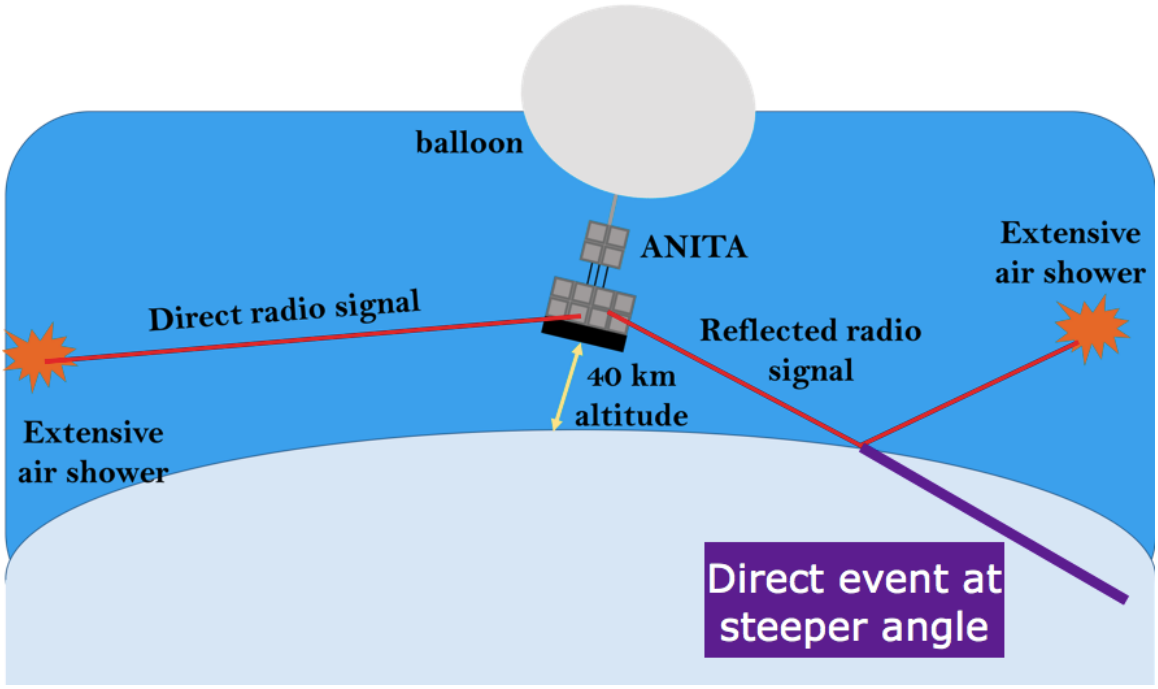

Figure 7.1: Cartoon explaining how ANITA observes extensive air showers. Red lines denote the paths of radio waves from extensive air showers interacting with the geomagnetic field reaching the ANITA payload. The purple line indicates the implicated trajectory of the mystery events.

right side.

7.1.1 Unusual upgoing events

We have reported on the observation of two unusual, upgoing events [4, 36]. They are referred to as mystery event 1 and 2, respectively. They were both EAS candidates. Mystery event 1 is from the ANITA-1 flight and mystery event 2 is from the ANITA-3 flight. They were both found to be HPol events and CR-like.

Whether ANITA observed an event directly or by reflection can be determined from the polarity of the event waveform. Typically, ANITA measures CR events as reflected events whose polarity is opposite to that of directly observed events. The two mystery events had polarity consistent with that of being directly observed events. The polarity of mystery event 2 can be seen in Figure 7.2. Here the field strength in mV per meter is in the vertical

axis and time is in the horizontal axis. A dip or trough in the waveform can be seen. This trough would be a peak for an event of opposite polarity.

It can be seen from Figure 7.1 that directly observed EAS events in ANITA have shallower elevation angles than those observed by reflection off of the ice. Directly observed CR events are relatively rare and usually observed at shallow angles of a few degrees below the horizontal. Both mystery events 1 and 2 have steeper elevation angles of -27.4° and -35°, respectively. These elevation angles are typical of reflected events, not direct. This is shown with a purple line on the right side of the cartoon in Figure 7.1.

To summarize, the mystery events had polarity consistent with being direct events but elevation angles similar to that of reflected events. The unusualness of the two mystery events lie in the incompatibility between their observed polarity and the elevation angle at which they were seen. We elaborate further by summarizing the publication on mystery event 1 in Section 7.1.2.

7.1.2 Detailed summary of Mystery Event 1

I summarize here the publication on Mystery Event 1 [36]. In this publication, we reported on four CR or CR-like events observed with ANITA. From ANITAs first flight in 2007, 16 ultra-high-energy cosmic ray (UHECR) air showers were reported, 13 of which were consistent with geomagnetically-induced radio pulses seen in reflection off the Antarctic ice surface. Three of these 16 events in the signal box (expected background was 1.6 events) from the initial blind analysis were deemed background: two of unknown origin and one a likely thermal noise fluctuation with no apparent signal content. Three additional CRs were also found in cross-correlation analysis after unblinding including two events that were identified as Earth-skimming CRs, a previously unobserved class of events. The Earth-skimming events were directly observed and thus had opposite polarity as the reflected events. In addition to these two Earth-skimming events observed in ANITA-1, another event of the same type was observed in ANITA-2.

On reviewing the events in the signal box of ANITA-1, it was found that one of the events, previously deemed background, was dominated by HPol content and consistent

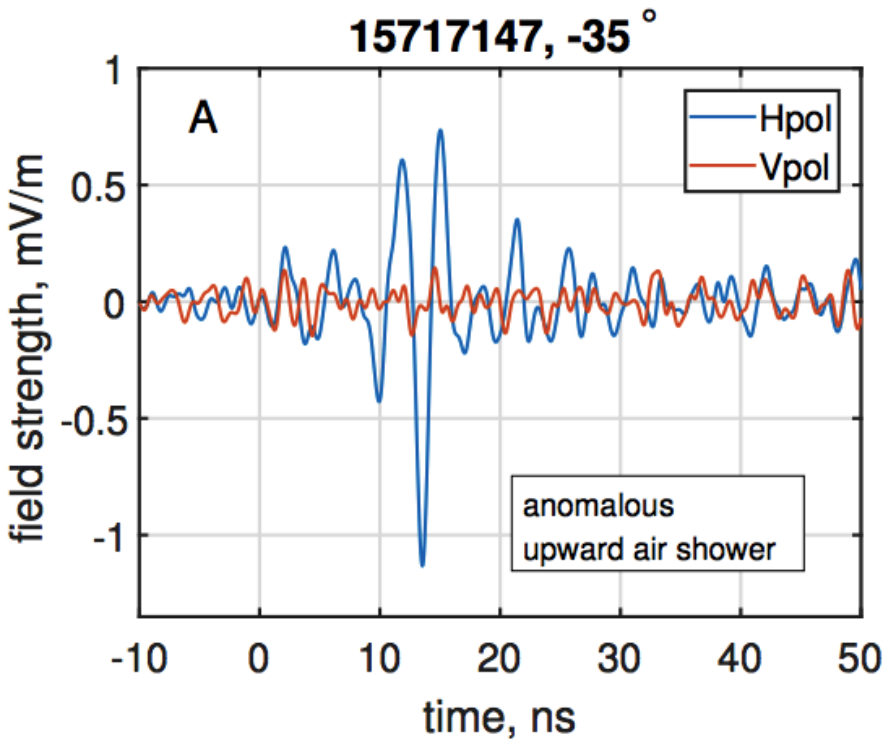

Figure 7.2: Figure from ANITA publication on mystery event 2 [4]. This shows the polarity of mystery event 2. The trough seen in the waveform would be a peak for a reflected event.

with geomagnetic parameters of a CR. It arrived at the payload from a direction of 27.4° below the horizontal, a fairly typical angle for a reflected CR event. Interestingly, however, it did not correlate well with a reflected CR signal shape. A re-evaluation of this event led to the finding that the polarity of this event is consistent with an air shower seen directly, without reflection. Naturally, then, this event was compared to the other class of CRs, the Earth-skimming events. But the three Earth-skimming CR events showed in [36] have much shallower angles associated with them, namely, 4.3, 3.3 and 3.0 degrees below horizontal. So, the steep angle of 27.4° below horizontal of this CR-like event poses interesting problems for interpretation.

The publication [36] investigates these four unusual upward-directed events seen by ANITA with the goal of explaining what relation, if any, these may have with tau lepton initiated air showers. In case any of these events are associated with tau leptons, then an exciting interpretation would be that the tau lepton originated from the charged current interaction of a UHE tau neutrino in the ice or, more likely, in the rock below the ice, and then survived long enough to produce a directly (as opposed to reflected) observed air shower.

A radio signal detected by ANITA can have a mix of polarization states, that is, it can be part unpolarized, part linearly polarized and part circularly polarized. Stokes parameters I, Q, U and V can be estimated for signals to figure out the different polarization components of a signal. The I parameter is for unpolarized, Q is for linearly polarized (+Q for Hpol and Q for Vpol), U is for linearly polarized along 45 degrees (+U for positive slope, -U for negative slope) and V is for circularly polarized (+V for left circularly polarized and V for right circularly polarized).

In case of CRs, at least a few percent of circular polarization may be expected in the signal due to possible interference between the primary geomagnetic radiation and secondary Cherenkov radiation. Upon estimating the Stokes parameters for the four events in [36], it was found that in addition to linear polarization, the two stronger Earth-skimming events have circular polarization components. The CR-like mystery event, too, has both linear and circular polarization (10%) components. The presence of circular polarization, the

good correlation with the other three upward-directed CR events and with the inverted reflected CR events, excess of noise in trailing part of the signal similar to reflected CRs, all support that the CR-like mystery event originates primarily from geomagnetically-induced radiation.

The two competing hypotheses about the CR-like mystery event are as follows: it could be a reflected CR event whose polarity got distorted by some unknown process OR it could be a direct air shower event caused by interactions or decay of a secondary lepton from a neutrino interaction in the Earth. The most probable candidate for a secondary lepton in the latter hypothesis is a tau lepton. After accounting for uncertainties, the minimum possible emergence angle for the hypothesized tau event is 25.4 degrees below horizontal which corresponds to an Earth chord distance of 5460 km. This chord distance is about 17,000 km water equivalent which is far greater than the Standard Model (SM) predicted neutrino interaction length of about 2000 km water equivalent. A neutrino with energy of order EeV or more with Standard Model cross section would not make it far enough through this Earth chord to produce a tau lepton late enough for the tau to then survive long enough to produce an air shower.

Since the energies of the events are known to be of order EeV or more from the observed radio pulses, the only other parameter that can be tweaked to consider the tau hypothesis is the cross section. It is found that for SM cross sections of the neutrino, more events closer to the horizon should have been seen. When the cross section is suppressed, however, ANITAs acceptance (prediction for the number of neutrinos expected to be seen by ANITA, call it apples) for such events agree with current limits (call it oranges) with the caveat that the limits are all derived using SM cross sections (cannot compare apples to oranges). However, it is interesting to see that suppressing the cross section by a factor of about 3-5, as initially estimated in [36], does make the CR-like mystery event present itself reasonably as a tau neutrino candidate.

7.2 Investigating the mystery events

Mystery event 2 was found at the same time as when we were completing a search for a diffuse flux of UHE neutrinos in data from the third flight of ANITA. Event 15717147 or mystery event 2 was cut in the binned analysis by the elevation angle cut. If forced to pass this cut, it was still removed by the CPol peak strength cut.

To look at where mystery event 2 reconstructed on the continent compared to other events from the ANITA-3 flight, I made the plot shown in Figure 7.3. Here most points are blue and denote the reconstructed location of events from the ANITA-3 flight that have passed all but a final set of cuts. The satellite stripe cut has also been applied to these events.

The solid red dots in Figure 7.3 denote the locations to which mystery event 1 and 2 were reconstructed on the continent. Note that we show mystery event 1 here although this event is from the ANITA-1 flight. A solid red cross is also shown near each red dot. These denote the location of the ANITA payload at the time of recording the corresponding mystery event. It can be seen that for both mystery events, the ANITA payload is located **above** the red dot, that is, above the reconstructed location of the mystery event. It could have been that one red dot was below the corresponding red cross, and the other red dot above the corresponding red cross. But that does not happen. From this, it is conceivable that there is a "source" in the direction towards the bottom of this plot that ANITA is "facing" during the time of recording both mystery event 1 and 2.

7.2.1 Satellite influence

A possible source that ANITA could be facing during the time of recording the mystery events is a satellite or group of satellites. It should be noted that the latitude of the ANITA payload is about -82° both during mystery event 1 and mystery event 2. Therefore, during both mystery events, ANITA was able to view the **same** satellites because which satellites come into view depend on the latitude of the observer. The two mystery events were plotted using red dots overlaid on the satellite stripe plot as shown in Figure 7.4. They are labeled

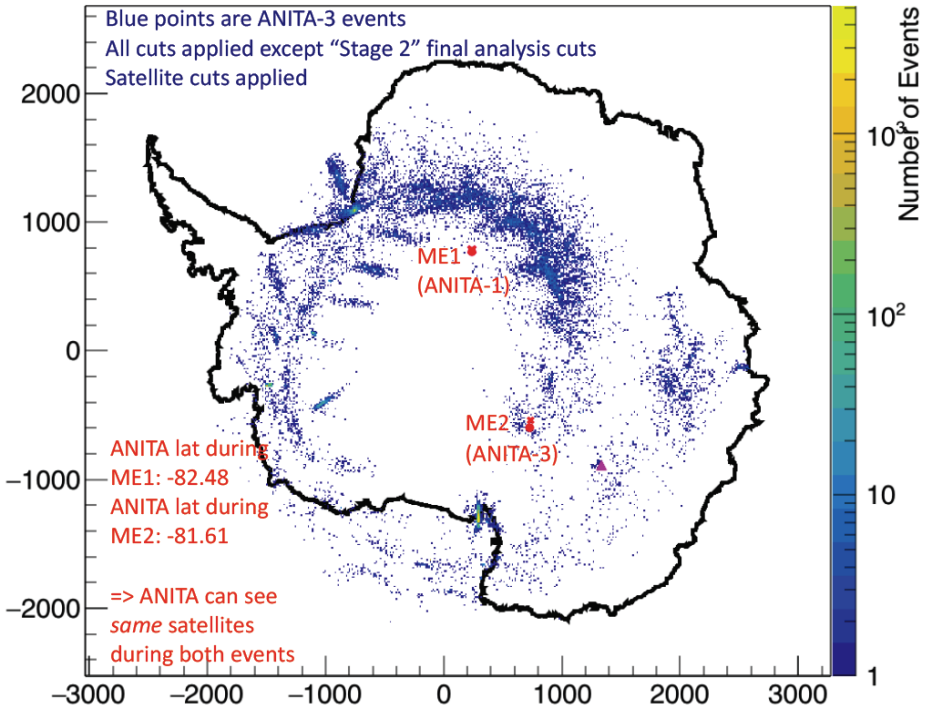

Figure 7.3: Map showing events (blue points) from the ANITA-3 flight before final cuts. Overlaid are positions of the mystery events 1 and 2, labeled here as ME1 and ME2. Note that the latitude of the ANITA payload during both mystery events is about −82°. The same satellites are viewable by the ANITA payload during both events.

in white as "ME1" and "ME2". In black dots are shown the events that passed all but a clustering cut in the binned analysis of the ANITA-2 flight.

Both mystery events can be seen to lie on the same central stripe in the satellite stripe plot in Figure 7.4. Although in this figure the central stripe shows up as faded in the middle, this is not a plot that shows the stripes as a function of time. At the time of recording mystery event 1, ANITA was at the same latitude as during recording mystery event 2 and was able to see the same satellite or group of satellites that is represented by the central stripe. Both mystery events lying on the same satellite stripe is consistent with ANITA viewing the same satellite or group of satellites during both.

So were the mystery events somehow caused by satellites? We are not yet sure about this. As is evident from [4, 36], both mystery events were impulsive in nature. Such a signature is not expected to come from satellites. Satellites have been known to cause

modulated CW noise, not impulsive events.

In addition to being impulsive, the mystery events were isolated and passed the clustering cuts of the clustering analyses. Could CW interference from satellites influence impulsive events from bases in Antarctica to reconstruct elsewhere, for example, as mystery events? This is something we started to investigate. We looked at events from the three different passes of the ANITA payload over Bin 3045 of the ANITA-2 binned analysis. The three passes of the payload are shown in Figure 3.7.

We plotted the events from each pass as shown in Figure 7.5 and 7.6. Here the elevation angle of event reconstruction is plotted in the vertical axis, the azimuth angle in the horizontal axis and the color represents the number of events. Figure 7.5 shows events from the first pass of the payload over Bin 3045. Figure 7.6 shows events from the third pass of the payload over Bin 3045. It can be seen that the reconstruction of events on the left is much better in the first pass than in the third pass. Assuming the events on the left are due to a base of human activity on the continent, the non-alignment of the base with a satellite during the first pass could be the reason why the reconstruction is tighter here. We hypothesized that when a satellite or group of satellites is **aligned** with a ground pulse in azimuth, it could cause events from the ground pulse to reconstruct less tightly. In other words, an event that should have reconstructed to a base could be influenced by satellites to reconstruct elsewhere and **appear** isolated. Whether satellites do have this effect or not needs to be further studied and quantified.

7.3 Simulating reduced cross sections

To investigate the effect of cross section on observable polarization angle, we simulated neutrinos of different energies and cross sections using icemc. We did this for three different energies: 10^{18} eV, 10^{19} eV and 10^{20} eV), and five different cross sections: Standard Model (SM) cross section, SM cross section times 0.3, 0.1, 0.03, and 0.01. We tested this with the ANITA-2 simulation because it is well-tested but we selected events that triggered in both LCP and RCP to remove any V/H bias. This had come up in discussions about designing

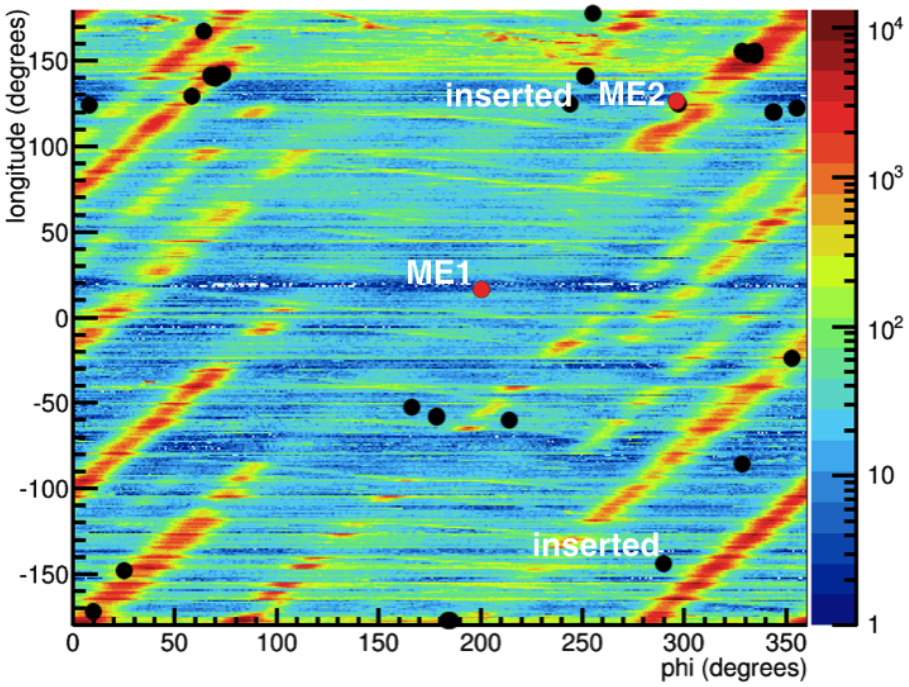

Figure 7.4: Mystery events 1 and 2 overlaid on the satellite stripe plot using solid red markers. The solid black indicate events that passed in the ANITA-2 binned analysis.

the ANITA-4 trigger, and when discussing the mystery event 1.

We made distributions of the plane-of-polarization angle with respect to the vertically polarized E-plane and calculated the corresponding cumulative distribution functions. We also made two-dimensional distributions of the VPol E-plane and HPol E-plane. These are shown in Figures 7.7, 7.8 and 7.9. As can be seen in Figure 7.7, the polarization component along the VPol E-plane is negative if the signal is coming from the bottom of the Cherenkov cone leading to direction of polarization being anti-parallel to the VPol E-plane. The vertical axis of the CDF in Figure 7.8 show the probability of getting a corresponding value or less in the horizontal axis.

For SM cross section, events tend to be close to vertical as expected (for Earth-skimming geometry) and for reduced cross sections we can see more of the Cherenkov cone which leads to a broader range of polarizations being observable. As can be seen in Figure 7.9, the options for observable polarization angles increase dramatically when the cross section is reduced from SM to 0.01 times SM. Similarly, in Figure 7.7, the distributions of polarization

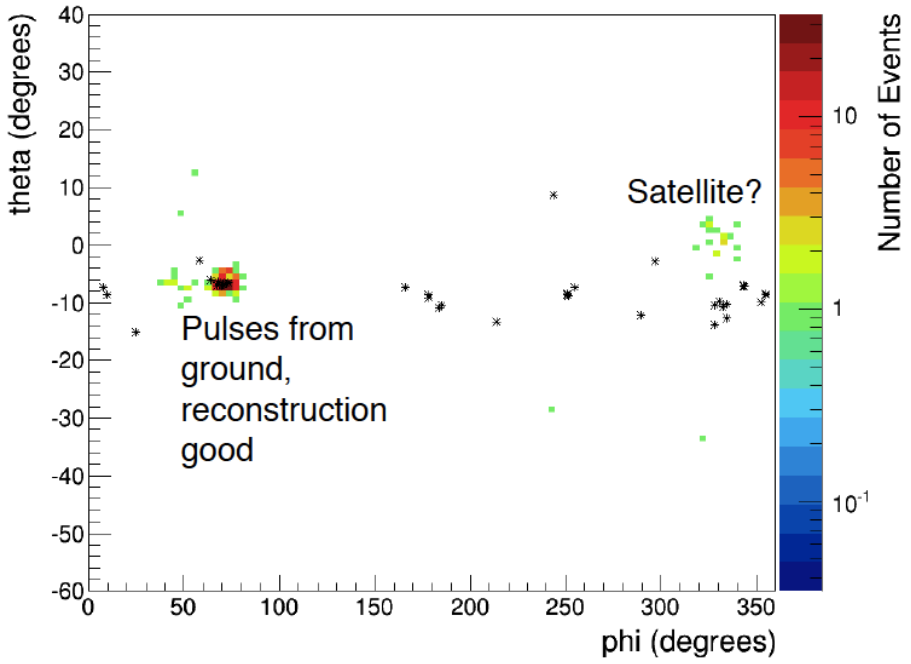

Figure 7.5: Events from pass 1 of the ANITA payload over Bin 3045 of the ANITA-2 binned analysis.

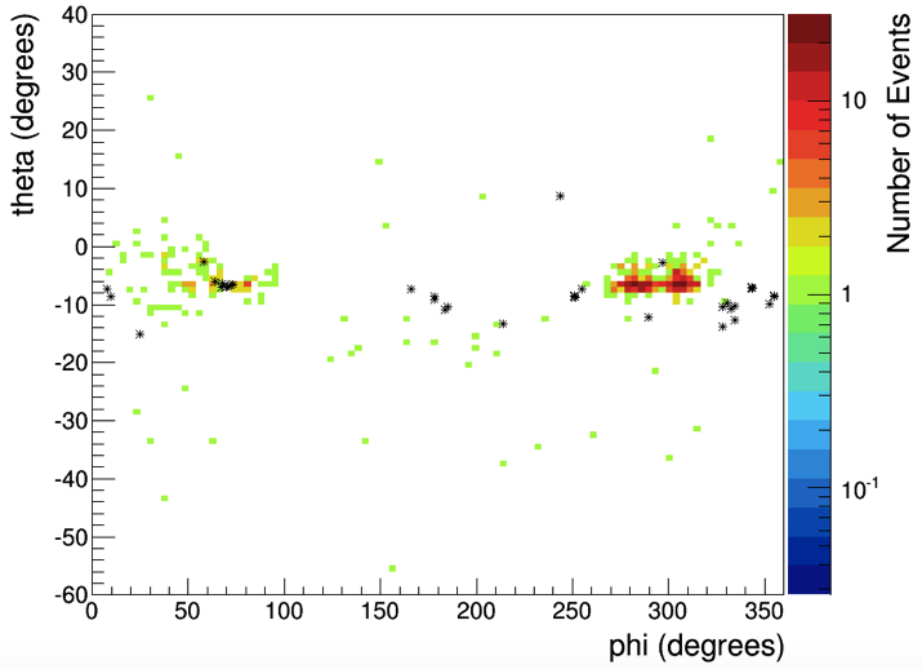

Figure 7.6: Events from pass 3 of the ANITA payload over Bin 3045 of the ANITA-2 binned analysis. This is the pass from which five excess events passed in this analysis.

angles become flatter and flatter with reduced cross section. We verified that for a VPol-based trigger there is even more of a bias for vertically polarized events.

7.4 ANITA as a potential long-lived SUSY particle detector

We investigated the potential of ANITA as a detector of long-lived, charged supersymmetric particles, such as staus. We propose that a stau could be detected by ANITA through measurement of the EAS from the secondary tau, as a directly incoming, horizontally-polarized signal. As explained in Section 7.1, EAS signals recorded with elevation angles steeper than 6.5° below the horizontal are typically ones that are reflected off of the ice, obtaining an opposite polarity. Thus, the non-inversion of the polarity of the recorded signal could be utilized to indicate their association with a stau.

We simulated the production of a stau inside the earth. It undergoes energy loss as it travels through the earth and then decays near the surface of the earth to create a tau. The tau also undergoes energy loss, leaves the earth and produces an air shower. This air shower, depending on geometry, could be observed by ANITA.

Figure 7.10 shows plots from this simulation. The top figure shows a two-dimensional distribution of stau masses and lifetimes. The color axis shows the probability of detection by ANITA corresponding to a particular set of stau mass and lifetime. The elevation angle used here is 6.5°. It can be seen that parts of the parameter space in mass and lifetime are more likely to be detectable than others. The bottom plot shows the differential probability of decay of a heavy, charged particle as a function of distance along its path through the earth. This is shown for four different combinations of stau masses and lifetimes.

The probability of the tau decaying in air is calculated as an integral which takes the form below. Here, the assumption is that the primary neutrino produces a stau in the earth which after traveling inside the earth produces a tau inside the earth close to the surface of the earth. The tau then pops out of the earth and produces an air shower.

$$P = exp(\frac{-(C - D_{stau} + (d_{air} - d_{shower}))}{d_{tau}} - exp(\frac{-(C - D_{stau} + d_{air})}{d_{tau}}$$

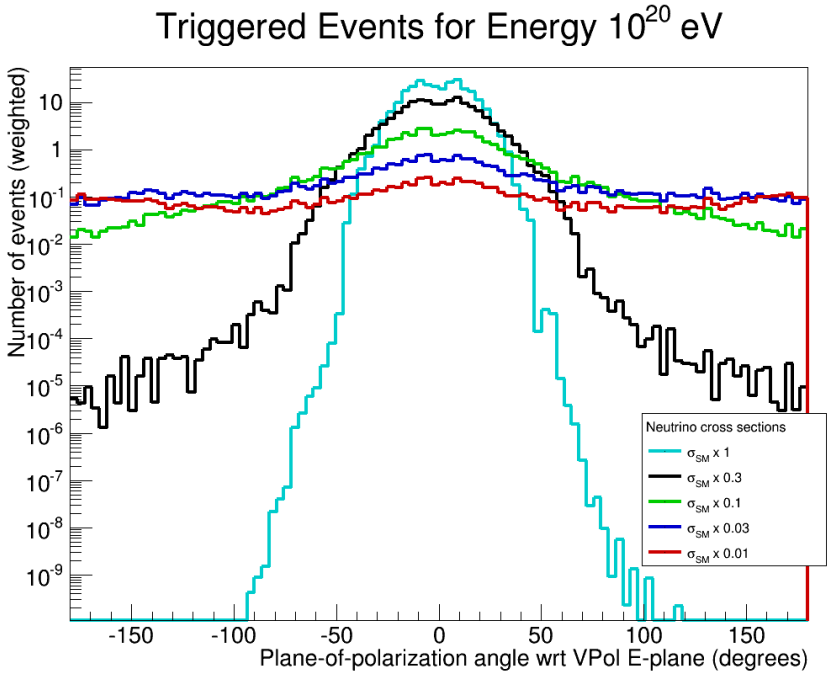

Figure 7.7: Distribution of the plane-of-polarization angle wrt vertically polarized E-plane of simulated neutrino events of energy 10^{20} eV for different cross sections.

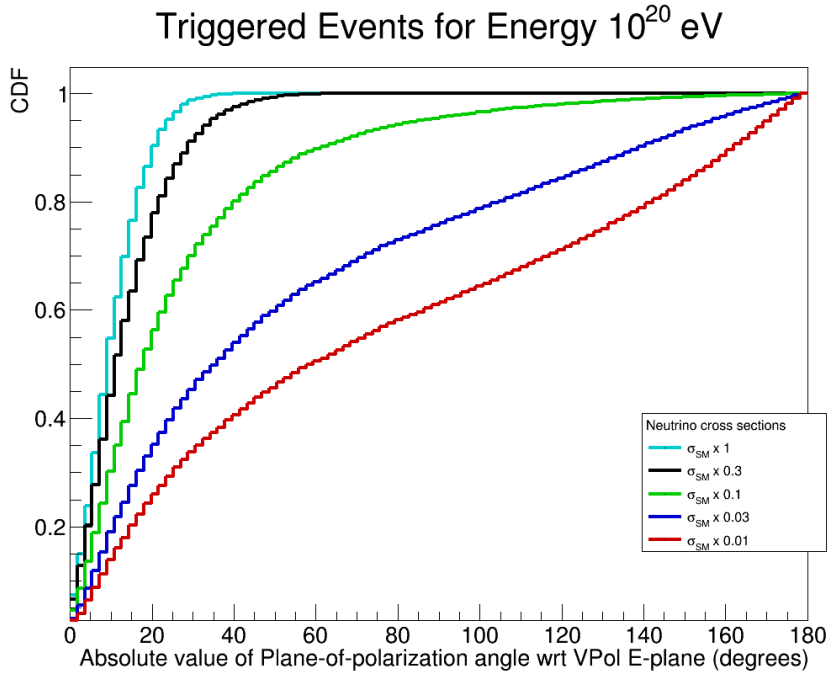

Figure 7.8: CDF of the above distributions.

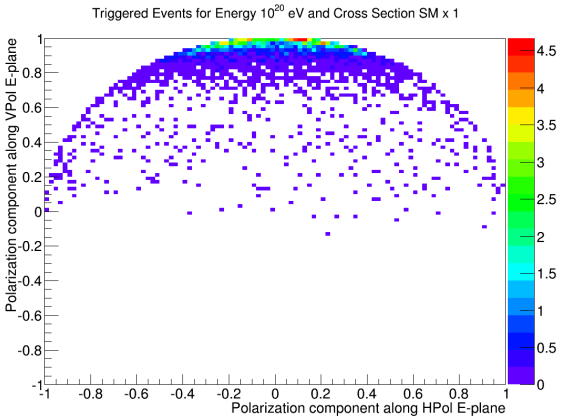

(a) SM x 1

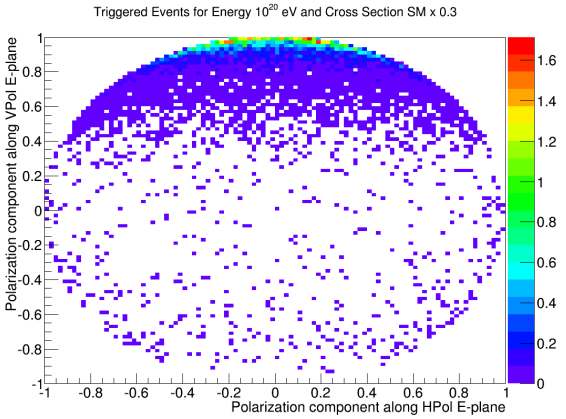

(b) SM x 0.3

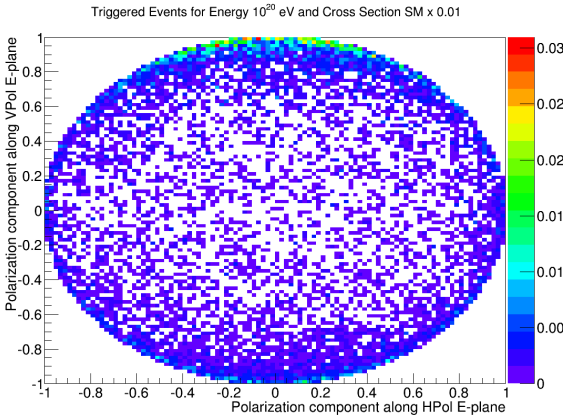

(c) SM x 0.01

Figure 7.9: Two dimensional distribution of the polarization component along the vertically polarized E-plane in the vertical axis and that along the horizontally polarized E-plane along the horizontal axis. Color denotes the number of simulated, triggered neutrino events of energy 10^{20} eV and cross section 1, 0.3 and 0.01 times the Standard Model cross section in the top, middle and bottom plots, respectively.

In the above equation, P is the probability of the tau decaying in air such that ANITA can view the resulting air shower. C is the total earth chord length traveled by neutrino-stau-tau. This is given purely by geometry utilizing the elevation angle, which is 35° for the second unusual upgoing event. The quantity D_{stau} is the distance traveled by the stau inside the earth before decaying to a tau. This is based on the stau mass and lifetime. We try this for several combinations of stau mass and lifetime as shown in Figure 7.10. d_{air} is the distance traveled by the tau shower in the air. This is based on geometry given that ANITA sees the shower. d_{shower} is the maximum distance away at which ANITA can start to see the shower. d_{tau} is the distance traveled by the tau before it decays. The shower energy is assumed to be half of the tau energy.

Although intended as mainly an investigation of ANITA's potential as a detector of long-lived, charged particles, this study also serves as an investigation of the mystery events and whether they can be explained by physics involving staus. From our simulations, we found that, although it is possible to detect a stau at an elevation angle of 35° for a particular set of stau mass and lifetime, it is more likely to detect stau signatures at shallower angles such as 6.5°. In other words, steeper angles may be possible but are not favored. The challenges of detecting this signature at steeper angles could be alleviated by the presence of a source sending bursts of UHE neutrinos in a particular direction. Such a possibility could be further investigated in future. We remain optimistic, however, that ANITA could serve as a detector of radio signatures of supersymmetric particles for complementary portions of the parameter space which cannot be probed by other experiments.

7.5 Conclusions

It is an exciting time for particle astrophysics. There have been major developments in the radio detection of UHE neutrinos and extensive air showers. ANITA has made two observations of potential UHE tau neutrino candidates for the first time. It has been found that ANITA also has the potential to be sensitive to exotic physics involving supersymmetric particles.

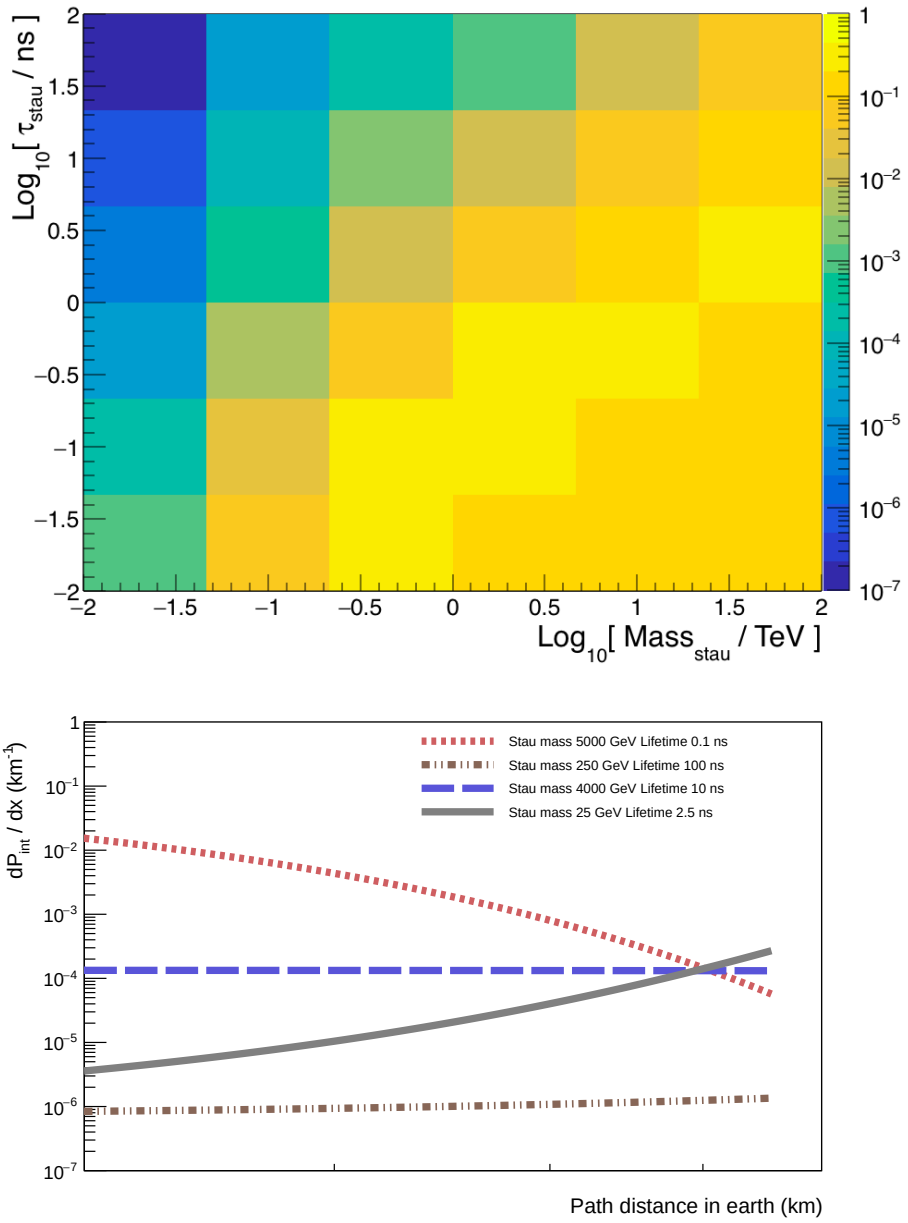

Figure 7.10: Top: Distribution of stau mass and lifetime with color indicating the probability of detection. Bottom: Differential probability of decay of a heavy, charged particle as a function of distance along its path through the earth. Different combinations of lifetimes and masses highlight different shapes that this can take.

The search for a diffuse flux of UHE neutrinos in data from the third flight of ANITA has been completed. A new limit has been placed on the diffuse flux of UHE neutrinos. Around 25 EAS candidates were also discovered in the ANITA-3 data, two of which were only discovered in the new binned analysis presented in this thesis. This thesis is also the first document to describe the details of the binned analysis results published for the first time in [2]. The binned analysis has also been successfully extended to perform a search for neutrinos from GRBs with progress made in the development of the first search constrained in time as well as direction.

Lastly, the total instrument livetime of ANITA has been tripled in ANITA-4 by the TUFF notch filters. Details on these filters and associated results along with the first descriptions of the ANITA-3 and -4 instruments are also part of this thesis and an associated publication [1]. This has paved the way for a much more (about 4 times more) sensitive instrument and the potential for further confirmation of ground-breaking observations as well as for new discoveries in particle astrophysics.

Appendix A
ANITA DATA STRUCTURE

The ANITA data is saved as multiple runs and each run has several ROOT files containing the data for that run. Each ROOT file has a TTree object saved inside it. Inside the TTree there is an object of a class from the ANITA analysis tools. The object has multiple members which show up as branches of the TTree. Each of these members hold a particular kind of information, for example, `eventNumber` holds the event number for each event in the data.

The ANITA-3 flight has runs going from 127 through 439, although in the analyses presented in [18, 21], only runs 175 through 439 are used. The ANITA-3 data can be found on the supercomputer Oakley at the following location:

`/fs/scratch/PAS0174/anita/data/`

For run 176, for example, there are multiple ROOT files used in the analysis as follows:

`calEventFile176.root`

`decimatedHeadFile176.root`

`gpsEvent176.root`

`timedHeadFile176.root`

Inside the header file, `timedHeadFile176.root`, for example, there is a TTree object called `headTree`. You can quickly look at what is in this tree by opening ROOT from the terminal and typing the commands below:

root -l `timedHeadFile176.root`

`.ls`

`headTree->Show(0)`

These commands are shown below along with part of the corresponding output upon investigating the data ROOT files. It can be seen that there is an object called `header` of type RawAnitaHeader inside the `timedHeadFile176.root` file. Members of the header object can be accessed by including the class called RawAnitaHeader in one's code. This class, along with other classes, can be found in the ANITA analysis tools which are maintained on GitHub at the following link:

https://github.com/anitaNeutrino/anitaBuildTool

To access the event number, for example, you would call upon:

`header->eventNumber`

A `headTree` exists inside the header file of each run, and to analyze the whole flight, one needs to access the `headTree` associated with each run.

Besides the header file, the data files containing GPS and event information are most important. The TTree inside the GPS file is called adu5PatTree. The data object inside this tree is called pat and is of type Adu5Pat. The TTree inside the event file is called eventTree. The data object inside this tree is called event and is of type CalibratedAnitaEvent. Adu5Pat and CalibratedAnitaEvent are also classes in the ANITA analysis tools. The data file, its tree, the associated object and the class that object inherits from for run 176 are summarized in a table for the most important data files.

File	TTree	Object	Class
timedHeadFile176.root	headTree	header	RawAnitaHeader
gpsEvent176.root	adu5PatTree	pat	Adu5Pat
calEventFile176.root	eventTree	event	CalibratedAnitaEvent

```
root -l timedHeadFile176.root

root [0]

Attaching file timedHeadFile176.root as _file0...

Warning in <TClass::Init>:

no dictionary for class RawAnitaHeader is available

(TFile *) 0x32a7510

root [1] .ls

TFile** timedHeadFile176.root

 TFile* timedHeadFile176.root

  KEY: TTree headTree;1

root [2] headTree->Show(0)

======> EVENT:0

 header          = (RawAnitaHeader*)0x3666c50

 fUniqueID       = 0

 fBits           = 50331648

 run             = 176

 realTime        = 1419062174

 payloadTime     = 1419062174

 payloadTimeUs   = 878296

 gpsSubTime      = 4294967295

 turfEventId     = 184549386

 eventNumber     = 15633901

 calibStatus     = 511

 priority        = 136

 turfUpperWord   = 0

 otherFlag       = 0

 errorFlag       = 0

 surfSlipFlag    = 0

 nadirAntTrigMask = 153
```

```
root -l gpsEvent176.root
root [0]
Attaching file gpsEvent176.root as _file0...
Warning in <TClass::Init>:
no dictionary for class Adu5Pat is available
(TFile *) 0x1e1d860
root [1] .ls
TFile** gpsEvent176.root
 TFile* gpsEvent176.root
  KEY: TTree adu5PatTree;1
Tree of Interpolated ADU5 Positions and Attitude
root [2] adu5PatTree->Show(0)
======> EVENT:0
 pat             = (Adu5Pat*)0x227a6d0
 fUniqueID       = 0
 fBits           = 50331648
 run             = 176
 realTime        = 1419062175
 readTime        = 1419062174
 payloadTime     = 1419062174
 payloadTimeUs   = 878296
 timeOfDay       = 28575396
 latitude        = -81.727478
 longitude       = 126.860802
 altitude        = 36012.253906
 heading         = 205.175720
```

```
root -l calEventFile176.root
root [0]
Attaching file calEventFile176.root as _file0...
Warning in <TClass::Init>:
no dictionary for class RawAnitaEvent is available
Warning in <TClass::Init>:
no dictionary for class CalibratedAnitaEvent is available
(TFile *) 0x12f0ea0
root [1] .ls
TFile** calEventFile176.root
 TFile* calEventFile176.root
  KEY: TTree eventTree;253
Tree of Anita Events
root [2] eventTree->Show(0)
======> EVENT:0
 run             = 176
 event           = (CalibratedAnitaEvent*)0x2c75610
 fUniqueID       = 0
 fBits           = 50331648
 whichPeds       = 1416109581
 eventNumber     = 15633901
 surfEventId[12] = 184549386 , 184549386 , 184549386 ,
 184549386 , 184549386 ,
                   184549386 , 184549386 , 184549386 ,
                   184549386 , 184549386 ,
                   184549386 , 184549386
 chanId[108]     = 0 , 1 , 2 , 3 , 4 , 5 , 6 , 7 , 8 ,
 9 , 10 , 11 , 12 , 13 , 14 , 15 , 16 , 17 , 18 , 19
```

Appendix B
How to run the ANITA-3 binned analysis

The ANITA binned analysis software is maintained, backed up and version-controlled on GitHub at the link:

https://github.com/osu-particle-astrophysics/BinnedAnalysis

Inside this repository, there exist code to perform the binned analysis for ANITA-2 as well as code for ANITA-3. These are located in the directories called `anita2code` and `anita3code`, respectively. In this appendix, we will cover how to run the analysis for ANITA-3. Note that the ANITA-3 analysis could be adapted to work for ANITA-4. The ANITA-2 flight had a significantly different triggering system, among other differences, making it difficult to adapt its analysis to newer flights. However, I will try to include a separate note on how to run the binned analysis for ANITA-2 as well.

Doing the ANITA-3 binned analysis involves running a set of code. Details on the development of this code base can be found in [18, 20, 21] and in various chapters of this thesis. To run the analysis, the order of operations to follow are below.

Run interferometry

Run analysis stage 1

Run analysis stage 2

Optimize LD cut

Run analysis stage 2

B.1 How to run the interferometry

Go into the file called runInterferometry.cxx and change two things: the input and the output. Specifically, this might involve setting the variables called `dataDirLocal`, `outputFilename`, and `outputDirStr`. I show below what I have set these to for my current work.

dataDirLocal: `$OINDREE_SIM/kotera_march30/Energy_222`

This is the simulated data over which I currently want to run the interferometry. It may not be what you need.

What you change this to depends on which simulation data you want to run interferometry over.

outputFilename: `/fs/scratch/PAS0174/anita/oindree/InterferometryOutput/simKoteraMarch30/geomFilter/analyzerResults..root`

outputDirStr: `$OINDREE`

You should change the outputDirStr and OutputFilename to something else, such as some directory where you want the output. Then run:

make `runInterferometry`

qsub `runInterferometrySim.job`

showq -u osu0426

The last command is to see whether the job started or not. A `.o` file will appear when the job has finished, check it and make sure everything looks right . Mainly you are checking that the input and output that you intended for it to use is actually being used. Once the job has finished go to the output dir and check the root file `analyzerResults*.root` that was made to make sure it looks fine. There should be only one root file, for one run.

We have not run the interferometry for all the runs yet. If this looks good we can run interferometry for all the runs now. This is done by running the following:

`./runInterferometrySim.sh`

This starts a job for each run.

Recap of code files we used for interferometry:

`runInterferometry.cxx`

`runInterferometrySim.job`

`runInterferometrySim.sh`

Also commonly useful to know is how to run the interferometry for a particular event from the real data:

`./runInterferometry-PB--FILTER_OPTION=4,-BbaselineSampleSmooth_1_2.00.root`

383 69969708

This command will run the interferometry for a single event 69969708 from run 383.

- $FILTER\_OPTION = 4$ invokes the geometric filter with a noise baseline from the file indicated in the -B parameter
- $FILTER\_OPTION = 2$ and $SINE\_SUBTRACT\_THRESHOLD = 0.1$ will give a reasonable implemetation of sine subtraction filter
- $FILTER\_OPTION = 0$ means no filtering
- -O parameter directs the output to the directory name contiguously following the -O
- -G displays the the interferometric maps interactively

B.2 How to run analysis stage 1

To run the analysis stage 1, you can compile the associated code as follows:

make `runAnalysisStage01`

Currently, there are lots of warnings that you get at this stage and that is the "normal." Next run it as follows.

For simulation:

qsub `stage01_sim.job`

For data:

qsub `stage01.job`

When stage 1 finishes running, it makes several files in the output folder you assigned. Most importantly, this file is made as an output from stage 1 :

`analysisOutput_1_99.root`

This is from me running the code for simulation with runs going from 1 to 99. The run numbers will depend on which runs you had the code run over. The more runs you run it over the longer it takes. This file is the input in stage 2 of the analysis, so in that sense this is the most important file because without this you cant do the next stage of the analysis.

If you want to run stage 1 for ONE event from data (ANITA-3), say, for an interesting event such as the mystery event 2 or ME2, this is how you could do it:

`./runAnalysisStage01 -CA -9`
`-D/fs/scratch/PAS0174/anita/2015_05_19/sample_90/geomFilter` 175 439 15717147

This would actually take a while as you are saying to run over all the runs used in the analysis so you would need to run a job with this command (see `stage01.job`)

To save time you could also just run using the run that the particular event is in, e.g. ME2 is in run 176 so you could do :

`./runAnalysisStage01 -CA -9`
`-D/fs/scratch/PAS0174/anita/2015_05_19/sample_90/geomFilter` 176 176 15717147

The `-CA` flag tells the stage 1 code to apply analysis cuts. The `-9` flag tells it to use the 90% data sample. The `-D` flag tells it the location of the interferometry results. The 176 and 176 tells it the run(s) to run the code over and the 15717147 is the specific event number for which the code would be run. When an event number is not specified at the end then the code is run for all events in the specified runs.

When you get to the point of running stage 1 and have made the `analysisOutput...root` file, you should try looking inside that file and see what things are in there and try to visualize them to get a better idea.

B.3 How to run analysis stage 2

The stage 2 code is run twice, once before the optimize code and once after. In this section, we discuss how to run it before the optimize code.

The stage 2 code takes as input a file that was output from the stage 1 code:

```
analysisOutput_188_193.root
```

The above file is made by running the stage 1 code over the ANITA-3 data using runs 188 through 193. If other runs were used the associated run numbers would appear in the filename instead. If stage 2 also needs to be run over those same runs then the following command can be used:

```
./runAnalysisStage02
-D/fs/scratch/PAS0174/anita/oindree/Stage1Output/BgOnly/GRB1
-I/fs/scratch/PAS0174/anita/2015_05_19/sample_10/geomFilter 188 193 -b -PV
-S_v -FanalysisOutput_188_193.root
```

The -D flag tells the stage 2 code where the file output from stage 1 is. The -I flag tells the code where the associated results from running the interferometry is. 188 and 193 are the start and end runs over which stage 2 will run. -b tells it to re-bin. -PV tells it to run for VPol. `-S_v` labels an output file with the subscript `_v` denoting VPol. The -F flag tells the stage 2 code the name of the input file from stage 1 that it has to use.

When stage 2 finishes running it also makes a file called `analysisOutput_188_193.root`, for example, which can then be used as input by the optimize code.

B.4 How to run the optimize code

Before running the optimize code, make sure to change the variables `outputDir` and `inFilename`. To run the optimize code using the optimized healpix orientations, use the following commands.

VPol: `./optimizeLDCut -pV -r --PHI_HP_OFFSET=.56 --THETA_HP_OFFSET=-5.04`

HPol: `./optimizeLDCut -pH -r --PHI_HP_OFFSET=3.92 --THETA_HP_OFFSET=0.00`

B.5 How to run analysis stage 2 again

After optimizing, the stage 2 analysis must be run again - this time, with final cuts. This should be the last step of the analysis resulting in finding out which events pass all cuts. To run the stage 2 analysis with final cuts for VPol run something like this command:

```
./runAnalysisStage02 -b -D/users/PAS0654/osu0426/BinnedAnalysis/anita3code/
                    Diffuse/stage2inputs/fullDataSet
-I/fs/scratch/PAS0174/anita/2015_05_19/sample_90/geomFilter 175 439 -PV -S_v
                    -a -FanalysisOutput_175_439.root
```

The `-a` says to apply final cuts. Use it when optimizeLDCut has been run and you want to know which events pass all cuts. Things are getting serious now!

In order to successfully run stage 2 with final cuts, you need two files per polarization. First, you need to provide a file containing the bin numbers of bins that you will be using for your search. These should be named as follows.

```
binsOver0.01_h.txt
binsOver0.01_v.txt
```

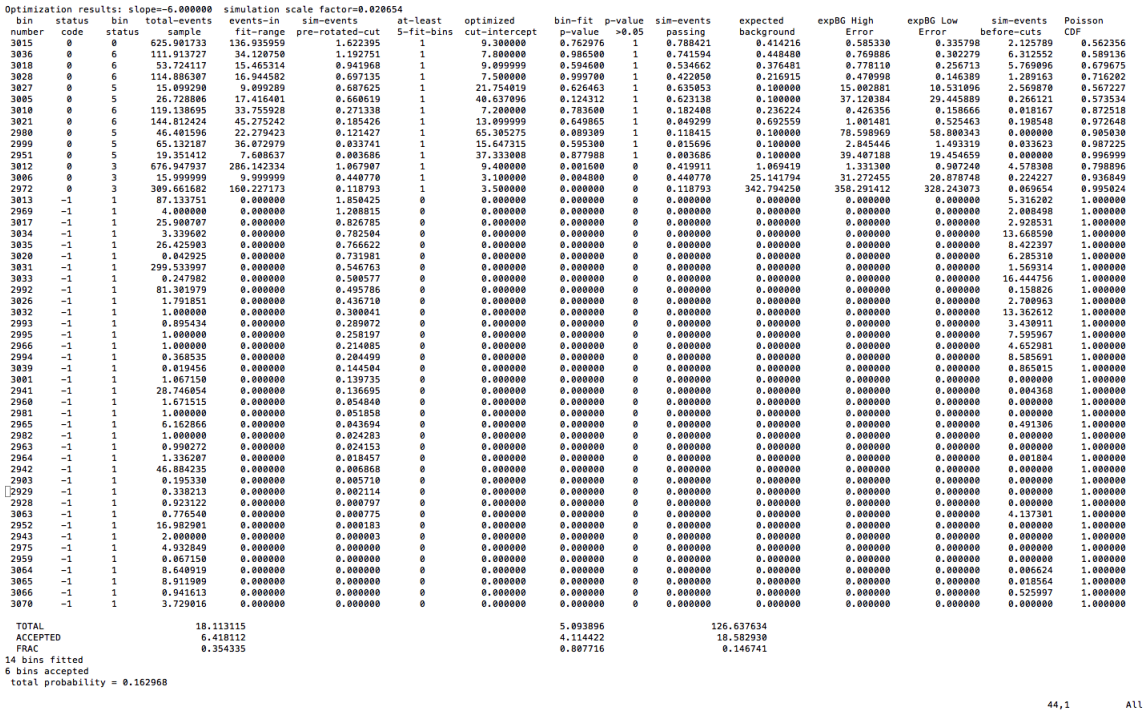

```
Optimization results: slope=-6.000000  simulation scale factor=0.020654
 bin    status    bin   total-events   events-in    sim-events      at-least    optimized      bin-fit  p-value  sim-events    expected      expBG High     expBG Low      sim-events   Poisson
number   code    status      sample      fit-range  pre-rotated-cut  5-fit-bins  cut-intercept   p-value   >0.05    passing     background       Error          Error       before-cuts    CDF
3015      0       0       625.901733   136.935959       1.622395         1         9.300000    0.762976     1     0.788421      0.414216       0.585330       0.335798      2.125789     0.562356
3036      0       6       111.913727    34.120750       1.192751         1         7.800000    0.986500     1     0.741594      0.448480       0.769886       0.302279      6.312552     0.589136
3018      0       6        53.724117    15.465314       0.941968         1         9.099999    0.594600     1     0.534662      0.376481       0.778110       0.256713      5.769096     0.679675
3028      0       6       114.886307    16.944582       0.697135         1         7.500000    0.999700     1     0.422050      0.216915       0.470998       0.146389      1.289163     0.716202
3027      0       5        15.899290     9.099289       0.687625         1        21.754019    0.626463     1     0.635053      0.100000      15.002881      10.531096      2.569870     0.567227
3005      0       5        26.728806    17.416401       0.660619         1        40.637096    0.124312     1     0.623138      0.100000      37.120384      29.445889      0.266121     0.573534
3010      0       6       119.138695    33.755928       0.271338         1         7.200000    0.783600     1     0.182408      0.236224       0.426356       0.158666      0.018167     0.872518
3021      0       6       144.812424    45.275242       0.185426         1        13.099999    0.649865     1     0.049299      0.692559       1.001481       0.525463      0.198548     0.972648
2980      0       5        46.401596    22.279423       0.121427         1        65.305275    0.089309     1     0.118415      0.100000      78.598969      58.800343     0.000000     0.905030
2999      0       5        65.132187    36.072979       0.033741         1        15.647315    0.595300     1     0.015696      0.100000       2.845446       1.493319     0.033623     0.987225
2951      0       5        19.351412     7.608637       0.003686         1        37.333008    0.877988     1     0.003686      0.100000      39.407188      19.454659     0.000000     0.996999
3012      0       3       676.947937   286.142334       1.067907         1         9.400000    0.001600     0     0.419911      1.069419       1.331300       0.907240      4.578308     0.798896
3006      0       3        15.999999     9.999999       0.440770         1         3.100000    0.004800     0     0.440770     25.141794      31.272455      20.878748      0.224227     0.936849
2972      0       3       309.661682   160.227173       0.118793         1         3.500000    0.000000     0     0.118793    342.794250     358.291412     328.243073      0.069654     0.995024
3013     -1       1        87.133751     0.000000       1.850425         0         0.000000    0.000000     0     0.000000      0.000000       0.000000       0.000000      5.316202     1.000000
2969     -1       1         4.000000     0.000000       1.208815         0         0.000000    0.000000     0     0.000000      0.000000       0.000000       0.000000      2.008498     1.000000
3017     -1       1        25.900707     0.000000       0.826785         0         0.000000    0.000000     0     0.000000      0.000000       0.000000       0.000000      2.928531     1.000000
3034     -1       1         3.339602     0.000000       0.782504         0         0.000000    0.000000     0     0.000000      0.000000       0.000000       0.000000     13.668590     1.000000
3035     -1       1        26.425903     0.000000       0.766622         0         0.000000    0.000000     0     0.000000      0.000000       0.000000       0.000000      8.422397     1.000000
3020     -1       1         0.042925     0.000000       0.731981         0         0.000000    0.000000     0     0.000000      0.000000       0.000000       0.000000      6.285310     1.000000
3031     -1       1       299.533997     0.000000       0.546763         0         0.000000    0.000000     0     0.000000      0.000000       0.000000       0.000000      1.569314     1.000000
3033     -1       1         0.247982     0.000000       0.500577         0         0.000000    0.000000     0     0.000000      0.000000       0.000000       0.000000     16.444756     1.000000
2992     -1       1        81.301979     0.000000       0.495786         0         0.000000    0.000000     0     0.000000      0.000000       0.000000       0.000000      0.158826     1.000000
3026     -1       1         1.791851     0.000000       0.436710         0         0.000000    0.000000     0     0.000000      0.000000       0.000000       0.000000      2.700963     1.000000
3032     -1       1         1.000000     0.000000       0.300041         0         0.000000    0.000000     0     0.000000      0.000000       0.000000       0.000000     13.362612     1.000000
2993     -1       1         0.895434     0.000000       0.289072         0         0.000000    0.000000     0     0.000000      0.000000       0.000000       0.000000      3.430911     1.000000
2995     -1       1         1.000000     0.000000       0.258197         0         0.000000    0.000000     0     0.000000      0.000000       0.000000       0.000000      7.595967     1.000000
2966     -1       1         1.000000     0.000000       0.214085         0         0.000000    0.000000     0     0.000000      0.000000       0.000000       0.000000      4.652981     1.000000
2994     -1       1         0.368535     0.000000       0.204499         0         0.000000    0.000000     0     0.000000      0.000000       0.000000       0.000000      8.585691     1.000000
3039     -1       1         0.019456     0.000000       0.144584         0         0.000000    0.000000     0     0.000000      0.000000       0.000000       0.000000      0.865015     1.000000
3001     -1       1         1.067150     0.000000       0.139735         0         0.000000    0.000000     0     0.000000      0.000000       0.000000       0.000000      0.000000     1.000000
2941     -1       1        28.746054     0.000000       0.136695         0         0.000000    0.000000     0     0.000000      0.000000       0.000000       0.000000      0.004368     1.000000
2960     -1       1         1.671515     0.000000       0.054840         0         0.000000    0.000000     0     0.000000      0.000000       0.000000       0.000000      0.000000     1.000000
2981     -1       1         1.000000     0.000000       0.051858         0         0.000000    0.000000     0     0.000000      0.000000       0.000000       0.000000      0.000000     1.000000
2965     -1       1         6.162866     0.000000       0.043694         0         0.000000    0.000000     0     0.000000      0.000000       0.000000       0.000000      0.491306     1.000000
2982     -1       1         1.000000     0.000000       0.024283         0         0.000000    0.000000     0     0.000000      0.000000       0.000000       0.000000      0.000000     1.000000
2963     -1       1         0.990272     0.000000       0.024153         0         0.000000    0.000000     0     0.000000      0.000000       0.000000       0.000000      0.000000     1.000000
2964     -1       1         1.336207     0.000000       0.018457         0         0.000000    0.000000     0     0.000000      0.000000       0.000000       0.000000      0.001804     1.000000
2942     -1       1        46.884235     0.000000       0.006868         0         0.000000    0.000000     0     0.000000      0.000000       0.000000       0.000000      0.000000     1.000000
2903     -1       1         0.195330     0.000000       0.005710         0         0.000000    0.000000     0     0.000000      0.000000       0.000000       0.000000      0.000000     1.000000
2929     -1       1         0.338213     0.000000       0.002114         0         0.000000    0.000000     0     0.000000      0.000000       0.000000       0.000000      0.000000     1.000000
2928     -1       1         0.923122     0.000000       0.000797         0         0.000000    0.000000     0     0.000000      0.000000       0.000000       0.000000      0.000000     1.000000
3063     -1       1         0.776540     0.000000       0.000775         0         0.000000    0.000000     0     0.000000      0.000000       0.000000       0.000000      4.137301     1.000000
2952     -1       1        16.982901     0.000000       0.000183         0         0.000000    0.000000     0     0.000000      0.000000       0.000000       0.000000      0.000000     1.000000
2943     -1       1         2.000000     0.000000       0.000003         0         0.000000    0.000000     0     0.000000      0.000000       0.000000       0.000000      0.000000     1.000000
2975     -1       1         4.932849     0.000000       0.000000         0         0.000000    0.000000     0     0.000000      0.000000       0.000000       0.000000      0.000000     1.000000
2959     -1       1         0.067150     0.000000       0.000000         0         0.000000    0.000000     0     0.000000      0.000000       0.000000       0.000000      0.000000     1.000000
3064     -1       1         8.640919     0.000000       0.000000         0         0.000000    0.000000     0     0.000000      0.000000       0.000000       0.000000      0.006624     1.000000
3065     -1       1         8.911909     0.000000       0.000000         0         0.000000    0.000000     0     0.000000      0.000000       0.000000       0.000000      0.018564     1.000000
3066     -1       1         0.941613     0.000000       0.000000         0         0.000000    0.000000     0     0.000000      0.000000       0.000000       0.000000      0.525997     1.000000
3070     -1       1         3.729016     0.000000       0.000000         0         0.000000    0.000000     0     0.000000      0.000000       0.000000       0.000000      0.000000     1.000000

 TOTAL                      18.113115                                                          5.093896              126.637634
 ACCEPTED                    6.418112                                                          4.114422               18.582930
 FRAC                        0.354335                                                          0.807716                0.146741
14 bins fitted
6 bins accepted
 total probability = 0.162968

                                                                                                                                                                                                  44,1          All
```

Figure B.1: The table produced by the optimize code and needs to be used as input to run the stage 2 analysis with final cuts.

You will know the final bins to use for the search from the table produced in the optimize step called something like `oindree_optimization_final_sl_06_sf_0.020654.txt`. This table also needs to be provided to stage 2 as an input. Re-name the `oindree_optimization_final_sl_06_sf_0.020654.txt` file as the following before doing so.

`intercept_h.txt`

`intercept_v.txt`

A screenshot of an example table is shown in Figure B.1. Note that the eighth column from the left shows the optimized LD cut for each bin. This information, for example, is needed to run stage 2 with final cuts.

Appendix C
Satellite stripe plot

The satellite stripe plot can be made with data from any flight, however, this appendix shows how to create the plot using data from the ANITA-2 and -3 flights (Figure C.1). The plot is a two-dimensional histogram made with ROOT. The longitude of the ANITA payload is in the vertical axis and the azimuthal reconstruction angle of events using their waveforms in LCP is in the horizontal axis. The quantity in the horizontal axis, phi, is corrected for heading of the payload and calculated as shown in Equation C.1. The color axis in the plot represents the number of events. Over-densities of events can be seen as stripes at certain longitudes. Each stripe is thought to be due to an individual group of satellites.

$$phi = fmod((phi_{LCP} - heading + 360), 360) \tag{C.1}$$

C.1 Code for satellite stripe plot

Example code used to make the satellite stripe plot for the ANITA-3 and -2 flights are shown below. The ANITA-3 code is a macro and runs independent of other ANITA software. It needs to be run on Oakley as the ANITA-3 data is located there. The ANITA-2 code is meant to be compiled and run inside the `anita2code` directory of the binned analysis software which is located at: https://github.com/osu-particle-astrophysics/BinnedAnalysis.

The code to make the ANITA-3 satellite stripe plot is a macro called `plotLonPhi`. A macro is a piece of code in ROOT meant to serve only one function. Inside the macro, that

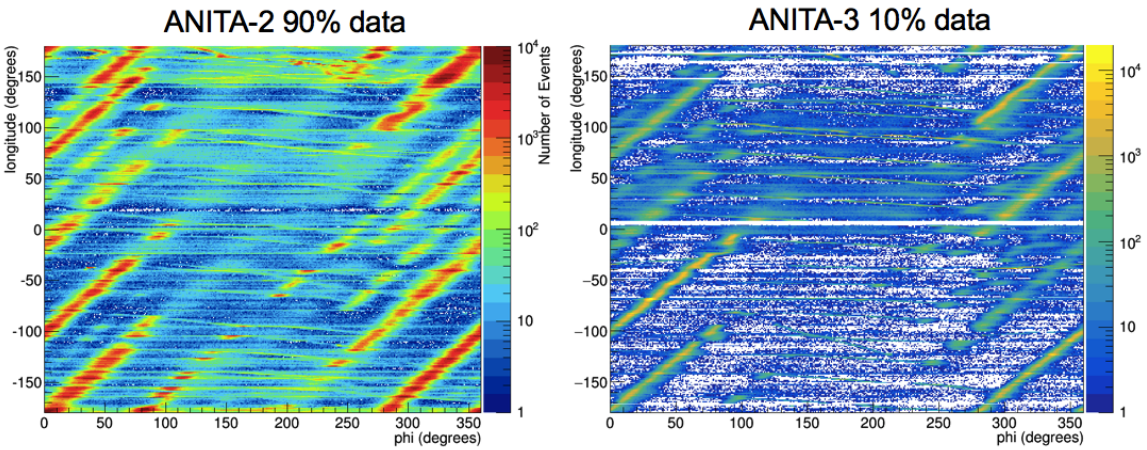

Figure C.1: Satellite stripe plots for the ANITA-2 and ANITA-3 flights.

function is written and the name of the macro is the same as the name of the function. In this particular macro, first I declare a TChain object. A TChain object is a collection of files containing TTrees. This is useful in ANITA as you can add together the TTrees associated with data files of multiple runs into one object. To make the satellite stripe plot for ANITA-3, we use the output files from runInterferometry.cxx of the ANITA-3 binned analysis. These are saved as multiple ROOT files, one file per run.

I used the 10% data to make the ANITA-3 plot. To use the 90% data, change `sample_10` in the directory name to `sample_90`. Note that Draw, a member function of both TTree and TChain, is used. This allows one to make the plot without including the classes that data objects inherit from. The function Draw accesses what is inside the TTree directly without requiring a definition of the data type inside the tree. The plot can also be made in the traditional way of filling a histogram with entries from a TChain inside a for loop.

The idea behind making the satellite stripe plot for ANITA-2 is the same, however, the ANITA-2 analysis software is unique. ANITA-2 data is on Kingbee and that is where `anita2code` have been run and tested. The code to make the satellite stripe plot for ANITA-2 is part of `oindreeskymap.cc` in `anita2code`. Note the `.h` files that must be included to run this code, especially `analysis_info_4pol.h`, which is a struct holding the necessary data variables.

```
//////////////////////FOR ANITA-3/////////////////////////
void plotLonPhi();
void plotLonPhi()
{
  //Declare a TChain object (collection of files containing TTrees)
  TChain tchain("resultTree");
  //Add files containing data processed by interferometry
  tchain.Add("/fs/scratch/PAS0174/anita
  /2015_05_19/sample_10/geomFilter/analyzerResults_*.root");
  //Declare a TH2D object
  //First argument is the name of the histogram
  //which is same as the variable name here
  TH2D hlonPhi00("hlonPhi00","ANITA-3 10% Data LPol;
  phi (degrees);longitude (degrees)",360,0,360,360,-180,180);
  //Declare a TCanvas object
  //which is needed to make a plot in ROOT
  TCanvas cL("cL","cL",900,800);
  //Use the Draw function to plot the histogram
  //TTree and TChain have this useful function Draw
  //Draws and puts the histogram in the TH2D object you specified
  tchain.Draw("longitude:(fmod((peak[0][0].phi - heading + 360),360))
  >> hlonPhi00", "circPol == 1", "colz");
  //Set the color axis to log scale
  cL.SetLogz();
  //Save plot as a .png (or other chosen format)
  cL.SaveAs("LonPhiPeak00CPol1.png");
  //Save plot as .root as well for quick changes as needed
  cL.SaveAs("LonPhiPeak00CPol1.root");
}
```

```
//////////////////////FOR ANITA-2/////////////////////////
#include "analysis_info_4pol.h" //struct holding data variables
using namespace std;
class MyCorrelator;
int main()
{
  char filename90[10000];
  char filename10[10000];
  sprintf(filename90,"/data/anita/btdailey/final_filter/
  90sample/geom_4pol_partial_0301/output*000.root");
  sprintf(filename10,"/data/anita/btdailey/final_filter/
  10sample/geom_4pol_partial_0301/output*.root");
  TChain tchain("analysis_info_4pol");
  tchain.Add(filename90);
  tchain.Add(filename10);
  //Create a pointer to instantiate struct
  analysis_info_4pol *pol4_Ptr = NULL;
  tchain.SetBranchAddress("pol4_Ptr",&pol4_Ptr);
  //Note: R & L are switched in ANITA-2
  TH2D LonPhiR("LonPhiR","ANITA-2 100% Data After Quality Cuts;
  phi (degrees); longitude (degrees)", 360,0,360,360,-180,180);
  TCanvas cRmap("cRmap","cRmap",1000,800);
  tchain.Draw("pol4_Ptr->anitaLon:
  (fmod((pol4_Ptr->phiMap[3]-pol4_Ptr->heading+360),360))
  >> LonPhiR","","colz"); //R & L are switched in ANITA-2
  cRmap.SetLogz();
  cRmap.SaveAs("LonPhiR100pc.png");
  cRmap.SaveAs("LonPhiR100pc.root");
}
```

Appendix D

Singlets from the diffuse search

Two singlets were found to pass in the VPol channel of the diffuse search as described in Chapter 4. These singlets belonged to bins 2998 and 3037, respectively. Information on the events is shown again in Table D.1. Note that in the bins 2998 and 3037, I had to remove one and three blasts, respectively, by hand after the LD cut.

Magic display waveforms for the singlet events are shown below. Waveforms recorded by each antenna for singlet event 21702154 are shown in Figure D.1. Waveforms recorded in the VPol channel are shown at the top and waveforms in the HPol channel are shown at the bottom. It can be seen that this event passed the trigger in both VPol and HPol.

Distributions for these bins are shown in Figures D.2, D.3, D.4, and D.5 using either the 10% or 90% sample of events before final cuts. Final cuts include the LD cut, bin cut, and event bin-weight cut.

Event	Pol	Run	Bin	Bin-Weight	Latitude	Longitude
21702154	V	207	3037	1.0	-82.7	118.4
73750661	V	397	2998	0.9	-77.3	163.4

Table D.1: My singlets from the diffuse search.

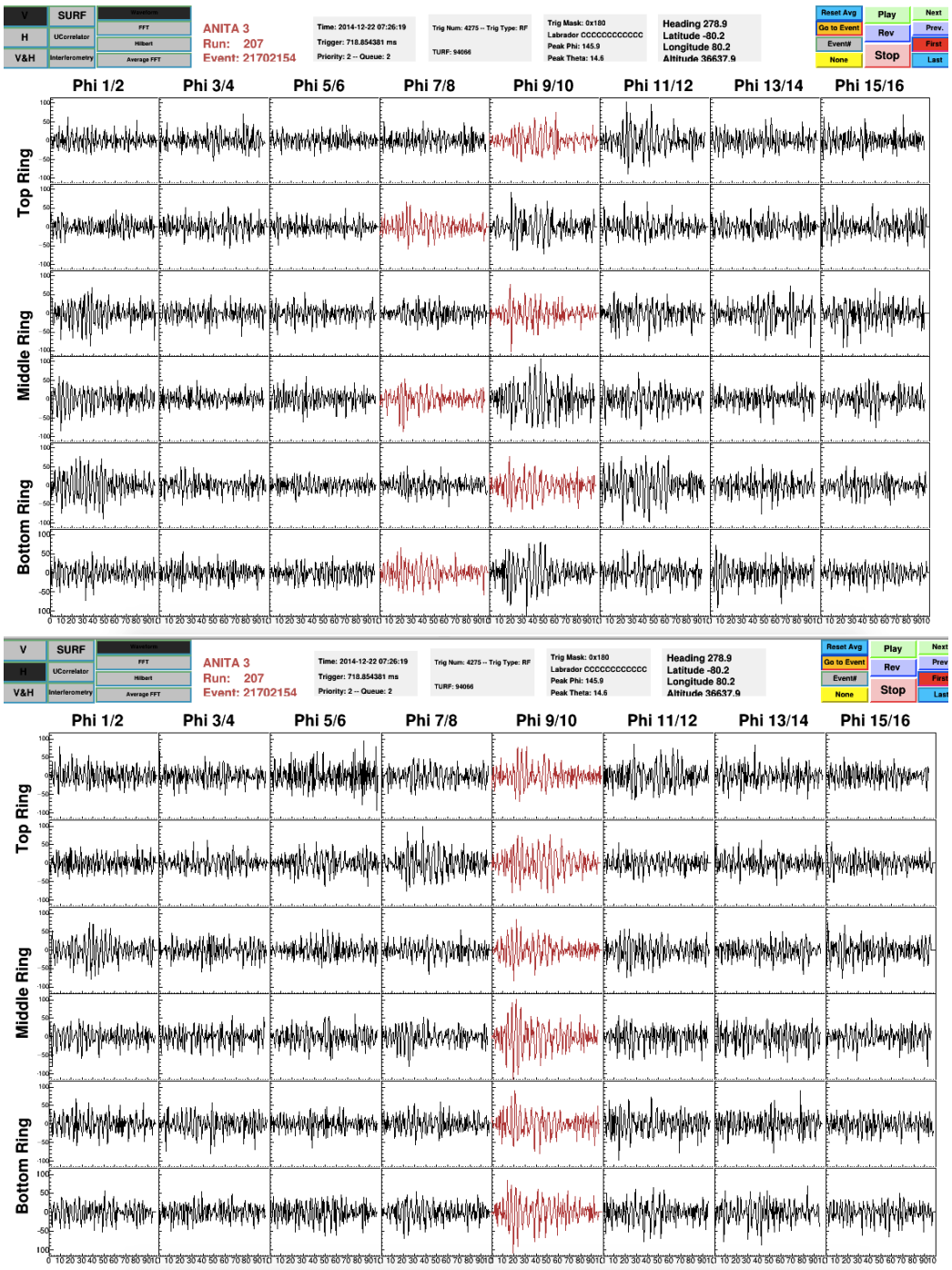

Figure D.1: Waveforms in VPol (top) and HPol (bottom) for singlet event 21702154.

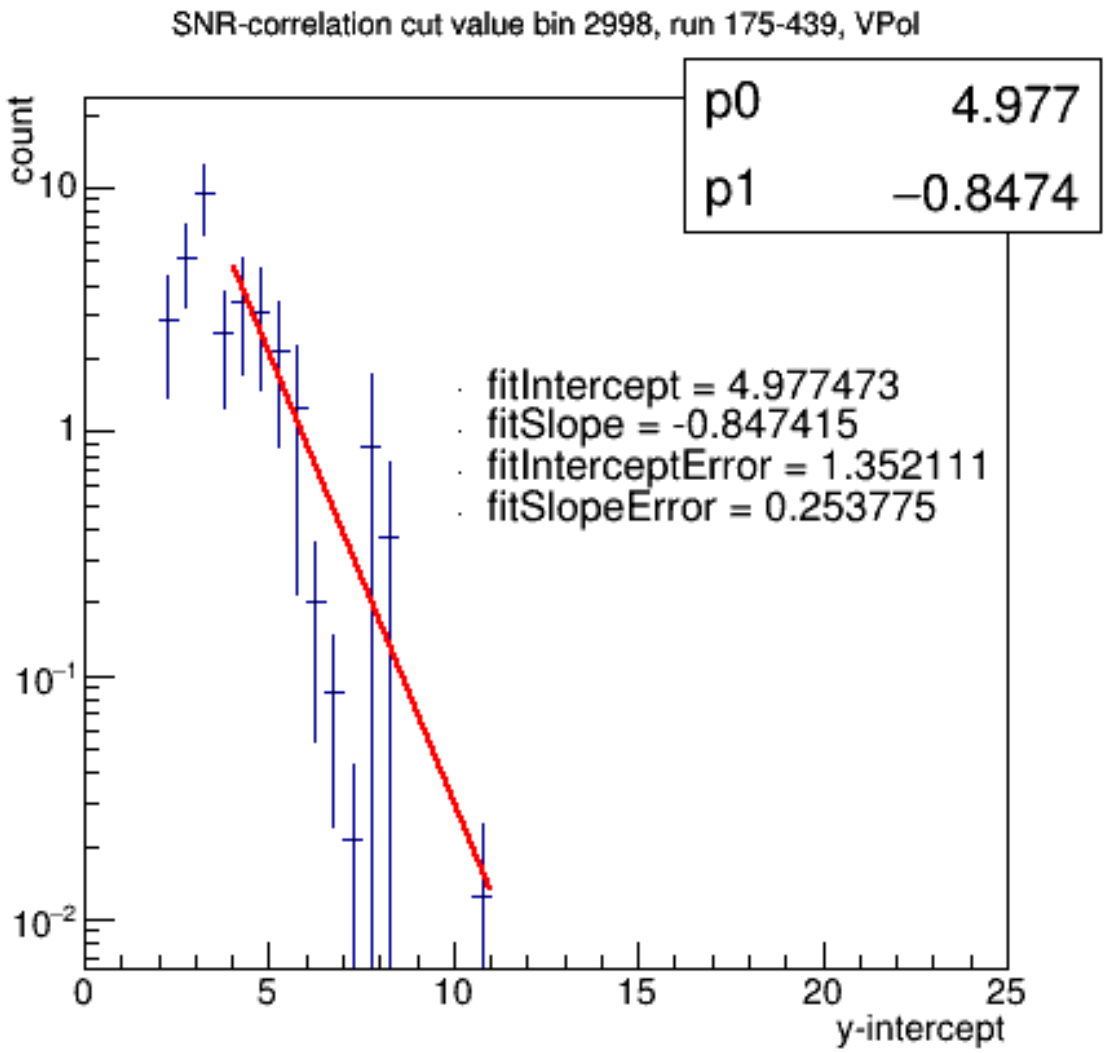

Figure D.2: Distribution and exponential fit for bin 2998 using the 10% dataset or burn sample before final cuts. This is the distribution based on which the optimized LD cut for this bin was determined.

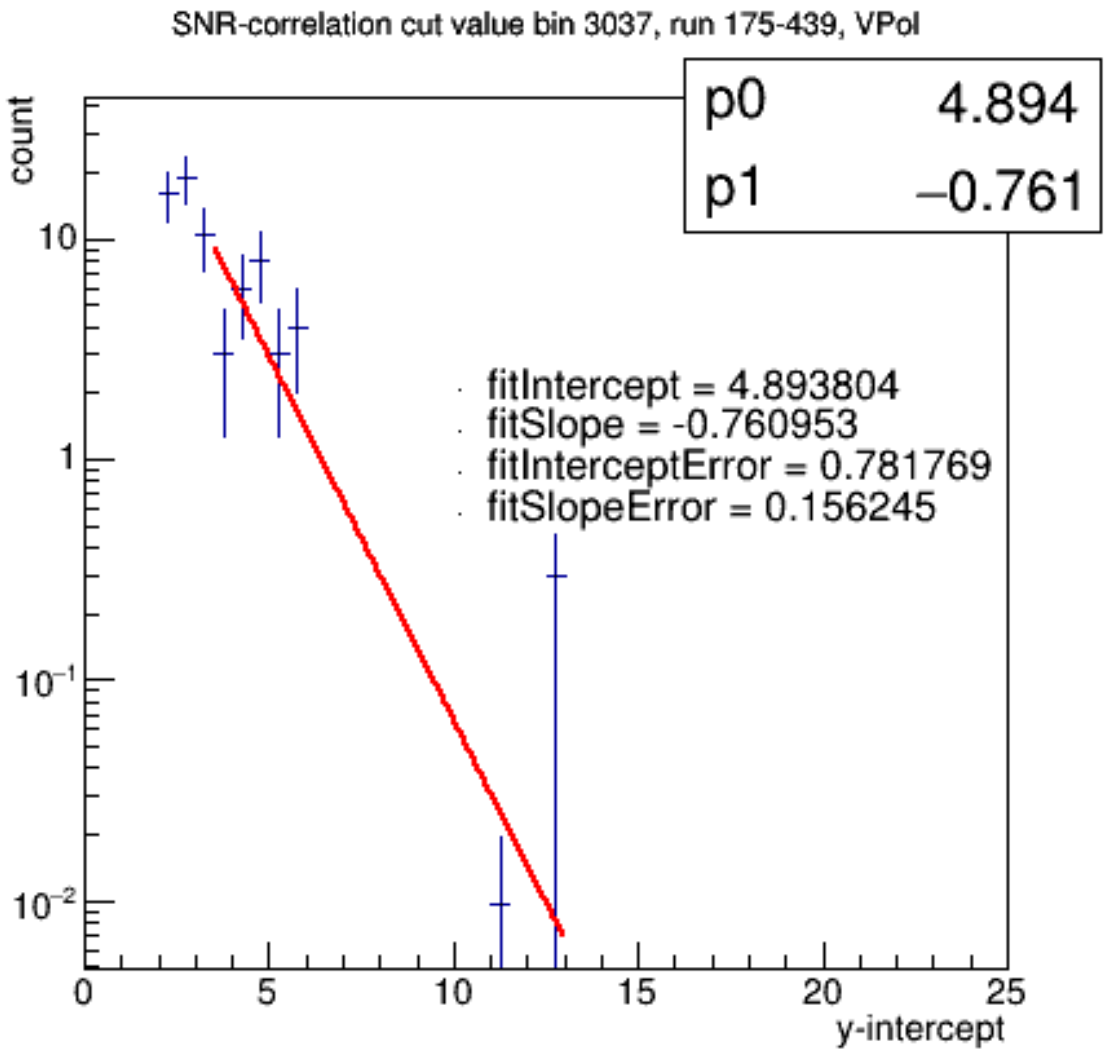

Figure D.3: Distribution and exponential fit for bin 3037 using the 10% dataset or burn sample before final cuts. This is the distribution based on which the optimized LD cut for this bin was determined.

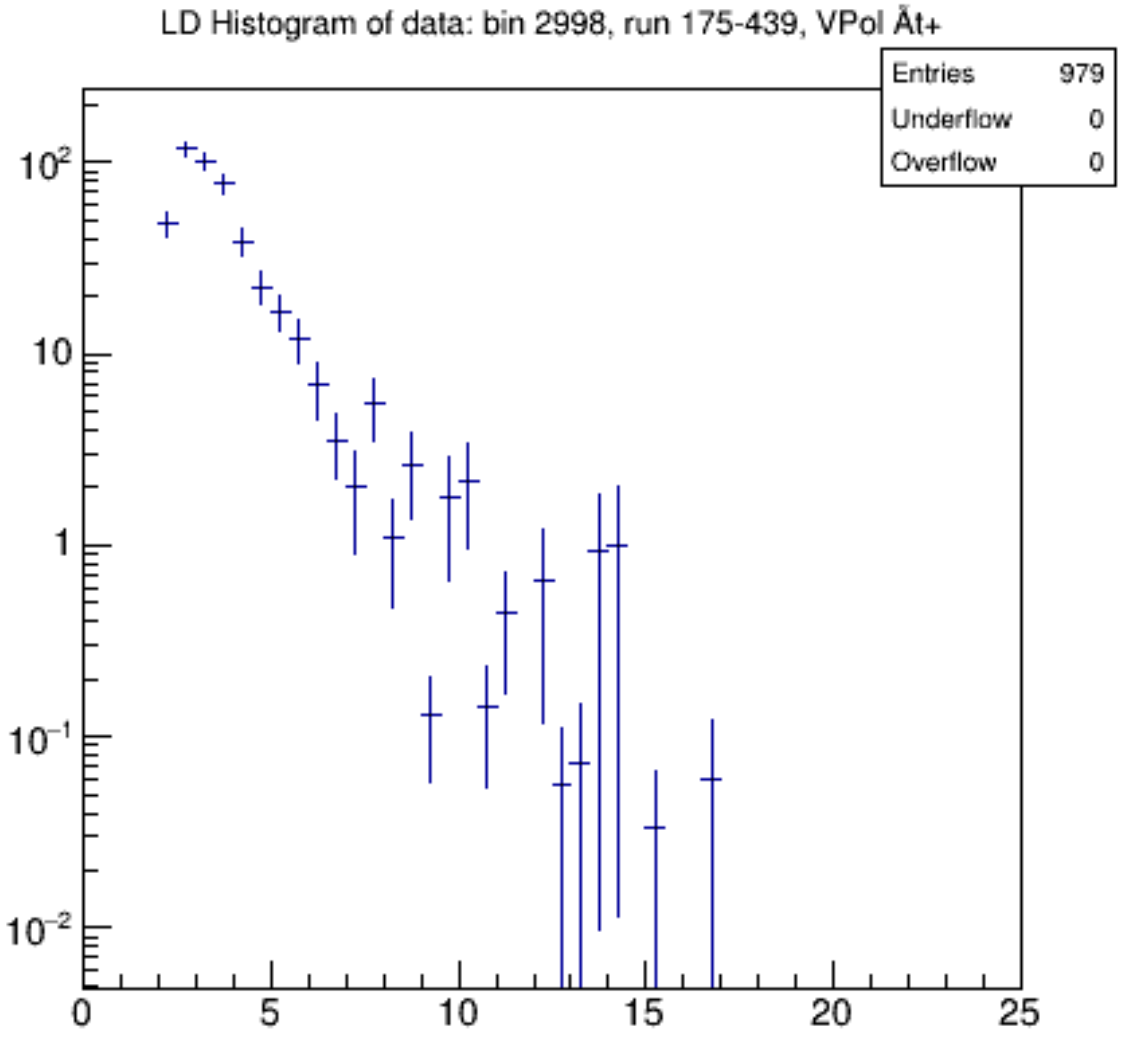

Figure D.4: Distribution and exponential fit for bin 2998 using the 90% dataset before final cuts. Passing singlet event 73750661 belongs to this distribution.

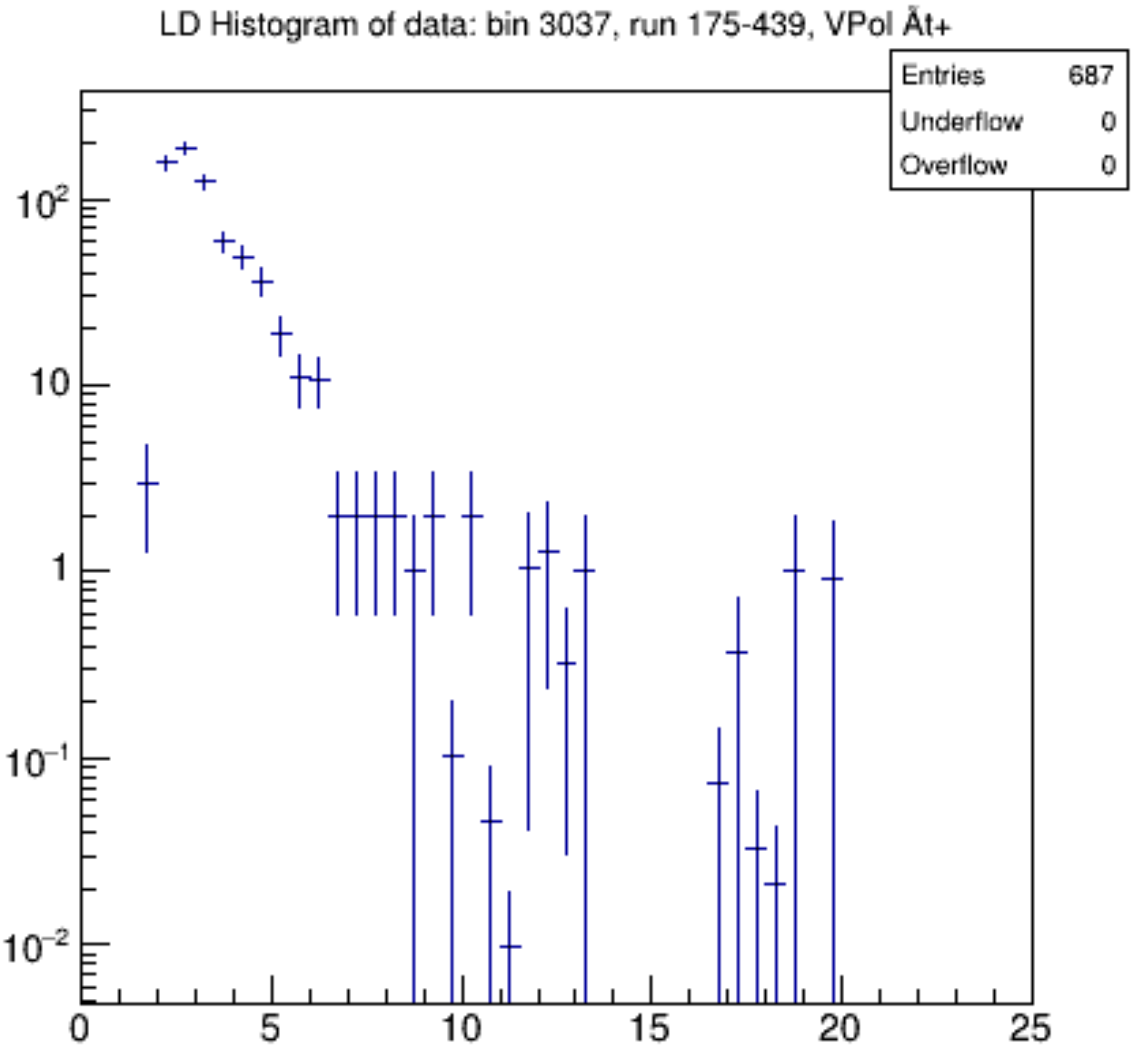

Figure D.5: Distribution and exponential fit for bin 3037 using the 90% dataset before final cuts. Passing singlet event 21702154 belongs to this distribution.

Bibliography

[1] P. Allison, O. Banerjee, J. J. Beatty, A. Connolly, C. Deaconu, J. Gordon, P. W. Gorham, M. Kovacevich, C. Miki, E. Oberla, J. Roberts, B. Rotter, S. Stafford, K. Tatem, L. Batten, K. Belov, D. Z. Besson, W. R. Binns, V. Bugaev, P. Cao, C. Chen, P. Chen, Y. Chen, J. M. Clem, L. Cremonesi, B. Dailey, P. F. Dowkontt, S. Hsu, J. Huang, R. Hupe, M. H. Israel, J. Kowalski, J. Lam, J. G. Learned, K. M. Liewer, T. C. Liu, A. Ludwig, S. Matsuno, K. Mulrey, J. Nam, R. J. Nichol, A. Novikov, S. Prohira, B. F. Rauch, J. Ripa, A. Romero-Wolf, J. Russell, D. Saltzberg, D. Seckel, J. Shiao, J. Stockham, M. Stockham, B. Strutt, G. S. Varner, A. G. Vieregg, S. Wang, S. A. Wissel, F. Wu, and R. Young. Dynamic tunable notch filters for the Antarctic Impulsive Transient Antenna (ANITA). *Nuclear Instruments and Methods Section A*, March 2018.

[2] P. Allison, O. Banerjee, L. Batten, J. J. Beatty, K. Bechtol, K. Belov, D. Z. Besson, W. R. Binns, V. Bugaev, P. Cao, C. C. Chen, C. H. Chen, P. Chen, J. M. Clem, A. Connolly, L. Cremonesi, B. Dailey, C. Deaconu, P. F. Dowkontt, B. D. Fox, J. W. H. Gordon, P. W. Gorham, C. Hast, B. Hill, S. Y. Hsu, J. J. Huang, K. Hughes, R. Hupe, M. H. Israel, K. M. Liewer, T. C. Liu, A. B. Ludwig, L. Macchiarulo, S. Matsuno, C. Miki, K. Mulrey, J. Nam, C. Naudet, R. J. Nichol, A. Novikov, E. Oberla, S. Prohira, B. F. Rauch, J. M. Roberts, A. Romero-Wolf, B. Rotter, J. W. Russell, D. Saltzberg, D. Seckel, H. Schoorlemmer, J. Shiao, S. Stafford, J. Stockham, M. Stockham, B. Strutt, M. S. Sutherland, G. S. Varner, A. G. Vieregg, S. H. Wang, and S. A. Wissel. Constraints on the diffuse high-energy neutrino flux from the third flight of

ANITA. *ArXiv e-prints*, March 2018.

[3] P. W. Gorham et al. Observational constraints on the ultra-high energy cosmic neutrino flux from the second flight of the ANITA experiment. *Phys. Rev. D*, 82:022004, 2010. [Erratum: Phys. Rev. D 85, 049901 (2012)].

[4] P. W. Gorham, B. Rotter, P. Allison, O. Banerjee, L. Batten, J. J. Beatty, K. Bechtol, K. Belov, D. Z. Besson, W. R. Binns, V. Bugaev, P. Cao, C. C. Chen, C. H. Chen, P. Chen, J. M. Clem, A. Connolly, L. Cremonesi, B. Dailey, C. Deaconu, P. F. Dowkontt, B. D. Fox, J. W. H. Gordon, C. Hast, B. Hill, K. Hughes, J. J. Huang, R. Hupe, M. H. Israel, A. Javaid, J. Lam, K. M. Liewer, S. Y. Lin, T. C. Liu, A. Ludwig, L. Macchiarulo, S. Matsuno, C. Miki, K. Mulrey, J. Nam, C. J. Naudet, R. J. Nichol, A. Novikov, E. Oberla, M. Olmedo, R. Prechelt, S. Prohira, B. F. Rauch, J. M. Roberts, A. Romero-Wolf, J. W. Russell, D. Saltzberg, D. Seckel, H. Schoorlemmer, J. Shiao, S. Stafford, J. Stockham, M. Stockham, B. Strutt, G. S. Varner, A. G. Vieregg, S. H. Wang, and S. A. Wissel. Observation of an Unusual Upward-going Cosmic-ray-like Event in the Third Flight of ANITA. *ArXiv e-prints*, March 2018.

[5] A. G. Vieregg, K. Palladino, P. Allison, B. M. Baughman, J. J. Beatty, K. Belov, D. Z. Besson, S. Bevan, W. R. Binns, C. Chen, P. Chen, J. M. Clem, A. Connolly, M. Detrixhe, D. De Marco, P. F. Dowkontt, M. DuVernois, P. W. Gorham, E. W. Grashorn, B. Hill, S. Hoover, M. Huang, M. H. Israel, A. Javaid, K. M. Liewer, S. Matsuno, B. C. Mercurio, C. Miki, M. Mottram, J. Nam, R. J. Nichol, A. Romero-Wolf, L. Ruckman, D. Saltzberg, D. Seckel, G. S. Varner, and Y. Wang. The First Limits on the Ultra-high Energy Neutrino Fluence from Gamma-Ray Bursts. *apj*, 736:50, July 2011.

[6] R. Abbasi, Y. Abdou, T. Abu-Zayyad, M. Ackermann, J. Adams, J.A. Aguilar, M. Ahlers, D. Altmann, K. Andeen, J. Auffenberg, and et al. An absence of neutrinos associated with cosmic-ray acceleration in *gamma*-ray bursts. *Nature*, 484(7394):351–354, April 2012.

[7] D. Guetta, D. Hooper, J. Alvarez-Mun˜Iz, F. Halzen, and E. Reuveni. Neutrinos from

individual gamma-ray bursts in the BATSE catalog. *Astroparticle Physics*, 20:429–455, January 2004.

[8] P. Allison, J. Auffenberg, R. Bard, J. J. Beatty, D. Z. Besson, C. Bora, C.-C. Chen, P. Chen, A. Connolly, J. P. Davies, M. A. DuVernois, B. Fox, P. W. Gorham, K. Hanson, B. Hill, K. D. Hoffman, E. Hong, L.-C. Hu, A. Ishihara, A. Karle, J. Kelley, I. Kravchenko, H. Landsman, A. Laundrie, C.-J. Li, T. Liu, M.-Y. Lu, R. Maunu, K. Mase, T. Meures, C. Miki, J. Nam, R. J. Nichol, G. Nir, A. O'Murchadha, C. G. Pfendner, K. Ratzlaff, M. Richman, B. Rotter, P. Sandstrom, D. Seckel, A. Shultz, J. Stockham, M. Stockham, M. Sullivan, J. Touart, H.-Y. Tu, G. S. Varner, S. Yoshida, and R. Young. First constraints on the ultra-high energy neutrino flux from a prototype station of the Askaryan Radio Array. *Astroparticle Physics*, 70:62–80, October 2015.

[9] S. Adrián-Martínez, A. Albert, I. A. Samarai, M. André, M. Anghinolfi, G. Anton, S. Anvar, M. Ardid, T. Astraatmadja, J.-J. Aubert, B. Baret, J. Barrios-Marti, S. Basa, V. Bertin, S. Biagi, C. Bigongiari, C. Bogazzi, B. Bouhou, M. C. Bouwhuis, J. Brunner, J. Busto, A. Capone, L. Caramete, C. Cârloganu, J. Carr, S. Cecchini, Z. Charif, P. Charvis, T. Chiarusi, M. Circella, F. Classen, R. Coniglione, L. Core, H. Costantini, P. Coyle, A. Creusot, C. Curtil, G. De Bonis, I. Dekeyser, A. Deschamps, C. Distefano, C. Donzaud, D. Dornic, Q. Dorosti, D. Drouhin, A. Dumas, T. Eberl, U. Emanuele, A. Enzenhöfer, J.-P. Ernenwein, S. Escoffier, K. Fehn, P. Fermani, V. Flaminio, F. Folger, U. Fritsch, L. A. Fusco, S. Galatà, P. Gay, S. Geißelsöder, K. Geyer, G. Giacomelli, V. Giordano, A. Gleixner, J. P. Gómez-González, K. Graf, G. Guillard, H. van Haren, A. J. Heijboer, Y. Hello, J. J. Hernández-Rey, B. Herold, J. Hößl, C. W. James, M. de Jong, M. Kadler, O. Kalekin, A. Kappes, U. Katz, P. Kooijman, A. Kouchner, I. Kreykenbohm, V. Kulikovskiy, R. Lahmann, E. Lambard, G. Lambard, G. Larosa, D. Lefèvre, E. Leonora, D. Lo Presti, H. Loehner, S. Loucatos, F. Louis, S. Mangano, M. Marcelin, A. Margiotta, J. A. Martínez-Mora, S. Martini, T. Michael, T. Montaruli, M. Morganti, C. Müller, M. Neff, E. Nezri, D. Palioselitis, G. E. Păvălaş,

C. Perrina, P. Piattelli, V. Popa, T. Pradier, C. Racca, G. Riccobene, R. Richter, C. Rivière, A. Robert, K. Roensch, A. Rostovtsev, D. F. E. Samtleben, M. Sanguineti, J. Schmid, J. Schnabel, S. Schulte, F. Schüssler, T. Seitz, R. Shanidze, C. Sieger, F. Simeone, A. Spies, M. Spurio, J. J. M. Steijger, T. Stolarczyk, A. Sánchez-Losa, M. Taiuti, C. Tamburini, Y. Tayalati, A. Trovato, B. Vallage, C. Vallée, V. Van Elewyck, P. Vernin, E. Visser, S. Wagner, J. Wilms, E. de Wolf, K. Yatkin, H. Yepes, J. D. Zornoza, J. Zúñiga, and P. Baerwald. Search for muon neutrinos from gamma-ray bursts with the ANTARES neutrino telescope using 2008 to 2011 data. *aap*, 559:A9, November 2013.

[10] M. G. Aartsen, R. Abbasi, Y. Abdou, M. Ackermann, J. Adams, J. A. Aguilar, M. Ahlers, D. Altmann, J. Auffenberg, X. Bai, and et al. First Observation of PeV-Energy Neutrinos with IceCube. *Physical Review Letters*, 111(2):021103, July 2013.

[11] B. P. Abbott, R. Abbott, T. D. Abbott, F. Acernese, K. Ackley, C. Adams, T. Adams, P. Addesso, R. X. Adhikari, V. B. Adya, and et al. Gravitational Waves and Gamma-Rays from a Binary Neutron Star Merger: GW170817 and GRB 170817A. *apjl*, 848:L13, October 2017.

[12] E. Waxman. Gamma-Ray Bursts: The Underlying Model. In K. Weiler, editor, *Supernovae and Gamma-Ray Bursters*, volume 598 of *Lecture Notes in Physics, Berlin Springer Verlag*, pages 393–418, 2003.

[13] IceCube Collaboration, R. Abbasi, Y. Abdou, T. Abu-Zayyad, M. Ackermann, J. Adams, J. A. Aguilar, M. Ahlers, M. M. Allen, D. Altmann, and et al. IceCube Sensitivity for Low-Energy Neutrinos from Nearby Supernovae. *ArXiv e-prints*, July 2011.

[14] G. A. Askar'yan. Excess negative charge of an electron-photon shower and its coherent radio emission. *Sov. Phys. JETP*, 14(2):441–443, 1962. [Zh. Eksp. Teor. Fiz.41,616(1961)].

[15] Ara Collaboration, P. Allison, J. Auffenberg, R. Bard, J. J. Beatty, D. Z. Besson, S. Böser, C. Chen, P. Chen, A. Connolly, J. Davies, M. Duvernois, B. Fox, P. W. Gorham, E. W. Grashorn, K. Hanson, J. Haugen, K. Helbing, B. Hill, K. D. Hoffman, E. Hong, M. Huang, M. H. A. Huang, A. Ishihara, A. Karle, D. Kennedy, H. Landsman, T. C. Liu, L. Macchiarulo, K. Mase, T. Meures, R. Meyhandan, C. Miki, R. Morse, M. Newcomb, R. J. Nichol, K. Ratzlaff, M. Richman, L. Ritter, C. Rott, B. Rotter, P. Sandstrom, D. Seckel, J. Touart, G. S. Varner, M.-Z. Wang, C. Weaver, A. Wendorff, S. Yoshida, and R. Young. Design and initial performance of the Askaryan Radio Array prototype EeV neutrino detector at the South Pole. *Astroparticle Physics*, 35:457–477, February 2012.

[16] G. S. Varner, L. L. Ruckman, P. W. Gorham, J. W. Nam, R. J. Nichol, J. Cao, and M. Wilcox. The large analog bandwidth recorder and digitizer with ordered readout (LABRADOR) ASIC. *Nucl. Instrum. Meth.*, A583:447–460, 2007.

[17] C. K. Matassa. Comparing the capabilities and performance of the ultra high frequency follow-on system with the mobile user objective system. Master's thesis, Naval Postgraduate School, 2011.

[18] S. Stafford. PhD thesis, The Ohio State University, 2017.

[19] P. W. Gorham et al. The Antarctic Impulsive Transient Antenna Ultra-high Energy Neutrino Detector Design, Performance, and Sensitivity for 2006-2007 Balloon Flight. *Astropart. Phys.*, 32:10–41, 2009.

[20] B. Dailey. PhD thesis, The Ohio State University, 2016.

[21] J.W.H Gordon. PhD thesis, The Ohio State University, 2018.

[22] P. W. Gorham et al. New Limits on the ultra-high energy cosmic neutrino flux from the ANITA experiment. *Phys. Rev. Lett.*, 103:051103, 2009.

[23] K. Kotera, D. Allard, and A. V. Olinto. Cosmogenic neutrinos: parameter space and detectabilty from PeV to ZeV. *J. Cosmol. Astropart. Phys.*, 10:13, 2010.

[24] K. M. Gorski et al. HEALPix - A Framework for high resolution discretization, and fast analysis of data distributed on the sphere. *Astrophys. J.*, 622:759–771, 2005.

[25] P. Mészáros. Gamma-ray bursts. *Reports on Progress in Physics*, 69:2259–2321, August 2006.

[26] M. Bustamante. Ultra-high-energy neutrinos and cosmic rays from gamma-ray bursts: exploring and updating the connection.

[27] E. Waxman and J. Bahcall. High Energy Neutrinos from Cosmological Gamma-Ray Burst Fireballs. *Physical Review Letters*, 78:2292–2295, March 1997.

[28] K. Hurley, B. L. Dingus, R. Mukherjee, P. Sreekumar, C. Kouveliotou, C. Meegan, G. J. Fishman, D. Band, L. Ford, D. Bertsch, T. Cline, C. Fichtel, R. Hartman, S. Hunter, D. J. Thompson, G. Kanbach, H. Mayer-Hasselwander, C. von Montigny, M. Sommer, Y. Lin, P. Nolan, P. Michelson, D. Kniffen, J. Mattox, E. Schneid, M. Boer, and M. Niel. Detection of a γ-ray burst of very long duration and very high energy. *nat*, 374:94, March 1995.

[29] M. Ackermann, K. Asano, W. B. Atwood, M. Axelsson, L. Baldini, J. Ballet, G. Barbiellini, M. G. Baring, D. Bastieri, K. Bechtol, R. Bellazzini, B. Berenji, P. N. Bhat, E. Bissaldi, R. D. Blandford, E. D. Bloom, E. Bonamente, A. W. Borgland, A. Bouvier, J. Bregeon, A. Brez, M. S. Briggs, M. Brigida, P. Bruel, S. Buson, G. A. Caliandro, R. A. Cameron, P. A. Caraveo, S. Carrigan, J. M. Casandjian, C. Cecchi, Ö. Çelik, E. Charles, J. Chiang, S. Ciprini, R. Claus, J. Cohen-Tanugi, V. Connaughton, J. Conrad, C. D. Dermer, F. de Palma, B. L. Dingus, E. d. C. e. Silva, P. S. Drell, R. Dubois, D. Dumora, C. Farnier, C. Favuzzi, S. J. Fegan, J. Finke, W. B. Focke, M. Frailis, Y. Fukazawa, P. Fusco, F. Gargano, D. Gasparrini, N. Gehrels, S. Germani, N. Giglietto, F. Giordano, T. Glanzman, G. Godfrey, J. Granot, I. A. Grenier, M.-H. Grondin, J. E. Grove, S. Guiriec, D. Hadasch, A. K. Harding, E. Hays, D. Horan, R. E. Hughes, G. Jóhannesson, W. N. Johnson, T. Kamae, H. Katagiri, J. Kataoka, N. Kawai, R. M. Kippen, J. Knödlseder, D. Kocevski, C. Kouveliotou, M. Kuss, J. Lande, L. Latron-

ico, M. Lemoine-Goumard, M. Llena Garde, F. Longo, F. Loparco, B. Lott, M. N. Lovellette, P. Lubrano, A. Makeev, M. N. Mazziotta, J. E. McEnery, S. McGlynn, C. Meegan, P. Mészáros, P. F. Michelson, W. Mitthumsiri, T. Mizuno, A. A. Moiseev, C. Monte, M. E. Monzani, E. Moretti, A. Morselli, I. V. Moskalenko, S. Murgia, H. Nakajima, T. Nakamori, P. L. Nolan, J. P. Norris, E. Nuss, M. Ohno, T. Ohsugi, N. Omodei, E. Orlando, J. F. Ormes, M. Ozaki, W. S. Paciesas, D. Paneque, J. H. Panetta, D. Parent, V. Pelassa, M. Pepe, M. Pesce-Rollins, F. Piron, R. Preece, S. Rainò, R. Rando, M. Razzano, S. Razzaque, A. Reimer, S. Ritz, A. Y. Rodriguez, M. Roth, F. Ryde, H. F.-W. Sadrozinski, A. Sander, J. D. Scargle, T. L. Schalk, C. Sgrò, E. J. Siskind, P. D. Smith, G. Spandre, P. Spinelli, M. Stamatikos, F. W. Stecker, M. S. Strickman, D. J. Suson, H. Tajima, H. Takahashi, T. Takahashi, T. Tanaka, J. B. Thayer, J. G. Thayer, D. J. Thompson, L. Tibaldo, K. Toma, D. F. Torres, G. Tosti, A. Tramacere, Y. Uchiyama, T. Uehara, T. L. Usher, A. J. van der Horst, V. Vasileiou, N. Vilchez, V. Vitale, A. von Kienlin, A. P. Waite, P. Wang, C. Wilson-Hodge, B. L. Winer, X. F. Wu, R. Yamazaki, Z. Yang, T. Ylinen, and M. Ziegler. Fermi Observations of GRB 090510: A Short-Hard Gamma-ray Burst with an Additional, Hard Power-law Component from 10 keV TO GeV Energies. *apj*, 716:1178–1190, June 2010.

[30] E. Waxman and J. Bahcall. High energy neutrinos from astrophysical sources: An upper bound. *prd*, 59(2):023002, January 1999.

[31] E. Waxman and J. N. Bahcall. Neutrino Afterglow from Gamma-Ray Bursts: ˜10^{18} EV. *apj*, 541:707–711, October 2000.

[32] J. Bahcall and E. Waxman. High energy astrophysical neutrinos: The upper bound is robust. *prd*, 64(2):023002, July 2001.

[33] S. Hümmer, M. Rüger, F. Spanier, and W. Winter. Simplified Models for Photohadronic Interactions in Cosmic Accelerators. *The Astrophysical Journal*, 721:630–652, September 2010.

[34] S. Hümmer, P. Baerwald, and W. Winter. Neutrino Emission from Gamma-Ray Burst Fireballs, Revised. *Physical Review Letters*, 108(23):231101, June 2012.

[35] K. Murase. High energy neutrino early afterglows from gamma-ray bursts revisited. *Phys. Rev. D*, 76(12):123001, December 2007.

[36] P. W. Gorham, J. Nam, A. Romero-Wolf, S. Hoover, P. Allison, O. Banerjee, J. J. Beatty, K. Belov, D. Z. Besson, W. R. Binns, V. Bugaev, P. Cao, C. Chen, P. Chen, J. M. Clem, A. Connolly, B. Dailey, C. Deaconu, L. Cremonesi, P. F. Dowkontt, M. A. Duvernois, R. C. Field, B. D. Fox, D. Goldstein, J. Gordon, C. Hast, C. L. Hebert, B. Hill, K. Hughes, R. Hupe, M. H. Israel, A. Javaid, J. Kowalski, J. Lam, J. G. Learned, K. M. Liewer, T. C. Liu, J. T. Link, E. Lusczek, S. Matsuno, B. C. Mercurio, C. Miki, P. Miočinović, M. Mottram, K. Mulrey, C. J. Naudet, J. Ng, R. J. Nichol, K. Palladino, B. F. Rauch, K. Reil, J. Roberts, M. Rosen, B. Rotter, J. Russell, L. Ruckman, D. Saltzberg, D. Seckel, H. Schoorlemmer, S. Stafford, J. Stockham, M. Stockham, B. Strutt, K. Tatem, G. S. Varner, A. G. Vieregg, D. Walz, S. A. Wissel, F. Wu, and Anita Collaboration. Characteristics of Four Upward-Pointing Cosmic-Ray-like Events Observed with ANITA. *Physical Review Letters*, 117(7):071101, August 2016.